Numerical Investigations of Flow Phenomena in Shock Tubes and Detonation Characteristics of Ozonated Mixtures

Von der Fakultät für Ingenieurwissenschaften, Abteilung Maschinenbau und Verfahrenstechnik

der

Universität Duisburg-Essen

zur Erlangung des akademischen Grades

eines

Doktors der Ingenieurwissenschaften

Dr.-Ing.

genehmigte Dissertation

von

Jonathan Timo Lipkowicz
aus
Düsseldorf

Tag der mündlichen Prüfung: 09.07.2024

1. Gutachter: Univ.-Prof. Dr.-Ing Andreas M. Kempf
2. Gutachter: Prof. Dr. Pascale Domingo

Declaration of Authorship

I, Jonathan Timo Lipkowicz, declare that this thesis entitled, ”Numerical Investigations of Flow Phenomena in Shock Tubes and Detonation Characteristics of Ozonated Mixtures“ and the presented work are my own. This work was done while in candidature for a research degree at the University of Duisburg-Essen. This thesis has not been previously submitted for a degree or any other qualification at any other institution. The published work of others has been referenced clearly.

Signed: Jonathan Timo Lipkowicz

Date:

Zusammenfassung

In dieser Arbeit wurden Modelle zur Simulation reaktiver Überschallströmungen entwickelt und implementiert. Dabei wurden einerseits Experimente in Stoßwellenrohren simuliert, um Zündphänomene und Grenzschichteinflüsse zu untersuchen. Zum anderen wurden Simulationen von Detonationswellen durchgeführt, um Eigenschaften bezüglich Zellstruktur und Zellstabilisierung zu analysieren.

Für die Simulation kompressibler Strömungen wurde zunächst der hauseigene Code PsiPhi erweitert. Hierbei kamen approximative Riemann-Löser und charakteristische Randbedingungen zum Einsatz. Aufgrund der dissipativen Natur von Upwind-Verfahren wurden außerdem Interpolationsverfahren höherer Genauigkeit getestet und angewendet, um turbulente Strömungen adäquat abzubilden. Zur Simulation von Zündprozessen wurde ein Verbrennungsmodell auf Basis der Finite-Raten-Chemie verwendet, welches im Vergleich zu tabellierten Verbrennungsmodellen rechenintensiver ist. Daher wurden implizite und semiimplizite Löser für Systeme gewöhnlicher Differentialgleichungen implementiert, um die Recheneffizienz zu verbessern. Die Integration eines Operator-Splitting-Frameworks führte zu einer weiteren Reduzierung der Rechenkosten.

Für die Simulation von Stoßwellenrohrexperimenten wurde im Anschluss ein Workflow entwickelt, bei dem nur ein kleiner Teil des Stoßwellenrohres berechnet werden muss. Dieser Teil kann jedoch räumlich hoch aufgelöst werden. Hierbei wird zunächst eine kleinere Hilfsrechnung benötigt, die das initiale Riemann-Problem zum Start des Experiments simuliert. Nachdem sich der einfallende Stoß vollständig entwickelt hat, wird ein vorab definierter Bereich um den einfallenden Stoß herum gespeichert und in der darauf folgenden Hauptsimulation, die nur den Endteil des Stoßwellenrohres abdeckt, als Startlösung verwendet. Aufgrund der Bildung einer Grenzschicht hinter dem einfallenden Stoß ändern sich die Zustandsgrößen am Einlassrand der Rechendomäne. Daher wurde eine Randbedingung entwickelt, die Modelle für laminare Grenzschichten, turbulente Grenzschichten, Grenzschichttransition und deren Einfluss auf die Kernströmung anhand der "Small Perturbation Theory" vereint und die Größen als Funktion des Wandabstandes und der Zeit vorgibt. Der Ansatz wurde anhand experimenteller Daten validiert und konnte Experimente reproduzieren, bei denen eine ungewollte Zündung fernab der Endwand auftrat. Darüber hinaus konnte eine der ersten 3D-Simulationen von Stoßwellenrohrexperimenten eine durch Stoßbirfukration verursachte Zündung nachweisen.

Im zweiten Teil dieser Arbeit wurde die Ausbreitung von Detonationswellen in Kanälen und Rohren untersucht. Um auch hier eine hohe numerische Auflösung zu ermöglichen, wurde ein relatives Koordinatensystem verwendet, sodass die gemittelte Detonationsfront stationär ist und mit einer kleinen Rechendomäne numerisch untersucht werden kann. Die Ergebnisse wurden anhand numerischer Rußfolien mit experimentellen Daten verglichen. Dabei konnte die mittlere Zellweite sowie die Größenverteilung zufriedenstellend reproduziert werden. Dies ist bislang nur wenigen Studien gelungen, da aus Kostengründen häufig stark vereinfachte 1-Schritt-Reaktionsmechanismen verwendet wurden. Die Daten dienten außerdem als Grundlage für die Entwicklung eines geometrischen, effizienten Modells für die Detonationszellstruktur. Eine Stabilitätshypothese für Detonationszellgrößen konnte anhand zeitlich hoch aufgelöster Ergebnisse überprüft und für die hier untersuchten Mischungen bestätigt werden.

Abstract

In this work, models for simulating reactive supersonic flows were developed and implemented. On one hand, experiments in shock tubes were simulated to investigate ignition phenomena and boundary layer effects. On the other hand, simulations of detonation waves were conducted to analyze properties related to cell structure and cell stabilization.

For the simulation of compressible flows, the in-house code PsiPhi was first expanded. Approximate Riemann solvers and characteristic boundary conditions were used. Due to the dissipative nature of Upwind methods, interpolation methods of higher accuracy were also tested and applied to adequately represent turbulent flows. For simulating ignition processes, a finite-rate chemistry combustion model was employed, which is computationally more intensive compared to tabulated combustion models. Therefore, implicit and semi-implicit solvers for systems of ordinary differential equations were implemented to enhance computational efficiency. The integration of an Operator-Splitting framework further led to a reduction in computational costs.

Subsequently, a workflow was developed for simulating shock tube experiments, where only a small portion of the shock tube needs to be computed, but with high spatial resolution. Initially, a smaller auxiliary calculation was needed to simulate the initial Riemann problem at the start of the experiment. After the incident shock wave has fully developed, a predefined region around the incident shock wave is saved and used as the initial solution in the subsequent main simulation, which covers only the end part of the shock tube. Due to the formation of a boundary layer behind the incident shock, the state variables at the inlet boundary of the computational domain change. Therefore, a boundary condition was developed, which combines models for laminar boundary layers, turbulent boundary layers, boundary layer transition, and their influence on the core flow based on the “Small Perturbation Theory”, specifying the variables as a function of wall distance and time. This approach was validated using experimental data and was able to reproduce experiments where an unintended ignition occurred far from the end wall. Additionally, one of the first 3D simulations of shock tube experiments was able to demonstrate ignition caused by reflected shock bifurcation.

In the second part of this work, the propagation of detonation waves in channels and tubes was investigated. To allow for high numerical resolution, a relative coordinate system was used, ensuring that the averaged detonation front is stationary and can be numerically examined with a small computational domain. The results were compared with experimental data using numerical soot foils. The average cell width and size distribution could be satisfactorily reproduced. This has been achieved by only a few studies so far, as often heavily simplified one-step reaction mechanisms were used due to cost considerations. The data also served as a basis to develop a geometrically efficient model for the detonation cell structure. A stability hypothesis for detonation cell sizes was also verified based on temporally highly resolved results and was confirmed for the mixtures investigated here.

Preface

The research presented in this thesis was conducted during my time as a research assistant at the Chair of Fluid Mechanics at the University of Duisburg-Essen. First and foremost, I would like to express my gratitude to my doctoral supervisor, Prof. Dr.-Ing. Andreas Kempf, who placed trust in me even as a student and provided me with the opportunity to delve into this captivating field. Moreover, Andreas enabled me to write my master's thesis at a prestigious university in the United States, which allowed me to establish vital connections. Throughout my doctoral studies, Andreas has been consistently available to guide me towards the core aspects of my research and offer inspiration when solutions seemed out of reach.

I would also like to extend my appreciation to Dr.-Ing. Irenäus Wlokas, who played a significant role in shaping the project for the first part of this thesis. His valuable advice on the required numerical techniques and insightful discussions, especially at the beginning of this work, have been immensely helpful.

Additionally, I am grateful to my colleagues at the Chair of Fluid Dynamics, namely Sylvia Helwig, Olaf Hasemann, Johannes Sellmann, Pascal Gruhlke, Patrick Wollny, Andreas Rittler, Peter Janas, Martin Rieth, Fabian Proch, Lei Deng, Thuong Nguyen, Nejra Sikalo, Miriam Rabacal, Eray Inanc, Hossein Janbazi, Seung-Jin Baik, Luis Cifuentes, Linus Engelmann, Dominik Meller, Monika Nanjaiah, Andreas Unterberger, Jonas Eigemann, Michael Vetter, Robert Externbrink, Vahid Sharifi, and Prof. Khadijeh Mohri. I cherish the wonderful moments we shared, the numerous fruitful discussions, and the enjoyable experiences outside of work and during conferences. Special thanks are due to Pascal Gruhlke, Johannes Sellmann, Linus Engelmann, and Dominik Meller for proofreading this work.

Furthermore, I would like to express my gratitude to my project partners at the Chair of Reaction Kinetics in Duisburg, Prof. Dr.-Ing. Christof Schulz, Dr. Damien Nativel, and Dr.-Ing. Mustapha Fikri, for their unwavering support and invaluable insights into the execution and challenges associated with shock-tube experiments. Together, we faced the task of striking a harmonious balance between the limitations imposed by numerical simulations and the need to address relevant experimental issues.

In the second part of this thesis, I had the privilege of working on an exceptionally exciting topic with the Department of Mechanical Engineering at Stanford University. I would like to extend my thanks to Prof. Hai Wang, Prof. Xian Shi, and Prof. Jackson Crane for their excellent collaboration and intriguing ideas.

Finally, I would like to express my deepest gratitude to my parents, Karin and Michael, and my sister, Larissa, for their constant support and encouragement. Of course, my deepest thanks go to my wife Denise. This work would not have been possible without her patience. I am profoundly grateful to Denise for her love and tremendous support throughout this journey.

Dedicated to my wife Denise, my daughter Ida Louisa, and our future children.

Contents

List of Figures

List of Tables

Nomenclature

Lower case roman symbols

a_j	Low-storage Runge Kutta model coefficients	1
a_α	Efficiency factor of species α	1
b_j	Low-storage Runge Kutta model coefficients	1
c	Speed of sound α	$\mathrm{m\ s^{-1}}$
c_p	Specific heat capacity of a mixture at constant pressure	$\mathrm{m^2\ s^{-2}\ K^{-1}}$
c_v	Specific heat capacity of a mixture at constant volume	$\mathrm{m^2\ s^{-2}\ K^{-1}}$
$c_{p,\alpha}$	Specific heat capacity of species α at constant pressure	$\mathrm{m^2\ s^{-2}\ K^{-1}}$
$c_{v,\alpha}$	Specific heat capacity of species α at constant volume	$\mathrm{m^2\ s^{-2}\ K^{-1}}$
d_h	Hydraulic diameter	m
f	Force per unit mass	$\mathrm{m\ s^{-2}}$
g_{ij}	Velocity gradient tensor	$\mathrm{s^{-1}}$
h	Specific sensible enthalpy	$\mathrm{m^2\ s^{-2}}$
$h^0_{\mathrm{f},\alpha}$	Specific enthalpy of formation of species α	$\mathrm{m^2\ s^{-2}}$
h^0_f	Specific enthalpy of formation	$\mathrm{m^2\ s^{-2}}$
h_α	Specific sensible enthalpy of species α	$\mathrm{m^2\ s^{-2}}$
$j_{i,\alpha}$	Diffusive mass flux of species α in i-direction	$\mathrm{kg\ m^{-2}\ s^{-1}}$
k	Wave number	$\mathrm{m^{-1}}$
k_b	Backward reaction rate constant	$\mathrm{s^{-1}}$
k_f	Cut-off wave number	$\mathrm{m^{-1}}$
k_f	Forward reaction rate constant	$\mathrm{s^{-1}}$
$k_{\mathrm{f},0}$	Forward reaction rate constant in low pressure limit	$\mathrm{s^{-1}}$
$k_{\mathrm{f},\infty}$	Forward reaction rate constant in high pressure limit	$\mathrm{s^{-1}}$
l_t	Integral length scale	m
l_0	Characteristic length scale	m
m_α	Mass of species α in a given system	kg
n_fp	Number of flame points	1
n_α	Amount of species α in a given system	mol
p	Static pressure	$\mathrm{kg\ m^{-1}\ s^{-2}}$
q_i	Heat flux vector in i-direction	$\mathrm{kg\ s^{-3}}$
q_j	Classic Runge Kutta weights	1
q_r	Rate of progress of reaction r	$\mathrm{mol\ m^{-3}\ s^{-1}}$
s	Specific entropy	$\mathrm{m^2\ s^{-2}\ K^{-1}}$
s^0_L	Unstretched laminar flame speed	$\mathrm{m\ s^{-1}}$
$s_{T\Delta}$	Sub-filter turbulent flame speed	$\mathrm{m\ s^{-1}}$
t	Time	s
t_tr	Boundary layer transition time	s
t_0	Characteristic time	s
u_s	Incident shock velocity	$\mathrm{m\ s^{-1}}$
u'	Velocity fluctuation	$\mathrm{m\ s^{-1}}$
u_i	Components of the velocity vector	$\mathrm{m\ s^{-1}}$
v	Specific volume	$\mathrm{m^3\ kg^{-1}}$
v_k	Kolmogorov velocity scale	$\mathrm{m\ s^{-1}}$
x_i	Components of the Cartesian coordinate vector	m

Upper case roman symbols

A	Pre-exponential coefficient in Arrhenius expression	1
C	Normalized flame progress variable	1
C_{m}	Constant of model m	1
C_{s}	Smagorinsky model constant	1
D	Diameter	m
D_{α}	Diffusion coefficient of species α in terms of mass fractions	$\mathrm{m^2\ s^{-1}}$
D'_{α}	Diffusion coefficient of species α in terms of mole fractions	$\mathrm{m^2\ s^{-1}}$
$D_{\mathrm{m},\alpha}$	Diffusion coefficient of species α into a mixture	$\mathrm{m^2\ s^{-1}}$
E	Efficiency function	1
E	Total internal energy	$\mathrm{m^2\ s^{-2}}$
$E(k)$	Kinetic energy spectrum	$\mathrm{m^3\ s^{-2}}$
E_{a}	Activation energy in Arrhenius expression	$\mathrm{kg\ m^2\ s^{-2}\ mol^{-1}}$
F	Fall-off factor	1
G	Filter kernel	1
IS_i	Smoothness indicator of i-th stencil candidate	1
K_{stokes}	Stokes constant	m
L	Length scale	m
L_{ij}	Germano identity	$\mathrm{kg\ m^{-1}\ s^{-2}}$
M	Mach number	1
M_{rs}	Mach number of reflected shock	1
M_{s}	Incident shock Mach number	1
P	Sub-grid filtered density function	1
P_{r}	Dimensionless pressure in terms of Fall-Off reactions	1
R_{s}	Specific gas constant	$\mathrm{m^2\ s^{-2}\ K^{-1}}$
R_{u}	Universal gas constant	$\mathrm{kg\ m^2\ mol^{-1}\ s^{-2}\ K^{-1}}$
S_{μ}	Fitting parameter in Sutherland law	K
S_{ij}	Strain rate tensor	$\mathrm{s^{-1}}$
S_{ij}^{d}	Deviatoric contribution strain rate tensor	$\mathrm{s^{-1}}$
T	Thermodynamic temperature	K
T_{r}	Recovery temperature	K
T^b	Temperature raised to the power of b in Arrhenius expression	K^b
T_{ref}	Reference temperature in Sutherland law	K
T_{ij}	Sub-grid scale stress tensor at test filter size	$\mathrm{kg\ m^{-1}\ s^{-2}}$
U_{m}	Mean velocity	$\mathrm{m\ s^{-1}}$
U_i	Components of the velocity vector in wave frame coordinates	$\mathrm{m\ s^{-1}}$
$V_{\mathrm{C},i}$	Diffusion correction velocity in i-direction	$\mathrm{m\ s^{-1}}$
$V_{i,\alpha}$	Diffusion velocity of species α in i-direction	$\mathrm{m\ s^{-1}}$
W	Mean molecular weight	$\mathrm{mol\ kg^{-1}}$
W_{α}	Molecular weight of species α	$\mathrm{mol\ kg^{-1}}$
X_{α}	Mole fraction of species α	1
Y_{α}	Mass fraction of species α	1
$[\mathrm{M}]$	Effective concentration	$\mathrm{mol\ m^{-3}}$
M	Third body	1

Lower case greek symbols

β_{ji}	Classic Runge Kutta model coefficients	1
δ	Boundary layer thickness	m
δ_{L}^0	Unstretched laminar flame thickness	m
δ^*	Boundary layer displacement thickness	m
δ_{ij}	Kronecker delta	1

$\dot{\omega}_\alpha$	Source term of species α	kg m^{-3} s^{-1}
ϵ	Dissipation rate	m^{2} s^{-3}
η	Similarity parameter laminar boundary layer	
η_i	Inner cut-off scale	m
η_k	Kolmogorov length scale	m
γ	Ratio of specific heats	1
γ_HR	High-resolution factor	1
λ	Thermal conductivity of a mixture	kg m s^{-3} K^{-1}
λ_α	Thermal conductivity of species α	kg m s^{-3} K^{-1}
μ	Dynamic viscosity of a mixture	kg m^{-1} s^{-1}
μ_ref	Reference viscosity in Sutherland law	kg m^{-1} s^{-1}
μ_α	Dynamic viscosity of species α	kg m^{-1} s^{-1}
ν	Kinematic viscosity	m s^{-2}
ν_t	Turbulent kinematic viscosity	m s^{-2}
ν''_α	Stoichiometric coefficient for species α in products	1
ν'_α	Stoichiometric coefficient for species α in reactants	1
ψ	Scalar streaming function	1
ρ	Mass density	kg m^{-3}
ρ_α	Partial mass density of species α	kg m^{-3}
σ_i	Singular values	1
σ_{ij}	Stress tensor	kg m^{-1} s^{-2}
τ_c	Chemical time scale	s
τ_k	Kolmogorov time scale	s
τ_m	Eddy turnover time	s
τ_t	Turbulent time scale	s
τ_{ij}	Viscous stress tensor	kg m^{-1} s^{-2}
ξ	Similarity parameter turbulent boundary layer	1

Upper case greek symbols

Δ	Filter size	m
Δ_x	Grid size	m
$\hat{\Delta}$	Test filter size	m
$\Phi_{\alpha\beta}$	Constant part in Wilke formula	1
$\psi(r)$	Limiter function	1
Θ	Boundary layer momentum thickness	m
Ξ_Δ	Sub-filter wrinkling factor	1

Upper case calligraphic symbols

$[\mathcal{X}]_\alpha$	Concentration of species α	mol m^{-3}
$\mathcal{C}_{ij}$	Cross sub-grid scale stress tensor	kg m^{-1} s^{-2}
$\mathcal{D}$	Domain	1
$\mathcal{D}_\mathrm{m}$	Differential operator of model m	1
$\mathcal{D}_{\alpha\beta}$	Binary diffusion coefficient of species α and β	m^{2} s^{-1}
$\mathcal{E}_1$	First unclosed term energy equation	kg m^{-1} s^{-3}
$\mathcal{E}_2$	Second unclosed term energy equation	kg m^{-1} s^{-3}
$\mathcal{E}_3$	Third unclosed term energy equation	kg m^{-1} s^{-3}
$\mathcal{E}_4$	Fourth unclosed term energy equation	kg m^{-1} s^{-3}
$\mathcal{J}_i$	Components of sub-grid scale turbulent diffusion	kg s^{-3}
$\mathcal{K}$	Sub-grid kinetic energy	kg m^{-1} s^{-2}
$\mathcal{L}_{ij}$	Leonard sub-grid scale stress tensor	kg m^{-1} s^{-2}
$\mathcal{M}^{+}$	Split Mach number function left to cell interface	1

$\mathcal{M}^-$	Split Mach number function right to cell interface	1
$\mathcal{P}^+$	Split pressure function left to cell interface	1
$\mathcal{P}^-$	Split pressure function right to cell interface	1
$\mathcal{Q}$	Net rate of external energy input	kg m^{-1} s^{-3}
$\mathcal{Q}_i$	Components of sub-grid scale heat fluxes	kg s^{-3}
$\mathcal{R}_{ij}$	Reynolds sub-grid scale stress tensor	kg m^{-1} s^{-2}
$\mathcal{S}$	Characteristic strain rate	s^{-1}
$\mathcal{S}_{i,\alpha}$	Components of unresolved scalar fluxes of species α	kg m^{-2} s^{-1}
$\mathcal{T}_{ij}$	Sub-grid scale stress tensor	kg m^{-1} s^{-2}
$\mathcal{T}_{ij}^{\text{d}}$	Deviatoric contribution of sub-grid scale stresses	kg m^{-1} s^{-2}
$\mathcal{T}_{kk}$	Isotropic contribution of sub-grid scale stresses	kg m^{-1} s^{-2}
$\mathcal{U}_1$	First unclosed term momentum equation	kg m^{-2} s^{-2}
$\mathcal{U}_2$	Second unclosed term momentum equation	kg m^{-2} s^{-2}
$\mathcal{X}_\alpha$	Chemical formula of species α	1
$\mathcal{Y}_1$	First unclosed term partial density equation	kg m^{-3} s^{-1}
$\mathcal{Y}_2$	Second unclosed term partial density equation	kg m^{-3} s^{-1}
$\mathcal{Y}_3$	Third unclosed term partial density equation	kg m^{-3} s^{-1}

Dimensionless numbers

Da	Damköhler number	1
Le	Lewis number	1
Pr	Prandtl number	1
Pr_t	Turbulent Prandtl number	1
Re	Reynolds number	1
Re_k	Kolmogorov Reynolds number	1
Re_tr	Transition Reynolds number	1
Re_t	Integral Reynolds number	1
Re_t	Turbulent Reynolds number	1
Sc	Schmidt number	1
Sc_t	Turbulent Schmidt number	1

Physical constants

R_m	Ideal gas constant	8.314459 J/mol/K

Subscripts

ϕ_B	Cell averaged value in bottom cell
ϕ_b	Interpolated value at bottom cell face
ϕ_E	Cell averaged value in eastern cell
ϕ_e	Interpolated value at eastern cell face
ϕ_e	Value in external flow
ϕ_N	Cell averaged value in northern cell
ϕ_n	Interpolated value at northern cell face
ϕ_S	Cell averaged value in southern cell
ϕ_s	Interpolated value at southern cell face
ϕ_T	Cell averaged value in top cell
ϕ_t	Interpolated value at top cell face
ϕ_W	Cell averaged value in western cell
ϕ_w	Interpolated value at western cell face
ϕ_w	Value at the wall
ϕ_0	Initial value
ϕ_1	Pre shock value

ϕ_1	Value in shock-tube region 1
ϕ_2	Post shock value
ϕ_2	Value in shock-tube region 2
ϕ_3	Value in shock-tube region 3
ϕ_4	Value in shock-tube region 4
ϕ_5	Value in shock-tube region 5

Superscripts

$\check{\phi}$	Computable term
ϕ^+	Right running wave contribution
ϕ^+	Value left to cell interface
ϕ^-	Left running wave contribution
ϕ^-	Value right to cell interface

Operators

$\bar{\phi}$	Filtered quantity
$\breve{\phi}$	Integration variable
$\check{\phi}$	Favre test filtered quantity
$\dot{\phi}$	Time derivative
$\hat{\phi}$	Test filtered quantity
$\partial\phi$	Partial differential
ϕ'^2	Sub-grid variance
ϕ''^2	Favre sub-grid variance
ϕ''	Favre sub-grid part
ϕ'	Sub-grid part
$\tilde{\phi}$	Favre filtered quantity
$\mathrm{d}\phi$	Differential
$\mathrm{D}\phi/\mathrm{D}t$	Material derivative

Abbreviations

0D	Zero Dimensional
1D	One Dimensional
2D	Two Dimensional
3D	Three Dimensional
AMR	Adaptive Mesh Refinement
AUSM	Advection Upstream Splitting Method
BDF	Backward Differentiation Formulas
CDS	Central Differencing Scheme
CFD	Computational Fluid Dynamics
CFL	Courant Friedrich Lewy
CV	Control Volume
D	Downwind
DDT	Deflagration to Detonation Transition
DFG	Deutsche Forschungs Gemeinschaft (German research foundation)
DNS	Direct Numerical Simulation
DS	Diffusive Stability
E	East
ENO	Essentially Non Oscillatory
EOS	Equation Of State
EU	Euler
FDF	Filtered Density Function

FDM	Finite Difference Method
FGM	Flamelet Generated Manifolds
FRC	Finite Rate Chemistry
FSD	Flame Surface Density
FVM	Finite Volume Method
IVP	Initial Value Problem
LES	Large Eddy Simulation
LHS	Left Hand Side
LODI	Local One Dimensional Inviscid
MP	Monotonicity Preserving
MPI	Message Passing Interface
MUSCL	Monotonic Upstream centered Scheme for Conservation Laws
N	North
NS	Navier Stokes
NSCBC	Navier Stokes Characteristic Boundary Condition
ODE	Ordinary Differential Equation
PDE	Partial Differential Equation
PDF	Probability Density Function
PPM	Parts Per Million
PPM	Piecewise Parabolic Method
RANS	Reynolds Averaged Navier Stokes
RCM	Rapid Compression Machines
RDE	Rotating Detonation Engine
RHS	Right Hand Side
S	South
SGS	Sub Grid Scale
SLAU	Simple Low dissipation Advection Upstream splitting method
SM	Supplementary Material
TTF	Dynamic Thickened Flame
TV	Total Variation
TVD	Total Variation Diminishing
U	Upwind
UDS	Upwind Differencing Scheme
W	West
WALE	Wall Adapting Local Eddy
WENO	Weighted Essentially Non Oscillatory
ZND	Zeldovich Neumann Döring

Chapter 1
Introduction

1.1 Motivation

Combustion has been used for thousands of years and is essential for the development of modern mankind. In today's world, the conversion of chemical energy through combustion into heat, mechanical, and electrical energy is deeply integrated into everyday life.

During the combustion of hydrocarbons, various products are formed through chemical conversion. These include water (H_2O), carbon dioxide (CO_2) and monoxide (CO), nitrogen oxides (NO_x), and sulfur oxides (SO_x). Some of these compounds are proven to be harmful to human health, while others, known as greenhouse gasses, absorb radiation in the infrared band. The greenhouse effect prevents the Earth's average temperature from falling below 0 °C and enables the existence of the plant and animal life we know. However, the escalating concentrations of greenhouse gasses, particularly CO_2 [2], intensify this effect, leading to irreversible climate changes with unforeseen consequences. Some of these consequences are already evident, such as the melting of glaciers. In response, global targets have been set to limit the temperature rise to 1.5 °C or, at the very least, below 2 °C [3]. Consequently, numerous countries have established ambitious objectives to reduce the usage of fossil fuels, thereby mitigating CO2 emissions and other pollutants.

Fossil fuels have consistently accounted for over 80 % of the total energy demand for several decades, while the total energy demand has simultaneously increased, driven by a growing population. However, according to the latest report by the International Energy Agency, there is a projected decrease in reliance on fossil fuels in the energy mix by 2030, indicating a significant shift. Although overall energy consumption will continue to rise, the additional demand will be met by renewable energies. Coal is expected to reach its maximum share of the energy mix by 2025, while gas and oil will plateau. By 2060, the share of fossil energy is anticipated to drop below 60 %. Nevertheless, the combustion of fossil fuels will remain integral to electrical energy generation, transportation, and heating for many decades to come. Therefore, reducing emissions requires not only the adoption of alternative renewable energies but also efficiency improvements in existing combustion concepts, cleaner combustion processes, and the utilization of alternative fuels such as bio fuels and hydrogen. Furthermore, a comprehensive understanding of fuel characteristics is imperative to enhance combustion processes.

Among alternative fuels, hydrogen holds a special position. Unlike commonly used fuels, hydrogen lacks carbon atoms, thereby eliminating carbon dioxide and carbon monoxide emissions. It possesses the lowest molar mass among fuels, making it highly volatile and posing storage challenges. Additionally, hydrogen exhibits high diffusivity, resulting in high laminar flame velocities and thermodiffusive instability. It has a short ignition delay time and is considered highly reactive. These characteristics have so far hindered the widespread adoption of hydrogen in combustion systems, especially due to safety concerns. Nonetheless, there has been a rise in government-funded hydrogen initiatives in recent years. One short-term approach to utilizing hydrogen is its simultaneous combustion with natural gas, for instance, in stationary gas turbines. However, well-established reaction kinetics models for methane combustion (*e.g.*, GRI-MECH 3.0 [4]) have proven inadequate in modeling these processes. Hence, there is an urgent need for new reaction kinetics models, not only for the simultaneous combustion of natural gas and hydrogen but also for combustion of other renewable fuels, to enhance combustion processes in the near future.

Fuel characterization has primarily been conducted in shock tubes since the 1950s, supplemented by the use of Rapid Compression Machines (RCM). A shock-tube experiment, in summary, involves compressing a combustible test mixture twice using a compression shock, which rapidly increases the temperature and initiates chemical reactions. The ignition process occurs at nearly constant pressure and temperature until the mixture ignites, resulting in a pressure spike. This allows to model the ignition process of the test mixture by a *zero-dimensional* (0D) reactor at constant volume and constant internal energy, aiding in the development of suitable reaction mechanisms for fuels. These mechanisms, in turn, are crucial for designing and optimizing combustion systems. Initially, shock-tube experiments involved mainly Argon diluted test mixtures, and were conducted at high initial temperatures to achieve short ignition delay times (below 1 ms). In the early 2000s, interest grew in replicating conditions encountered in gas turbine combustion chambers or internal combustion engines, leading to the use of undiluted mixtures across a wide temperature range, including temperatures below 1100 K and thus larger ignition delay times [5]. Discrepancies between measurement results and expectations based on existing kinetics models and zero-dimensional reactor simulations became evident in many of the experiments under those conditions. It became clear that multidimensional effects become more influential with longer test times, resulting in so called *non-idealities*. For example, pre-ignition pressure changes can be observed during the experiment, challenging the assumptions of constant volume and constant internal energy in 0D reactor simulations. Gaining a detailed understanding of these multidimensional effects is crucial to ensure that experimental results do not lead to significant errors in the kinetic models based on them.

1.2 Aim of the thesis

The primary objective of this work is to contribute to the advancement of clean and efficient combustion. Achieving this goal requires a comprehensive understanding of the physical and chemical processes involved in combustion. While experiments provide valuable insights, the extreme conditions of combustion systems often limit optical access to small areas and single quantities. In contrast, numerical simulations provide a plethora of quantities in each point of the numerical domain. Furthermore, simulations have become more cost and time-efficient than experiments due to the increasing power and size of processors and hard drives. To further enhance the affordability of simulations, lower-order models that approximate larger-scale simulations with appropriate boundary conditions prove to be a valuable tool.

This thesis focuses on various aspects of reactive supersonic flows. The first part, which was funded by a DFG project, investigates non-ideal effects in shock tubes through *two-dimensional* (2D) and *three-dimensional* (3D) *computational fluid dynamics* (CFD) simulations. In the 2D simulations, special focus was put on time changing variables on the inlet boundary using the so-called perturbation theory. The impact of this newly developed boundary condition on end-wall pressure histories and ignition events are examined. In the 3D simulations, conditions leading to reflected shock bifurcation, are explored in terms of remote ignition events. The obtained results aim to raise awareness of the challenges associated with reflected shock bifurcation under realistic conditions. Additionally, the findings from the 2D simulations contribute to the development of more cost-effective low-order models. For instance, a potential low-order model could involve a 0D reactor featuring a constant internal energy and a volume that changes size as a function of a previously predicted pressure evolution. Several of these reactors could be placed with different distance from the shock tube end wall to predict remote ignition.

The second part of this thesis focuses on the numerical investigation of detonation wave propagation. Utilizing detonations (combustion at constant volume) in propulsion systems holds the promise of efficiency advantages over the currently employed Joule process (combustion at constant pressure). Conceptual designs, such as *rotating detonation engines* (RDE), have been proposed. However, it is crucial to ensure that detonations can stably propagate at nearly constant speeds within narrow confinements. It has been established that sustained detonation propagation is not possible when the channel height (or tube diameter) falls below a critical threshold linked to the characteristic size of the detonation cell structure. Consequently, this study explores detonation propagation of hydrogen-oxygen mixtures, both with and without ozone, to elucidate propagation characteristics and establish a connection between the size of the detonation cellular structure and the mixture-dependent separation rate between the pressure wave and reaction zone.

1.3 Structure

Following the introductory chapter, the second chapter of the thesis provides the necessary theoretical foundations to address the research problems. These include the conservation equations for compressible and reactive systems, premixed combustion waves, and turbulence modeling in *large eddy simulations* (LES). In order to solve the equations efficiently on highly parallelized systems, they must be discretized first, and the algorithms necessary to accomplish the task are discussed in detail in Chapter 3. Chapter 4 is dedicated to exploring the unique characteristics of shock tubes and provides the modeling of laminar and turbulent boundary layers behind incident shock waves and investigates their influence on the flow outside the boundary layer in confined systems.

Chapters 5-8 consist of journal papers that have either been published or are currently under review [6–8]. Chapter 5 presents a highly resolved LES of a shock tube simulation using a stoichiometric hydrogen/oxygen mixture. This particular case exhibits reflected shock bifurcation, resulting in a complex flow field and unintended ignition far from the end wall. Remarkably, this is the first 3D simulation demonstrating such ignition. In Chapter 6, 2D simulations of shock tube experiments are presented, involving non-reactive mixtures at varying pressure levels and experiments with a diluted hydrogen/oxygen mixture at higher pressure. Notably, the non-reactive cases reveal unexpected pressure profiles near the end wall. To address this, a new inlet boundary condition is introduced to accurately describe both the boundary layer and the temporal changes in the core flow, effectively reproducing the pressure evolution. The same inlet boundary condition is subsequently employed in the reactive simulations to replicate remote ignition and to further validate the approach. Chapter 7 showcases 2D simulations of detonation waves in narrow channels using a stoichiometric hydrogen/oxygen mixture, with and without the addition of ozone. The investigation focuses on two channel heights and assesses the impact of viscous terms on cell structure and velocity deficit. Furthermore, a comprehensive analysis of all detonation cells is conducted to verify a previously proposed hypothesis regarding a detonation cell size stabilization mechanism. Chapter 8 expands upon the previous chapter by conducting 3D simulations of detonation waves using the same ozonated mixture as in Chapter 7. This study specifically explores the influence of geometric confinement on the three-dimensional structure of the detonation wave front.

Chapter 9 provides a summary of additional publications with co-authorship, highlighting the broader contributions made by the author. The final chapter offers a comprehensive summary of the most significant results obtained throughout the thesis and provides an outlook on potential improvements and extensions based on the current state of research.

Chapter 2
Theory

2.1 Governing Equations for Multicomponent Combustion Systems

This section introduces the fundamental conservation equations used to describe single-phase reactive multicomponent flow problems and can be found in many classical textbooks (*e.g.,* [9, 10]). The fluid phase can be treated as a continuum in many combustion problems and also applies to the combustion systems presented in this work. It is then unnecessary to consider each molecule individually. Instead, the macroscopic quantities pressure, temperature, and density define the state of the gas phase. This general assumption allows the flow description by a system of coupled *partial differential equations* (PDE). Other classical assumptions are made, including the coupling of pressure, density, and temperature via the ideal *equation of state* (EOS) and the assumption of thermodynamic equilibrium. The Einstein index notation is used in many of the equations outlined below, suggesting summation over a set of indices given in a formula.

2.1.1 Mass Conservation Equation

Without consideration of any nuclear processes, the mass in a control volume can change in time only by fluxes across the system boundaries. The continuity equation thus postulates that mass can neither be created nor destroyed:

$$\frac{\partial \rho}{\partial t} + \frac{\partial \rho u_i}{\partial x_i} = 0, \quad i = 1, 2, 3 \tag{2.1}$$

Equation 2.1 features the fluid mass density ρ and the velocity vector component u_i in i^{th} direction. The equation further simplifies to a divergent-free condition for velocity fields, if the density is constant.

2.1.2 Species Conservation Equations

The composition of a gas mixture must be known in terms of multicomponent reacting systems and can be described by both mass fractions Y_α or mole fractions X_α, defined as:

$$Y_\alpha = \frac{m_\alpha}{\sum_{\alpha=1}^{N_\mathrm{S}} m_\alpha} \tag{2.2}$$

$$X_\alpha = \frac{n_\alpha}{\sum_{\alpha=1}^{N_\mathrm{S}} n_\alpha} \tag{2.3}$$

Equations 2.2 and 2.3 feature the species index α and the number of species N_S involved in the mixture. A transport equation for individual species partial densities can be derived which, when summed over all species, yields the continuity equation and is therefore the preferred choice:

$$\frac{\partial \rho Y_\alpha}{\partial t} + \frac{\partial \rho Y_\alpha u_i}{\partial x_i} + \frac{\partial \rho Y_\alpha V_{i,\alpha}}{\partial x_i} = \dot{\omega}_\alpha, \quad \alpha = 1, 2, \ldots, N_\mathrm{S} \tag{2.4}$$

Equation 2.4 introduces the partial mass density ρY_α, the chemical source term $\dot{\omega}_\alpha$ defining the rate at which a species is produced or consumed, as well as the species diffusion velocity $V_{i,\alpha}$ (caused by inter-diffusion processes), which is considered relative to the bulk velocity u_i.

2.1.2.1 Diffusion Velocities

The exact computation of the species diffusion velocities $V_{i,\alpha}$ requires the solution of a linear system with a coefficient matrix size of $N_\mathrm{S}{\times}N_\mathrm{S}$ at each point in space and time [10]. The calculation considers species diffusion by concentration gradients (*Maxwell-Stefan diffusion*), species diffusion by temperature gradients (*Soret effect*), species diffusion by pressure gradients, and species diffusion by volume forces acting differently on individual species. In the context of numerical simulations, solving the linear system can quickly take up the majority of the computational time. It is therefore common to resort to approximations and simpler models that are, however, suitable for the investigated problems. The most common approach is *Fick's first law of mass diffusion*, where species diffusion is exclusively driven by mass fraction/molar fraction gradients:

$$j_{i,\alpha} = \rho Y_\alpha V_{i,\alpha} = -\rho D_\alpha \frac{\partial Y_\alpha}{\partial x_i} = -\rho D'_\alpha \frac{\partial X_\alpha}{\partial x_i} \tag{2.5}$$

$$D'_\alpha = \frac{W}{W_\alpha} D_\alpha \tag{2.6}$$

Here, j_α is the diffusive mass flux of species α, D_α is the diffusion coefficient in terms of mass fraction gradients, D'_α is the diffusion coefficient in terms of mole fraction gradients, W is the mean molecular weight of the mixture and W_α is the molecular weight of species α. It has been shown in numerical tests to be beneficial to express the diffusive mass flux by means of molar fraction gradients [9] and which is therefore applied preferably. The mean molecular weight is computed from:

$$W = \frac{1}{\sum_{\alpha=1}^{N_\mathrm{S}} Y_\alpha / W_\alpha} \tag{2.7}$$

If the diffusion velocities vary greatly among the species (*e.g.,* hydrogen combustion), a popular choice for the diffusion coefficient is the mixture averaged diffusion coefficient according to the *Hirschfelder-Curtiss approximation* [11]:

$$\frac{1}{D_{\mathrm{m},\alpha}} = \sum_{\beta\neq\alpha}^{N_\mathrm{S}} \frac{X_\beta}{\mathcal{D}_{\alpha\beta}} + \frac{X_\alpha}{1-Y_\alpha} \sum_{\beta\neq\alpha}^{N_\mathrm{S}} \frac{Y_\beta}{\mathcal{D}_{\alpha\beta}} \tag{2.8}$$

Here, the subscript m,α implies diffusion of species α into a mixture of gases and can be used directly in Eq. 2.5 replacing D_α. The sum of the diffusion mass fluxes in a single point, as computed by Eq. 2.8, can deviate from zero (in contrast to the multicomponent formulation), therefore violating the continuity equation. To remove the inconsistency between the continuity equation and the mass species conservation equations, a correction velocity $V_{\mathrm{C},i}$ can be introduced [11]:

$$j_{i,\alpha} = \rho Y_\alpha V_{i,\alpha} + \rho Y_\alpha V_{\mathrm{C},i} \tag{2.9}$$

$$V_{\mathrm{C},i} = -\sum_{\alpha=1}^{N_\mathrm{S}} Y_\alpha V_{i,\alpha} \tag{2.10}$$

In cases where an inert species with a simultaneously large mass fraction is present in the gas mixture, the error can alternatively be compensated by the mass fraction of the inert species (*e.g.,* by nitrogen, when air is used as oxidizer). Here, only $(N_\mathrm{S} - 1)$ species evolve following Eq. 2.4, while the mass fraction of the inert species with index $\alpha = N_\mathrm{S}$ is defined as:

$$Y_{N_\mathrm{S}} = 1 - \sum_{\alpha=1}^{N_\mathrm{S}-1} Y_\alpha \tag{2.11}$$

Another common approach to model species diffusion is the assumption of constant diffusion coefficients among all species, where the diffusion coefficient is computed based on a constant Lewis number Le, relating thermal conduction and mass diffusion:

$$\mathrm{Le} = \frac{\lambda}{\rho \, D_\alpha \, c_p} \tag{2.12}$$

$$j_{i,\alpha} = -\frac{\lambda}{\mathrm{Le} \, c_p} \frac{\partial Y_\alpha}{\partial x_i} \tag{2.13}$$

Equation 2.12 features the specific heat capacity c_p of the mixture at constant pressure and the heat conductivity λ of the mixture. The Lewis number is often set to unity, thus referring to the *Unity Lewis number* approach and, by definition, does not require a correction velocity. Especially for methane flames, the Unity Lewis assumption is in good approximation to the reference solution, whereas the assumption is not suitable for hydrogen flames due to the high diffusive velocities of hydrogen.

2.1.2.2 Chemical Reaction Source Terms

The source terms on the right-hand side of Eq. 2.4 can be evaluated by reaction kinetics. In general, the source term of each species is a function of all species in the system, as well as the thermodynamic state:

$$\dot{\omega}_\alpha = f(p, T, Y_1, Y_2, ..., Y_{N_\mathrm{S}}) \tag{2.14}$$

In Eq. 2.14, p is the static pressure and T is the thermodynamic temperature. The vector of species source terms is then governed by a set of coupled *ordinary differential equations* (ODE). Typically, fuel and oxidizer (educts) do not react to the products in a single reaction step, but instead decompose to intermediate species that will eventually form the stable products. The description of these processes is based on a reaction mechanism via N_R intermediate reactions, which can be represented as follows:

$$\sum_{\beta=1}^{N_\mathrm{S}} \nu'_{\beta r} \mathcal{X}_\beta \rightleftharpoons \sum_{\beta=1}^{N_\mathrm{S}} \nu''_{\beta r} \mathcal{X}_\beta, \quad r = 1, 2, \dots, N_\mathrm{R} \tag{2.15}$$

Expression 2.15 features the forward and backward molar stoichiometric coefficients ν'_β and ν''_β of species β with the chemical formula $\mathcal{X}_\beta$ and illustrates that reaction r can proceed both in forward and backward direction involving all the species with molar stoichiometric coefficients that are nonzero.

2.1.2.3 Elementary Reactions

Various expressions exist for describing a reaction and calculating its *rate of progress*. The most frequently used type is the elementary reaction. An example is the reaction of a hydrogen molecule (H_2) and a hydroxyl radical (OH) to atomic hydrogen (H) and a water molecule (H_2O):

$$\mathrm{H_2 + OH \rightleftharpoons H + H_2O} \tag{2.16}$$

The *rate of progress* q_r of an elementary reaction r can be computed as the difference of forward and backward reaction rates, both following the *law of mass action* [10]:

$$q_r = k_{\mathrm{f},r}(T) \prod_{\beta=1}^{N_\mathrm{S}} \left[\mathcal{X}_\beta\right]^{\nu'_{\beta r}} - k_{\mathrm{b},r}(T) \prod_{\beta=1}^{N_\mathrm{S}} \left[\mathcal{X}_\beta\right]^{\nu''_{\beta r}} \tag{2.17}$$

Equation 2.17 states that the rates of forward and backward reaction are proportional to the product of the corresponding molar concentrations of the involved species $\left[X_\beta\right]$ raised to the power of the respective molar stoichiometric coefficients. The proportionality constants k_f and k_b are exclusively a function of temperature and referred to as *reaction rate constants*. The forward reaction rate constant k_f can be calculated with the *Arrhenius law* [11]:

$$k_\mathrm{f}(T) = A\,T^b \exp\left(-\frac{E_\mathrm{a}}{R_\mathrm{m}\,T}\right) \tag{2.18}$$

Here, the expression $A\,T^b$ represents a collision frequency, whereby the exponential function, which is also denoted as the *Boltzmann factor*, features the activation energy E_a and the universal gas constant R_u. Once the forward reaction rate constant is known, the corresponding backward reaction rate constant k_b can be derived using the equilibrium constant K_C via $k_\mathrm{b} = k_\mathrm{f}/K_C$. Finally, the reaction source term for a species α can be calculated based on all reactions in which the respective species is present either on the reactant or product side. Taking the molar stoichiometric coefficients into account yields:

$$\dot{\omega}_\alpha = W_\alpha \sum_{r=1}^{N_\mathrm{R}} (\nu''_{\alpha r} - \nu'_{\alpha r})\, q_r \tag{2.19}$$

2.1.2.4 Three-Body Reactions

Some reaction descriptions can benefit from the inclusion of a *third body* collision, providing energy and thus changing the rate of the reaction without being chemically transformed. Every species present in the mixture can act as a *third body*, although notably some third body species might have an enhanced or reduced impact on the reaction rate. An example for a three-body reaction is the thermal dissociation of $\mathrm{H_2}$:

$$\mathrm{H_2 + M \rightleftharpoons 2\,H + M} \tag{2.20}$$

In chemical formulas, a third body is depicted as M, while the concentration of the *third body* is generally described by [M] and commonly referred to as *effective concentration*:

$$[M] = \sum_{\beta=1}^{N_\mathrm{S}} a_{\beta r} \left[X_\beta\right] \tag{2.21}$$

Here, $a_{\beta r}$ is the efficiency factor of species β in the r^th reaction. If all species have the same efficiency of unity, the effective concentration becomes the total concentration of the mixture. The rate of progress of these type of reactions can be computed as:

$$q_r = [M]\left(k_{\mathrm{f},r}(T) \prod_{\beta=1}^{N_\mathrm{S}} \left[X_\beta\right]^{\nu'_{\beta r}} - k_{\mathrm{b},r}(T) \prod_{\beta=1}^{N_\mathrm{S}} \left[X_\beta\right]^{\nu''_{\beta r}}\right) \tag{2.22}$$

Equation 2.22 thus replaces equation 2.17 in terms of *Three-Body* reactions, whereby the first expression on the right-hand-side (RHS) is added to the previous formulation.

2.1.2.5 Pressure Dependent Reactions

Pressure dependent reactions can only be described by two different reaction-rate formulations at low and high pressure, respectively. This could be the case, for example, if a reaction at low pressures requires a third-body collision in order to proceed, but is perfectly described by an elementary reaction at high pressure (or vice versa). The reaction rate must be described by suitable interpolation of the limit solutions between these pressure limits. An example for a pressure-dependent reaction is the formation of a hydroperoxyl (HO_2) molecule:

$$\mathrm{H} + \mathrm{O_2}\,(+\,\mathrm{M}) \rightleftharpoons \mathrm{HO_2}\,(+\,\mathrm{M}) \tag{2.23}$$

The brackets indicate that the third body is only active in a pressure limit. Software, specifically developed for the computation of chemical systems like Cantera [12] or Chemkin [13], provide two types of pressure dependent reactions, that is *Fall-Off* reactions and *Chemically Activated Bimolecular* reactions. The reaction mechanisms used in the present work exclusively use *Fall-Off* reactions in the context of pressure-dependent reactions. The forward reaction-rate constant of *Fall-Off* reactions is given as:

$$k_\mathrm{f} = k_{\mathrm{f},\infty}\left(\frac{P_\mathrm{r}}{1+P_\mathrm{r}}\right)F \tag{2.24}$$

$$P_\mathrm{r} = \frac{k_{\mathrm{f},0}\,[\mathrm{M}]}{k_{\mathrm{f},\infty}} \tag{2.25}$$

Equations 2.24 and 2.25 feature the upper pressure limit forward reaction rate constant $k_{\mathrm{f},\infty}$, the lower pressure limit forward reaction rate constant $k_{\mathrm{f},0}$, both of which are computed by an *Arrhenius* expression, the dimensionless pressure P_r and the *Fall-Off* parameter F. Different models exist for describing the *Fall-Off* parameter from Lindemann [14], Gilbert et al. [15] and Stewart et al. [16]. After computing the forward and backward reaction rate constants, Eq. 2.17 can be used to determine the rate of progress variable.

2.1.3 Momentum Conservation Equations

The momentum conservation equations express *Newton's second law of motion*, which states that momentum in an infinitesimal volume can only change by convection and forces that act on the volume:

$$\frac{\partial \rho u_i}{\partial t} + \frac{\partial \rho u_i u_j}{\partial x_j} = -\frac{\partial p}{\partial x_i} + \frac{\partial \tau_{ij}}{\partial x_j} + \rho \sum_{\alpha=1}^{N_\mathrm{S}} Y_\alpha f_{i,\alpha} \tag{2.26}$$

Here, τ_{ij} denotes the viscous stress tensor with stress components due to deformation, while $f_{i,\alpha}$ is the net volume force of component α per unit mass. Continuous, isotropic fluids whose shear stress is proportional to the deformation rate are called *Newtonian fluids* and the viscous stress tensor is given by:

$$\tau_{ij} = \tau_{ji} = \left(\mu' - \frac{2}{3}\mu\right)\frac{\partial u_k}{\partial x_k}\delta_{ij} + \mu\left(\frac{\partial u_i}{\partial x_j} + \frac{\partial u_j}{\partial x_i}\right) \tag{2.27}$$

Equation 2.27 features the bulk viscosity μ', the *Kronecker* symbol δ_{ij} and the dynamic viscosity μ. Not only is the bulk viscosity very difficult to determine reliably [10], it is also negligible in most combustion applications and will therefore be discarded in the following. The term of $-2/3\ \mu$ is then needed to ensure that the bulk viscosity is zero. Equations 2.26 are referred to as *Navier-Stokes equations* [17, 18], if Eq. 2.27 is used to determine the stress components. The proportionality constant μ that relates the rate of deformation with the stress, must be known to solve Eq. 2.26 and can be determined using mixture-averaged models or polynomial functions specifically fitted for mixtures or gases. An example of a mixture-averaged model is the one by Bird et al. [19] (which in turn is a modification to a model by Wilke [20]):

$$\mu = \sum_{\alpha=1}^{N_\mathrm{S}} \frac{X_\alpha \mu_\alpha}{\sum_\beta^{N_\mathrm{S}} X_\beta \Phi_{\alpha\beta}} \tag{2.28}$$

$$\Phi_{\alpha\beta} = \frac{1}{\sqrt{8}} \left(1 + \frac{W_\alpha}{W_\beta}\right)^{-1/2} \left(1 + \left(\frac{\mu_\alpha}{\mu_\beta}\right)^{1/2} \left(\frac{W_\beta}{W_\alpha}\right)^{1/4}\right)^2 \tag{2.29}$$

If the mass fraction Y_α of species α is known, the corresponding mole fraction X_α can be computed from:

$$X_\alpha = Y_\alpha \frac{W}{W_\alpha} \tag{2.30}$$

The sums incorporated in Eq. 2.28 can make the calculation of the mixture-averaged viscosity at any point at any time expensive. Polynomial fits reduce the computational effort, whereby *Sutherland's law* is a frequently used method in this context [21]:

$$\mu = \mu_\mathrm{ref} \left(\frac{T}{T_\mathrm{ref}}\right)^{3/2} \frac{T_\mathrm{ref} + S_\mu}{T + S_\mu} \tag{2.31}$$

Here, μ_ref and T_ref are reference values of viscosity and temperature for a specific gas mixture and S_μ is the fitting parameter.

2.1.3.1 Pressure Gradient

The pressure in the conservation of momentum equation (Eq. 2.26) appears only as a pressure gradient, which implies that the exact pressure is not needed to solve the equation, if the gradient can be approximated otherwise. This fact is especially important in the low Mach number limit, where Eq. 2.1 and 2.26 can be discretized and recast into a *Poisson* type equation that can be solved to provide a pressure field.

If compressibility has to be taken into account, the previous approach can no longer be used and the pressure must be approximated via material laws instead. In this work, the ideal gas law is used for this purpose:

$$\frac{p}{\rho} = T \frac{R_\mathrm{m}}{W} = T R_\mathrm{s} \tag{2.32}$$

According to Eq. 2.32, pressure can be determined based on density, temperature and the specific gas constant R_s. The temperature is typically computed from a transported energy, as pointed out in Sec. 2.1.4, whereas in the low Mach number limit, the additional transport of energy is not necessarily required. Alternative material laws exist, *i.e.* if pressures are very high, as is the case in rocket engines, or temperatures are very low, *real gas effects* must be considered [9].

2.1.4 Energy Conservation Equation

The energy conservation equation is necessary for the closure of temperature. There are eight different energy definitions that are candidates for conservation, which are all mathematically consistent, but have advantages and disadvantages in the context of computational fluid dynamics [9]. The energy conservation in terms of absolute, total, internal energy stems directly from the energy balance of an infinitesimal volume element fixed in space. Since this formulation features a single time derivative and also incorporates kinetic and chemical energy, both of which are vital in high Mach reactive flows, it is the preferred choice for simulation of compressible flow:

$$\frac{\partial \rho E}{\partial t} + \frac{\partial (\rho E + p) u_i}{\partial x_i} = -\frac{\partial q_i}{\partial x_i} + \frac{\partial \tau_{ij} u_i}{\partial x_j} + \dot{Q} \tag{2.33}$$

Here, E is the total internal chemical energy, q_i is the heat flux vector and $\dot{Q}$ is the net rate of external energy input. The attribute *chemical* implies the inclusion of standard formation enthalpies (h_f^0) and *total* implies the addition of kinetic energy ($1/2\ u_k u_k$):

$$E = h - \frac{p}{\rho} + \frac{u_k u_k}{2} \tag{2.34}$$

$$h = \sum_{\alpha=1}^{N_\mathrm{S}} Y_\alpha h_\alpha \tag{2.35}$$

$$h_\alpha = \int_{T_0}^{T} c_{p,\alpha}(T)\, dT + \Delta h_{\mathrm{f},\alpha}^0 \tag{2.36}$$

Equations 2.34-2.36 feature the sensible chemical enthalpy h of the mixture, the sensible chemical enthalpy h_α of species α, the specific heat capacity $c_{p,\alpha}$ of species α at constant pressure and the standard formation enthalpy $\Delta h_{\mathrm{f},\alpha}^0$ of species α. The first term on the right hand side of Eq. 2.36 represents the sensible enthalpy, while the second term presents the chemical part. The heat flux vector q_i considers heat conduction according to *Fouriers's law* and heat fluxes due to interdiffusion processes [10, 11]:

$$q_i = -\lambda \frac{\partial T}{\partial x_i} + \sum_{\alpha=1}^{N_\mathrm{S}} h_\alpha\, j_{i,\alpha} \tag{2.37}$$

The heat conductivity λ of the mixture can be either derived by temperature polynomials (similar to the one used in Eq. 2.31), or the averaging formula by Mathur et al. [22]:

$$\lambda = \frac{1}{2}\left(\sum_{\alpha=1}^{N_\mathrm{S}} X_\alpha \lambda_\alpha + \frac{1}{\sum_{\alpha=1}^{N_\mathrm{S}} X_\alpha/\lambda_\alpha}\right) \tag{2.38}$$

Equation 2.33 can be further used to derive additional energy conservation equations that may be advantageous in certain situations. For example, a transport equation for kinetic energy can be derived using the momentum conservation equation (Eq. 2.26) and subtracted from Eq. 2.33. As a result, a transport equation for absolute, internal energy e is obtained, from which, in turn, a transport equation for absolute enthalpy h can be obtained [23]:

$$\frac{\partial \rho h}{\partial t} + \frac{\partial \rho h u_i}{\partial x_i} = \frac{\mathrm{D}p}{\mathrm{D}t} - \frac{\partial q_i}{\partial x_i} + \tau_{ji}\frac{\partial u_j}{\partial x_i} + \dot{Q} \tag{2.39}$$

$$\frac{\mathrm{D}p}{\mathrm{D}t} = \frac{\partial p}{\partial t} + u_i \frac{\partial p}{\partial x} \tag{2.40}$$

Here, $\frac{\mathrm{D}p}{\mathrm{D}t}$ is the *material derivative* of pressure and approaches a value of zero in the low Mach limit. The effect due to friction (3^{rd} term on the *right hand side* (RHS) of Eq. 2.39) can also be neglected if velocities are small, so that a much simpler enthalpy conservation equation can be used:

$$\frac{\partial \rho h}{\partial t} + \frac{\partial \rho h u_i}{\partial x_i} = -\frac{\partial q_i}{\partial x_i} + \dot{Q} \tag{2.41}$$

Equation 2.41 was used in the present work for the validation of combustion models using one-dimensional adiabatic flames.

Table 2.1: Typical Mach numbers and normalized post-shock quantities of detonations and deflagrations [24].

	Detonation	Deflagration
u_1/c_1	5 – 10	0.0001 – 0.03
u_2/u_1	0.4 – 0.7	4 – 16
p_2/p_1	13 – 55	0.98 – 0.99999996
T_2/T_1	8 – 21	4 – 16
ρ_2/ρ_1	1.7 – 2.6	0.06 – 0.25

2.2 Combustion

Combustion only takes place in regions, where both fuel and oxidizer are present. Furthermore, the ratio between the quantities of fuel and oxidizer must fall within a precise range known as the *flammability limits*. The lower and upper bounds of this ratio signify the thresholds beyond which sustained combustion cannot take place. Upon fulfilling these criteria, the initiation of net exothermic reactions occurs through an external energy source, which can be a spark or the transfer of heat from an already existing flame. In technical combustion systems, such as those employed for power generation or the facilitation of targeted material production, it is of high importance to ensure the thorough mixing of reactants and oxygen. The mixing process can be completed before entering the combustion chamber, which is then called a *perfectly premixed flame*. Alternatively, fuel and oxygen can be fed separately into the combustion chamber, where convection and diffusion create flammable regions by mixing, referred to as *non-premixed flames* or *diffusion flames*.

Both approaches have advantages and disadvantages in terms of operational security, emission tendencies and flame characteristics. For example, a perfectly premixed flame can be designed to be lean, which means that more oxygen is present, as would be necessary to completely convert the fuel into the reaction products. As a result, unwanted emissions, such as toxic CO emissions, will be prohibited. Simultaneously, due to the fact that the incoming fresh gases entering the combustion chamber are within the flammability limits, there is a possibility of flame occurrence upstream of the designated combustion chamber in machine components that are not specifically engineered to withstand the associated stresses and high heat fluxes, a phenomenon referred to as *flashback*. Furthermore, premixed flames have a susceptibility to instabilities or the occurrence of self ignition. Ultimately, such behaviors can cause the total damage of the device. For this reason, the non-premixed approach is often used where such behavior is inherently impossible. Safety on the one hand is bought by flame characteristics that are in many respects inferior to those of a premixed flame. These characteristics include the formation of regions that can be excessively lean or rich due to the mixing process. As a result, higher emission levels are often observed as a consequence of these conditions. In practical applications, modern combustion approaches frequently incorporate a combination of premixed streams and non-premixed streams to achieve the desired properties and balance safety considerations. This hybrid approach allows for the optimization of combustion processes while mitigating potential risks.

2.2.1 Premixed Combustion Waves

The numerical studies presented in this work have exclusively addressed perfectly premixed mixtures. Premixed flame properties and wave speeds are therefore discussed briefly. In general, combustible mixtures can react to products in three ways:

(1) **Explosion:** A combustible mixture is suddenly subjected to an extreme state (with a high temperature) leading to a rapid consumption of the entire fuel almost at once. Explosions can be observed in rapid compression machines.

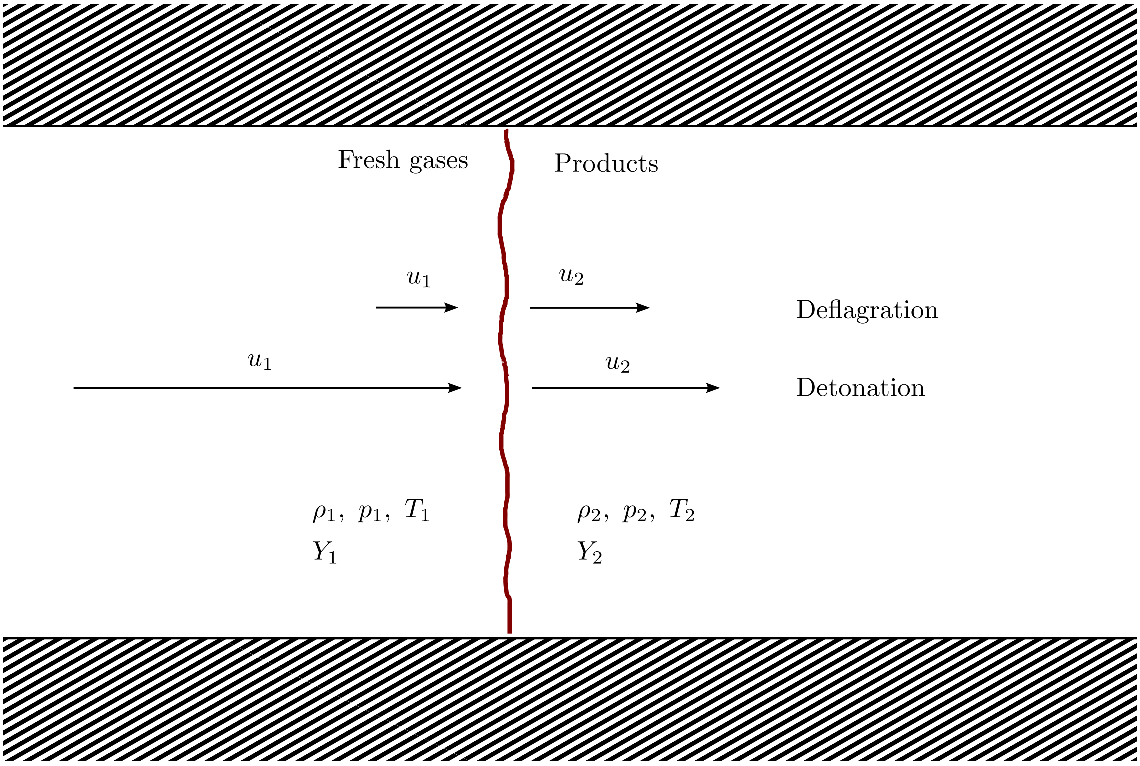

Figure 2.1: Combustion wave in a one-dimensional representation. The combustion wave is fixed in space with unburned products approaching from the left.

(2) **Deflagration:** The mixture is consumed within a thin flame region, referred to as combustion wave as it propagates into the fresh mixture. The combustion wave travels at a subsonic speed. Fluid expands in the flame and is thus accelerated.

(3) **Detonation:** The mixture is compressed by a shock propagating at supersonic speed. It thus shares similarities with the explosion and the deflagration. Since the reactions are triggered by a compression shock moving at supersonic speed into the fresh gas, a combustion wave is present, as in the case of a deflagration. Simultaneously, the compression itself induces a sudden temperature increase, analogous to that observed in explosions.

2.2.1.1 Jump Conditions

Due to drastically different propagation speeds, deflagrations and detonations will feature equally different states behind the combustion wave [24], as presented in Tab. 2.1. The state behind a normal and steady combustion wave can be determined using conservation laws in one dimension [10, 25, 26]. It is common to use a control volume moving at the speed of the combustion wave, referred to as wave frame approach, as depicted in Fig. 2.1. Velocities in a wave frame can be computed from the wave speed u_w and their counterparts in the laboratory frame and are syntactically differentiated by capital letters:

$$U_1 = u_\mathrm{w} - u_1 \tag{2.42}$$

$$U_2 = u_\mathrm{w} - u_2 \tag{2.43}$$

Here, U_1 is the velocity of the fresh gases and U_2 is the velocity of the burnt gases, both in wave frame coordinates. The conservation equations for mass, momentum, and energy then read:

$$\rho_1 U_1 = \rho_2 U_2 \tag{2.44}$$

$$p_1 + \rho_1 U_1^2 = p_2 + \rho_2 U_2^2 \tag{2.45}$$

$$h_1 + \frac{U_1^2}{2} = h_2 + \frac{U_2^2}{2} \tag{2.46}$$

Equations that relate the post-wave state to the initial state are referred to as *jump conditions*. Post-wave pressure p_2 and post-wave enthalpy h_2, for example, can be displayed as functions of initial pressure p_1, initial density ρ_1, initial composition Y_1, combustion wave speed U_1, and density jump ρ_1/ρ_2 by combining mass conservation (Eq. 2.44) with momentum conservation (Eq. 2.45) and energy conservation (Eq. 2.46), respectively [25]:

$$p_2 = p_1 + \rho_1 U_1^2 \left(1 - \frac{\rho_1}{\rho_2}\right) \tag{2.47}$$

$$h_2(p_2, \rho_2, Y_{\alpha,2}) = h_1(p_1, \rho_1, Y_{\alpha,1}) + \frac{U_1^2}{2}\left[1 - \left(\frac{\rho_1}{\rho_2}\right)^2\right] \tag{2.48}$$

Eq. 2.47 and 2.48 can be solved iteratively to obtain the post-wave state for a given wave speed, *e.g.* following approaches by Browne et al. [25] or by Press et al. [27]. When solving for the post-wave state, a choice must be made for the post-wave composition Y_2. Two approaches have been proven to be useful in that regard: (a) frozen compositions or (b) equilibrium compositions. Frozen compositions keep the exact mass fractions of the initial state ($Y_2 = Y_1$) and are strictly valid for inert gases at moderate wave speeds only. However, the analysis sheds light on the state directly behind a detonation wave before reactions take place and can be helpful to analyze a detonation structure. Equilibrium compositions are in chemical equilibrium for a given post-wave pressure and density [25]. The post-wave enthalpy can then be calculated with:

$$h_2(p_2, \rho_2, Y_{\alpha,2}) = \sum_{\alpha=1}^{N_S} Y_{\alpha,2}^{\mathrm{eq}}(p_2, \rho_2)\, h_\alpha(p_2, \rho_2) \tag{2.49}$$

2.2.1.2 Chapman Jouguet

The propagation speed of detonations and deflagrations can be graphically constructed in a *p*–*v* diagram using *Rayleigh lines* and *Hugoniot curves*. Rayleigh lines can be obtained by rewriting Eq. 2.47 in terms of specific volumes v_1 and v_2:

$$p_2 = p_1 - (\rho_1 U_1)^2 (v_2 - v_1) \tag{2.50}$$

$$m = \frac{p_2 - p_1}{v_2 - v_1} = -\left(\frac{U_1}{v_1}\right)^2 \tag{2.51}$$

Post-wave pressure p_2 is a linear function of post-wave specific volume v_2 for a fixed initial state, while the slope m is exclusively a function of wave speed U_1, as evident from Eq. 2.50 and Eq. 2.51. It is important to note that both, initial state (1) and post-wave state (2), must lie on the same Rayleigh line. If the initial state is fixed, the point in p_1 and v_1 acts as a pivot, as demonstrated in Fig 2.2 (panel a). The initial conditions considered in Fig 2.2 are that of a stoichiometric H_2–O_2 mixture at a pressure of 1 atm and a temperature of 300 K. Also evident from Fig 2.2 (panel a) is a steepening trend of the *Rayleigh lines* with increasing Mach numbers, whereby the slopes are always negative irrespective of wave speed. The Hugoniot curves, in contrast, arise from the utilization of the energy conservation equation in which the velocity terms are substituted with thermodynamic expressions:

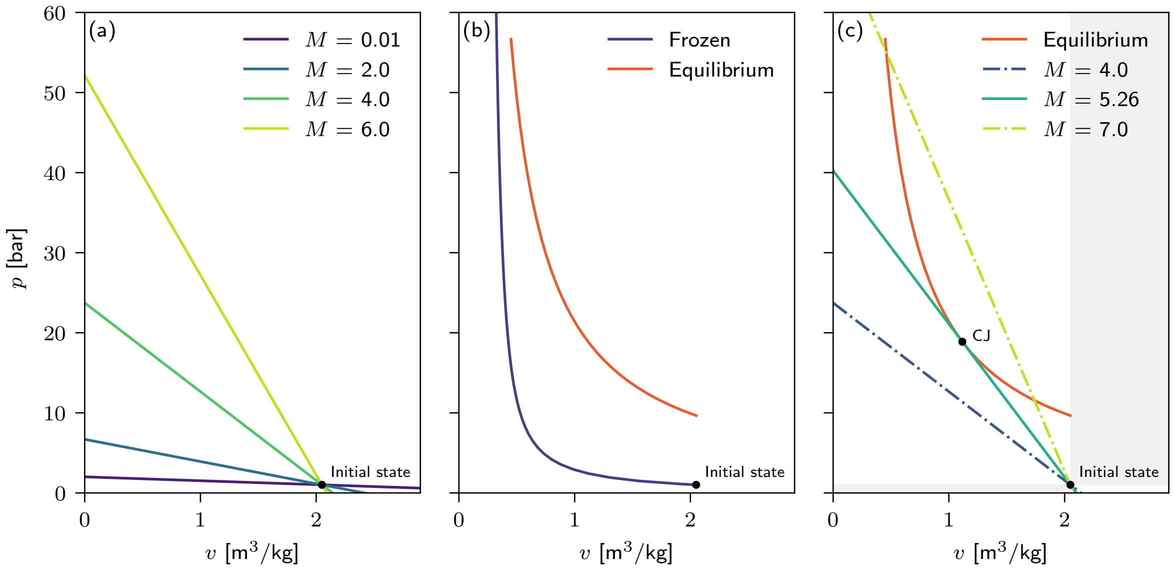

Figure 2.2: *Rayleigh lines* and *Hugoniot curves* in a p–v diagram calculated for a stoichiometric H_2–O_2 mixture at initial pressure of 101325 Pa and initial temperature of 300 K, respectively, showing **(a)** a set of *Rayleigh lines* at different wave speeds, **(b)** frozen and equilibrium *Hugoniot curves*, and **(c)** intersecting *Rayleigh lines* with *Hugoniot curves* to construct the upper Chapman Jouguet Point.

$$h_2(p_2, v_2, Y_{\alpha,2}) - h_1(p_1, v_1, Y_{\alpha,1}) = \frac{1}{2}\dot{m}^2\left(\frac{1}{\rho_2^2} - \frac{1}{\rho_1^2}\right) \tag{2.52}$$

$$h_2(p_2, v_2, Y_{\alpha,2}) - h_1(p_1, v_1, Y_{\alpha,1}) = \frac{1}{2}(v_2 + v_1)(p_2 - p_1) \tag{2.53}$$

Here, $\dot{m} = \rho_1 U_1 = \rho_2 U_2$ is the constant mass flux. Thus, Eq. 2.53 provides another set of possible post-wave states on which the solution must lie. In contrast to the set of states given by Rayleigh lines, Hugoniots are strictly thermodynamic relations and thus, independent of wave speed. Hugoniot curves can be calculated for frozen mixtures or post-wave compositions in chemical equilibrium. Fig 2.2 (b) shows the solution of both a frozen Hugoniot curve as well as a Hugoniot curve at chemical equilibrium. While the frozen curve intersects with the initial state, a displacement is observed for the equilibrium curve due to heat of formation. It must be noted that solutions for post-wave states must fulfill requirements from both, Rayleigh lines and Hugoniot curves, and are therefore restricted to intersections at a given wave speed. Figure 2.2 (c) presents the Hugoniot curve at chemical equilibrium and Rayleigh lines for three different wave speeds.

Due to the requirement of a negative slope for Rayleigh lines, certain regions in the p–v space exhibit nonphysical characteristics with respect to steady combustion wave solutions. These regions are identified by a shaded background. Thus, the Hugoniot curve is separated into three segments: (1) an upper branch with pressure $p_2 > p_1$ and specific volume $v_2 < v_1$, referred to as detonation branch, (2) a nonphysical segment characterized by pressure $p_2 > p_1$ and specific volume $v_2 > v_1$, and (3) a lower branch with pressure $p_2 < p_1$ and specific volume $v_2 > v_1$, denoted as deflagration branch. In order to intersect with the detonation branch of the Hugoniot curve, Rayleigh lines must feature significant steeper slopes, indicating higher wave speeds. Rigorous analysis (*e.g.,* by Browne et al. [25]) further proves that combustion waves of the detonation branch are always supersonic ($U_1 > c_1$), while combustion waves of the deflagration branch are always subsonic ($U_1 < c_1$). This circumstance has significant influence on the interpretation of the solutions discussed here. As detonation waves are supersonic, they cannot impact the flow upstream, whereas deflagration waves change the flow upstream and are also affected by local flow phenomena (*e.g.,* turbulence) due to their typically low propagation speed. Jump conditions as a solution method for wave propagation speeds have therefore been primarily used for the analysis of detonation waves. For this reason, features of the detonation branch are discussed in more detail. Of the 3 Rayleigh lines drawn in Fig 2.2 (c), one Rayleigh line has exactly one intersection and is therefore tangent with the Hugoniot curve. The respective solution is unique and called *Chapman Jouguet* (CJ) solution and marks the minimum wave speed for a steady propagating detonation wave. It can be shown that the entropy along the Hugoniot line is minimum at the CJ point. It follows that entropy, as well as the Rayleigh and Hugoniot lines are tangent in the CJ point. The slopes are thus equal and Eq 2.51 can be combined with the differential equation for speed of sound [25]:

$$a^2 = \left.\frac{\partial p}{\partial \rho}\right|_s = -v^2 \left.\frac{\partial p}{\partial v}\right|_s \tag{2.54}$$

$$\frac{\Delta p}{\Delta v} = -\left(\frac{U_2}{v_2}\right)^2 = \left.\frac{\partial p}{\partial v}\right|_s = -\left(\frac{a_2}{v_2}\right)^2 \tag{2.55}$$

$$\implies U_2 = a_2$$

Consequently, the gas flow behind CJ detonation waves equals the speed of sound. At lower detonation wave speeds ($U_1 < U_{\mathrm{CJ}}$), there is no intersection, and thus, no solution. At wave speeds larger than CJ ($U_1 > U_{\mathrm{CJ}}$), there are two intersections. The two possible solutions for higher wave speeds are denoted as strong and weak solution. According to Chapman [28] and Fickett and Davis [29] only the strong solution is physically viable for detonation waves, which is explained by the fact that in this case, the flow behind the wave is subsonic and pressure perturbations can travel upstream to alter the propagation speed. In contrast, the flow behind the combustion wave of the weak solution is supersonic and cannot influence the propagation speed. Additionally, as pressure perturbations can weaken the detonation wave, the speed will decrease until CJ speed is reached. In fact, detonation waves propagating at the CJ speed are usually observed in experiments in tubes [26].

2.3 Turbulence

A fundamental distinction is made between laminar and turbulent flows, where most flows in technical combustion devices are turbulent, as they increase the flame speed and thus help to stabilize the flame [9, 30]. While laminar flows are well ordered and for the most part steady, turbulent flows appear chaotic, random, and unsteady. Nevertheless, turbulent flows are deterministic and, like laminar flows, are described by the conservation equations (Eq. 2.1, 2.26, 2.33). The chaotic nature of turbulent flows arises from motions (also referred to as perturbations) relative to the overall flow direction, which cannot be damped by viscous friction [31]. Perturbations are also present in laminar flows, but here they are damped by the viscous terms in the momentum transport equations. Whether a flow is laminar or turbulent thus depends decisively on the influence of these two terms.

A criterion for predicting the flow condition was recognized early by Reynolds [32]. This was preceded by the realization that measurements of the velocity field in tubes agreed almost perfectly with the singular solution of the Navier-Stokes equations under the condition that the velocities were low and/or the cross-section was small [32]. At higher velocities and / or larger cross sections, the agreement was no longer present, and at the same time a higher resistance of the flow was observed. Stokes hypothesized that the observed deviations were caused by eddies, and that the flow in a pipe would adjust itself either as *direct* (laminar), or *sinuous* (turbulent), if the mean velocity U_{m} (cross-section averaged) was below or above a critical value obtained from the following expression [32]:

$$\frac{K_{\mathrm{stokes}}\,\mu}{\rho\, D} \tag{2.56}$$

Here, D is the diameter of the tube and $\mathrm{K}_{\mathrm{stokes}}$ is a constant defining the flow condition. In terms of round tubes, a *direct* motion was observed for values of $\mathrm{K}_{\mathrm{stokes}}$ below 1,900 and *sinuous* motion for values of $\mathrm{K}_{\mathrm{stokes}}$ above 2,000 (The critical value for flows in smooth tubes was later corrected to a value of 2,300). Stokes' observations were analyzed and elaborated upon by Reynolds, which is why the dimensionless constant is now known as Reynolds number Re and is used to characterize flow conditions in a wide variety of applications and contexts:

$$\mathrm{Re} = \frac{\rho\, u\, L}{\mu} = \frac{u\, L}{\nu} \tag{2.57}$$

Here, L is a length scale (*e.g.,* diameter of a tube or length of a plate), characterizing the respective flow problem and ν is the kinematic viscosity. The Reynolds number can be interpreted as the ratio of inertial to viscous forces.

Turbulent flows include a continuous spectrum of vortices / eddies different in size and strength, a circumstance first described by Richardson [33] in 1921. According to his observations, the characteristic length scales of the largest eddies correspond to those of the flow-defining geometry and can therefore be strongly anisotropic. The kinetic energy necessary to maintain the largest eddies is taken from the main flow. Henceforth, the energy is transferred to smaller and smaller eddies contained within the largest vortices until, at a certain length scale, the viscous effects dominate and the kinetic energy is dissipated into heat by friction. Notably, the large vortices retain a substantial amount of energy, rendering them highly stable. As a result, it requires a longer duration for turbulent friction to break up these vortices. Consequently, the lifespan of the vortices diminishes proportionally with their size. This energy transfer is designated as *turbulent energy cascade*. As the eddies decrease in size, the velocity field tends toward greater homogeneity, as a significant amount of geometric information is lost during the transfer of kinetic energy. Each characteristic length scale r of eddies present in the turbulent flow can be assigned to a corresponding Reynolds number using the velocity fluctuation u', which in turn is a function of the length scale r:

$$\mathrm{Re} = \frac{u'(r)\, r}{\nu} \tag{2.58}$$

Length scales of large eddies that feature the highest kinetic energy, are referred to as integral length scales l_{t} with the integral Reynolds number Re_{t} defined as:

$$\mathrm{Re}_{\mathrm{t}} = \frac{u'(l_{\mathrm{t}})\, l_{\mathrm{t}}}{\nu} \tag{2.59}$$

Typical values of the integral Reynolds number range from 100 to 2,000 [9], emphasizing that these eddies are controlled by inertia forces and hardly by viscosity. The integral length scale can be determined based on velocity two-point correlations, as demonstrated by Peters [30].

The smallest length scales η_{k}, on the other hand, at which the eddies dissipate, are denoted as Kolmogorov length scales with the Kolmogorov Reynolds number Re_{k} having values of unity [34]:

$$\mathrm{Re}_{\mathrm{k}} = \frac{\nu_{\mathrm{k}}\, \eta_{\mathrm{k}}}{\nu} = 1 \tag{2.60}$$

Since all kinetic energy eventually dissipates, when the length scales r approach the Kolmogorov length scale η_{k}, the dissipation rate of kinetic energy ϵ must be equal to the rate at which the largest scales acquire kinetic energy. The dissipation rate can therefore be linked to the motion of the largest scales and be estimated as [34, 35]:

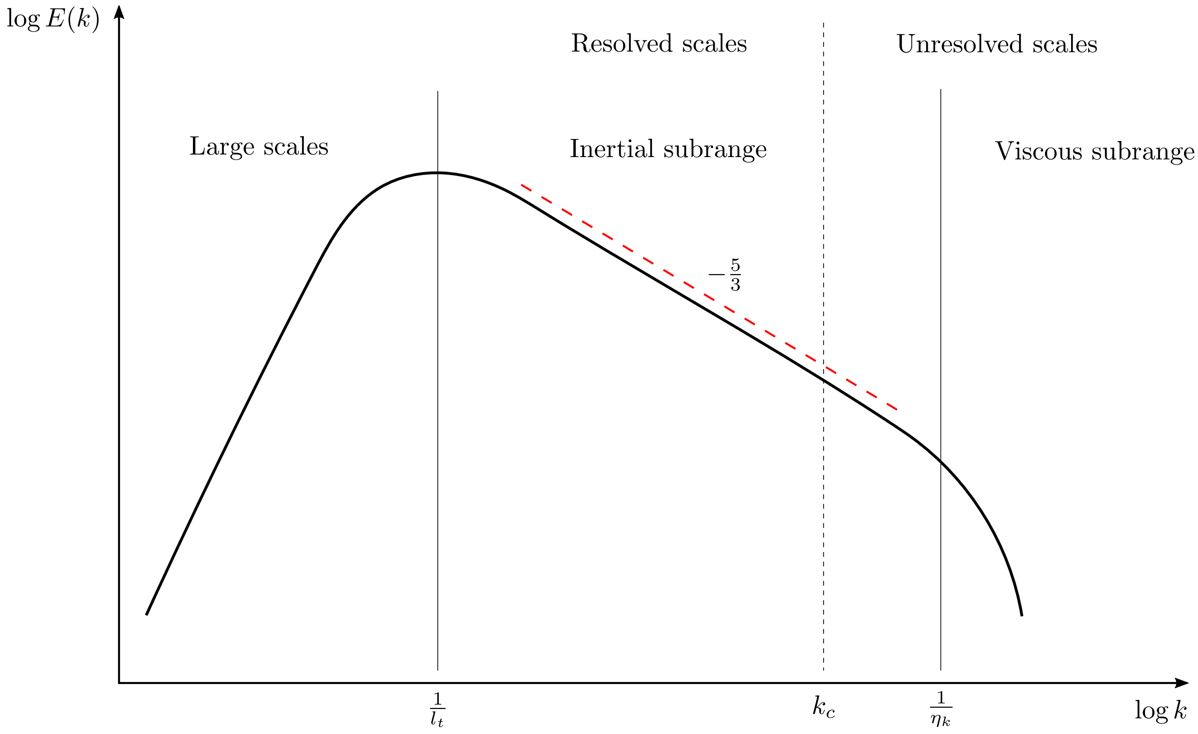

Figure 2.3: Kinetic energy $E(k)$ spectrum as a function of wave number $k = 1/L$. The figure is based on the one presented by Peters. [30].

$$\epsilon = \frac{u'^2(l_\mathrm{t})}{\tau_m(l_\mathrm{t})} = \frac{u'^3(l_\mathrm{t})}{l_\mathrm{t}} \tag{2.61}$$

$$\tau_m(l_\mathrm{t}) = \frac{l_\mathrm{t}}{u'(l_\mathrm{t})} \tag{2.62}$$

Equation 2.61 states that dissipation of kinetic energy is proportional to the reciprocal of the characteristic *turnover* time τ_m and proportional to the square of the characteristic velocity fluctuation, emphasizing that the eddy transfers the majority of kinetic energy within one *turnover* time [34]. The dissipation mechanism in that regard is independent on viscosity, but instead is carried out by the non-linear terms, transferring kinetic energy down to smaller scales. Since the energy transfer rate is constant along scales, this relation also holds true in the viscous limit [30]:

$$\epsilon = \frac{u'^3(l_\mathrm{t})}{l_\mathrm{t}} = \frac{u'^3(r)}{r} = \frac{v_\mathrm{k}^3}{\eta_\mathrm{k}} \tag{2.63}$$

The Kolmogorov hypothesis for locally isotropic turbulence postulates that the motion of the smallest scales is governed uniquely by the dissipation rate ϵ and the kinematic viscosity ν. From dimensional analysis, the three Kolmogorov micro scales for length, velocity and time can be derived [36]:

$$\eta_\mathrm{k} = \left(\frac{\nu^3}{\epsilon}\right)^{\frac{1}{4}}, \ v_\mathrm{k} = \left(\nu^3\epsilon\right)^{\frac{1}{4}}, \ \tau_\mathrm{k} = \left(\frac{\nu}{\epsilon}\right)^{\frac{1}{2}} \tag{2.64}$$

The ratio of the integral length scale and the Kolmogorov length scale illustrates the scale separation and can be computed by combining Eq. 2.58, 2.61, and 2.64:

$$\frac{l_\mathrm{t}}{\eta_\mathrm{k}} = \frac{\frac{\nu \mathrm{Re}_\mathrm{t}}{u'(l_\mathrm{t})}}{\left(\frac{\nu^3}{\epsilon}\right)^{\frac{1}{4}}} = \mathrm{Re}_\mathrm{t}^{\frac{3}{4}} \tag{2.65}$$

It is evident from Eq. 2.65 that the size of the smallest scales will adapt to the Reynolds number, given constant integral length scales. It is common to sketch the kinetic energy density $E(k)$ as a function of wave number to demonstrate the distribution of kinetic energy in turbulent flows. The wave number in this context is defined as the reciprocal of the characteristic length scale $k = 1/r$. Kinetic energy scales with the square of velocity and can be related to the dissipation rate and the length scale r using Eq.2.63:

$$u'^2(k = 1/r) \propto \epsilon^{2/3}\, r^{2/3} = \epsilon^{2/3}\, k^{-2/3} \tag{2.66}$$

In order to sketch the kinetic energy spectrum over wave number Eq. 2.66 must be differentiated with k to yield:

$$E(k) = \frac{du'^2(k)}{dk} \propto \epsilon^{2/3}\, k^{-5/3} \tag{2.67}$$

Note that Eq. 2.67 is only valid with the assumptions made by Kolmogorov in the region between the integral length scale and the Kolmogorov length scale, where the kinetic energy scales with the famous $-5/3$ slope in log-log coordinates. The qualitative energy spectrum of turbulent flow is presented in Fig. 2.3. Kinetic energy decays in exponential fashion for wave numbers greater than the inverse of the Kolmogorov scale in the viscous sub range. Scaling of eddies with length scales even larger than the integral length scale does not follow universal laws but instead is highly problem dependent [30].

2.3.1 Direct Numerical Simulation

A computational fluid dynamics simulation requires a discretization of the numerical domain in terms of finite volumes or finite differences with a corresponding mesh size Δ_x. If this mesh size is in the order or smaller than the Kolmogorov length scale, no further modelling is required and the conservation equations (Eq. 2.1, 2.26, 2.33, and 2.4) can be solved directly. This class of simulation is called a *direct numerical simulation* (DNS). Note that the simulation of a reactive flow may involve other length scales that must also be resolved by the simulation and may be significantly smaller than the Kolmogorov length scale. For example, this could be an adequate resolution of the flame front or a mixing length scale. Assuming now that the Kolmogorov length scale is the smallest scale to be resolved, the mesh resolution can be related to the integral Reynolds number. In this context, it should be noted that the order of magnitude of the integral Reynolds number corresponds approximately to the flow-defining Reynolds number:

$$\Delta_x \sim \eta_\mathrm{k} \propto \mathrm{Re}_\mathrm{t}^{-3/4} \sim \mathrm{Re}^{-3/4} \tag{2.68}$$

Further, we assume that the cost of a simulation (per unit core-h) is proportional to the inverse of the required grid resolution to the power of 4. The exponent stems from the fact that the simulation is carried out in three-dimensional space where the integration step size is proportional to the inverse of the grid size (as pointed out in Sec. 3.1):

$$[\mathrm{core}-\mathrm{h}] \propto \left(\frac{1}{\Delta_x}\right)^4 = \mathrm{Re}^3 \tag{2.69}$$

Equation 2.69 thus states that the cost of a three-dimensional DNS scales with the cube of the Reynolds number. Even the latest *high performance computers* (HPC) are therefore limited to DNS of very restricted cases, both in terms of domain size and Reynolds number.

2.4 Large-Eddy Simulation

Large-eddy simulations (LES) are very common to overcome the limitations presented by the resolution criterion of a DNS and can be used to simulate problems beyond the scope of a DNS, (*e.g.*, semi-industrial coal furnace [37], internal combustion engines [38], and gas turbine combustion chambers [39]). The fundamental idea of a LES is to simulate only medium sized to large scales, as illustrated in Fig. 2.3. The large scales contain most of the kinetic energy and cannot be considered universal, while the small scales are assumed to be homogeneous and universal, allowing to consider the effect of the small scales with rather simple models. Each quantity ϕ is thus decomposed into a filtered (or resolved) part and a residual (or subgrid) part:

$$\phi(\boldsymbol{x}, t) = \bar{\phi}(\boldsymbol{x}, t) + \phi'(\boldsymbol{x}, t) \tag{2.70}$$

Here, the bar $(\bar{\cdot})$ indicates the resolved component $\bar{\phi}(\boldsymbol{x}, t)$ with $\phi'(\boldsymbol{x}, t)$ being the unresolved contribution. The decomposition is at first glance equivalent to the well-known Reynolds decomposition [31] in terms of *Reynolds Averaged Navier-Stokes* (RANS) equations, where a quantity is decomposed into a time-averaged component and a fluctuation. Since RANS is not used in any of the simulations presented in this work, the approach will not be further discussed. However, due to the similarities and the popularity of RANS, it is important to point out that general rules for simplifying the conservation equations after the decomposition are not transferable. For example, filtering a subgrid quantity does not yield a value of zero, unlike time averaging a fluctuation:

$$\bar{\phi}'(\boldsymbol{x}, t) \neq 0 \tag{2.71}$$

Also, filtering a quantity twice does not yield the result after the first filtering operation:

$$\bar{\bar{\phi}}(\boldsymbol{x}, t) \neq \bar{\phi}(\boldsymbol{x}, t) \tag{2.72}$$

Analogous to the Favre time averaging, the Favre filtering [40] is introduced at this point, *i.e.* the density-weighted filtering of a quantity:

$$\tilde{\phi} = \frac{\overline{\rho\phi}}{\bar{\rho}} \tag{2.73}$$

$$\phi(\boldsymbol{x}, t) = \tilde{\phi}(\boldsymbol{x}, t) + \phi''(\boldsymbol{x}, t) \tag{2.74}$$

2.4.1 Filtering of the Conservation Equations

In order to remove the small scales from a turbulent flow field, a filter operation is applied to every conservation equation employed in the simulation. The filter operation can be accomplished in physical space for an arbitrary quantity $\phi(\boldsymbol{x})$ distributed in the three-dimensional domain $\mathcal{D}$, using the following convolution operator introduced by Leonard [41]:

$$\bar{\phi}(\boldsymbol{x}, t) = \int_{\mathcal{D}} \phi(\check{\boldsymbol{x}}, t)\, G(\boldsymbol{x} - \check{\boldsymbol{x}}; \Delta)\, d\check{\boldsymbol{x}} \tag{2.75}$$

Here, G represents a convolution kernel for a filter with the filter width Δ. Different filter types have been used in the past, including *cut-off spectral* filters, *gaussian* filters, and *top-hat* filters, as discussed in many textbooks [9, 31, 42]. A *cut-off* filter in spectral space is the preferred choice in terms of spectral CFD codes, while a Gauss filter is preferred to explicitly filter the conservation equations in physical space. An explicit filter is particularly suitable for fundamental studies, since numerical errors of the grid and filter are separated. On the other hand, the full grid resolution is not used to resolve the smallest possible structures, such that explicit LES is rarely used. Instead, most LES use implicit filtering, where the filtering is performed by a numerical grid that is incapable to resolve the small scales in the first place, in addition to a filter contribution that stems from the numerical schemes used. The effective filter width can be therefore expressed as:

$$\Delta = (1+q)\,\Delta_x, \quad q > 0 \tag{2.76}$$

Here, q is a constant that depends on the discretization scheme. An implicit LES may become a DNS when the grid size Δ_x approaches the Kolmogorov length scale, under the condition that q is small. The grid contribution of the filter resembles a top-hat filter, where the filter width equals the grid size and can be considered the spatial average over the filter volume [9]:

$$G(\boldsymbol{x}) = G(x_1, x_2, x_3) = \begin{cases} 1/\Delta^3 & \text{if } |x_i| < \Delta/2 \quad (i = 1, 2, 3), \\ 0 & \text{else.} \end{cases} \tag{2.77}$$

Applying a filter to the continuity equation yields:

$$\overline{\frac{\partial \rho}{\partial t}} + \overline{\frac{\partial \rho u_i}{\partial x_i}} = 0 \tag{2.78}$$

Equation 2.78 can be recast, assuming commutativity of the filter operator and derivative operator ($\overline{\partial \rho} = \partial \bar{\rho}$), and by replacing a filtered product of density with another quantity by the Favre filtered quantity ($\overline{\rho u}/\bar{\rho} = \tilde{u}$):

$$\frac{\partial \bar{\rho}}{\partial t} + \frac{\partial \bar{\rho} \tilde{u}_i}{\partial x_i} = 0 \tag{2.79}$$

The introduction of the Favre filter thus results in a filtered continuity equation that is free of terms that require modelling.

After performing the aforementioned steps of commutativity and Favre filtering, the filtered momentum conservation equations read:

$$\frac{\partial \bar{\rho} \tilde{u}_j}{\partial t} + \frac{\partial \bar{\rho} \tilde{u}_j \tilde{u}_i}{\partial x_i} + \frac{\partial \bar{p}}{\partial x_i} - \frac{\partial \check{\tau}_{ji}}{\partial x_i} = \underbrace{-\frac{\partial \bar{\rho} \left(\widetilde{u_j u_i} - \tilde{u}_j \tilde{u}_i \right)}{\partial x_i}}_{\mathcal{U}_1} + \underbrace{\frac{\partial \bar{\tau}_{ji} - \check{\tau}_{ji}}{\partial x_i}}_{\mathcal{U}_2} \tag{2.80}$$

$$\bar{\tau}_{ji} = \overline{-\frac{2}{3} \mu \frac{\partial u_k}{\partial x_k} \delta_{ij} + \mu \left(\frac{\partial u_i}{\partial x_j} + \frac{\partial u_j}{\partial x_i} \right)} \tag{2.81}$$

$$\check{\tau}_{ji} = -\frac{2}{3} \bar{\mu} \frac{\partial \tilde{u}_k}{\partial x_k} \delta_{ij} + \bar{\mu} \left(\frac{\partial \tilde{u}_i}{\partial x_j} + \frac{\partial \tilde{u}_j}{\partial x_i} \right) \tag{2.82}$$

Equation 2.80 is formulated with all computable terms on the *left hand side* (LHS) and two additional unclosed terms $\mathcal{U}_1$ and $\mathcal{U}_2$ on the right hand side. The check symbol $(\check{\ })$ indicates a computable term, replacing all unknowns by the favre-filtered or filtered counterparts. The unclosed term $\mathcal{U}_1$, also referred to as *subgrid scale stresses* (SGS), results from the filtered non-linear term that cannot be computed directly from the filtered solution:

$$\frac{\partial \overline{\rho u_j u_i}}{\partial x_i} = \frac{\partial \bar{\rho} \widetilde{u_j u_i}}{\partial x_i} = \frac{\partial \bar{\rho} \tilde{u}_j \tilde{u}_i}{\partial x_i} + \frac{\partial \bar{\rho} \left(\widetilde{u_j u_i} - \tilde{u}_j \tilde{u}_i \right)}{\partial x_i} = \frac{\partial \bar{\rho} \tilde{u}_j \tilde{u}_i}{\partial x_i} - \mathcal{U}_1 \tag{2.83}$$

The term is commonly written in terms of a subgrid-scale stress tensor $\mathcal{T}_{ij}$:

$$\mathcal{U}_1 = \frac{\partial \mathcal{T}_{ij}}{\partial x_i} \tag{2.84}$$

$$\Rightarrow \mathcal{T}_{ij} = -\bar{\rho}\left(\widetilde{u_j u_i} - \tilde{u}_j \tilde{u}_i\right) \tag{2.85}$$

This subgrid-scale stress tensor can be separated, using the filter decomposition from Eq. 2.74, to yield three different subgrid-scale stress contributions [42]:

$$\mathcal{T}_{ij} = -\bar{\rho}\left(\widetilde{\tilde{u}_j \tilde{u}_i} - \tilde{u}_j \tilde{u}_i\right) - \bar{\rho}\left(\widetilde{u''_j \tilde{u}_i} - \widetilde{\tilde{u}_j u''_i}\right) - \bar{\rho}\, \widetilde{u''_j u''_i} \tag{2.86}$$

$$= \mathcal{L}_{ij} + C_{ij} + \mathcal{R}_{ij} \tag{2.87}$$

Here, $\mathcal{L}_{ij}$ denotes the *Leonard* subgrid-scale stresses describing the interaction among filtered velocities, C_{ij} presents the *Cross* subgrid-scale stresses between filtered velocities and subgrid velocities, and $\mathcal{R}_{ij}$ are the *Reynolds* subgrid-scale stresses for the interaction between subgrid velocities.

The filtered transport equation for the species mass fractions, after applying all the assumptions used previously, results in:

$$\frac{\partial \bar{\rho}\tilde{Y}_\alpha}{\partial t} + \frac{\partial \bar{\rho}\tilde{Y}_\alpha \tilde{u}_i}{\partial x_i} + \frac{\partial \check{j}_{i,\alpha}}{\partial x_i} = \underbrace{-\frac{\partial \bar{\rho}(\widetilde{Y_\alpha u_i} - \tilde{Y}_\alpha \tilde{u}_i)}{\partial x_i}}_{\mathcal{Y}_1} \underbrace{-\frac{\partial \bar{j}_{i,\alpha} - \check{j}_{i,\alpha}}{\partial x_i}}_{\mathcal{Y}_2} \underbrace{+\overline{\dot{\omega}}_\alpha}_{\mathcal{Y}_3} \tag{2.88}$$

$$\mathcal{Y}_1 = \frac{\partial \mathcal{S}_{i,\alpha}}{\partial x_i} \Rightarrow \mathcal{S}_{i,\alpha} = -\bar{\rho}(\widetilde{Y_\alpha u_i} - \tilde{Y}_\alpha \tilde{u}_i) \tag{2.89}$$

$$\bar{j}_{i,\alpha} = \overline{-\rho\, D_\alpha \frac{\partial Y_\alpha}{\partial x_i}} \tag{2.90}$$

$$\check{j}_{i,\alpha} = -\bar{\rho}\, \bar{D}_\alpha \frac{\partial \tilde{Y}_\alpha}{\partial x_i} \tag{2.91}$$

Here, $\mathcal{S}_i$ denotes the unresolved scalar fluxes, while the term $\mathcal{Y}_2$ results from filtering the diffusion term. The filtered source term $\overline{\dot{\omega}}_\alpha$ has great importance due to strongly non-linear dependencies of state variables and must be modeled in the vast majority of cases.

Filtering the conservation equation for total internal energy adds complexity and results in a rather high number of terms that could be modeled [42], compared to the filtered conservation equations for momentum and species partial densities. Applying a filter yields:

$$\overline{\rho E} = \bar{\rho}\tilde{E} = \bar{\rho}\tilde{e} + \bar{\rho}\frac{\widetilde{u_k u_k}}{2} \tag{2.92}$$

The filtered conserved quantity $\overline{\rho E}$ in Eq. 2.92 thus incorporates the unclosed term $\widetilde{u_k u_k}$. Various approaches have been postulated in the past to circumvent the issue and are presented in detail in the book of Sagaut [42]. Among the more popular approaches is the consideration of a subgrid kinetic energy $\mathcal{K}$ (*e.g.,* Dubois et al. [43], Piomelli [44], Kosović et al. [45], and Ragab et al. [46]):

$$\bar{\rho}\tilde{E} = \bar{\rho}\tilde{e} + \bar{\rho}\frac{\tilde{u}_k \tilde{u}_k}{2} + \mathcal{K} \tag{2.93}$$

$$\mathcal{K} = \frac{1}{2}\bar{\rho}\,(\widetilde{u_k u_k} - \tilde{u}_k \tilde{u}_k) = \frac{\mathcal{T}_{kk}}{2} \tag{2.94}$$

Other popular approaches have been defined by Vreman [47, 48] that include a conservation equation for the computable total internal energy $\check{E}$:

$$\bar{\rho}\check{E} = \frac{\bar{p}}{\gamma - 1} + \bar{\rho}\frac{\tilde{u}_k\tilde{u}_k}{2} \tag{2.95}$$

It is important to note, however, that all the approaches align if the subgrid kinetic energy $\mathcal{K}$ can be neglected, as will be discussed in Sec 2.4.2. The filtered conservation equation for the total internal energy $\tilde{E}$ then reads [42] without consideration of net rate of external energy input:

$$\begin{aligned}
&\frac{\partial\bar{\rho}\tilde{E}}{\partial t} + \frac{\partial(\bar{\rho}\tilde{E} + \bar{p})\tilde{u}_i}{\partial x_i} - \frac{\partial\check{\tau}_{ji}\tilde{u}_j}{\partial x_i} + \frac{\partial\check{q}_i}{\partial x_i} \\
&= -\left(\frac{\partial\bar{\rho}\widetilde{Eu_i} - \bar{\rho}\tilde{E}\tilde{u}_i}{\partial x_i}\right) - \left(\frac{\partial\overline{pu_i} - \bar{p}\tilde{u}_i}{\partial x_i}\right) - \left(\frac{\partial\bar{q}_i - \check{q}_i}{\partial x_i}\right) + \left(\frac{\partial\overline{\tau_{ji}u_j} - \check{\tau}_{ji}\tilde{u}_j}{\partial x_i}\right) \\
&= \underbrace{-\left(\frac{\partial\bar{\rho}\widetilde{hu_i} - \bar{\rho}\tilde{h}\tilde{u}_i}{\partial x_i}\right)}_{\mathcal{E}_1} \underbrace{-\left(\frac{\partial\frac{\bar{\rho}}{2}\widetilde{u_iu_ku_k} - \frac{\bar{\rho}}{2}\tilde{u}_i\tilde{u}_k\tilde{u}_k - \tilde{u}_i\mathcal{K}}{\partial x_i}\right)}_{\mathcal{E}_2} \underbrace{-\left(\frac{\partial\bar{q}_i - \check{q}_i}{\partial x_i}\right)}_{\mathcal{E}_3} \underbrace{+\left(\frac{\partial\overline{\tau_{ji}u_\mathrm{j}} - \check{\tau}_{ji}\tilde{u}_j}{\partial x_i}\right)}_{\mathcal{E}_4}
\end{aligned} \tag{2.96}$$

$$\mathcal{E}_1 = \frac{\partial Q_i}{\partial x_i} \Rightarrow Q_i = -\bar{\rho}(\widetilde{hu_i} - \tilde{h}\tilde{u}_i) \tag{2.97}$$

$$\mathcal{E}_2 = \frac{\partial\mathcal{J}_i}{\partial x_i} \Rightarrow \mathcal{J}_i = -\frac{\bar{\rho}}{2}(\widetilde{u_iu_ku_k} - \tilde{u}_i\tilde{u}_k\tilde{u}_k) + \tilde{u}_i\mathcal{K} \tag{2.98}$$

Equations 2.97 and 2.98 feature the subgrid-scale heat fluxes Q_i and the subgrid-scale turbulent diffusion $\mathcal{J}_i$.

2.4.2 Neglected Terms

There are only a few studies in which the influence of all terms that could be modeled have been examined. These include works by Vreman et al. [47] and Martín et al. [49], who draw similar conclusions despite different configurations in terms of the Mach numbers used. The influences were put in relation to the magnitudes of the convective term and the diffusive term. Terms that are at least one order of magnitude smaller than the diffusive term are classified as small and terms with an impact of less than two orders of magnitude are classified as negligible. In the filtered equations discussed here, the terms $\mathcal{U}_2$, $\mathcal{E}_3$, and $\mathcal{E}_4$ have been not considered, based on these findings. Also, because of the similarity of term $\mathcal{Y}_2$ with the terms $\mathcal{U}_2$ and $\mathcal{E}_3$, it has been also neglected without further proof.

The subgrid kinetic energy $\mathcal{K}$, which presents the isotropic part of the subgrid stress tensor $\mathcal{T}_{ij}$, appears both in the filtered conservation equation for momentum and total internal energy. Although a model for this term has been proposed by Yoshizawa [50], it was deliberately disregarded here and the effects of unresolved subgrid kinetic energy were neglected throughout this work. The decision stems primarily from observations made by Charles et al. [51], Erlebacher et al. [52]. First, the authors examined the extent to which the model matches the correct value by analyzing results from DNS. A very weak correlation coefficient of 15% was determined in that regard. More importantly, they found that the influence of the isotropic component of the subgrid kinetic energy is significantly less than that of the static pressure. The only exception are regions with particularly strong compression. However, shock-capturing numerical schemes are used in this work, which dissipate significant amounts of kinetic energy exactly in the vicinity of shocks, rendering a model for subgrid kinetic energy useless [42]. Ultimately, based on the simplifications made, this results in the following set of filtered conservation equations used in this work:

$$\frac{\partial \bar{\rho}}{\partial t} + \frac{\partial \bar{\rho}\tilde{u}_i}{\partial x_i} = 0 \tag{2.99}$$

$$\frac{\partial \bar{\rho}\tilde{u}_j}{\partial t} + \frac{\partial \bar{\rho}\tilde{u}_j\tilde{u}_i}{\partial x_i} + \frac{\partial \bar{p}}{\partial x_i} - \frac{\partial \bar{\tau}_{ji}}{\partial x_i} = \frac{\partial \mathcal{T}_{ij}}{\partial x_i} \tag{2.100}$$

$$\frac{\partial \bar{\rho}\tilde{E}}{\partial t} + \frac{\partial (\bar{\rho}\tilde{E} + \bar{p})\tilde{u}_i}{\partial x_i} - \frac{\partial \bar{\tau}_{ji}\tilde{u}_j}{\partial x_i} + \frac{\partial \bar{q}_i}{\partial x_i} = \frac{\partial Q_i}{\partial x_i} + \frac{\partial \mathcal{J}_i}{\partial x_i} \tag{2.101}$$

$$\frac{\partial \bar{\rho}\tilde{Y}_\alpha}{\partial t} + \frac{\partial \bar{\rho}\tilde{Y}_\alpha\tilde{u}_i}{\partial x_i} + \frac{\partial \bar{j}_{i,\alpha}}{\partial x_i} = \frac{\partial S_{i,\alpha}}{\partial x_i} + \overline{\dot{\omega}}_\alpha \tag{2.102}$$

This leaves 5 terms on the RHS whose modeling is discussed in the following.

2.4.3 Eddy Viscosity Models

In subgrid-scale modeling, a distinction is made between structural and functional models. Structural modeling tries to approximate the modeled term as best as possible, whereas in functional models only the effect that the subgrid scales have on the resolved scales is approximated by diffusion processes. Since only functional models were used in this work, they will be briefly discussed below. It should also be mentioned that besides the energy transfer from the resolved scales to the unresolved scales, the reverse process also exists, *i.e.* the transfer from unresolved scales to the resolved ones, but being much weaker and often neglected. For a long time, the focus of turbulence modeling was on the subgrid-scale stress tensor $\mathcal{T}_{ij}$, since this is the only term to be modeled in incompressible flows. The Boussinesq hypothesis is usually used in this context, which states that the energy transfer from large to small scales essentially corresponds to a molecular diffusion process. The deviatoric part of the subgrid stresses is thus defined in analogy to the deviatoric part of the stress tensor:

$$\mathcal{T}^{\mathrm{d}}_{ij} = \mathcal{T}_{ij} - \frac{1}{3}\mathcal{T}_{kk}\delta_{ij} = -\bar{\rho}\,\nu_{\mathrm{t}}\left(\frac{\partial \tilde{u}_i}{\partial x_j} + \frac{\partial \tilde{u}_j}{\partial x_i} - \frac{2}{3}\frac{\partial \tilde{u}_k}{\partial x_k}\delta_{ij}\right) \tag{2.103}$$

Accordingly, in Eq. 2.103, only the molecular viscosity was replaced by a sub grid scale viscosity, also referred to as turbulent kinematic viscosity ν_{t}. Likewise, the approach is suitable for closing the term $\mathcal{J}_i$ describing subgrid diffusion in the energy conservation equation, whereby the approach is based on previous RANS models [53]:

$$\mathcal{J}_i \approx \mathcal{T}^{\mathrm{d}}_{ij}\tilde{u}_i = -\bar{\rho}\,\nu_{\mathrm{t}}\left(\frac{\partial \tilde{u}_i}{\partial x_j} + \frac{\partial \tilde{u}_j}{\partial x_i} - \frac{2}{3}\frac{\partial \tilde{u}_k}{\partial x_k}\delta_{ij}\right)\tilde{u}_i \tag{2.104}$$

Furthermore, it is assumed that the subgrid scales can be described by a characteristic length scale l_0 and time scale t_0 [42]. Dimensional analysis then yields the following expression for the subgrid-scale viscosity:

$$\nu_{\mathrm{t}} = \frac{l_0^2}{t_0} \tag{2.105}$$

This class of models is thus referred to as *Eddy viscosity* models and it is common to represent the characteristic length scale by the product of the grid size, at which the kinetic energy must be adequately dissipated, and a model constant C_{m}. The characteristic time scale, on the other hand, is represented by a differential operator $\mathcal{D}_{\mathrm{m}}$, which has the resolved velocity field as argument and has unit per time.

$$\nu_{\mathrm{t}} = (\Delta C_{\mathrm{m}})^2\,\mathcal{D}_{\mathrm{m}}(\tilde{u}_i) \tag{2.106}$$

The first proposed SGS model to compute the turbulent viscosity following Eq. 2.106 has been the Smagorinsky model [54] which continues to find widespread use due to its simplicity, robustness, and low implementation effort. The differential operator used for this model is the characteristic filtered rate of strain $\mathcal{S} = \sqrt{2\tilde{S}_{ij}\tilde{S}_{ij}}$, with $\tilde{S}_{ij} = 1/2(\tilde{g}_{ij} + \tilde{g}_{ji})$, $\tilde{g}_{ij} = \partial\tilde{u}_i/\partial x_j$. The following expression is then obtained for the turbulent viscosity:

$$\nu_\mathrm{t} = (C_\mathrm{s}\Delta)^2\,\mathcal{S} \tag{2.107}$$

Theoretical considerations exist for determining the model constant C_s when the constant is interpreted as the ratio of the mixing length to the filter cut-off scale in analogy to Prandtl's mixing theory [31]. Calculations result in values for the model constant of $C_\mathrm{s} = 0.148$ [42]. The model constant, however, is local, both in space and in time and usually takes values in a range between 0.1 and 0.2. Compared to the exact turbulent viscosity in a posteriori analyses, the correlation is thus rather poor. Among the known weaknesses of the Smagorinsky model is an increased damping of turbulence in regions with high mean strain, during flow transition and near walls since the differential operator does not vanish for pure shear [55].

Several models have addressed this deficiency like the *wall adapting local eddy viscosity* (WALE) model [56] and the Vreman model [57]. However, while the differential operators used in these models vanish for pure shear, they do not cancel for pure rotation unlike the characteristic filtered rate of strain. Thus, Nicoud et al. [55] proposed a set of desirable properties for differential operators, both from a physical but also from a numerical standpoint. Besides the already mentioned requirement that the differential operator should take values of zero for pure shear or pure rotation, the differential operator should:

- be defined by local values
- only take positive values, thus neglecting backscatter
- approach values of zero near solid boundaries and scale with the cube of wall distance
- take values of zero for two-dimensional flows
- take values of zero for axisymmetric expansion or contraction

A differential operator that satisfies all aforementioned properties and that has been established by the authors is based solely on the singular values $(\sigma_1, \sigma_2, \sigma_3)$ obtained from the resolved velocity gradient tensor $(\tilde{g}_{ij} = \partial\tilde{u}_i/\partial x_j)$. It is therefore usually referred to as the sigma model:

$$\mathcal{D}_\sigma = \frac{\sigma_3\,(\sigma_1 - \sigma_2)\,(\sigma_2 - \sigma_3)}{\sigma_1^2}, \quad 0 \le \sigma_3 \le \sigma_2 \le \sigma_1 \tag{2.108}$$

It is important to note that the differential operator in Eq. 2.108 vanishes, whenever σ_3 vanishes, which is the case in two-dimensional flows. Since the sigma model has been used throughout this work, the calculation of the singular values is outlined below. First, the three invariants $\mathcal{I}_1, \mathcal{I}_2, \mathcal{I}_3$ of matrix $G_{ij} = \tilde{g}_{ki}\tilde{g}_{kj}$ are computed, where $\mathrm{tr}(G_{ij})$ denotes the trace and $\mathrm{det}(G_{ij})$ denotes the determinant:

$$\mathcal{I}_1 = \mathrm{tr}(G_{ij}) \tag{2.109}$$

$$\mathcal{I}_2 = 0.5\left(\mathrm{tr}(G_{ij})^2 - \mathrm{tr}(G_{ij}^2)\right) \tag{2.110}$$

$$\mathcal{I}_3 = \mathrm{det}(G_{ij}) \tag{2.111}$$

Subsequently, angles $\alpha_1, \alpha_2, \alpha_3$ can be calculated as a function of the invariants:

$$\alpha_1 = \frac{\mathcal{I}_1^2}{9} - \frac{\mathcal{I}_2}{3} \tag{2.112}$$

$$\alpha_2 = \frac{\mathcal{I}_1^3}{27} - \frac{\mathcal{I}_1\mathcal{I}_2}{6} + \frac{\mathcal{I}_3}{2} \tag{2.113}$$

$$\alpha_3 = \frac{1}{3}\arccos\left(\frac{\alpha_2}{\alpha_1^{3/2}}\right) \tag{2.114}$$

The singular values are then defined by:

$$\sigma_1 = \sqrt{\frac{\mathcal{I}_1}{3} + 2\sqrt{\alpha_1}\cos(\alpha_3)} \tag{2.115}$$

$$\sigma_2 = \sqrt{\frac{\mathcal{I}_1}{3} - 2\sqrt{\alpha_1}\cos\left(\frac{\pi}{3} + \alpha_3\right)} \tag{2.116}$$

$$\sigma_3 = \sqrt{\frac{\mathcal{I}_1}{3} - 2\sqrt{\alpha_1}\cos\left(\frac{\pi}{3} - \alpha_3\right)} \tag{2.117}$$

Nicoud et al. [55] as well as Rieth et al. [58] found promising results in different setups for a model constant of $C_\sigma = 1.5$, when used directly as a static model. Nonetheless, as pointed by the authors, the sigma model can also be used as a starting model with intrinsic superior properties to be used in the framework of dynamic procedures.

The dynamic procedure has been originally developed by Germano et al. [59] and extended for variable density flows by Moin et al. [60]. The central motivation has been accuracy improvements of eddy-viscosity type subgrid scale models by calculating the model constant dynamically, thus reflecting the local flow state. Therefore, another test filter (typically with twice the filter width [61]) is applied to the LES filtered momentum balance equation. Introducing a Favre filter at test filter level ($\widehat{\bar{\rho}\tilde{u}}/\hat{\bar{\rho}} = \check{\tilde{u}}$) yields:

$$\frac{\partial\widehat{\bar{\rho}\tilde{u}_j}}{\partial t} + \frac{\partial\widehat{\bar{\rho}\tilde{u}_j\tilde{u}_i}}{\partial x_i} + \frac{\partial\hat{\bar{p}}}{\partial x_i} - \frac{\partial\hat{\bar{\tau}}_{ji}}{\partial x_i} = -\frac{\partial\bar{\rho}\left(\widecheck{\widetilde{u_j u_i}} - \widecheck{\tilde{u}_j\tilde{u}_i}\right)}{\partial x_i} \tag{2.118}$$

$$\frac{\partial\widehat{\bar{\rho}\tilde{u}_j}}{\partial t} + \frac{\partial\hat{\bar{\rho}}\check{\tilde{u}}_j\check{\tilde{u}}_i}{\partial x_i} + \frac{\partial\hat{\bar{\rho}}\left(\widecheck{\tilde{u}_j\tilde{u}_i} - \check{\tilde{u}}_j\check{\tilde{u}}_i\right)}{\partial x_i} + \frac{\partial\hat{\bar{p}}}{\partial x_i} - \frac{\partial\hat{\bar{\tau}}_{ji}}{\partial x_i} = -\frac{\partial\bar{\rho}\left(\widecheck{\widetilde{u_j u_i}} - \widecheck{\tilde{u}_j\tilde{u}_i}\right)}{\partial x_i} \tag{2.119}$$

$$\frac{\partial\widehat{\bar{\rho}\tilde{u}_j}}{\partial t} + \frac{\partial\hat{\bar{\rho}}\check{\tilde{u}}_j\check{\tilde{u}}_i}{\partial x_i} + \frac{\partial\hat{\bar{p}}}{\partial x_i} - \frac{\partial\hat{\bar{\tau}}_{ji}}{\partial x_i} = \underbrace{-\frac{\partial\hat{\bar{\rho}}\left(\widecheck{\tilde{u}_j\tilde{u}_i} - \check{\tilde{u}}_j\check{\tilde{u}}_i\right)}{\partial x_i}}_{-\partial L_{ij}/\partial x_i}\underbrace{-\frac{\partial\bar{\rho}\left(\widecheck{\widetilde{u_j u_i}} - \widecheck{\tilde{u}_j\tilde{u}_i}\right)}{\partial x_i}}_{-\partial\hat{\mathcal{T}}_{ij}/\partial x_i} = -\frac{\partial T_{ij}}{\partial x_i} \tag{2.120}$$

Equation 2.120 introduces the subgrid scale stresses T_{ij} at test filter size $\hat{\Delta}$ and the Germano Identity L_{ij}, which describes the resolved stresses of those scales that fall in between the two filter sizes. The Germano Identity relates both of the subgrid scale tensors and is computable:

$$L_{ij} = \widecheck{\tilde{u}_j\tilde{u}_i} - \check{\tilde{u}}_i\check{\tilde{u}}_j = T_{ij} - \hat{\mathcal{T}}_{ij} \tag{2.121}$$

It is further assumed that the deviatoric parts of both subgrid scale tensors can be described by the same functional model (*e.g.,* Smagorinsky model) and identical model constant C_m:

$$\mathcal{T}_\mathrm{ij} - \frac{1}{3}\mathcal{T}_{kk}\delta_{ij} = -2C_\mathrm{m}\Delta^2\bar{\rho}\mathcal{D}_\mathrm{m}(\tilde{u}_i)\tilde{S}_{ij}^\mathrm{d} = -2C_\mathrm{m}\beta_{ij} \tag{2.122}$$

$$T_{ij} - \frac{1}{3}T_{kk}\delta_{ij} = -2C_\mathrm{m}\hat{\Delta}^2\hat{\bar{\rho}}\mathcal{D}_\mathrm{m}(\check{\tilde{u}}_i)\check{\tilde{S}}_{ij}^\mathrm{d} = -2C_\mathrm{m}\alpha_{ij} \tag{2.123}$$

Equations 2.122 and 2.123 both feature the traceless strain rate tensor S_{ij}^{d} and can be substituted into the traceless formulation of Eq. 2.121 to yield:

$$L_{ij} - \frac{1}{3}L_{kk}\delta_{ij} = -2C_{\mathrm{m}}\alpha_{ij} + 2\widehat{C_{\mathrm{m}}\beta}_{ij} = 2C_{\mathrm{m}}M_{ij} \tag{2.124}$$

$$2\widehat{C_{\mathrm{m}}\beta}_{ij} = 2C_{\mathrm{m}}\Delta^2\hat{\bar{\rho}}\widehat{\mathcal{D}_{\mathrm{m}}(\widetilde{u_i})\tilde{S}_{ij}^{\mathrm{d}}} \tag{2.125}$$

Because Eq. 2.124 is tensorial with tensors that are symmetric, six independent equations are provided to solve for a single model constant C_{m}, thus presenting an over determined system of equations. To address the problem, Germano proposed to contract with another tensor (*e.g.,* strain rate tensor S_{ij}), in the course of which a scalar equation is obtained. As a further improvement, Lilly [62] suggested a least-squares method to minimize the error, essentially resulting in a contraction with the tensor M_{ij}. Introducing the error Q_{L}:

$$Q_{\mathrm{L}} = L_{ij} - \frac{1}{3}L_{kk}\delta_{ij} - 2C_{\mathrm{m}}M_{ij} \tag{2.126}$$

Under the minima condition ($dQ_{\mathrm{L}}/dC = 0$), C_{m} can be obtained by:

$$C_{\mathrm{m}} = \frac{(L_{ij} - \frac{1}{3}L_{kk}\delta_{ij})M_{ij}}{M_{kl}M_{kl}} \tag{2.127}$$

The presented dynamic approach results in a more accurate prediction of the subgrid stresses and is able to withdraw some of the inherent model deficiencies, but again comes with other disadvantages. Initially presented as an advantage, namely the ability of the model of modelling backscatter (kinetic energy transfer from small to larger scales) through negative model coefficients, can in practice lead to numerical instabilities through negative effective viscosities. It is therefore common to clip the values of the obtained model coefficients. Another issue is temporally and spatially fluctuating values of the model coefficients, arguably a result of very small values of the denominator in Eq. 2.127. Spatial averaging of both the numerator and denominator in the respective equation is therefore desirable. Finally, the aforementioned field operations (filtering and averaging operators) lead to significantly higher computational costs compared to the static models.

2.4.4 Eddy Diffusivity Model

The Boussinesq hypothesis can also be applied to the unresolved scalar and enthalpy fluxes, *i.e.,* the $\mathcal{S}_i$ and Q_i terms. Thus, according to this theory, the unresolved structures primarily increase mixing on the subgrid level. Since the eddy viscosity is typically calculated beforehand, the turbulent diffusion coefficients can be determined via a turbulent Schmidt number Sc_{t} and Prandtl number Pr_{t}. In this context, dynamic methods have also been developed to determine the relations locally [60, 63]. However, in most situations it is appropriate to use constant values, *e.g.,* $\mathrm{Sc}_{\mathrm{t}} = \mathrm{Pr}_{\mathrm{t}} = 0.7$. This results in the following equations to close the terms $\mathcal{S}_{i,\alpha}$ and Q_i:

$$\mathcal{S}_{i,\alpha} = \rho\frac{\nu_{\mathrm{t}}}{\mathrm{Sc}_{\mathrm{t}}}\frac{\partial\tilde{Y}_\alpha}{\partial x_i} \tag{2.128}$$

$$Q_i = \rho\frac{\nu_{\mathrm{t}}c_p}{\mathrm{Pr}_{\mathrm{t}}}\frac{\partial\bar{T}}{\partial x_i} \tag{2.129}$$

2.4.5 Filtered Source Term Modeling

In addition to modeling the subgrid stresses, closure of the filtered source term $\overline{\dot{\omega}}_\alpha$ is essential for a proper LES of combustion systems. As shown in Sec. 2.1.2.2, the source term is determined by the thermochemical state (*e.g.,* density ρ, temperature T, and composition Y). In certain situations, it is permissible to derive the source term directly from the filtered quantities (*e.g.,* [64, 65]):

$$\overline{\dot{\omega}}_\alpha = f(\bar{\rho}, \bar{T}, \tilde{\boldsymbol{Y}}) \tag{2.130}$$

However, this assumption is the exception and must be justified, since the source term depends highly nonlinear on the quantities, in particular exponentially on temperature through the Arrhenius term. Therefore, to use the filtered variables directly is recommended only, when the numerical grid is very fine, or when the solution domain does not contain a flame front, but instead the ignition of a nearly homogeneous mixture is simulated. In the past, many different approaches have been developed for source term closure. Therefore, only those two approaches are presented below that have been implemented in the course of this work or have been used in a publication.

2.4.6 Subgrid Probability Density Functions

Probability density function (PDF) methods were originally developed in the RANS context and later suggested for application in LES by Givi [66] and Pope [67], who also introduced the *filtered density function* (FDF) as a distinction to RANS. In the LES context, the FDF can be interpreted as a subgrid distribution of the independent variables within a LES cell. Essentially, if the single point joint subgrid FDF P of the independent variables is known, the exact value of the filtered source term can be computed by integration over the entire sample space of the independent variables:

$$\overline{\dot{\omega}}_\alpha = \int \dot{\omega}\left(\breve{\rho}, \breve{T}, \breve{Y}_1, \breve{Y}_2, ..., \breve{Y}_{N_\mathrm{S}}\right) P\left(\breve{\rho}, \breve{T}, \breve{Y}_1, \breve{Y}_2, ..., \breve{Y}_{N_\mathrm{S}}\right) d\breve{\rho}\; d\breve{T}\; d\breve{Y}_1\; d\breve{Y}_2\; \cdots\; d\breve{Y}_{N_\mathrm{S}} \tag{2.131}$$

Here, the breve symbol ($\breve{\Phi}$) denotes a sample space variable. Equation 2.131 can be simplified, if statistical independence between between the independent variables can be assumed (*e.g.,* between density, temperature, and mass fractions). In that case, the single point joint FDF can be determined as the product of the marginal FDF's:

$$P\left(\breve{\rho}, \breve{T}, \breve{Y}_1, \breve{Y}_2, ..., \breve{Y}_{N_\mathrm{S}}\right) = \prod_{n=1}^{N} P_n\left(\breve{n}\right) = P_\rho\left(\breve{\rho}\right) P_T\left(T\right) P_{Y_1}\left(Y_1\right) P_{Y_2}\left(Y_2\right)\; \cdots\; P_{Y_{N_\mathrm{S}}}\left(Y_{N_\mathrm{S}}\right) \tag{2.132}$$

The FDF can be determined by transport equations using stochastic particles (Lagrangian method [68]) or stochastic fields (Eulerian method [69]). This approach has the advantage that the subgrid PDF can evolve to take any form. The disadvantages include a significantly higher implementation effort, higher computational costs and the need for other closure models (*e.g.,* the subgrid mixing term). For this reason, presumed FDFs are primarily used, which prescribe the shape of the FDF and are typically determined by the first two moments (subgrid mean and subgrid variance) of the independent variable.

Gerlinger [70] investigated the suitability of presumed PDF methods specifically when using the finite rate combustion model in RANS simulations. This is a particular challenge due to the typically high number of scalars required to calculate the averaged source term, as the time average and variance are required per scalar respectively. For this reason, a clipped *Gaussian* PDF was selected for Temperature, as well as a joint multivariate β-PDF for Composition, as proposed by Girimaji [71]. The joint multivariate β-PDF is fully defined when the means of the mass fractions and the sum of the variances are known for which a transport equation has been derived. This approach was later adapted for use in a LES by Wang et al. [72]. Again, assuming statistical independence between density, temperature and mass fractions, the subgrid FDF reads:

$$P(\breve{\rho},\breve{T},\breve{Y}_1,\breve{Y}_2,...\breve{Y}_{N_\mathrm{S}}) = \delta\,(\breve{\rho}-\bar{\rho})\,P_T\left(\breve{T}\right)P_Y\left(\breve{Y}_1,\breve{Y}_2,...,\breve{Y}_{N_\mathrm{S}}\right) \tag{2.133}$$

Equation 2.133 introduces the *Dirac delta* distribution δ, which is only non zero if the argument is exactly zero. Recall that Eq. 2.22, the *law of mass action*, can also be written in terms of mass fractions and substituted into Eq. 2.19. After applying a spatial filter and neglecting reaction reversibility and third body effects for clarity, the following expression is obtained:

$$\overline{\dot{\omega}}_\alpha = W_\alpha \sum_{r=1}^{N_\mathrm{R}} (\nu''_{\alpha r}-\nu'_{\alpha r}) \left[\prod_{s=1}^{N_\mathrm{S}} \left(\frac{1}{W_s}\right)^{\nu'_{sr}}\right] \overline{\rho^{m_r}\, k_{\mathrm{f},r} I_{\mathrm{f},r}} \tag{2.134}$$

$$= W_\alpha \sum_{r=1}^{N_\mathrm{R}} (\nu''_{\alpha r}-\nu'_{\alpha r}) \left[\prod_{s=1}^{N_\mathrm{S}} \left(\frac{1}{W_s}\right)^{\nu'_{sr}}\right] \overline{\rho^{m_r}}\; \tilde{k}_{\mathrm{f},r}\tilde{I}_{\mathrm{f},r}, \tag{2.135}$$

$$I_{\mathrm{f},r} = \prod_{s=1}^{N_\mathrm{S}} Y_s^{\nu'_{sr}} \tag{2.136}$$

$$m_r = \sum_{s=1}^{N_\mathrm{S}} \nu'_{sr} \tag{2.137}$$

Due to statistical independence, the filtered terms can now be treated sequentially. The *Dirac delta* distribution essentially keeps the density constant at the filtered value:

$$\overline{\rho^{m_r}} = \int_\rho \breve{\rho}^{m_r}\; \delta\,(\breve{\rho}-\bar{\rho})\, d\breve{\rho} = \bar{\rho}^{m_r} \tag{2.138}$$

Using a *Gaussian* PDF[70, 73] or FDF[72] for temperature, allows to determine the filtered reaction rate constant by integration over the entire temperature sample space:

$$\widetilde{k}_{\mathrm{f},r} = \int_T A\,\breve{T}^b \exp\left(-\frac{E_a}{R_\mathrm{m}\,\breve{T}}\right) P_T\left(\breve{T}\right) d\breve{T} \tag{2.139}$$

$$P_T\left(\breve{T}\right) = \frac{1}{\sqrt{2\pi\widetilde{T''^2}}} \exp\left(-\frac{(\breve{T}-\tilde{T})^2}{2\,\widetilde{T''^2}}\right) \tag{2.140}$$

Here, $\widetilde{T''^2}$ is the subgrid variance of temperature and can be calculated with algebraic models that are based on the scale similarity assumption. Thus, approaches using a local test filter, for example proposed by Cook and Riley [74], are suitable for determining the variance. In addition, gradient type models [75] can be used that yield consistent results with the test filter approach on a structured grid, if a top-hat test filter is used [76].

A viable alternative for single scalar PDF's in LES has been proposed by Floyd et al. [76]. They showed that a *top-hat* PDF is the preferred choice over a β-PDF or *Gaussian* PDF in many situations. Deficiencies of the β-PDF are demonstrated for scalar mixing in multi stream configurations or for scalar spatial evolution [76]. At the same time, the top-hat PDF is a comparatively simple distribution, namely an equally likelihood of a scalar value within a given range of values. The PDF for temperature now reads:

$$P_T(\breve{T}) = \begin{cases} t_0 & \text{if} \quad T_\mathrm{a} \geq \breve{T} \geq T_\mathrm{a}, \\ 0 & \text{else.} \end{cases} \tag{2.141}$$

The temperature limits T_a and T_b, as well as the probability t_0 can be calculated using the Favre filtered temperature and subgrid temperature variance [76]:

$$\widetilde{T''^2} \approx \frac{1}{12}\Delta_x^2 \left(\frac{\partial \tilde{T}}{\partial x_i}\right)^2 \tag{2.142}$$

$$T_\mathrm{a} = \tilde{T} - \frac{1}{2}\sqrt{12\,\widetilde{T''^2}} \tag{2.143}$$

$$T_\mathrm{b} = \tilde{T} + \frac{1}{2}\sqrt{12\,\widetilde{T''^2}} \tag{2.144}$$

$$t_0 = \frac{1}{T_\mathrm{b} - T_\mathrm{a}} \tag{2.145}$$

In order to avoid the expensive integration in Eq. 2.139 during a simulation, the values of the reaction rate constants can be calculated in advance as a function of temperature and stored in a table. The resulting table can then be integrated so that the filtered value of the reaction rate constant is defined just over two values $K^\mathrm{a}_{\mathrm{f},r}$ and $K^\mathrm{b}_{\mathrm{f},r}$ from the integrated table:

$$\tilde{k}_{\mathrm{f},r} = t_0 \left(\underbrace{\int_0^{T_\mathrm{b}} k_{\mathrm{f},r}(\check{T})\, d\check{T}}_{K^\mathrm{b}_{\mathrm{f},r}} - \underbrace{\int_0^{T_\mathrm{a}} k_{\mathrm{f},r}(\check{T})\, d\check{T}}_{K^\mathrm{a}_{\mathrm{f},r}} \right) \tag{2.146}$$

Last, the expression $\widetilde{I_{f,\mathrm{r}}}$ must be closed to compute the filtered reaction rate $\overline{\dot{\omega}_\alpha}$ by applying the multivariate β-FDF which is defined as follows [71]:

$$P_Y(\check{Y}_1, \check{Y}_2, ..., \check{Y}_{N_\mathrm{S}}) = \frac{\Gamma\left(\sum_{\mathrm{s}=1}^{N_\mathrm{S}} \beta_\mathrm{s}\right)}{\prod_{\mathrm{s}=1}^{N_\mathrm{S}} \Gamma(\beta_\mathrm{s})}\, \delta\left(1 - \sum_{\mathrm{s}=1}^{N_\mathrm{S}} \check{Y}_\mathrm{s}\right) \left[\prod_{\mathrm{s}=1}^{N_\mathrm{S}} \check{Y}_\mathrm{s}^{\beta_\mathrm{s}-1}\right] \tag{2.147}$$

Equation 2.147 features the *Gamma* function Γ and also a *Dirac delta* function function which ensures at any time that only distributions with a sum of exactly one over all mass fractions are considered. The model parameters β_m themselves are functions of the Favre filtered mass fractions and the sum of subgrid variances σ_Y, denoted as subgrid scalar energy [72]:

$$\beta_\mathrm{s} = \tilde{Y}_\mathrm{s}\left(\frac{1 - S_\beta}{\sigma_Y} - 1\right) \tag{2.148}$$

$$S_\beta = \sum_{\mathrm{s}=1}^{N_\mathrm{S}} \tilde{Y}_\mathrm{s}^2 \tag{2.149}$$

$$\sigma_Y = \sum_{\mathrm{s}=1}^{N_\mathrm{S}} \widetilde{Y''^2_\mathrm{s}} \tag{2.150}$$

Equation 2.136 in Favre filtered formulation and substitution of Eq. 2.147 yields the expression:

$$\tilde{I}_{f,\mathrm{r}} = \int_{\boldsymbol{Y}} \left[\prod_{\mathrm{s}=1}^{N_\mathrm{S}} \check{Y}_\mathrm{s}^{\nu'_\mathrm{sr}}\right] P_Y(\check{Y}_1, \check{Y}_2, ..., \check{Y}_{N_\mathrm{S}})\, d\check{\boldsymbol{Y}} \tag{2.151}$$

$$= \int_{\boldsymbol{Y}} \left[\prod_{\mathrm{s}=1}^{N_\mathrm{S}} \check{Y}_\mathrm{s}^{\nu'_\mathrm{sr}}\right] \frac{\Gamma\left(\sum_{\mathrm{s}=1}^{N_\mathrm{S}} \beta_\mathrm{s}\right)}{\prod_{\mathrm{s}=1}^{N_\mathrm{S}} \Gamma(\beta_\mathrm{s})}\, \delta\left(1 - \sum_{\mathrm{s}=1}^{N_\mathrm{S}} \check{Y}_\mathrm{s}\right) \left[\prod_{\mathrm{s}=1}^{N_\mathrm{S}} \check{Y}_\mathrm{s}^{\beta_\mathrm{s}-1}\right] d\check{\boldsymbol{Y}} \tag{2.152}$$

The integral in Eq. 2.152 can be solved analytically, as demonstrated by Wang et al. [72], for closure of $\tilde{I}_{f,\mathrm{r}}$:

$$\tilde{I}_{f,\mathrm{r}} = \frac{\prod\limits_{\mathrm{s}=1}^{N_\mathrm{S}} \prod\limits_{\mathrm{q}=1}^{\nu'_\mathrm{sr}} \nu'_\mathrm{sr} + \beta_\mathrm{s} - \mathrm{q}}{\prod\limits_{\mathrm{p}=1}^{m_\mathrm{r}} m_\mathrm{r} + B_\beta - \mathrm{p}} \tag{2.153}$$

$$\text{with } m_\mathrm{r} = \sum_{\mathrm{s}=1}^{N_\mathrm{S}} \nu'_\mathrm{sr}, \;\; B_\beta = \sum_{\mathrm{s}=1}^{N_\mathrm{S}} \beta_\mathrm{s} \tag{2.154}$$

2.4.7 Thickened Flame Model

Another popular choice for modeling the turbulence-chemistry interaction in LES with *finite-rate chemistry* (FRC), which can be used in conjunction with PDF methods or alone, is the flame thickening approach. In contrast to PDF methods, the flame thickening approach can only be used if the chemical conversion takes place almost entirely in a subsonic flame zone (deflagration). Thus, this method is not suitable for the simulation of detonations and auto ignition. The theory underlying this approach goes back to considerations by Butler and O'Rourke [77]. Proportionality relations of laminar flame speed s_L^0 and flame thickness δ_L^0 to thermal diffusion coefficient D_th and heat-release rate $\dot{\omega}_\mathrm{th}$ are essential in the context:

$$s_L^0 \propto \sqrt{D_\mathrm{th}\,\dot{\omega}_\mathrm{th}} \tag{2.155}$$

$$\delta_L^0 \propto \sqrt{\frac{D_\mathrm{th}}{\dot{\omega}_\mathrm{th}}} \tag{2.156}$$

Accordingly, if all diffusion coefficients in the species conservation equations and the thermal conductivity in the energy conservation equation are multiplied by a factor F, while all reaction source terms are divided by the same factor F, the flame can be thickened to $\delta_L^0 F$ to be resolved on a typical LES grid and maintaining the laminar flame speed. The additional computational effort is very low as well as the implementation effort, which makes this approach so attractive. However, the method comes with one major drawback. While the laminar flame velocity is preserved, the interaction of the turbulent eddies and the flame front is significantly affected, which is expressed by the Damköhler number:

$$\mathrm{Da} = \frac{\tau_t}{\tau_c} = \frac{l_t}{\delta_L^0}\frac{s_L^0}{u'} \tag{2.157}$$

The Damköhler number compares turbulent time scales (τ_t) with chemical time scales (τ_t) and is reduced by F in terms of thickened flames. Thus, the ability of eddies to wrinkle a flame, when thickened, is reduced, which has implications for total fuel consumption and thus the turbulent flame speed. For this reason, an efficiency function E is introduced to consider sub-filter flame wrinkling and therefore to model the sub-filter turbulent flame speed $s_{T\Delta}$. Using classical relations, the sub-filter turbulent flame speed can be derived in terms of a sub-filter wrinkling factor Ξ_Δ:

$$s_{T\Delta} = s_L^0\,\Xi_\Delta \tag{2.158}$$

$$\Xi_\Delta = \frac{\overline{|\nabla C|}}{|\nabla \bar{C}|} \tag{2.159}$$

Here, C is the dimensionless flame progress variable. The sub-filter wrinkling factor Ξ_Δ can be determined on the basis of transport equations (*e.g.,* [78]) or by algebraic relations (*e.g.,* [79–82]) that are based on DNS results (*e.g.,* [83]). According to Charlette et al. [81], the sub-filter wrinkling factor can be approximated by a power law of the form:

$$\Xi_\Delta = \left(1 + \frac{\Delta}{\eta_i}\right)^\beta \tag{2.160}$$

Equation 2.160 features the inner cut-off scale η_i that denotes the size of the smallest eddies to wrinkle the flame. The term Δ/η_i is parameterized as a function of the ratios Δ/δ_L^0 and u'/s_L^0 taking asymptotic behavior and equilibrium assumptions of sub filter flame surface density production and destruction into account. The efficiency function proposed by Charlette and modified by Wang et al. [84] then reads:

$$E = \Xi_\Delta = \left(1 + \min\left[F_{\max} - 1, \Gamma_\Delta \frac{u'_\Delta}{s_L^0}\right]\right)^\beta \tag{2.161}$$

$$F_{\max} = \max\left(\frac{n_{\mathrm{fp}}\Delta_x}{\Delta_L^0}, 1\right) \tag{2.162}$$

Equation 2.161 features the sub filter velocity fluctuations u'_Δ and a function Γ_Δ, which is supposed to model the net straining effects of all eddies with a characteristic size below the filter size. It is important to note that the respective filter size is much larger than the implicit LES filter size ($\approx \Delta_x$) due to the scaling of flame thickness [80]. The exponent β is usually set to a value of 0.5, while a dynamic procedure proposed by Charlette et al. [85] can be used alternatively, promising more accurate results.

In order to avoid enhanced diffusion outside the flame region, a flame sensor Ω is introduced. Both flame thickening factor and efficiency function are subsequently used exclusively within the flame front, while the *Eddy diffusivity* model is turned off in the flame front. This approach is referred to as *dynamic thickened flame* (DTF) model:

$$F = 1 + (F_{\max} - 1)\,\Omega \tag{2.163}$$

Several formulations for the flame sensor exist that either use the normalized flame progress or net production rates / heat release rate to determine the flame front. A simple, yet popular flame sensor has been proposed by Durand and Polifke [86], featuring a smooth transition of the thickening region and is characterized by computational efficiency:

$$\Omega_{\mathrm{Polifke}} = 16\,[C\,(C-1)]^2 \tag{2.164}$$

Here, C denotes the normalized flame progress variable. Another popular flame sensor was introduced by Legier et al. [87], which uses heat release as an indicator and typically has a broader thickening zone compared to the Polifke flame sensor:

$$\Omega_{\mathrm{Legier}} = \tanh\left(100\,\frac{\dot{\mathrm{Q}}}{\mathrm{Q}_{\max}}\right) \tag{2.165}$$

The conservation equations for total internal energy and partial densities now read under the assumption that the chemical source term is sufficiently resolved due to flame thickening:

$$\frac{\partial \bar{\rho}}{\partial t} + \frac{\partial \bar{\rho} \tilde{u}_i}{\partial x_i} = 0 \tag{2.166}$$

$$\frac{\partial \bar{\rho} \tilde{u}_i}{\partial t} + \frac{\partial \bar{\rho} \tilde{u}_i \tilde{u}_j}{\partial x_j} = -\frac{\partial \bar{p}}{\partial x_i} + \frac{\partial \bar{\tau}_{ij}}{\partial x_j} \tag{2.167}$$

$$\frac{\partial \bar{\rho} \tilde{E}}{\partial t} + \frac{\partial (\bar{\rho} \tilde{E} + \bar{p}) \tilde{u}_i}{\partial x_i} = \frac{\partial}{\partial x_i} \left[\left(E\, F\, \bar{\lambda} + (1 - \Omega)\, \bar{c}_p\, \frac{\mu_\mathrm{t}}{\mathrm{Pr}_\mathrm{t}} \right) \frac{\partial \bar{T}}{\partial x_i} + \sum_{\alpha=1}^{N_\mathrm{S}} \bar{h}_\alpha\, \bar{j}_{i,\alpha} \right] + \frac{\partial \bar{\tau}_{ij} \tilde{u}_i}{\partial x_j} \tag{2.168}$$

$$\frac{\partial \bar{\rho} \tilde{Y}_\alpha}{\partial t} + \frac{\partial \bar{\rho} \tilde{Y}_\alpha \tilde{u}_i}{\partial x_i} = \frac{\partial}{\partial x_i} \left[\left(E\, F\, \bar{\rho}\, \bar{D}_\alpha + (1 - \Omega)\, \frac{\mu_\mathrm{t}}{\mathrm{Sc}_\mathrm{t}} \right) \frac{\partial \tilde{Y}_\alpha}{\partial x_i} \right] + \frac{E}{F} \dot{\omega}_\alpha \tag{2.169}$$

Chapter 3
Numerical Modeling

3.1 Temporal Discretization

The main objectives of LES are the investigation of unsteady phenomena and the computation of statistics by sampling the available data. Naturally, the governing equations, as presented in Chapter 2, are advanced in time using integration:

$$\frac{\mathrm{d}\boldsymbol{\phi}}{\mathrm{d}t} = \boldsymbol{f}\left(\boldsymbol{\phi}(t)\right) \tag{3.1}$$

$$\int_{\boldsymbol{\phi}(t)}^{\boldsymbol{\phi}(t+\Delta t)} d\boldsymbol{\phi} = \int_{t}^{t+\Delta t} \boldsymbol{f}\left(\boldsymbol{\phi}(t)\right) dt \tag{3.2}$$

Here, $\boldsymbol{\phi}(t)$ is the vector of conserved variables defining the system state at time t and $\boldsymbol{f}\left(\boldsymbol{\phi}(t)\right)$ is the function vector to compute the respective time derivatives. In our case, the function $\boldsymbol{f}$ is the sum of all terms present in the governing equations written on the RHS, with the exception of the accumulation term on the LHS, *i.e.*, the sum of convective, diffusive, and source terms. Also, the function is time invariant and only depends on the system state. Because it involves spatial derivatives and non linear terms, numerics are required to approximate the integral. A straightforward discrete formulation is the *Euler forward* method:

$$\frac{\boldsymbol{\phi}^{(n+1)} - \boldsymbol{\phi}^{(n)}}{\Delta t} = \boldsymbol{f}\left(\boldsymbol{\phi}^{(n)}\right) \tag{3.3}$$

$$\Leftrightarrow \quad \boldsymbol{\phi}^{(n+1)} = \boldsymbol{\phi}^{(n)} + \Delta t\, \boldsymbol{f}\left(\boldsymbol{\phi}^{(n)}\right) \tag{3.4}$$

The superscript in $\boldsymbol{\phi}^{(n)}$ denotes the system state at time step n, with the system state at the subsequent time step $\boldsymbol{\phi}^{(n+1)}$, separated by the time step Δt. The Euler forward method is considered an *explicit* method, since all quantities on the RHS are evaluated at time level n, which allows to directly compute the system state of the subsequent time step. The truncation error of this discretization is of second order, *i.e.* reducing the time step by a factor of 2, will reduce the discretization error by a factor of 4. However, twice as many time steps will be required to reach the same time level. Thus, the scheme is considered locally 2nd order accurate, but globally only 1st order [88]. The Euler explicit scheme is easy to implement but rarely used due to its stability properties, which can be studied in terms of time step size and discretization methods for convection and diffusion. Typically, the scalar transport equation (linear advection with constant velocity) is used as model equation, so the findings are not necessarily applicable to the Navier-Stokes equations that involve non linear terms. Nevertheless, the insights are valuable and are suitable for guidance even in more complex cases. For example, if central discretization methods (Sec. 3.2.3.1) are used for the convective and diffusive terms and a flow is considered that is dominated by convection, then the explicit Euler method is unconditionally unstable. This means that the scheme will be unstable for every value of Δt. If, on the other hand, the upwind discretization method (Sec. 3.2.3.2) is used for the convective term, the following stability criterion for the time step size Δt is obtained in absence of diffusion [88]:

$$\mathrm{CFL} = \frac{u\Delta t}{\Delta_x} \leq 1 \tag{3.5}$$

Here, the *Courant Friedrich Lewy* (CFL) number [89] is introduced. The criterion states that the scheme will be stable, if information can ideally travel by one computational cell within a single time integration step and the scheme can be considered *conditionally stable*. If diffusion is present at the same time, another constraint must be met additionally [88]:

$$\Delta t \leq \mathrm{DS}\, \frac{\rho\, \Delta_x^2}{2\, D} \tag{3.6}$$

$$\mathrm{DS} = \frac{1}{d}, \quad d = 1, 2, 3 \tag{3.7}$$

The equation features the diffusion coefficient D and the *diffusive stability* (DS) coefficient whose value depends on the number of spatial dimensions d considered. In the vast majority of cases, the time step will be limited by convection. However, the diffusive limit is proportional to the square of the grid size, while the convective limit is only proportional. Thus, when the grid size approaches very small values (in a DNS, for example), it may well be the case that diffusion limits the time step size. It should also be mentioned that in the case of a compressible LES, a different CFL criterion must be used. In a more general form, the time step is limited by the maximum propagation speed of information. In the case of compressible flow, this is the propagation velocity of pressure information:

$$\mathrm{CFL} = \frac{|u \pm c|\, \Delta t}{\Delta_x} \tag{3.8}$$

This criterion is referred to as *acoustic* CFL criterion.

Another globally first order accurate method is the *Euler backward* method:

$$\frac{\boldsymbol{\phi}^{(n+1)} - \boldsymbol{\phi}^{(n)}}{\Delta t} = \boldsymbol{f}\left(\boldsymbol{\phi}^{(n+1)}\right) \tag{3.9}$$

In contrast to the Euler forward method, the function $\boldsymbol{f}$ is now evaluated for the system state at time level $n + 1$, which by itself is the quantity of interest. An approximation for $\boldsymbol{f}\left(\boldsymbol{\phi}^{(n+1)}\right)$ is thus needed:

$$\boldsymbol{f}\left(\boldsymbol{\phi}^{(n+1)}\right) = \boldsymbol{f}\left(\boldsymbol{\phi}^{(n)}\right) + \boldsymbol{J}^{(n)} \Delta\boldsymbol{\phi} \tag{3.10}$$

$$\boldsymbol{J}^{(n)} = \frac{\partial \boldsymbol{f}\left(\boldsymbol{\phi}^{(n)}\right)}{\partial \boldsymbol{\phi}^{(n)}} \tag{3.11}$$

$$\Delta\boldsymbol{\phi} = \boldsymbol{\phi}^{(n+1)} - \boldsymbol{\phi}^{(n)} \tag{3.12}$$

Equation 3.10 features the Jacobian $\boldsymbol{J}^{\mathrm{n}}$ of the system at time level n, which can be calculated using *finite differences* for each component. Substituting this expression into Eq. 3.9 yields:

$$\underbrace{\left(\boldsymbol{I} - \Delta t\, \boldsymbol{J}^{(n)}\right)}_{\boldsymbol{A}} \underbrace{\Delta\boldsymbol{\phi}}_{\boldsymbol{x}} = \underbrace{\Delta t\, \boldsymbol{f}\left(\boldsymbol{\phi}^{(n)}\right)}_{\boldsymbol{b}} \tag{3.13}$$

Equation 3.13 presents a system of linear equations ($\boldsymbol{Ax} = \boldsymbol{b}$) that can be solved using functions provided by the *LAPACK* [90] library. This implicit scheme will be stable irrespective of the time step size Δt, and is therefore considered *unconditionally stable*. However, the costs associated with the computation of the Jacobian matrix and the solution of the linear system are high. At the same time, the time integration step size cannot be chosen arbitrarily large, otherwise acoustic waves would not be resolved correctly on the numerical grid. For these reasons, explicit time integration schemes with higher accuracy and improved stability behavior are the preferred choice for LES.

In the special case of the finite rate chemistry model, the restrictions on time step size will, in most cases, be even more severe than those caused by convection and diffusion. During chemical reactions, some of the species, referred to as radicals, are produced and consumed at very high rates. As a result, a very small time step size must be chosen such that errors are damped and not amplified [11], while much larger integration time steps could be used for many other species that are produced / consumed at a lower rate (*e.g.* nitrogen oxide). This time disparity among the species leads to a stiff system of coupled differential equations. In fact, solving reactive systems explicitly, usually requires integration step sizes much below those values required for an accurate solution [11]. For stiff systems of differential equations, implicit time integration schemes allow for larger integration time steps and are consequently favored.

This leads to the situation that an explicit method is best suited for the temporal changes caused by convection and diffusion, whereas an implicit method is mandatory to ensure that the time step size is not overly small. Operator splitting methods are appropriate to meet both requirements.

3.1.1 Operator Splitting

Operator splitting methods have been introduced to integrate individual terms with different integration schemes to account for drastically different properties among the terms. The method was originally postulated by Strang [91] and the associated procedure is called *Strang splitting* from here on. In general, the integration takes place in three successive steps, which have a symmetrical structure:

$$\frac{\mathrm{d}\boldsymbol{\phi}^{(1)}}{\mathrm{d}t} = \mathcal{T}\left(\boldsymbol{\phi}^{(1)}\right), \qquad \boldsymbol{\phi}^{(1)} = \boldsymbol{\phi}\,(t) \tag{3.14}$$

$$\frac{\mathrm{d}\boldsymbol{\phi}^{(2)}}{\mathrm{d}t} = \mathcal{R}\left(\boldsymbol{\phi}^{(2)}\right), \qquad \boldsymbol{\phi}^{(2)} = \boldsymbol{\phi}^{(1)}\,(t + \Delta t) \tag{3.15}$$

$$\frac{\mathrm{d}\boldsymbol{\phi}^{(3)}}{\mathrm{d}t} = \mathcal{T}\left(\boldsymbol{\phi}^{(3)}\right), \qquad \boldsymbol{\phi}^{(3)} = \boldsymbol{\phi}^{(2)}\,(t + 2\,\Delta t) \tag{3.16}$$

$$\boldsymbol{\phi}^{(n+1)} = \boldsymbol{\phi}^{(3)}\,(t + 2\,\Delta t) \tag{3.17}$$

In the equations, $\mathcal{T}$ is the vector of temporal changes resulting from transport processes, *i.e.* convection and diffusion. Similarly, $\mathcal{R}$ is the vector of temporal changes due to source terms. In the first operator splitting step, the sum of the convection and diffusion terms is integrated in time using an appropriate explicit method together with the integration width Δt, which is obtained using the CFL criterion. The resulting system solution $\boldsymbol{\phi}^{(1)}\,(t + \Delta t)$ is used as the initial solution for the second operator splitting step. Subsequently, the chemical source term is integrated by two times Δt, using suitable semi implicit or fully implicit integration schemes. The third step mirrors the first step, just with an updated initial solution $\boldsymbol{\phi}^{(2)}\,(t + 2\,\Delta t)$. The operator splitting presented has only second order accuracy in time. However, the efficiency gained outweighs this drawback.

As noted by Wu et al. [92], deviations can occur in the vicinity of the extinction and ignition limits, whereupon a new splitting algorithm has been proposed that circumvents the issue by adding constant parameters in each step, where the magnitude of the constants is dictated by $\mathcal{T}$ at time t. This approach eliminates the issues associated with extinction and ignition limits, but increases the memory usage:

$$\boldsymbol{C}^n = \mathcal{T}\left(\boldsymbol{\phi}(t)\right) \tag{3.18}$$

$$\frac{\mathrm{d}\boldsymbol{\phi}^{(1)}}{\mathrm{d}t} = \mathcal{T}\left(\boldsymbol{\phi}^{(1)}\right) + \boldsymbol{C}^n, \qquad \boldsymbol{\phi}^{(1)} = \boldsymbol{\phi}\,(t) \tag{3.19}$$

$$\frac{\mathrm{d}\boldsymbol{\phi}^{(2)}}{\mathrm{d}t} = \mathcal{R}\left(\boldsymbol{\phi}^{(2)}\right) - \boldsymbol{C}^n, \qquad \boldsymbol{\phi}^{(2)} = \boldsymbol{\phi}^{(1)}\,(t + \Delta t) \tag{3.20}$$

$$\frac{\mathrm{d}\boldsymbol{\phi}^{(3)}}{\mathrm{d}t} = \mathcal{T}\left(\boldsymbol{\phi}^{(3)}\right) + \boldsymbol{C}^n, \qquad \boldsymbol{\phi}^{(3)} = \boldsymbol{\phi}^{(2)}\,(t + 2\,\Delta t) \tag{3.21}$$

$$\boldsymbol{\phi}^{(n+1)} = \boldsymbol{\phi}^{(3)}\,(t + 2\,\Delta t) \tag{3.22}$$

Because $\mathcal{T}\left(\boldsymbol{\phi}^{(1)}\right)$ and $\boldsymbol{C}^n$ are identical, the first integration step can be omitted, reducing the number of successive integration steps.

3.1.2 Runge Kutta

Throughout this work, Runge Kutta time integration methods have been used to advance the flow solution in time due to convection and diffusion. Runge Kutta methods are explicit multi-step methods and in essence a sequence of Euler explicit integration steps in which the RHS of the conservation equations is calculated at various points in time. In the end, these evaluations k_j (basically slopes) are used to estimate a higher order solution using weight coefficients w_j. A general p^{th} order Runge Kutta scheme can be written as [26]:

$$\boldsymbol{\phi}^{(n+1)} = \boldsymbol{\phi}^{(n)} + \sum_{j=1}^{p} w_j\,\boldsymbol{k}_j \tag{3.23}$$

$$\boldsymbol{k}_j = \Delta t\,\boldsymbol{f}\left(\boldsymbol{\phi}^{(n)} + \sum_{i=1}^{j-1} \beta_{ji}\boldsymbol{k}_i\right) \tag{3.24}$$

This classical approach stores each of these evaluations in memory in addition to the original solution at time step n and an intermediate solution. Low Storage Runge Kutta procedures, on the other hand, update the solution with each step and require only the current evaluation and the one from the previous Runge Kutta step. Low storage Runge Kutta schemes can be expressed as [26]:

$$\boldsymbol{q}_j = a_j\boldsymbol{q}_{j-1} + \Delta t\,\boldsymbol{f}\left(\boldsymbol{\phi}_{j-1}\right) \tag{3.25}$$

$$\boldsymbol{\phi}_j = \boldsymbol{\phi}_{j-1} + b_j\boldsymbol{q}_j \tag{3.26}$$

The low storage Runge Kutta scheme used in this work features 3 consecutive steps:

$$\boldsymbol{\phi}^{(1)} = \boldsymbol{\phi}^{(n)} + b_1\boldsymbol{q}_1, \qquad \boldsymbol{q}_1 = \qquad \Delta t\,\boldsymbol{f}\left(\boldsymbol{\phi}^{(n)}\right) \tag{3.27}$$

$$\boldsymbol{\phi}^{(2)} = \boldsymbol{\phi}^{(1)} + b_2\boldsymbol{q}_2, \qquad \boldsymbol{q}_2 = a_2\boldsymbol{q}_1 + \Delta t\,\boldsymbol{f}\left(\boldsymbol{\phi}^{(1)}\right) \tag{3.28}$$

$$\boldsymbol{\phi}^{(3)} = \boldsymbol{\phi}^{(2)} + b_3\boldsymbol{q}_3, \qquad \boldsymbol{q}_3 = a_3\boldsymbol{q}_2 + \Delta t\,\boldsymbol{f}\left(\boldsymbol{\phi}^{(2)}\right) \tag{3.29}$$

The model coefficients a_j and b_j can be computed from the coefficients β_{ji} and w_j from the classical Runge Kutta scheme. The following coefficients have been used:

$$a_1 = 0, \qquad b_1 = \frac{1}{3} \tag{3.30}$$

$$a_2 = -\frac{5}{9}, \qquad b_2 = \frac{15}{16} \tag{3.31}$$

$$a_3 = -\frac{153}{128}, \qquad b_3 = \frac{8}{15} \tag{3.32}$$

3.1.3 Solving Stiff Chemistry

To solve systems of stiff differential equations, semi implicit and implicit methods are well suited. Which method is more adequate depends in particular on the time step size given by the CFL criterion. In a reactive LES, the time step size typically has a range of $\Delta t = [1\text{e-}8,\ 1\text{e-}5]$ s. On the other hand, to explicitly integrate the systems of stiff differential equations, time step sizes of $\Delta t \leq 1\text{e-}9$ s are usually required. Thus, there are often several orders of magnitude between the characteristic time scales. If the discrepancy is particularly large, the stiffness of the system of equations is especially pronounced and fully implicit methods are the best choice. However, if the CFL dependent time step size takes values of 1e-7 s and less, then the stiffness is also less distinctive and semi-implicit methods are more efficient.

Because the chemical source term is integrated in an operator splitting framework, the differential equations do not contain spatial gradients and are therefore classified as ordinary differential ordinary differential equations. During time integration of the system, the density and internal energy are constant, while temperature changes (if a Low Mach formulation is used, pressure and enthalpy are constant instead). For this reason, a differential equation for temperature is added. Otherwise, an iterative Newton Raphson algorithm would be required to update the temperature. This leads to the following system of ordinary differential equations:

$$\frac{\mathrm{d}\boldsymbol{Y}}{\mathrm{d}t} = \frac{\mathrm{d}}{\mathrm{d}t}\begin{bmatrix} Y_1 \\ Y_2 \\ \vdots \\ Y_{N_\mathrm{S}} \\ T \end{bmatrix} = \begin{bmatrix} \dot{\omega}_1 \\ \dot{\omega}_2 \\ \vdots \\ \dot{\omega}_{N_\mathrm{S}} \\ \dot{\omega}_T \end{bmatrix} \tag{3.33}$$

$$\dot{\omega}_T = -\sum_{\alpha}^{N_\mathrm{S}} \dot{\omega}_\alpha h^0_{\mathrm{f},\alpha} \tag{3.34}$$

To distinguish this system from the system of conserved variables, the vector of the system is now denoted by $\boldsymbol{Y}$. Appropriate integration methods are discussed in the following.

3.1.3.1 CVODE

CVODE is a fully implicit ODE solver for *initial value problems* (IVP) embedded in the open source SUNDIALS [93, 94] library. Stiff problems are solved using multi step variable order *backward differentiation formulas* (BDF) [95]. One of the biggest advantages of CVODE is stability, which is due to years of development, testing and superior error control. It is for this reason that CVODE has been used in all publications presented in this thesis [6–8], despite more efficient alternatives are available. The library is written in C, however, an interface for Fortran77 is provided, as well as a module for modern Fortran2003 to access CVODE C functions and structures via pointers. Both approaches have been implemented in the scope of this work, whereby the Fortran77 interface has been preferred due the ease of use. The main drawback of CVODE is the computational cost, which increases with the cube of the species involved [92]. Hence, the usefulness of CVODE is somewhat limited to small to medium sized mechanisms, *e.g.* hydrogen mechanisms featuring up to 9 species and less than 40 reactions.

3.1.3.2 ODEPIM

The point implicit integration scheme for ordinary differential equations ODEPIM is based on ideas of Liang et al. [96]. The authors decomposed the source term into a production term $\mathcal{P}$ and a destruction term $\mathcal{D}$ and observed that the stability can be increased, if the destruction term is scaled by the ratio $\boldsymbol{Y}^{(n+1)}/\boldsymbol{Y}^{(n)}$:

$$\frac{\boldsymbol{Y}^{(n+1)}-\boldsymbol{Y}^{(n)}}{\Delta t}=\mathcal{P}\left(\boldsymbol{Y}^{(n)}\right)-\mathcal{D}\left(\boldsymbol{Y}^{(n)}\right)\frac{\boldsymbol{Y}^{(n+1)}}{\boldsymbol{Y}^{(n)}} \tag{3.35}$$

Since the quantity $\boldsymbol{Y}^{(n+1)}$ appears on the RHS, while production and destruction terms are calculated with the system state at the previous time step $\boldsymbol{Y}^{(n)}$, this integration procedure is considered semi implicit [97]. In contrast to the presented fully implicit Euler backward method, the equation can be solved for $\boldsymbol{Y}^{(n+1)}$ without introducing the Jacobian and the necessity to solve a linear system of equations:

$$\boldsymbol{Y}^{(n+1)}=\frac{\boldsymbol{Y}^{(n)}+\Delta t\,\mathcal{P}\left(\boldsymbol{Y}^{(n)}\right)}{1+\dfrac{\Delta t\,\mathcal{D}\left(\boldsymbol{Y}^{(n)}\right)}{\boldsymbol{Y}^{(n)}}} \tag{3.36}$$

The denominator in Eq. 3.36 has a dampening effect and leads to strictly non-negative results for $\boldsymbol{Y}^{n+1}$ [96]. As evident from Eq. 3.35, the integration scheme has only first order global accuracy like the Euler forward scheme. Higher order procedures can be constructed using the same scaling approach [96]. Another way to improve both accuracy and stability is the application of an inner iteration loop with iterator m [97, 98]:

$$\boldsymbol{Y}^{(n+1,m)}=\frac{\boldsymbol{Y}^{(n)}+\Delta t\,\mathcal{P}\left(\boldsymbol{Y}^{(n,m)}\right)}{1+\dfrac{\Delta t\,\mathcal{D}\left(\boldsymbol{Y}^{(n,m)}\right)}{\boldsymbol{Y}^{(n,m)}}} \tag{3.37}$$

$$\boldsymbol{Y}^{(n,m=1)}=\boldsymbol{Y}^{(n)} \tag{3.38}$$

The iteration loop can be stopped, once all components of the system state vector have sufficiently converged. In this work, the criterion of Yang et al. [98] has been adapted:

$$\max_{1\leq\alpha\leq N_S}\left(\left|\frac{\log_{10}Y_\alpha^{(n,m+1)}}{\log_{10}Y_\alpha^{(n,m)}}\right|\right)\leq 10^{-5}\ \wedge\ |T^{(n,m+1)}-T^{(n,m)}|\leq 10^{-3}\ \mathrm{K} \tag{3.39}$$

It is important to note that the discussed integration scheme does not involve any error control. Therefore, if the CFL based time step size is too large, the scheme will face convergence issues. It was also found that analytical calculations of the source term (*e.g.*, using Cantera [12]) lead to better convergence behavior than internal calculation methods, which are more efficient by tabulating only temperature-dependent quantities, but thereby introduce discretization errors at the same time. The accuracy is on par with fully implicit methods, whereby the efficiency is close to explicit methods.

3.2 Spatial Discretization

The governing equations for multi component combustion systems, as described in Sec 2.1, have to be solved numerically. Analytical solutions for systems of coupled partial differential equations only exist for a few cases, where several assumptions can be made to cancel a majority of the individual terms, e.g., steady laminar flow between two parallel plates. In general, the equations are solved on a solution domain that is decomposed into a finite number of elements. Popular approaches to decompose the numerical domain are the *finite difference method* (FDM) and the *finite volume method* (FVM). In terms of the finite difference method, the values of the conservation variables are stored in grid points that represent the domain. The spatial derivatives present in the equations are approximated at the grid nodes by finite differences. In contrast, in the finite volume method, the domain is represented by a finite number of small volumes, also denoted as cells, where the cells do not overlap and share faces with the neighboring cells. One of the biggest advantages of the FVM is the conservation property of all transported quantities as well as the application to complex geometries. The finite volume method was used in this work and is presented in the following.

3.2.1 Finite Volume Method

In order to apply the finite volume method, the conservation equations need to be represented in *integral form*, hence, the integration of the conservation equations over a finite volume ΔV. In the following, the conservation equation of an arbitrary scalar ϕ is used to derive the integral form. After volume integration the conservation equation reads:

$$\int\limits_{\Delta V} \frac{\partial \rho\phi}{\partial t}\, dV + \int\limits_{\Delta V} \frac{\partial \rho u_i \phi}{\partial x_i}\, dV = \int\limits_{\Delta V} \frac{\partial}{\partial x_i}\left(\rho D_\phi \frac{\partial \phi}{\partial x_i}\right) dV + \int\limits_{\Delta V} \dot{\omega}_\phi\, dV \tag{3.40}$$

According to the *Gauß theorem* [99], volume integrals of the divergence of vector fields $\boldsymbol{F}$ can be replaced by integrals of the respective fluxes normal to the surface enclosing the integration volume:

$$\int\limits_{\Delta V} \nabla \cdot \boldsymbol{F}\, dV = \oint\limits_{\Delta A} \boldsymbol{F} \cdot \boldsymbol{n}\, dA \tag{3.41}$$

Equation 3.41 features the surface normal vector $\boldsymbol{n}$. Rewriting Eq 3.40 with the divergence terms replaced by surface integrals and with the temporal derivative term on the left and all other terms on the RHS yields:

$$\underbrace{\int\limits_{\Delta V} \frac{\partial \rho\phi}{\partial t}\, dV}_{\text{Temporal change}} = -\underbrace{\int\limits_{\Delta A} (\rho u_i \phi)\; n_i\, dA}_{\text{Convection term}} + \underbrace{\int\limits_{\Delta A} \left(\rho D_\phi \frac{\partial \phi}{\partial x_i}\right) n_i\, dA}_{\text{Diffusion term}} + \underbrace{\int\limits_{\Delta V} \dot{\omega}_\phi\, dV}_{\text{Source term}} \tag{3.42}$$

As evident from Eq. 3.42, finite volume methods ensure global conservation of the conserved quantity, regardless of whether conservation makes sense from a physical perspective. This is due to the fact that the flux is strictly assigned to the interface between two neighboring cells. If the flux between two adjacent cells leads to a decrease in, for example, the left cell, the value in the right cell will increase by the same amount. This holds true for arbitrary cell shapes. In practice, however, simple geometries like tetrahedron- and hexahedron-shapes are used. Tetrahedrons are preferred in commercial software to allow simulations of flows confined by complex geometries. In this work, equally sized cubic cells (hexahedron with equidistant edge lengths) have been used, whose normalized surface normal vectors coincide with the Cartesian direction vectors. Cubic Cartesian equidistant grids have several advantages, these include, for example, preservation of the theoretical accuracy of numerical schemes, user-friendly implementation of complex models, potential use of high order schemes and computational efficiency. The grid setup and nomenclature is sketched in Fig 3.1.

3.2.2 Approximation of Integrals

The volume and surface integrals in Eq. 3.42 need to be approximated. The most common method is the second order accurate mid-point rule [88], where volume integrals are approximated by cell center values multiplied with volume and surface integrals are approximated by surface mid point values multiplied

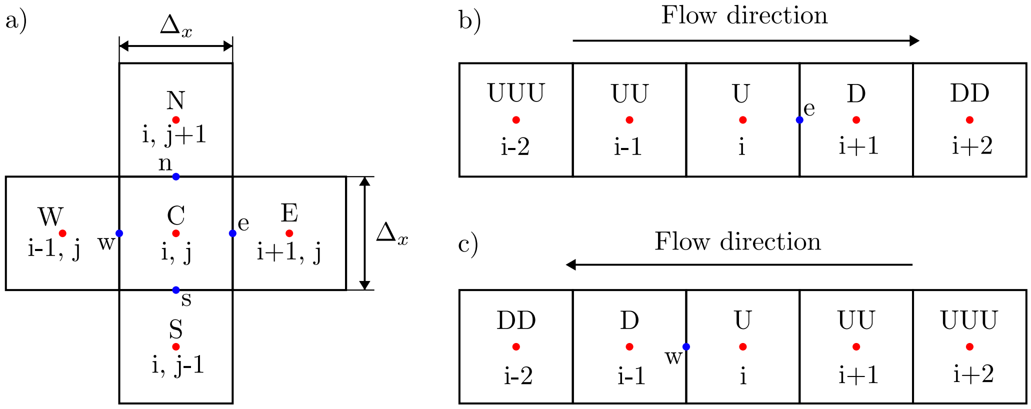

Figure 3.1: Illustration of the nomenclature used for cartesian, equidistant *control volumes* (CV) in the FVM context: (a) Sketch in two dimensions of *central* (C) cell with indices i / j and the direct neighboring cells denoted by celestial directions *west* (W), *east* (E), *south* (S), and *north* (N). Interfaces that are shared among the cells mentioned are written in lower case letters. (b) Sketch to show the *upwind* (U) and *downwind* (D) cells required to calculate the flow on the eastern face with flow direction from left to right and (c) vice versa at western face with flow direction from right to left.

with area. By using equidistant grids, the volumes and areas of all cells are identical and result directly from the global grid size ($dA = \Delta_x^2$, $dV = \Delta_x^3$). Also, each cell is composed of six surfaces, such that the surface integral equals the sum of six individual surface evaluations:

$$\int_{\Delta V} \frac{\partial \rho \phi}{\partial t}\, dV \approx \frac{\partial \rho \phi}{\partial t}\, \Delta_x^3 \tag{3.43}$$

$$\int_{\Delta A} (\rho u_i \phi)\ n_i\ dA \approx \sum_{l=1}^{6} (\rho u_i \Phi)_l\ n_i\ \Delta_x^2 \tag{3.44}$$

$$\int_{\Delta A} \left(\rho D_\phi \frac{\partial \phi}{\partial x_i} \right) n_i\ dA \approx \sum_{l=1}^{6} \left(\rho D_\phi \frac{\partial \phi}{\partial x_i} \right)_l n_{i,l}\ \Delta_x^2 \tag{3.45}$$

$$\int_{\Delta V} \dot{\omega}_\phi\ dV \approx \dot{\omega}_\phi\ \Delta_x^3 \tag{3.46}$$

In general, values of conserved variables are stored and advanced at cell centers so that value evaluations at cell centers are obsolete. However, quantities on the surfaces to determine fluxes are initially unknown and suitable spatial discretization schemes are needed.

3.2.3 Convective Fluxes

The discretization of convective fluxes (Eq. 3.44) requires interpolation of quantities at the center point of the surface, if the mid point approximation is used. For this purpose, spatial discretization schemes are utilized that use the quantities at nearby cell centers for interpolation. At least two cell center values next to the surface are required, but often values of several cell centers are used, which is also denoted as cell stencil. The methods differ in accuracy, whereby higher accuracy is usually accompanied by lower stability and higher computational costs. Accuracy in this context describes the decrease of the error with refinement of the grid. Furthermore, discretization schemes can be investigated with respect to numerical dissipation and numerical dispersion. Numerical dissipation has a diffusive effect on the solution, which is therefore smeared, while numerical dispersion leads to oscillations in the solution.

3.2.3.1 Central Differencing Scheme

Among the more popular spatial discretization schemes is the *central differencing scheme* (CDS). The term *differencing* stems from the finite difference scheme that is reminiscent in determining the first derivative, whereas in finite volume methods *central interpolation* would be more adequate [88]. To determine a value at the eastern surface (e.g., that of the scalar ϕ_e) only the cell center values of the direct neighbors ϕ_C and ϕ_E are needed:

$$\phi_\mathrm{e} = \frac{\phi_\mathrm{C} + \phi_\mathrm{E}}{2} \tag{3.47}$$

The Taylor series expansions for the approximation of values ϕ_E and ϕ_C (see Fig. 3.1) developed at the eastern surface read:

$$\phi_\mathrm{E} = \phi_\mathrm{e} + \frac{\Delta x}{1!}\left(\frac{\partial \phi}{\partial x}\right)_\mathrm{e} + \frac{\Delta x^2}{2!}\left(\frac{\partial^2 \phi}{\partial x^2}\right)_\mathrm{e} + \frac{\Delta x^3}{3!}\left(\frac{\partial^3 \phi}{\partial x^3}\right)_\mathrm{e} + O(\Delta x^4) \tag{3.48}$$

$$\phi_\mathrm{C} = \phi_\mathrm{e} - \frac{\Delta x}{1!}\left(\frac{\partial \phi}{\partial x}\right)_\mathrm{e} + \frac{\Delta x^2}{2!}\left(\frac{\partial^2 \phi}{\partial x^2}\right)_\mathrm{e} - \frac{\Delta x^3}{3!}\left(\frac{\partial^3 \phi}{\partial x^3}\right)_\mathrm{e} + O(\Delta x^4) \tag{3.49}$$

Equations 3.48 and 3.49 can be combined to resemble the CDS formulation in Eq. 3.47 in addition to terms that are not considered by the discretization scheme and are thus classified as discretization errors. It should be noted that terms with odd derivatives cancel out when adding Eq. 3.48 and 3.49:

$$\phi_\mathrm{e} = \underbrace{\frac{\phi_\mathrm{C} + \phi_\mathrm{E}}{2}}_{\text{CDS}} - \underbrace{\left[\frac{\Delta x^2}{2!}\left(\frac{\partial^2 \phi}{\partial x^2}\right)_\mathrm{e} + O(\Delta x^4)\right]}_{\text{Discretization errors}} \tag{3.50}$$

According to Eq. 3.50, the leading truncation error for CDS is proportional to the square of Δx, making the scheme 2^{nd} order accurate. Also, because the leading error term features a second derivative, this scheme is expected to suffer from dispersion errors, also known as wiggles or numerical oscillations. At the same time, however, the error term responsible for numerical diffusion disappears, which is why this scheme is generally a suitable choice for the simulation of turbulent flows, if numerical oscillations can be suppressed. In the case of incompressible CFD solvers or in the case of low Mach solution algorithms, CDS can be used in the momentum equations for the discretization of convective fluxes, since the pressure gradient is determined implicitly and dispersion errors are thus smoothed. In the case of compressible solvers, however, the pressure gradient is calculated explicitly and CDS can therefore not be used without the use of appropriate filters [100, 101] or artificial viscosity methods [102, 103]. Another problem concerns the transport of scalars that may take physically meaningful values only in a bounded range. This applies, for example, to density, whose values must be greater than zero, or to coupled mass fractions, whose minimum values are zero and maximum values respectively at one and whose sum must equal exactly one. Even small oscillations can lead to a violation of the valid range, which is why further spatial discretization methods are necessary for simulations of reactive flow.

3.2.3.2 Upwind Differencing Scheme

As with CDS, the *upwind differencing scheme* (UDS) has its name in the forward and backward differencing schemes known from FDM. In contrast to CDS, UDS uses exactly the solution of the neighboring cells as a function of the flow direction and thus reads:

$$\phi_\mathrm{e} = \phi_\mathrm{U} \tag{3.51}$$

$$\phi_\mathrm{U} = \begin{cases} \phi_\mathrm{C} & \text{if} \quad u_\mathrm{e} \geq 0, \\ \phi_\mathrm{E} & \text{else.} \end{cases} \tag{3.52}$$

From here on, the notation with upwind values ϕ_U and downwind values ϕ_D will be used according to Fig. 3.1 when the cell stencil is determined by the sign of the interpolated surface velocity. The Taylor series expansion at point C to approximate the value on the east surface (UDS for $u_\mathrm{e} \geq 0$) immediately shows that the method is only 1st order accurate and that the leading error term corresponds to that of a diffusive process:

$$\phi_\mathrm{e} = \phi_\mathrm{C} + \underbrace{\left[\frac{\Delta x}{1!} \left(\frac{\partial \phi}{\partial x} \right)_\mathrm{C} + O(\Delta x^2) \right]}_{\text{Discretization errors}} \tag{3.53}$$

The low order accuracy and diffusive properties make UDS one of the most stable discretization schemes for convective fluxes and can even handle discontinuities in the flow solution, such as compression shock waves, and it keeps the boundedness of conserved scalars. However, there are alternatives for UDS that also exhibit stable behavior while allowing significantly higher accuracy if the local solution permits. These methods typically consider the sign of the velocity to apply an upwind biased cell stencil and are non-linear. This means that the weighting coefficients in the interpolation stencil are a function of the local solution.

3.2.3.3 Total Variation Diminishing Scheme

The *total variation diminishing* (TVD) scheme blends dynamically between UDS and CDS to combine the stable behavior of UDS if it is necessary, while allowing the accuracy and low dissipation behavior of CDS if possible. Generally, TVD schemes use a three point cell stencil with the two adjacent upwind cells ϕ_U, ϕ_UU and the first downwind cell ϕ_D. It is assumed that CDS can be used only when the solution is sufficiently smooth, whereas UDS is necessary when a change in gradient (i.e. second derivative) is detected. In order to satisfy the TVD property, the total variation (TV) of a quantity at time step $n+1$ must be less than or equal to the total variation at time step n with the following definition of TV by Harten [104]:

$$TV(\phi^n) = \sum_k |\phi_k^n - \phi_{k-1}^n| \tag{3.54}$$

$$TV(\phi^{n+1}) \leq TV(\phi^n) \tag{3.55}$$

Here, k describes a cell index with the sum covering all cells in the numerical domain. Given the definition, it is natural to use a limiter function $\psi(r)$ that takes the ratio of gradients as an argument leading to the following interpolation scheme:

$$\phi_\mathrm{e} = \phi_\mathrm{U} + \frac{1}{2} \psi(r) \left(\phi_\mathrm{U} - \phi_\mathrm{UU} \right) \tag{3.56}$$

$$r = \frac{\phi_\mathrm{D} - \phi_\mathrm{U}}{\phi_\mathrm{U} - \phi_\mathrm{UU}} \tag{3.57}$$

Accordingly, UDS is recovered for limiter function values equal to zero and CDS is recovered for $\psi(r) = r$. A stable second order TVD region for flux limiters in terms of r has been defined by Sweby [105]:

Table 3.1: Definitions of popular flux limiter functions.[1].

Flux limiter function	Definition
Min-mod limiter	$\psi(r) = \max[0, \min(r,\ 1)]$
Superbee limiter	$\psi(r) = \max[0, \min(r,\ 2), \min(2r,\ 1)]$
Van Leer limiter	$\psi(r) = (r + \|r\|)\ /\ (1 + r)$
Van Albada limiter	$\psi(r) = (r + r^2)\ /\ (1 + r^2)$
Charm limiter	$\psi(r) = \max(r,\ 0)\ (3\max(r,\ 0) + 1)\ /\ (\max(r,\ 0) + 1)^2$

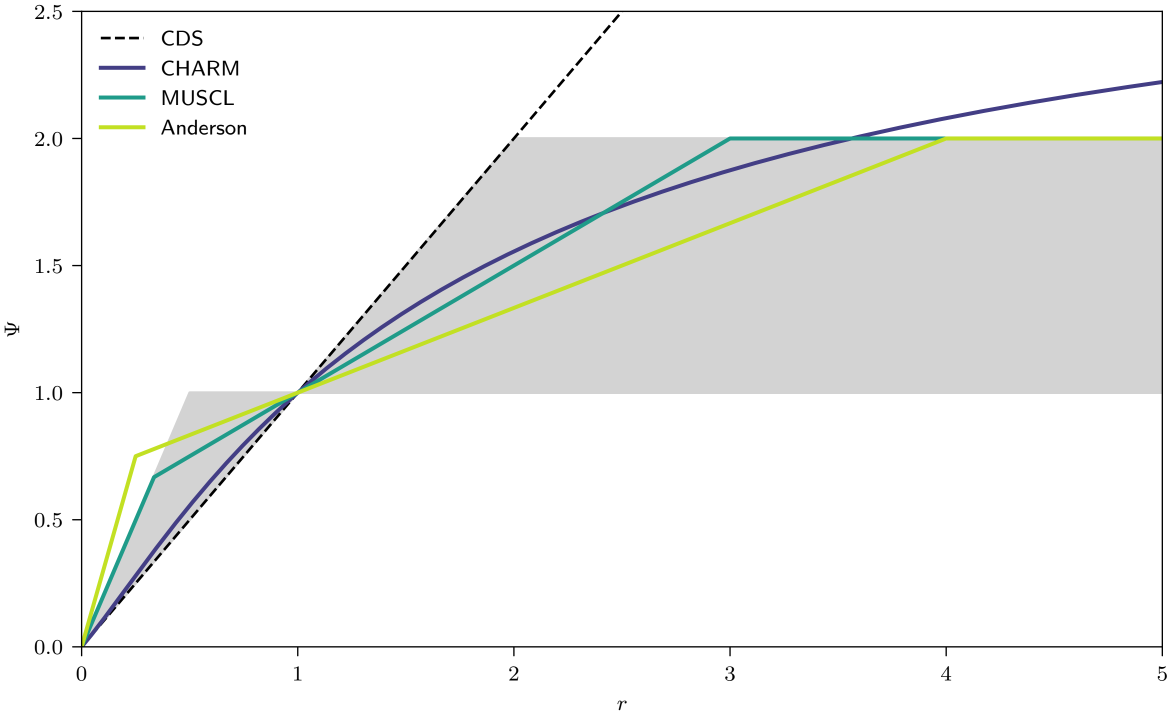

Figure 3.2: Illustration of limiter functions ψ from Anderson et al. [111], Leer [112] (MUSCL), and Zhou [108] (CHARM) as a function of gradient ratio r. The 2nd order TVD region, as introduced by Sweby [105], is highlighted by a shaded background.

$$\psi(r) = \begin{cases} 0 \leq \psi(r) \leq \min(2r,\ 2) & \text{if} \quad r \geq 0, \\ \psi(r) = 0 & \text{else.} \end{cases} \tag{3.58}$$

Several limiter functions $\psi(r)$ have been developed [106–108] with the aim of increasing the CDS portion of the scheme within the TVD bounds and whose function definitions are presented in Tab. 3.1. A comprehensive comparison of the limiter functions available to the code used in this work has been presented by Kempf [109] and Proch [110]. Following these results, the Charm limiter [108] has been utilized in terms of TVD schemes.

3.2.3.4 Monotonic Upstream Scheme for Conservation Laws

The *monotonic upstream scheme for conservation laws* (MUSCL) is another non-linear scheme with the aim to achieve higher accuracy while maintaining oscillation free solutions and has been originally conceptualized by Van Leer [107, 112, 113]. Unlike the algebraic definition of total variation, the monotonicity constraint introduced by Godunov [114] is of geometric type, which states that an initially monotonic distribution of quantity ϕ remains monotonic in the subsequent timesteps. For this purpose, the distributions of individual quantities in each cell are linearly approximated. For the respective slopes, conditions arise to ensure monotonicity. For example, the boundary values of the linear approximation in cell C must lie within an interval whose boundaries are defined by the averaged cell values of cell W and cell E. Accordingly, the limiter proposed in scope of the original MUSCL scheme is also geometrically motivated to limit slopes. It should be noted that any scheme with TVD property also preserves monotonicity [115]. Apart from the specific limiter, however, an interpolation method different to the one used for TVD schemes is used. The interpolation is based on the linear κ schemes, which were also introduced by Van Leer [107]:

$$\phi_{\mathrm{e}} = \phi_{\mathrm{U}} + \psi(r)\left[\frac{1+\kappa}{4}\left(\phi_{\mathrm{D}} - \phi_{\mathrm{U}}\right) + \frac{1-\kappa}{4}\left(\phi_{\mathrm{U}} - \phi_{\mathrm{UU}}\right)\right] \tag{3.59}$$

Accordingly, the interpolated value ϕ_{e} equals that of UDS in addition to a higher order term that takes both upwind and downwind gradients into account. Slope limiters $\psi(r)$ can be applied to both of the gradients, turning the linear scheme into a non-linear scheme. Equation 3.59 also introduces the parameter κ that allows to adjust the weights of upwind and downwind gradients. It can be shown [115] that κ-schemes have a leading truncation error of 2nd order that, however, vanishes if $\kappa = 1/3$, resulting in an upwind biased scheme of 3rd order. Numerical tests also showed superior behavior for $\kappa = 1/3$ [115]. According to Roe [116], κ schemes can also be expressed in the general form of non-linear, flux limited schemes:

$$\phi_{\mathrm{e}} = \phi_{\mathrm{U}} + \frac{1}{2}\psi(r)\left(\phi_{\mathrm{U}} - \phi_{\mathrm{UU}}\right) \tag{3.60}$$

$$\psi(r) = \max\left[0,\ \min\left(2r,\ \frac{1+\kappa}{2}r + \frac{1-\kappa}{2},\ M\right)\right] \tag{3.61}$$

The limiter function in Eq. 3.61 is piece-wise linear in terms of r with upper limit M. Improvements of the original MUSCL scheme have been proposed since. Billet and Louedin [117] for example introduced a *triad* of limiters that adapt to certain flow configurations, while Anderson et al. [111] presented an improved limiter of 3rd order that has been used in this work with $\kappa = 1/3$:

$$\psi^{\mathrm{Anderson}}(r) = \frac{1}{2}\left[(1-\kappa)\min\left(r,\ \frac{3-\kappa}{1-\kappa}\right) + (1+\kappa)\min\left(1,\ r\frac{3-\kappa}{1-\kappa}\right)\right] \tag{3.62}$$

The limiter of Anderson et al. [111] is presented in the *Sweby* limiter diagram in Fig. 3.2 along with the original MUSCL slope limiter (Eq. 3.61, $\kappa = 0$, $M = 2$) and the CHARM TVD limiter.

3.2.3.5 Weighted Essentially Non Oscillatory Scheme

The *weighted essentially non oscillating* (WENO) class of schemes, developed by Liu et al. [118], uses a very different interpolation approach and takes the basic idea of *essentially non oscillating* (ENO) schemes, proposed by Harten and Osher [119, 120], one step further. In contrast to the non-linear interpolation methods mentioned so far, ENO schemes do not use a limiter, but instead adapt the interpolation stencil in order to select the smoothest polynomial for inner cell reconstruction. In turn, WENO schemes weight the individual solutions of a finite number of sub stencils based on indicators for smoothness (IS) to interpolate the quantity with a high order of accuracy. In general, WENO schemes can be constructed with arbitrary formal accuracy, whereby the formal accuracy is only achieved in vicinity of smooth solutions. Those sub stencils that incorporate discontinuities are omitted to remove oscillations. The WENO method used in this work has 5th order formal accuracy, utilizes an upwind biased five point stencil (ϕ_{UUU}, ϕ_{UU}, ϕ_{U}, ϕ_{D}, ϕ_{DD}) and is often referred to as classical WENO or WENO5. First, three candidates for the interpolated value ϕ_{e} are computed, whereby each stencil is composed of three cells:

$$\phi_{\mathrm{e},1} = 2\,\phi_{\mathrm{UUU}} - 7\,\phi_{\mathrm{UU}} + 11\,\phi_{\mathrm{U}} \tag{3.63}$$

$$\phi_{\mathrm{e},2} = -\phi_{\mathrm{UU}} + 5\,\phi_{\mathrm{U}} + 2\,\phi_{\mathrm{D}} \tag{3.64}$$

$$\phi_{\mathrm{e},3} = 2\,\phi_{\mathrm{U}} + 5\,\phi_{\mathrm{D}} - \phi_{\mathrm{DD}} \tag{3.65}$$

Further, a criterion for weighting the individual candidates is needed to increase accuracy while maintaining oscillation free solutions. Jiang and Shu [121] have proposed the following smoothness indicators:

$$IS_1 = \frac{13}{12}\,(\phi_{\mathrm{UUU}} - 2\,\phi_{\mathrm{UU}} + \phi_{\mathrm{U}})^2 + \frac{3}{12}\,(\phi_{\mathrm{UUU}} - 4\,\phi_{\mathrm{UU}} + 3\,\phi_{\mathrm{U}})^2 \tag{3.66}$$

$$IS_2 = \frac{13}{12}\,(\phi_{\mathrm{UU}} - 2\,\phi_{\mathrm{U}} + \phi_{\mathrm{D}})^2 + \frac{3}{12}\,(\phi_{\mathrm{UU}} - \phi_{\mathrm{D}})^2 \tag{3.67}$$

$$IS_3 = \frac{13}{12}\,(\phi_{\mathrm{U}} - 2\,\phi_{\mathrm{D}} + \phi_{\mathrm{DD}})^2 + \frac{3}{12}\,(3\,\phi_{\mathrm{U}} - 4\,\phi_{\mathrm{D}} + \phi_{\mathrm{DD}})^2 \tag{3.68}$$

The weights ω_k of the individual candidate solutions can then be calculated according to Liu et al. [118]:

$$\omega_k = \frac{\alpha_k}{\alpha_1 + \alpha_2 + \alpha_3}, \quad k = 1, 2, 3 \tag{3.69}$$

$$\alpha_k = \frac{C_k}{(IS_k + \epsilon)^2} \tag{3.70}$$

$$C_1 = \frac{1}{12},\ C_2 = \frac{6}{10},\ C_3 = \frac{3}{10} \tag{3.71}$$

Here, C_k are the optimal coefficients, that is, the smoothness indicators approach unity if the solution is smooth, while ϵ is a small number to avoid division by zero. The final interpolated quantity at the eastern face is calculated accordingly:

$$\phi_{\mathrm{e}} = \frac{1}{6}\left(\omega_1\,\phi_{\mathrm{e},1} + \omega_2\,\phi_{\mathrm{e},2} + \omega_3\,\phi_{\mathrm{e},3}\right) \tag{3.72}$$

3.2.3.6 Monotonicity Preserving Scheme

The monotonicity preserving (MP) scheme of Suresh and Huynh [122] is a formally 5th order accurate scheme that ensures monotonicity by limiting the interpolated face value to a certain range in contrast to slope limiting methods. The face limiting procedure has been originally proposed by Colella and Woodward [123] in scope of the development of the *piecewise parabolic method* (PPM). However, the limiting approach used in terms of the monotonicity preserving 5th order (MP5) scheme is different in a few key aspects, as it is specifically designed for Runge Kutta time integration and because it widens the allowed range in vicinity of extrema to increase accuracy following geometric considerations. In calculating the interface value ϕ_{e}, an original interface value $\phi_{\mathrm{e}}^{\mathrm{OR}}$ is calculated first, using a fourth degree polynomial [122]:

$$\phi_{\mathrm{e}}^{\mathrm{OR}} = \frac{1}{60}\,(2\,\phi_{\mathrm{UUU}} - 13\,\phi_{\mathrm{UU}} + 47\,\phi_{\mathrm{U}} + 27\,\phi_{\mathrm{D}} - 3\,\phi_{\mathrm{DD}}) \tag{3.73}$$

In smooth regions, the original value will be an accurate approximation for the interface value, but violate monotonicity near discontinuities. For this purpose, an upper limit value ϕ^{UL} is proposed which ensures that the value ϕ^{n+1} will lie between the values ϕ_{UU} and ϕ_{U} after a Runge Kutta stage:

$$\phi_{\mathrm{e}}^{\mathrm{UL}} = \phi_{\mathrm{U}} + \alpha\,(\phi_{\mathrm{U}} - \phi_{\mathrm{UU}}) \tag{3.74}$$

$$\mathrm{CFL} \leq \frac{1}{1+\alpha} \tag{3.75}$$

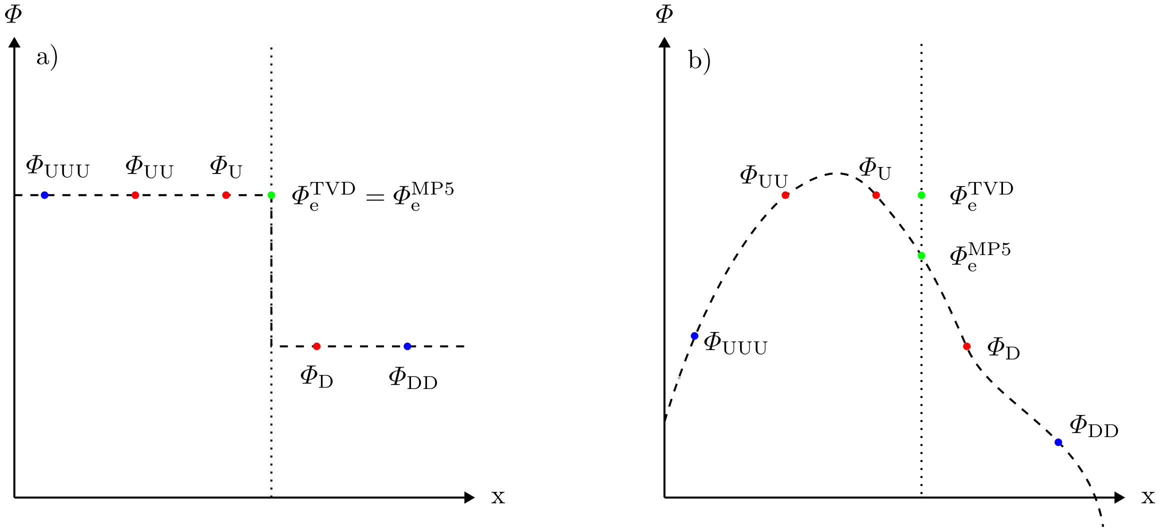

Figure 3.3: Spatial distributions of scalar ϕ with a) jump in the solution and b) with local extreme. Stencils to compute the eastern interface value ϕ_{e} (green symbols) are presented by red symbols (TVD) and additional blue symbols (MP5).

It is evident, that higher CFL numbers will result in a more restrictive upper limit value. In this work, a value of $\alpha = 4$ is used, with a theoretical CFL number limit of 0.2, which however can be increased by a factor of 2 and still yield stable results. At the same time, if the cell averages are monotonic, then the interface values should also be monotonic. Thus, ϕ_{e} is also restricted to the value range given by ϕ_{U} and ϕ_{D}. The strictly monotonicity preserving interface value can now be expressed as:

$$\phi_{\mathrm{e}}^{\mathrm{MP}} \in \left[\phi_{\mathrm{U}}, \phi_{\mathrm{e}}^{\mathrm{UL}}\right] \quad \wedge \quad \phi_{\mathrm{e}}^{\mathrm{MP}} \in \left[\phi_{\mathrm{U}}, \phi_{\mathrm{D}}\right] \tag{3.76}$$

Thus, the first interval ensures that the cell averages after a Runge Kutta stage are monotonic, while the second interval ensures that the interpolated point values themselves are monotonic. In practice, the strictly monotonicity preserving value can be calculated using the median function that takes three values as input and returns the single value that lies between the other two. The *median* function also can be formulated in a way that uses the efficient *minmod* function [122]:

$$\phi_{\mathrm{e}}^{\mathrm{MP}} \leftarrow \mathrm{median}\left(\phi_{\mathrm{U}}, \phi_{\mathrm{e}}^{\mathrm{UL}}, \phi_{\mathrm{D}}\right) \tag{3.77}$$

$$\mathrm{median}\left(\phi_{\mathrm{U}}, \phi_{\mathrm{e}}^{\mathrm{UL}}, \phi_{\mathrm{D}}\right) = \phi_{\mathrm{U}} + \mathrm{minmod}\left(\phi_{\mathrm{D}} - \phi_{\mathrm{U}}, \phi_{\mathrm{e}}^{\mathrm{UL}} - \phi_{\mathrm{U}}\right) \tag{3.78}$$

$$\mathrm{minmod}\,(x, y) = 0.5\,(\mathrm{sgn}(x) + \mathrm{sgn}(y))\;\min(|x|, |y|) \tag{3.79}$$

The strictly monotonicity preserving scheme is very accurate in smooth regions, but it will have only first order accuracy near extrema, a property shared with TVD and MUSCL schemes. To preserve accuracy near extrema, the 5 point stencil employed in this scheme can be used in distinguishing extrema from discontinuities. It is important to note that a 3 point stencil is insufficient, as demonstrated in Fig. 3.3.

This figure presents spatial distributions of a scalar ϕ at time $t = 0$, which are supposed to be convected from left to right at constant velocity u. The cell averages initially correspond to the local values of the exact solution and for the determination of the numerical flux the face value ϕ_{e} is needed. In panel a), the scalar distribution exhibits a jump in the solution, which will lead to oscillations, when a higher order reconstruction is used. For this reason, the spatial order of the scheme must degenerate to first order accuracy in vicinity of discontinuities to yield $\phi_{\mathrm{e}} = \phi_{\mathrm{U}}$. In panel b), however, the spatial distribution is smooth with a local extreme value, while the cell averages ϕ_{UU}, ϕ_{U}, and ϕ_{D}, *i.e.* the stencil for TVD and MUSCL schemes, are identical to those in panel a). Consequently, in the case of a TVD or MUSCL scheme, the spatial accuracy will be reduced to first order again, which, however, is not necessary in this case. Only by the additional information provided from the cell averages ϕ_{UUU} and ϕ_{DD} it becomes clear that no discontinuity is present, a circumstance which is used by MP5 not to limit the valid interval range to the upstream value. In order to preserve accuracy near extrema, the intervals in Expression 3.76 must be enlarged.

In the case where a local extreme lies between the two closest cell averages ϕ_{U} and ϕ_{D} to the interface, the interpolated value of the strictly monotonicity preserving scheme is inappropriately limited by the interval $[\phi_{\mathrm{U}}, \phi_{\mathrm{D}}]$ and is therefor not accuracy preserving. A viable choice to widen the interval is the introduction of the so called median value, proposed by Huynh [124]:

$$\phi^{\mathrm{MD}} \leftarrow \mathrm{median}\left(\phi^{\mathrm{AV}}, \phi^{\mathrm{FL}}, \phi^{\mathrm{FR}}\right) \tag{3.80}$$

$$\phi^{\mathrm{AV}} = 0.5\,(\phi_{\mathrm{U}} + \phi_{\mathrm{D}}) \tag{3.81}$$

$$\phi^{\mathrm{FL}} = \phi_{\mathrm{U}} + 0.5\,(\phi_{\mathrm{U}} - \phi_{\mathrm{UU}}) \tag{3.82}$$

$$\phi^{\mathrm{FR}} = \phi_{\mathrm{D}} + 0.5\,(\phi_{\mathrm{D}} - \phi_{\mathrm{DD}}) \tag{3.83}$$

Expressions 3.80 - 3.83 feature the median value ϕ^{MD}, the average value ϕ^{AV}, the linearly left extrapolated value ϕ^{FL}, and the linearly right extrapolated value ϕ^{FR}. The constraint of monotonic interpolated values can be extended accordingly:

$$\phi_{\mathrm{e}}^{\mathrm{MP}} \in \left[\phi_{\mathrm{U}}, \phi_{\mathrm{D}}, \phi^{\mathrm{MD}}\right] \tag{3.84}$$

However, in order to preserve accuracy in the situation shown in Fig. 3.3 it is also necessary to extend the interval, which was previously limited by ϕ_{U} and ϕ^{UL}. For this purpose, Suresh and Huynh [122] have proposed the large curvature value ϕ^{LC} as an additional quantity to enlarge the interval. A parabola is used to determine ϕ^{LC}, using mostly upstream cell averages to construct the differences:

$$\phi^{\mathrm{LC}} = \phi_{\mathrm{U}} + \frac{1}{2}\,(\phi_{\mathrm{U}} - \phi_{\mathrm{UU}}) + \frac{1}{3}d \tag{3.85}$$

$$d = 4\,d_{\mathrm{w}}^{\mathrm{MM}} = 4\;\mathrm{minmod}\,(d_{\mathrm{U}}, d_{\mathrm{UU}}) \tag{3.86}$$

$$d_{\mathrm{U}} = \phi_{\mathrm{UU}} - 2\phi_{\mathrm{U}} + \phi_{\mathrm{D}} \tag{3.87}$$

$$d_{\mathrm{UU}} = \phi_{\mathrm{UUU}} - 2\phi_{\mathrm{UU}} + \phi_{\mathrm{U}} \tag{3.88}$$

In this context, d is a general second order difference and $d_{\mathrm{w}}^{\mathrm{MM}}$ is the smaller of the second order differences adjacent to the western face, if both second order differences share the same sign. The interpolated value that preserves both monotonicity and accuracy is then constrained by:

$$\phi_{\mathrm{e}} \in \left[\phi_{\mathrm{U}}, \phi_{\mathrm{e}}^{\mathrm{UL}}, \phi_{\mathrm{e}}^{\mathrm{LC}}\right] \quad \wedge \quad \phi_{\mathrm{e}} \in \left[\phi_{\mathrm{U}}, \phi_{\mathrm{D}}, \phi_{\mathrm{e}}^{\mathrm{MD}}\right] \tag{3.89}$$

In order to calculate the final interface value, the minimum and maximum values of both constraints must be used:

$$\phi_{\mathrm{e}}^{\min} = \max\left[\min\left(\phi_{\mathrm{U}}, \phi_{\mathrm{e}}^{\mathrm{UL}}, \phi_{\mathrm{e}}^{\mathrm{LC}}\right), \min\left(\phi_{\mathrm{U}}, \phi_{\mathrm{D}}, \phi_{\mathrm{e}}^{\mathrm{MD}}\right)\right] \tag{3.90}$$

$$\phi_{\mathrm{e}}^{\max} = \min\left[\max\left(\phi_{\mathrm{U}}, \phi_{\mathrm{e}}^{\mathrm{UL}}, \phi_{\mathrm{e}}^{\mathrm{LC}}\right), \max\left(\phi_{\mathrm{U}}, \phi_{\mathrm{D}}, \phi_{\mathrm{e}}^{\mathrm{MD}}\right)\right] \tag{3.91}$$

$$\phi_{\mathrm{e}} \leftarrow \mathrm{median}\left(\phi_{\mathrm{e}}^{\mathrm{OR}}, \phi_{\mathrm{e}}^{\min}, \phi_{\mathrm{e}}^{\max}\right) \tag{3.92}$$

3.2.3.7 Linear Test Case

The performance of the interpolation schemes can be tested using the linear advection equation at a constant convection velocity u:

$$\frac{\partial \phi}{\partial t} + u \frac{\partial \phi}{\partial x} = 0 \tag{3.93}$$

In the simulations, a scalar with a defined initial distribution is convected exactly once through a one-dimensional domain, enabled by the use of periodic boundary conditions. The domain of all cases presented here ranges from -1 m to 1 m, thus has a total length of 2 m discretized by 200 finite volumes, which thus corresponds to a grid width Δ_x of 0.01 m. In terms of time integration, the explicit low storage Runge Kutta scheme with 3rd order accuracy has been used. Here, the CFL number for all schemes is set to 0.4, since this value is near the stability limit for MP5. It should be noted that for the remaining interpolation schemes, including the formally 5th accurate WENO scheme, a larger CFL number could have been chosen. A total of 3 cases with individual distributions have been tested with increasing demands on the numerical methods.

The first distribution is a sine wave, presented in Fig. 3.4 a), *i.e.* a distribution featuring very shallow gradients. In fact, it is difficult to keep the results of each interpolation method apart, except for UDS, which is the only method that is 1st order accurate with a leading dissipative error term. Therefore, UDS has visibly smoothed the sine wave after one run through. The initial profile in the second test case in Fig. 3.4 b) corresponds to that of a Gaussian distribution, with the gradients near the maximum being significantly steeper compared to those of the sine wave. This is also reflected in the results with more pronounced differences between the schemes. To see the differences even more clearly, panel d) of Fig 3.4 shows a zoomed cutout in vicinity of the profile maximum. The TVD scheme smoothed the Gaussian profile the most of those schemes, with a spatial accuracy of order of 2 or higher. The MUSCL method behaves similarly to the TVD method with slightly less numerical dissipation. The CDS scheme stands out in that the profile is phase shifted after one run though, but otherwise retained the initial profile satisfactory. The phase shift can be attributed to the leading error being dispersive. For the schemes with a 5th order formal accuracy, no difference from the initial solution can be identified. The profile of the third case is given as [122]:

$$\phi(x) = \begin{cases} \exp\left(-\log(2)(x+0.7)^2/0.0009\right) & \text{if } -0.8 \le x \le -0.6, \\ 1 & \text{if } -0.4 \le x \le -0.2, \\ 1 - |10(x-1)| & \text{if } 0 \le x \le 0.2, \\ \text{sqrt}\left(1 - 100(x-0.5)^2\right) & \text{if } 0.4 \le x \le 0.6, \\ 0 & \text{else.} \end{cases} \tag{3.94}$$

This case involves not only a tophat profile, but also very narrow waves with sudden changes of the slope. Evident from Fig. 3.4 c) are the oscillations that arise when CDS is used. For this case, two regions were selected for a magnified view, see Fig 3.4 panel e) and f). These show an enlarged region around the first wave, and an enlarged region of the discontinuity on the right side of the tophat profile. In particular, panel e) reveals accurate behavior of MP5 near extrema. In addition, the discontinuity is also the least smeared of all schemes tested. However, because the theoretical CFL limit for monotonicity preservation is 0.2, while CFL = 0.4 has been used, small over- and undershoots can be seen. The observed behavior can be critical in simulations of reactive flow with strictly bounded scalars, *e.g.* mass fractions must not take negative values and values larger one. Lowering the CFL number will help in those situations, with the drawback of higher CPU cost.

3.2.4 Diffusive Fluxes

Diffusive fluxes (Eq. 3.45) can be discretized using the second order accurate mid point rule along with an approximation of the gradient on the face center. In contrast to the discretization of convective fluxes,

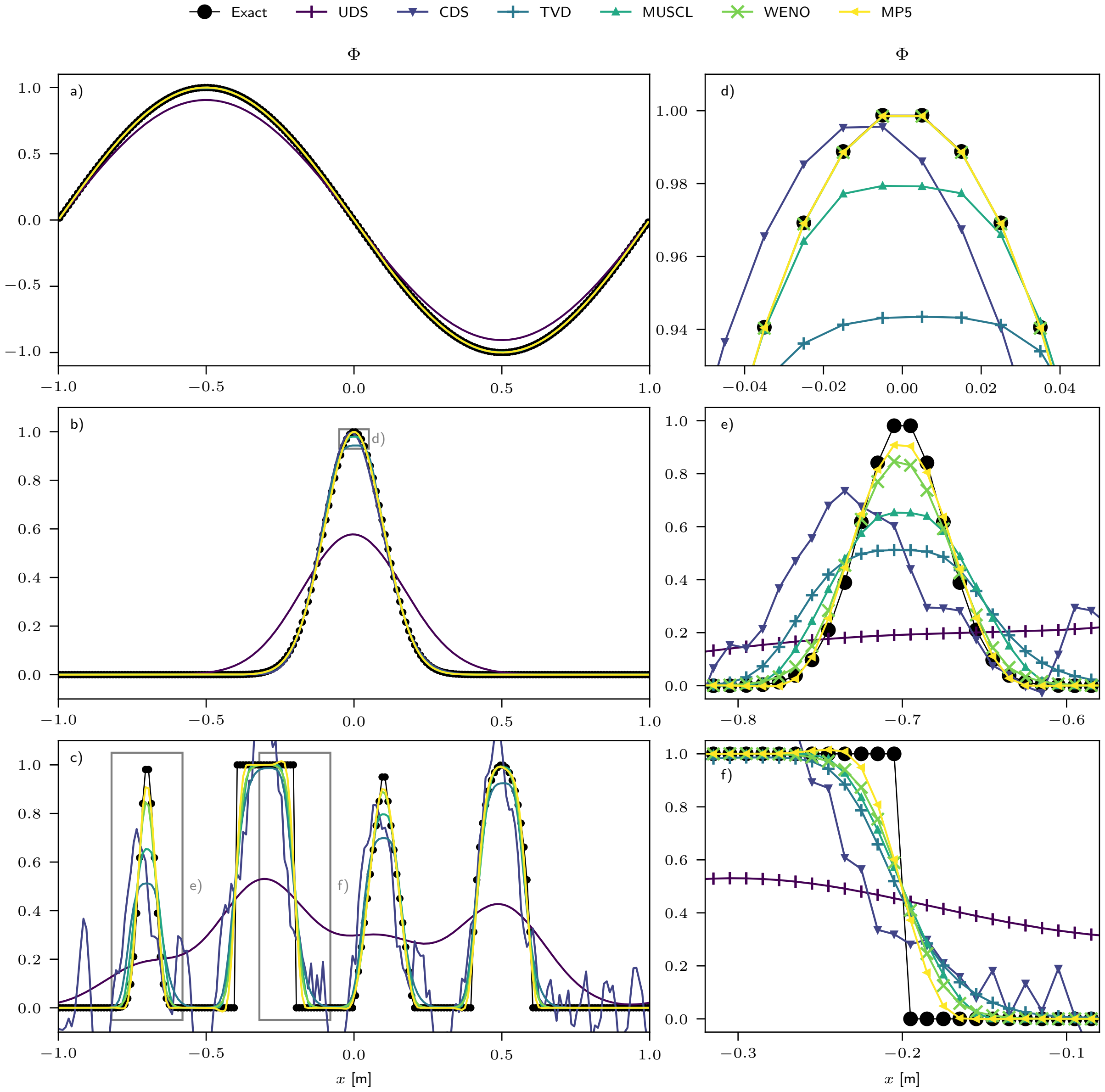

Figure 3.4: Linear advection of scalar ϕ with the initial solution of a) sine wave, b) Gaussian distribution, and c) four different challenging profiles with steep gradients and jumps. The panels in the right column show close ups as highlighted by gray rectangles in the left panels.

diffusive fluxes can be approximated by central difference schemes without the occurrence of dispersive errors:

$$\left(\frac{\partial \phi}{\partial x}\right)_{\mathrm{e}} \approx \frac{\phi_{\mathrm{E}} - \phi_{\mathrm{C}}}{\Delta_x} \tag{3.95}$$

3.2.5 Approximate Riemann Solver

Hyperbolic systems of partial differential equations, such as the Euler equations of gas dynamics, require numerical flux functions that add dissipation to capture discontinuities (*e.g.*, compression shock waves and contact discontinuities) without introducing excessive amount of numerical oscillations. Godunov type schemes [125] approximate continuous data as piece wise constant on a numerical grid and the arising discontinuity at each cell interface constitutes a Riemann initial value problem. Originally, the exact solution for this local Riemann problem has been calculated to advance the solution in time. Near physical discontinuities, accurate results are achieved making this approach shock capturing. In practice, however, this scheme is highly dissipative in smooth regions and the computational cost for computing the exact solution of the Riemann problem is high, due to iterative procedures. Dissipation can be reduced by higher order spatial reconstruction of the state vectors to the left and right of the cell interface. In order to reduce computational cost, Roe [106] proposed the use of an approximate Riemann solver that mimics the exact solver in key aspects. Since then, several approximate Riemann solvers have been developed [126]. The different procedures include flux difference splitting methods [127, 128], flux vector splitting methods [129, 130], and flux splitting methods [131, 132]. Many of which may introduce unexpected results in some situations. For example, the approximate Riemann solver proposed by Roe is prone for the so called *carbuncle phenomenon*, where planar shocks collapse [133]. Other deficiencies have been pointed out by Quirk [133]: (1) non-physical expansion shocks due to entropy violations, (2) negative pressures in high Mach number flows, (3) post-shock oscillations due to slowly moving shocks, and (4) odd even decoupling of planar shocks if aligned with the grid.

Moreover, the approximate Riemann solver used in this work is supposed to be suitable for combustion simulations, so that numerical flux functions with matrix evaluations and partial derivatives with respect to individual species were discarded. Instead, the computational cost should increase linearly with the number of species. A method to which many of the mentioned deficiencies do not apply is the AUSM method and its direct successor AUSM+.

3.2.5.1 AUSM+

The successor of the *advection upstream splitting method* (AUSM) [131] is denoted as AUSM+ [134] and is more simple compared to flux vector and flux difference splitting methods. Thus it can be easily incorporated into an existing CFD solver and additionally corrects problems of its predecessor. These include, for example, the elimination of low frequency oscillations behind the compression shock. Fundamentally, in AUSM and in all methods based on it, the inviscid flux $\tilde{\boldsymbol{F}}$ at a cell interface is divided into the convective flux and the pressure flux to treat them separately:

$$\tilde{\boldsymbol{F}} = \tilde{c}\,\frac{\tilde{M} + |\tilde{M}|}{2} \begin{bmatrix} \rho \\ \rho u \\ \rho v \\ \rho w \\ \rho H \\ \rho Y_1 \\ \rho Y_2 \\ \vdots \\ \rho Y_{N_\mathrm{S}} \end{bmatrix}^{+} + \tilde{c}\,\frac{\tilde{M} - |\tilde{M}|}{2} \begin{bmatrix} \rho \\ \rho u \\ \rho v \\ \rho w \\ \rho H \\ \rho Y_1 \\ \rho Y_2 \\ \vdots \\ \rho Y_{N_\mathrm{S}} \end{bmatrix}^{-} + \tilde{p} \begin{bmatrix} 0 \\ n_x \\ n_y \\ n_z \\ 0 \\ 0 \\ 0 \\ \vdots \\ 0 \end{bmatrix} \tag{3.96}$$

Here, $\tilde{\cdot}$ denotes an interface quantity and the superscripts $\cdot^+$ and $\cdot^-$ denote a quantity left and right to the interface. When higher order interpolation methods are used, a left biased stencil is used to compute the state left to the interface and vice versa for the state to the right. Therefore, a definition of the interface speed of sound $\tilde{c}$ and the interface Mach number $\tilde{M}$ is needed to compute the convective flux. The vector components will be convected in upwind fashion with the resulting interface velocity $\tilde{c}\tilde{M}$. For example, if the interface Mach number is positive, the second term will cancel out, and the vector components to the left will be convected. There are several options to compute the interface speed of sound, like using the upwind value, the arithmetic average, the geometric average or a function based on the critical speed of sound [134]. All options are available in the CFD solver used in this work, whereby the arithmetic average has been used.

The interface Mach number on the other hand is split into a left and a right running wave contribution that are calculated via polynomials that exclusively depend on the non linear Eigenvalues $u \pm c$ (used here as $M \pm 1$):

$$\tilde{M} = \mathcal{M}^+ + \mathcal{M}^- \tag{3.97}$$

$$\mathcal{M}^\pm = \begin{cases} \frac{1}{2}\left(M^\pm \pm |M^\pm|\right) & \text{if} \quad |M^\pm| > 1, \\ \mathcal{M}^\pm_\beta & \text{else.} \end{cases} \tag{3.98}$$

$$\mathcal{M}^\pm_\beta = \pm\frac{1}{2}\left(M^\pm \pm 1\right)^2 \pm \beta(M^{\pm 2} - 1)^2, \quad -\frac{1}{16} \leq \beta \leq \frac{1}{2} \tag{3.99}$$

The equations feature the split Mach numbers $\mathcal{M}^+$ and $\mathcal{M}^-$, the Mach numbers left and right to the interface $M^\pm$ and the higher order model coefficient β, which has been set to $\beta = 1/8$ as suggested by Liou and Steffen [131].

Similar to the determination of the Mach number, the pressure is determined via the pressure splitting functions $\mathcal{P}^+$ and $\mathcal{P}^-$:

$$\tilde{p} = \mathcal{P}^+(M^+)p^+ + \mathcal{P}^-(M^-)p^- \tag{3.100}$$

$$\mathcal{P}^\pm = \begin{cases} \frac{1}{2}\left(1 + \operatorname{sgn}(\pm M^\pm)\right) & \text{if} \quad |M^\pm| > 1, \\ \mathcal{P}^\pm_\alpha & \text{else.} \end{cases} \tag{3.101}$$

$$\mathcal{P}^\pm_\alpha = \frac{1}{4}(2 \mp M^\pm)(M^\pm \pm 1)^2 \pm \alpha M^\pm (M^{\pm 2} - 1)^2, \quad -\frac{3}{4} \leq \alpha \leq \frac{3}{16} \tag{3.102}$$

The higher order pressure coefficient is set to a value of $\alpha = 3/16$ according to the original authors recommendation of AUSM+. Naturally, the sum of the contributions equals unity, irrespective of the Mach numbers. It can also be seen from the equations that the method switches to pure upwinding as soon as the flow becomes supersonic.

In general, AUSM+ is a very well suited method when it comes to simulating transonic and supersonic flows. However, like many other upwind methods, AUSM+ suffers from excessive numerical dissipation at low Mach numbers, which can be problematic, for example, when simulating turbulent flows where energy is also contained in small scale vortices and is dissipated prematurely [135]. In fact, many shock capturing schemes prevent the accumulation of kinetic energy at the grid level, which raises the question of whether a subgrid scale model should be used at all. This disadvantage was also addressed by Liou, the leading author of AUSM and AUSM+, and a so-called low speed alternative AUSM+-up [136] was developed with the aim of better performance for low Mach number flows. However, this algorithm is not parameter-free, and settings would need to be adjusted on a case-by-case basis.

3.2.5.2 SLAU2

The simple low dissipation AUSM family (SLAU) scheme by Shima and Kitamura [137] and its successor SLAU2 [138] are, like AUSM+-up, all speed schemes. Unlike, the all speed version of AUSM however, this family of schemes does not use any case dependent parameters. In SLAU2, the inviscid flux is split into a convective flux and a pressure flux. Yet an interface mass flux $\tilde{m}$ is used now instead of an interface speed of sound and an interface Mach number:

$$\tilde{\boldsymbol{F}} = \frac{\tilde{m} + |\tilde{m}|}{2} \begin{bmatrix} 1 \\ u \\ v \\ w \\ H \\ Y_1 \\ Y_2 \\ \vdots \\ Y_{N_\mathrm{S}} \end{bmatrix}^+ + \frac{\tilde{m} - |\tilde{m}|}{2} \begin{bmatrix} 1 \\ u \\ v \\ w \\ H \\ Y_1 \\ Y_2 \\ \vdots \\ Y_{N_\mathrm{S}} \end{bmatrix}^- + \tilde{p} \begin{bmatrix} 0 \\ n_x \\ n_y \\ n_z \\ 0 \\ 0 \\ 0 \\ \vdots \\ 0 \end{bmatrix} \tag{3.103}$$

The pressure splitting approach is also adopted from AUSM+, but rearranged in a formulation with three different terms, each serving a specific purpose:

$$\begin{aligned} \tilde{p} &= \mathcal{P}^+ \, p^+ + \mathcal{P}^- \, p^- \\ &= \underbrace{\frac{p^+ + p^-}{2}}_{\text{Central Difference}} + \underbrace{\frac{\mathcal{P}^+ - \mathcal{P}^-}{2}(p^+ - p^-)}_{\text{High Speed Damping}} + \underbrace{(\mathcal{P}^+ + \mathcal{P}^- - 1)\frac{p^+ + p^-}{2}}_{\text{Numerical Damping}} \end{aligned} \tag{3.104}$$

Thus, the AUSM pressure function consists of a central difference term, a damping term that is important only when the pressure split functions $\mathcal{P}^+$ and $\mathcal{P}^-$ differ greatly, and a numerical dissipation term. According to the authors, neglecting the third term is not an option, as instabilities will arise. Instead, in order to decrease numerical damping at low speeds, the third term is scaled with a velocity dependent function. The SLAU2 pressure function then reads:

$$\begin{aligned} \tilde{p} = &\frac{p^+ + p^-}{2} + \frac{\mathcal{P}^+ - \mathcal{P}^-}{2}(p^+ - p^-) \\ &+ \frac{1}{\tilde{c}} \sqrt{\frac{u^{+2} + u^{-2} + v^{+2} + v^{-2} + w^{+2} + w^{-2}}{2}} (\mathcal{P}^+ + \mathcal{P}^- - 1)\frac{p^+ + p^-}{2} \end{aligned} \tag{3.105}$$

The interface mass flux is identical among all SLAU schemes and is based on the Roe mass flux in terms of the primitive variables ρ, V_n, and p, where V_n is the face normal velocity component. A Roe flux is essentially the sum of a central flux and several dissipation fluxes resulting from the Roe matrix multiplication with the difference vector of the dependent variables ($\Delta\rho$, $\Delta V_\mathrm{n}, \Delta p$). Accordingly, this would be the central mass flux, the density difference term, the velocity difference term and the pressure difference term. As stated by the authors of SLAU2, not every difference term is necessary for a mass flux function. The pressure difference term, for example, may cause the Carbuncle phenomenon at high Mach numbers. In the process, disturbances are amplified in the shock tangential direction and cause the structure of stable and planar shock waves to break up. Therefore, the pressure difference term is only active at low Mach numbers, while the velocity difference term is omitted altogether. These considerations result in the following interface mass flux:

$$\tilde{m} = \left[\underbrace{\frac{(\rho V_\mathrm{n})^+ + (\rho V_\mathrm{n})^-}{2}}_{\text{Central Flux}} - \underbrace{\frac{|\bar{V}_\mathrm{n}|}{2}\Delta\rho}_{\text{Density Difference}} \right](1-g) \quad - \quad \underbrace{\chi \frac{1}{2\bar{c}}\Delta p}_{\text{Pressure Difference}} \tag{3.106}$$

$$V_\mathrm{n} = u\, n_x + v\, n_y + w\, n_z \tag{3.107}$$

$$|\bar{V}_\mathrm{n}| = \frac{\rho^+ |V_\mathrm{n}|^+ + \rho^- |V_\mathrm{n}|^-}{\rho^+ + \rho^-} \tag{3.108}$$

$$g = g^+ g^-, \quad g^+ = -\max[\min(M^+, 0), -1], \quad g^- = \min[\max(M^-, 0), 1] \tag{3.109}$$

$$\chi = (1 - \hat{M})^2 \tag{3.110}$$

$$\hat{M}^2 = \min\left(1, \frac{1}{\bar{c}} \sqrt{\frac{u^{+2} + u^{-2} + v^{+2} + v^{-2} + w^{+2} + w^{-2}}{2}}\right) \tag{3.111}$$

Here, χ is the function to disable the pressure difference term at high Mach numbers. The function g meanwhile, is purely added for the special case of a supersonic expansion, to correct the mass flux under those conditions. But in most situations, $(1 - g)$ will be close to unity and have no effect.

There is also a high resolution modification of SLAU2 in which the third term of the pressure expression is multiplied by a so-called high resolution factor γ_HR, denoted as HR-SLAU2 [139]:

$$\begin{aligned} \tilde{p} = {} & \frac{p^+ + p^-}{2} + \frac{\mathcal{P}^+ - \mathcal{P}^-}{2}(p^+ - p^-) \\ & + \gamma_\mathrm{HR} \frac{1}{\tilde{c}} \sqrt{\frac{u^{+2} + u^{-2} + v^{+2} + v^{-2} + w^{+2} + w^{-2}}{2}} (\mathcal{P}^+ + \mathcal{P}^- - 1) \frac{p^+ + p^-}{2} \end{aligned} \tag{3.112}$$

For this purpose, the numerical dissipation term will be disabled as soon as the field is sufficiently smooth, which means that no oscillations (wiggles) are present. The pressure field is generally used as the test field and the high resolution factor can be calculated via a specified minimum value (*e.g.*, $\gamma_\mathrm{min} = 0.2$) and a wiggle detector value γ_w:

$$\gamma_\mathrm{HR} = \max(\gamma_\mathrm{min}, \gamma_\mathrm{w}) \tag{3.113}$$

$$\gamma_\mathrm{w} = \frac{1 - \tanh\left[5\pi \min(p_1, p_2)\right]}{2} \tag{3.114}$$

$$p_1 = (p_{i+1} - p_i)\,(p_i - p_{i-1}) \tag{3.115}$$

$$p_2 = (p_{i+1} - p_i)\,(p_{i+2} - p_{i+1}) \tag{3.116}$$

As is evident from Eq. 3.114, if either p_1 or p_2 are negative due to different signs of the adjacent differences, this will translate to unity wiggle detector values and as a result, the numerical dissipation term will be identical to that of SLAU2. In smooth regions on the other hand, the high resolution factor will approach the minimum value γ_min.

3.2.5.3 Characteristic Variables

In order to compute all quantities left (+) and right (-) to the interface, a set of variables for interpolation must be chosen on the basis of which all the remaining quantities are calculated. Possible variables are, for example, the primitive variables $\boldsymbol{V}$ or the conservative variables $\boldsymbol{U}$:

$$\boldsymbol{V} = \begin{bmatrix} \rho \\ u \\ v \\ w \\ p \\ Y_1 \\ Y_2 \\ \vdots \\ Y_{N_\mathrm{S}} \end{bmatrix} \qquad \boldsymbol{U} = \begin{bmatrix} \rho \\ \rho u \\ \rho v \\ \rho w \\ \rho E \\ \rho Y_1 \\ \rho Y_2 \\ \vdots \\ \rho Y_{N_\mathrm{S}} \end{bmatrix}$$

It is important to note that the variables are not independent from each other. It is thus questionable to interpolate the variables independently and neglecting interaction among them. In fact, using primitive or conservative variables will result in over/under shoots near discontinuities as a result [140]. A solution is the characteristic formulation of the Euler equations. First of all, the starting point are the Euler equations in primitive notation and quasi-linear formulation using the flux Jacobian $\boldsymbol{A}$ for a one-dimensional system [141]:

$$\frac{\partial}{\partial t}\begin{bmatrix} \rho \\ u \\ p \end{bmatrix} + \boldsymbol{A}\frac{\partial}{\partial x}\begin{bmatrix} \rho \\ u \\ p \end{bmatrix} = 0, \quad \boldsymbol{A} = \begin{bmatrix} u & \rho & 0 \\ 0 & u & 1/\rho \\ 0 & \rho & c^2 u \end{bmatrix} \tag{3.117}$$

Because all the Eigenvalues of the flux Jacobian are real (hyperbolic system of PDE's), the matrix can be converted to the diagonal matrix $\boldsymbol{\Lambda}$ with the matrix of the left $\boldsymbol{L}$ and right Eigenvectors $\boldsymbol{R}$:

$$\boldsymbol{A} = \boldsymbol{R}\,\boldsymbol{\Lambda}\,\boldsymbol{L}, \tag{3.118}$$

$$\boldsymbol{R} = \begin{bmatrix} 1 & 1 & 1 \\ -\frac{c}{\rho} & 0 & \frac{c}{\rho} \\ c^2 & 0 & c^2 \end{bmatrix}, \quad \boldsymbol{\Lambda} = \begin{bmatrix} u-c & 0 & 0 \\ 0 & u & 0 \\ 0 & 0 & u+c \end{bmatrix}, \quad \boldsymbol{L} = \begin{bmatrix} 0 & 1 & 0 \\ -\frac{\rho}{2c} & 0 & \frac{\rho}{2c} \\ \frac{1}{2c^2} & -\frac{1}{c^2} & \frac{1}{2c^2} \end{bmatrix} \tag{3.119}$$

The Euler equations can now be written as:

$$\frac{\partial}{\partial t}\begin{bmatrix} \rho \\ u \\ p \end{bmatrix} + \boldsymbol{R}\,\boldsymbol{\Lambda}\,\boldsymbol{L}\frac{\partial}{\partial x}\begin{bmatrix} \rho \\ u \\ p \end{bmatrix} = 0 \tag{3.120}$$

$$\Leftrightarrow \quad \frac{\partial}{\partial t}\boldsymbol{W} + \boldsymbol{\Lambda}\,\frac{\partial}{\partial x}\boldsymbol{W} = 0, \quad d\boldsymbol{W} = \boldsymbol{L}\,d\begin{bmatrix} \rho \\ u \\ p \end{bmatrix} \tag{3.121}$$

Most importantly, the new system of equations is decoupled, where the components of $\boldsymbol{W}$ are convected like a scalar at the respective characteristic speed. The variables are thus denoted characteristic variables, whereby interpolation of characteristic variables is known to suppress oscillations [140]. In practice, the coefficients of the matrices $\boldsymbol{L}$ and $\boldsymbol{R}$ must be frozen locally [122]. Thus, an interpolation stencil with 5 points would use a single left Eigenvector matrix to determine the characteristic variables in all 5 points. In this work, the coefficients of the left Eigenvector matrix are calculated from the values in the adjacent cells left or right to the interface. The characteristic decomposition can also be carried out for the Euler equations with conservative variables. The left and right Eigenvector matrices are presented by Suresh and Huynh [122] and read:

$$\boldsymbol{R}_{\mathrm{c}} = \begin{bmatrix} 1 & 1 & 1 \\ u-c & u & u+c \\ H-uc & \frac{1}{2}u^2 & H+uc \end{bmatrix}, \quad \boldsymbol{L}_{\mathrm{c}} = \begin{bmatrix} \frac{b_2}{2}+\frac{u}{2c} & -\frac{b_1 u}{2}-\frac{1}{2c} & \frac{b_1}{2} \\ 1-b_2 & b_1 u & -b_1 \\ \frac{b_2}{2}-\frac{u}{2c} & -\frac{b_1 u}{2}+\frac{1}{2c} & \frac{b_1}{2} \end{bmatrix} \tag{3.122}$$

$$b_1 = \frac{\gamma-1}{c^2}, \quad b_2 = \frac{u^2 b_1}{2} \tag{3.123}$$

After interpolation, the characteristic variables must be transformed into either primitive or conservative variables via:

$$\begin{bmatrix} \rho \\ u \\ p \end{bmatrix} = \boldsymbol{R}\,\boldsymbol{W} \quad \vee \quad \begin{bmatrix} \rho \\ \rho u \\ \rho E \end{bmatrix} = \boldsymbol{R}_{\mathrm{c}}\,\boldsymbol{W}_{\mathrm{c}} \tag{3.124}$$

For the application in three spatial dimensions, 5x5 matrices could also be constructed [142], a step that further increases the already high computational costs. However, it has been shown that it is sufficient to perform the characteristic decomposition only for a local one-dimensional system using the corresponding normal velocity component. The tangential velocity components and scalars are then interpolated using standard interpolation formulae.

Another problem that has been observed in scope of this work, is the appearance of numerical noise in stagnant regions, when SLAU2 is used with characteristic variable decomposition. Supposedly, numerical noise is introduced as consequence of variable transformations, whereby SLAU2 fails at damping the noise, if the magnitude of velocity takes very small values. Using AUSM+ instead, prevents the occurrence of the observed numerical noise, indicating that the low Mach corrections of SLAU2 are responsible. Therefore both primitive (or conservative) and the corresponding characteristic variables are interpolated. The final value is calculated as a blend between the interpolated values using the blending function from SLAU2. This approach is even more costly, but has proven to be very stable, while providing oscillation free and accurate results. However, if the simulation of shock waves or detonation waves is not of major interest, the author of this work strongly suggests to use the primitive variables instead of characteristic variables.

Lastly, it must be addressed that the use of large stencils and characteristic decomposition can lead to nonphysical states in isolated cases. Therefore, recursive order reduction (ROR) is used in this work [143]. Thereby it is checked whether the interpolated pressure or the interpolated density take a negative value. If this is the case, successive methods with lower accuracy and smaller stencils are used. As soon as an interpolation procedure yields a physical result, the algorithm is stopped. In this work, the following interpolation schemes were used in the appropriate order for ROR: MP5 (1), MP (2), WENO5 (3), MUSCL (4), TVD (5), and UDS (6). A log file is written during each simulation to access the number of required order reductions.

3.2.5.4 Thornber Correction

In order to decrease numerical damping of approximate Riemann solvers at low Mach numbers, a simple correction has been introduced by Thornber et al. [144]. The authors state that most of the numerical damping stems from the velocity jump at the interface, whereby the jump is purely mathematical in smooth regions and can thus be decreased:

$$\boldsymbol{u}^{+} = \frac{\boldsymbol{u}^{+}+\boldsymbol{u}^{-}}{2} + z\frac{\boldsymbol{u}^{+}-\boldsymbol{u}^{-}}{2} \tag{3.125}$$

$$\boldsymbol{u}^{-} = \frac{\boldsymbol{u}^{+}+\boldsymbol{u}^{-}}{2} + z\frac{\boldsymbol{u}^{-}-\boldsymbol{u}^{+}}{2} \tag{3.126}$$

$$z = \min(M_{\mathrm{local}}, 1), \quad M_{\mathrm{local}} = \max(M^{-}, M^{+}) \tag{3.127}$$

Here, $\boldsymbol{u}$ is the velocity vector and z is the blending function. The authors reported of highly improved performance in three dimensional simulations of decaying turbulence and scalar mixing.

3.2.5.5 High Order Schemes

It should be emphasized that the combination of high order spatial schemes and the midpoint rule for the approximation of surface integrals, is not necessarily recommended. The reason is that the global spatial accuracy will be limited to second order accuracy due to the the midpoint rule, irrespective of the spatial interpolation method [88]. However, the application of high order spatial schemes is reasonable when a Riemann type solver is used. This is because any jump in the states at an interface results in numerical dissipation being applied to the fields. In smooth regions, this state difference becomes smaller with refined grids, provided the solution is smooth. The rate at which the difference decreases is naturally higher for higher order spatial schemes, significantly improving the solution quality at a given grid resolution.

3.3 Boundary Conditions

The numerical solution of coupled partial differential equations requires, in addition to the discussed integration and spatial discretization methods, an initial condition and suitable boundary conditions, which can have a significant impact on the computed solution. The boundary conditions in this work are all realized using the concept of ghost cells. Here, the numerical domain covers the physical domain and an additional adjacent boundary region that is comprised of a certain number of ghost cell layers. The amount of layers needed is governed by the maximum stencil size of all discretization methods used. For instance, the 5-point stencil of MP5 requires 3 layers of ghost cells, with 3 points covered by ghost cells and 2 points covered by interior cells at an inlet.

Boundary conditions can usually be divided into 2 classes: (1) Dirichlet boundary conditions with fixed values for the boundary values and (2) von Neumann boundary conditions where the boundary values result from prescribed gradients. Suitable examples would be, an atmospheric pressure prescribed at the outlet, or zero gradient boundary conditions where the solution on the boundary always matches that of the inner solution, *e.g.* for the temperature field in terms of an adiabatic wall. The use of a partitioned domain, which allows parallel computation of the problem on multiple CPU cores, creates inner boundaries between the local domains of different computational regions in addition to the physical boundaries. Ghost cells are also used here, where the values correspond to those of the adjacent inner cells of the neighboring computational domain through *message passing interface* (MPI) communication. Details regarding the standard boundary conditions available in *PsiPhi* and communication can be found in the work of Proch [110].

3.3.1 NSCBC

For the simulation of compressible flows, additional requirements are imposed concerning boundary conditions. A fixed value of pressure at the outlet of the numerical domain will inevitably reflect any acoustic wave to some extent. This circumstance can be problematic if, for instance, the reflected waves interact with a flame or the flow in inlet ducts, and has encouraged the development of non-reflective boundary conditions.

The *Navier Stokes characteristic boundary conditions* (NSCBC) proposed by Poinsot and Lele [145] have been intended to provide a framework for the development of boundary conditions that are suitable for compressible LES and rely on the concept of characteristic waves. The approach can be used to derive non-reflective inlet and outlet boundary conditions, as well as reflective boundary conditions for viscous walls and many other. The cornerstones of the approach include well-posedness of the boundary conditions according to the analysis of Oliger and Sundström [146] and Dutt [147] as well as a general abandonment of extrapolation of individual quantities (*e.g.* zero gradient boundary condition). Instead, the Navier Stokes equations are solved on the boundary with the boundary normal gradients (only those of the Euler equations) being replaced by characteristic expressions. The following set of equations is valid for boundaries normal to x-direction [9, 145]:

$$\frac{\partial \rho}{\partial t} + d_1 + \frac{\partial \rho v}{\partial y} + \frac{\partial \rho w}{\partial z} = 0 \tag{3.128}$$

$$\frac{\partial \rho u}{\partial t} + u d_1 + \rho d_3 + \frac{\partial \rho u v}{\partial y} + \frac{\partial \rho u w}{\partial z} = \frac{\partial \tau_{1j}}{\partial j} \tag{3.129}$$

$$\frac{\partial \rho v}{\partial t} + v d_1 + \rho d_4 + \frac{\partial \rho v v}{\partial y} + \frac{\partial \rho v w}{\partial z} + \frac{\partial p}{\partial y} = \frac{\partial \tau_{2j}}{\partial j} \tag{3.130}$$

$$\frac{\partial \rho w}{\partial t} + w d_1 + \rho d_5 + \frac{\partial \rho w v}{\partial y} + \frac{\partial \rho w w}{\partial z} + \frac{\partial p}{\partial z} = \frac{\partial \tau_{3j}}{\partial j} \tag{3.131}$$

$$\begin{aligned} &\frac{\partial \rho E_{\mathrm{s}}}{\partial t} + k d_1 + \frac{d_2}{\gamma - 1} + \rho u d_3 + \rho v d_4 + \rho w d_5 + ... \\ &\qquad + \frac{\partial \rho H_{\mathrm{s}} v}{\partial y} + \frac{\partial \rho H_{\mathrm{s}} w}{\partial z} = -\frac{\partial q_i}{\partial x_i} + \frac{\partial \tau_{ji} u_j}{\partial x_i} + \dot{\omega}_T \end{aligned} \tag{3.132}$$

$$\frac{\partial \rho Y_\alpha}{\partial t} + Y_\alpha d_1 + \rho d_{5+\alpha} + \frac{\partial \rho Y_\alpha v}{\partial y} + \frac{\partial \rho Y_\alpha w}{\partial z} = \frac{\partial j_{\alpha,i}}{\partial i} + \dot{\omega}_\alpha \tag{3.133}$$

It is important to note that the presented energy equation considers only the sensible and kinetic contribution. Therefore, a heat release term appears on the RHS of Eq. 3.132. This energy formulation is thus inconsistent with the one used in this work, where the formation enthalpy is transported alongside the sensible and kinetic energy. An expression for the space derivative of the mixture averaged formation enthalpy must be added in Eq.,3.132 accordingly, while removing the heat release rate $\dot{\omega}_T$:

$$\frac{\partial \rho h_{\mathrm{f}}^0 u}{\partial x} = h_{\mathrm{f}}^0 d_1 + \rho \sum_{\alpha=1}^{N_{\mathrm{S}}} \Delta h_{\mathrm{f},\alpha}^0 d_{5+\alpha} \tag{3.134}$$

However, this energy equation is strictly valid only for the FRC combustion model and would fail for other combustion models such as *flamelet generated manifolds* (FGM) or the *flame surface density* (FSD) model. Instead, formation enthalpy is removed from the conserved energy prior to time integration. Once time integration is finished, formation enthalpy is added based on the updated scalars on the boundary.

Equations 3.128 - 3.133 further feature the kinetic energy k and characteristic terms d_i to replace normal gradients and which are provided by the analysis of Thompson [148] and presented by Poinsot and Veynante [9]:

$$\boldsymbol{d} = \begin{bmatrix} d_1 \\ d_2 \\ d_3 \\ d_4 \\ d_5 \\ d_{5+\alpha} \end{bmatrix} = \begin{bmatrix} \frac{1}{c^2}\left[\mathcal{L}_2 + \frac{1}{2}(\mathcal{L}_5 + \mathcal{L}_1)\right] \\ \frac{1}{2}(\mathcal{L}_5 + \mathcal{L}_1) \\ \frac{1}{2\rho c}(\mathcal{L}_5 - \mathcal{L}_1) \\ \mathcal{L}_3 \\ \mathcal{L}_4 \\ \mathcal{L}_{5+\alpha} \end{bmatrix} = \begin{bmatrix} \frac{\partial \rho u}{\partial x} \\ \rho c^2 \frac{\partial u}{\partial x} + u \frac{\partial p}{\partial x} \\ u \frac{\partial u}{\partial x} + \frac{1}{\rho} \frac{\partial p}{\partial x} \\ u \frac{\partial v}{\partial x} \\ u \frac{\partial w}{\partial x} \\ u \frac{\partial Y_\alpha}{\partial x} \end{bmatrix} \tag{3.135}$$

The equations include the amplitudes $\mathcal{L}_i$ of characteristic waves, which can be retrieved from the characteristic decomposition in Sec. 3.2.5.3:

$$\mathcal{L}_1 = \lambda_1\left(\frac{\partial p}{\partial x} - \rho c\frac{\partial u}{\partial x}\right) \tag{3.136}$$

$$\mathcal{L}_2 = \lambda_2\left(c^2\frac{\partial \rho}{\partial x} - \frac{\partial p}{\partial x}\right) \tag{3.137}$$

$$\mathcal{L}_3 = \lambda_3\frac{\partial v}{\partial x} \tag{3.138}$$

$$\mathcal{L}_4 = \lambda_4\frac{\partial w}{\partial x} \tag{3.139}$$

$$\mathcal{L}_5 = \lambda_5\left(\frac{\partial p}{\partial x} + \rho c\frac{\partial u}{\partial x}\right) \tag{3.140}$$

$$\mathcal{L}_{5+\alpha} = \lambda_{5+\alpha}\frac{\partial Y_{5+\alpha}}{\partial x} \tag{3.141}$$

Here, λ_i are the characteristic speeds $\lambda_1 = u - c,\ \lambda_2 = \lambda_3 = \lambda_4 = \lambda_{5+\alpha} = u,\ \lambda_5 = u + c.$

Characteristic amplitudes of outgoing waves can be calculated directly from interior points, while those of ingoing waves are unknown. Determining unknown amplitudes is the last piece of the puzzle and is achieved in the NSCBC strategy by analyzing the *local one dimensional inviscid* LODI relations:

$$\frac{\partial \rho}{\partial t} + \frac{1}{c^2}\left[\mathcal{L}_2 + \frac{1}{2}(\mathcal{L}_5 + \mathcal{L}_1)\right] = 0 \tag{3.142}$$

$$\frac{\partial u}{\partial t} + \frac{1}{2\rho c}(\mathcal{L}_5 - \mathcal{L}_1) = 0 \tag{3.143}$$

$$\frac{\partial v}{\partial t} + \mathcal{L}_3 = 0 \tag{3.144}$$

$$\frac{\partial w}{\partial t} + \mathcal{L}_4 = 0 \tag{3.145}$$

$$\frac{\partial p}{\partial t} + \frac{1}{2}(\mathcal{L}_5 + \mathcal{L}_1) = 0 \tag{3.146}$$

$$\frac{\partial Y_\alpha}{\partial t} + \mathcal{L}_{5+\alpha} = 0 \tag{3.147}$$

$$\frac{\partial T}{\partial t} + \frac{T}{\rho c^2}\left[-\mathcal{L}_2 + \frac{1}{2}(\gamma - 1)(\mathcal{L}_5 + \mathcal{L}_1)\right] = 0 \tag{3.148}$$

For the case of a subsonic inlet boundary condition at the western side of the computational domain with fixed velocities, fixed temperature, and fixed composition, the time derivatives in the respective LODI relations vanish. It is now evident from Eq. 3.143 that $\mathcal{L}_5 = \mathcal{L}_1$. Because $\mathcal{L}_1$ is an outgoing wave and can be calculated from interior points, the LODI relation allows to estimate $\mathcal{L}_5$. Using the LODI relation for the temperature time derivative, $\mathcal{L}_2$ can be calculated as a function of $\mathcal{L}_1$ and $\mathcal{L}_5$. The remaining amplitudes are all zero, if the time derivative is zero, which allows to compute all derivative terms d_i and to advance the solution on the boundary in time.

If a non-reflective boundary is desired to be used at the right outlet, all amplitudes can be calculated except $\mathcal{L}_1$, which is set to zero for a perfectly non-reflective boundary. In that case, as noted by Poinsot and Lele [145], the boundary condition is no longer well-posed. Since no information enters the domain by ingoing waves, an increasing divergence of the boundary pressure from the ambient reference pressure can be the result. A better boundary condition in this case is a partially reflecting outlet boundary condition, where the ingoing wave $\mathcal{L}_1$ must be functionally correlated to the ambient pressure. This makes sense from a physical point of view, because any local pressure deviation on the outlet boundary, will result in ingoing waves that compensate for the pressure difference. A natural choice is thus to relate the amplitude of the ingoing wave to the pressure difference and a proportionality coefficient K:

$$\mathcal{L}_1 = K\,(p - p_\infty) \tag{3.149}$$

$$K = \sigma(1 - M_{\max}^2)\frac{c}{L} \tag{3.150}$$

Here, $M_{\max}$ is the maximum Mach number, L is a characteristic length scale and chosen to equal the length of the domain, whereby σ is a constant to control the relaxation toward the fixed reference pressure p_∞. According to Selle et al. [149], a suitable range for σ is $0.1 \leq \sigma \leq \pi$.

Chapter 4
Shock Tubes

Shock tubes are an essential measuring device to establish important characteristics of various fuels. A shock tube is a pipe made up of two chambers that are initially separated by a diaphragm. The low-pressure chamber (driven section) usually contains a combustible mixture, while the high-pressure chamber (driver section) contains an inert gas. At the beginning of the experiment, the pressure in the high pressure chamber is gradually increased until the diaphragm bursts. In the following, a compression shock develops and propagates into the gas of the low-pressure chamber. Simultaneously, an expansion fan establishes towards the high-pressure chamber, which expands the initially quiescent high-pressure gas to an intermediate pressure corresponding to the pressure behind the compression shock. Eventually, the incident shock will reflect at the end wall of the driven section of the shock tube and elevate both, pressure and temperature at the end wall, and thus initiate the ignition of the combustible mixture.

In this work, the following notation is used for the five different gas states in the shock tube. It is common to indicate the initial state in the driver section with subscript “4” and subscript “1” for the driven section respectively. The region of compressed driven gas behind the incident shock is denoted by subscript “2”, where the following relationship applies: $p_1 < p_2 < p_4$. The region of the expanded driver gas is indicated by subscript “3”, where the pressure equals that of region 2: $p_2 = p_3$. The expanded material in region 3 has a lower temperature, whereas the compressed material has a higher temperature compared to the initial state: $T_3 < T_4 = T_1 < T_2$. Therefore, regions 2 and 3 are separated by a contact discontinuity due to significantly different thermodynamic states. Nevertheless, particles in region 2 and 3 have the same velocity: $u_2 = u_3$. The region behind the reflected shock is specified by subscript “5”.

Velocities will be written in capital letters when the definition refers to a reference frame moving at wave speed, or in lowercase letters, for definitions in laboratory coordinates. For example, the gas in region 1 is at rest and thus, has no velocity in laboratory coordinates, but the Mach number of the incident shock M_s can be written in terms of a velocity U_1 in a reference frame moving with the incident shock speed u_s:

$$u_1 = 0 \tag{4.1}$$

$$M_\mathrm{s} = \frac{U_1}{c_1} = \frac{u_\mathrm{s}}{c_1} \tag{4.2}$$

4.1 Ideal Shock Tube Relations

Under ideal conditions, assuming an inviscid and adiabatic flow and a calorically perfect fluid, essential objectives can be determined on the basis of the initial parameters. These initial parameters are: the temperatures T_1 and T_4, the pressures p_1 and p_4, the ratios of specific heats γ_1 and γ_4, and the molecular weights W_1 and W_4 of the test and driver gas. Usually, the initial temperatures are equal to the ambient temperature, leaving only the pressure ratio to vary the experiment, once the driver and test gas have been chosen. Many of the relations discussed in the following can be found in the work of Mark [150] and Glass et al. [151].

The one-dimensional conservation equations can be formulated in a reference frame moving with the incident shock, as outlined in Sec. 2.2.1.1. The state quantities behind the incident shock may then be specified with the jump conditions for a calorically perfect gas as a function of the initial states and the incident shock Mach number M_s:

$$M_2 = \sqrt{\frac{(\gamma-1)M_\mathrm{s}^2+2}{2\gamma M_\mathrm{s}^2-(\gamma-1)}} \tag{4.3}$$

$$p_2 = p_1\frac{2\gamma M_\mathrm{s}^2-(\gamma-1)}{\gamma+1} \tag{4.4}$$

$$\rho_2 = \rho_1\frac{(\gamma+1)M_\mathrm{s}^2}{(\gamma-1)M_\mathrm{s}^2+2} \tag{4.5}$$

$$T_2 = T_1\frac{2\gamma M_\mathrm{s}^2-(\gamma-1)}{(\gamma+1)^2M_\mathrm{s}^2}\frac{(\gamma-1)M_\mathrm{s}^2+2}{(\gamma+1)^2M_\mathrm{s}^2} \tag{4.6}$$

This leaves the incident Mach number M_1 as the remaining unknown to compute the post shock state. Since isentropic relations can be used to describe the change of state across the expansion fan (region 4 to region 3) and because the pressure of compressed and expanded fluid is identical ($p_2 = p_3$), an expression for the pressure ratio p_4/p_1 can be derived as a function of the incident Mach number:

$$\frac{p_4}{p_1} = \left(\frac{2\gamma_1}{\gamma_1+1}M_\mathrm{s}^2 - \frac{\gamma_1-1}{\gamma_1+1}\right)\left[1-\frac{\gamma_4-1}{\gamma_4+1}\,\frac{c_1}{c_4}\,\left(M_\mathrm{s}-\frac{1}{M_\mathrm{s}}\right)\right]^{\frac{-2\gamma_4}{\gamma_4-1}} \tag{4.7}$$

Although there is no analytical solution for M_s, an approximate solution can be calculated using root finding algorithms. Special care must be taken to start with a suitable guess, otherwise the root finding algorithms often fail to find a solution for Eq. 4.7. It emerges from Eq. 4.7 that the incident shock Mach number depends not only on the initial pressure ratio p_4/p_1, but also on the ratio of speed of sounds c_1/c_4. Therefore, in order to achieve high incident Mach numbers, it is crucial to use a driver gas with a small molecular weight (which translates to high speed of sounds c_4), as demonstrated by Mark [150].

Once the incident shock reaches the end wall of the shock tube, the fluid directly following the shock is brought to rest in an instance. Mass will accumulate at the end wall and pressure will increase, resulting in a reflected shock that moves away from the end wall with the velocity u_rs into the previously accelerated fluid in region 2. The pressure behind the reflected shock balances the reflected shock velocity, such that the fluid passing through the reflected shock is subsequently at rest. Any variation in the velocity of the reflected shock results in either compression or expansion of the accumulated fluid, and thus, in a strengthening or weakening of the reflected shock. The Mach number of the reflected shock is then given as:

$$M_\mathrm{rs} = \frac{u_\mathrm{rs}+u_2}{c_2} \tag{4.8}$$

Both velocities u_2 and u_rs are unknown yet. The particle velocity u_2 in laboratory coordinates can be expressed as the difference of the incident shock speed u_s and the particle velocity U_2 in the shock reference frame, which can be calculated using Eq. 4.3 [150]:

$$U_2 = u_\mathrm{s} - u_2 \tag{4.9}$$

$$M_2 = \frac{u_\mathrm{s}-u_2}{c_2} = M_\mathrm{s}\frac{c_1}{c_2} - \frac{u_2}{c_2} \tag{4.10}$$

Equations 4.6 and 4.10 can be combined to obtain:

$$u_2 = c_1\,\frac{2\left(M_\mathrm{s}^2-1\right)}{(\gamma+1)M_\mathrm{s}} \tag{4.11}$$

Unlike the incident shock, the reflected shock does not travel into gas at rest but rather it travels with velocity u_{rs} into a gas with the velocity u_2, whereby the gas velocity behind the reflected shock u_5 is zero in laboratory coordinates. However, the coordinate system can be transformed into a system in which the reflected shock travels into quiescent gas by shifting all velocities by u_2. In this coordinate system, the flow velocity behind the reflected shock is $U_5 = u_2$ and can be calculated via Eq. 4.11, using appropriate values for the speed of sound and Mach number:

$$U_5 = c_2 \frac{2\left(M_{\mathrm{rs}}^2 - 1\right)}{(\gamma+1)M_{\mathrm{rs}}} = c_1 \frac{2\left(M_{\mathrm{s}}^2 - 1\right)}{(\gamma+1)M_{\mathrm{s}}} = u_2 \tag{4.12}$$

The equation thus relates the Mach numbers of both incident shock and reflected shock and allows to calculate the reflected shock Mach number [150]:

$$M_{\mathrm{rs}} = \sqrt{\frac{2\gamma M_{\mathrm{s}}^2 - (\gamma-1)}{(\gamma-1)M_{\mathrm{s}}^2 + 2}} \tag{4.13}$$

$$M_{\mathrm{rs}} = \frac{1}{M_2} \tag{4.14}$$

The RHS of Eq. 4.13 is the inverse of Eq. 4.3, which then allows to compute the reflected shock Mach number using the simple relation in Eq. 4.14. Once the Mach number of the reflected shock is known, the main quantities of interest p_5 and T_5 can be determined by jump conditions, whereby p_5 and T_5 specify the conditions supporting the ignition.

In the shock tube simulations that are part of this work, the state variables of the individual regions are required. First, to determine the time steps that characterize reflection and ignition to log these events, and second, to solve the boundary layer equations. Argon or helium, which are calorically perfect gases, are frequently used in the driver section, while gas mixtures with temperature-dependent heat capacities are usually present in the test section. The equations presented so far can thus not be used unconditionally. Instead, a different approach is used to determine the incident shock speed. Crucial in that regard is the *Aitken* root finding algorithm [152], that is used to minimize the error of *Riemann invariants* [153] providing expressions for a constant along the characteristics $u \pm c$, if the flow is isentropic:

$$\frac{2c_4}{\gamma-1} + u_4 = \frac{2c_3}{\gamma-1} + u_3 \tag{4.15}$$

$$\text{Error} \leftarrow \frac{2c_4}{\gamma-1} + u_4 - \frac{2c_3}{\gamma-1} - u_3 \tag{4.16}$$

The error will approach zero if the incident shock speed approaches the exact value. The following algorithm has thus been used:

1. The mixture averaged states of region 1 and 4 are calculated using the composition and single species tabulated gas properties as function of temperature together with pressure.

2. Another Aitken root finding algorithm with temperature T_2 as the unknown, is used to find the post-shock state of a calorically imperfect fluid with frozen composition $\boldsymbol{Y}_2 = \boldsymbol{Y}_1$, where the error is defined as:

$$\text{Error} \leftarrow \frac{u_1^2}{2} - \frac{u_2^2}{2} + h_1(T_1, p_1, \boldsymbol{Y}_1) - h_2(T_2, p_2, \boldsymbol{Y}_2) \tag{4.17}$$

   Alternatively, a multi variable Newton-Raphson iteration can be used to solve the jump conditions for a calorically imperfect gas [25].

3. The state in region 3 can be determined using pressure $p_3 = p_2$, entropy $s_3 = s_4$ and composition $\boldsymbol{Y}_3 = \boldsymbol{Y}_4$. An iterative Newton-Raphson procedure is used to compute temperature using the known entropy of the mixture:

$$dT = \frac{T}{c_p} ds \tag{4.18}$$

$$ds = s(T, \boldsymbol{Y_3}) - s_3 \tag{4.19}$$

4. The thermochemical states of all regions have been calculated and the error of the *Riemann invariants* expression (4.16) can be derived. If a certain accuracy is met, the algorithm will stop and return a suitable approximation of the incident shock speed. Otherwise, the guess for the incident shock Mach number will be corrected and steps 1 - 4 will be repeated.

4.2 Boundary Layer Modeling

A major reason for the popularity of shock tubes is the simple design and the well-defined and nearly constant pressure and temperature behind the reflected shock. In particular, when the experimental duration is very short, the assumption of constant pressure and temperature holds. Still, if the experiment lasts longer (*i.e.* up to the point of ignition), smaller changes in pressure are measured, which equally implies changes in temperature. Even if these changes are minor, they can have a decisive influence on the ignition delay time, which is strongly non-linearly dependent on temperature. One of the most significant contributors to the observed pressure changes is the boundary layer, which develops behind the incident shock. As a result, once the shock is reflected, it propagates into an inhomogeneous flow, which is why the state behind the reflected shock changes in time. To estimate and capture these effects in simulations and experiments, a description of boundary layers behind shock waves is necessary.

For this analysis, it is important to notice that the laminar boundary layer will eventually transition into a turbulent boundary layer. This point of transition for boundary layers behind shock waves was studied experimentally by Hartunian et al. [154] and is defined in terms of a transition Reynolds number:

$$\mathrm{Re}_{\mathrm{tr}}\left(T_{\mathrm{w}}/T_{\mathrm{e}}\right) = \rho_{\mathrm{e}} \frac{\left(u_{\mathrm{s}} - u_{\mathrm{e}}\right)^2}{\mu_{\mathrm{e}}} \frac{u_{\mathrm{s}} t_{\mathrm{tr}}}{u_{\mathrm{e}}} \tag{4.20}$$

Here, the subscript “w” represents a gas phase quantity at the wall, while the subscript “e” represents a quantity in the external flow (outside the boundary layer), while t_{tr} is the time needed for the shocked boundary layer to transition. According to the experiments [154], $\mathrm{Re}_{\mathrm{tr}}$ is also a function of the temperature ratio $T_{\mathrm{w}}/T_{\mathrm{e}}$. At very high Mach numbers, hence high external temperatures and small values of $T_{\mathrm{w}}/T_{\mathrm{e}}$, respectively, the flow is stabilized and transition is shifted towards larger Reynolds numbers. Two different power fits to the experimental data have been tested in this work to estimate the transition Reynolds number as function of $T_{\mathrm{w}}/T_{\mathrm{e}}$, as the experimental data are scattered and differ by a factor of two, even at low Mach numbers. Another valuable input from the experiments is the transition duration until the turbulent boundary layer has fully evolved. In this thesis, it is assumed that the transition requires 100 µs to finish.

Solutions for fully laminar and fully turbulent boundary layers have been conceptualized by Mirels [155, 156] and will be discussed briefly.

4.2.1 Laminar Boundary Layer

For a fully laminar boundary layer solution, the Prandtl boundary layer equations for compressible flow [157] can be used in a coordinate system, whose origin lies at the intersection of the shock tube wall and the foot of the shock wave. Also, it is assumed that the axial pressure gradient dp/dx is negligible:

$$\frac{\partial \rho u}{\partial x} + \frac{\partial \rho v}{\partial y} = 0 \tag{4.21}$$

$$\rho \left(u \frac{\partial u}{\partial x} + v \frac{\partial u}{\partial y} \right) = \frac{\partial}{\partial y} \left(\mu \frac{\partial u}{\partial y} \right) \tag{4.22}$$

$$\rho c_p \left(u \frac{\partial T}{\partial x} + v \frac{\partial T}{\partial y} \right) = \frac{\partial}{\partial y} \left(\lambda \frac{\partial T}{\partial y} \right) + \mu \frac{\partial^2 u}{\partial x^2} \tag{4.23}$$

Further, a scalar streaming function ψ is introduced for a flow with variable density (from Eq. 4.21), where the velocity components can be calculated from the stream function [155]:

$$\frac{\rho u}{\rho_\mathrm{w}} = \frac{\partial \psi}{\partial y} \tag{4.24}$$

$$\frac{\rho v}{\rho_\mathrm{w}} = -\frac{\partial \psi}{\partial x} \tag{4.25}$$

In order to solve the equations, the approach of Blasius can be used [157], who recognized that the solution is self-similar. Thus, the distribution of the quantities within the boundary layer can be described by a single similarity parameter η:

$$\eta(x, y) = \frac{y_T}{\delta(x)} \tag{4.26}$$

$$y_T = \int_0^y \frac{T_\mathrm{w}}{T(y)} \mathrm{d}y \tag{4.27}$$

$$\delta(x) = \sqrt{\frac{\nu x}{u_\mathrm{e}}} \tag{4.28}$$

$$\psi = \sqrt{\nu u_\mathrm{e} x}\, f(\eta) \tag{4.29}$$

Here, $\delta(x)$ is the boundary layer thickness at a distance x to the shock wave front, y_T is a temperature-related wall distance, $f(\eta)$ is an arbitrary function to be determined yet, and u_e is the velocity of the external flow. The boundary layer thickness is determined as the ratio of two information propagation speeds, which represent the information propagation in the axial direction, dominated by convection and the information propagation in the vertical direction, dominated by diffusion. The wall distance is temperature-corrected to account for a change in viscosity with temperature, which increases the information transport by diffusion. It is assumed here that the viscosity increases linearly with temperature. Substituting the expressions into momentum Eq. 4.22 yields [155]:

$$\frac{\mathrm{d}^3 f}{\mathrm{d}\eta^3} + \frac{\mathrm{d}^2 f}{\mathrm{d}\eta^2} f = 0 \tag{4.30}$$

$$f(0) = 0, \quad \frac{\mathrm{d}f}{\mathrm{d}\eta}(0) = \frac{u_\mathrm{w}}{u_\mathrm{e}}, \quad \frac{\mathrm{d}f}{\mathrm{d}\eta}(\infty) = 1 \tag{4.31}$$

Equation 4.30 is thus a third-order non-linear differential equation. In this work, the higher order differential equation has been transformed into a set of ordinary differential equations and integrated with a classic

4th-order accurate Runge-Kutta integrator. The solution is stored in a table with η as lookup parameter. Similarly, the energy Eq. 4.23 can be reformulated with functions $f(\eta)$, $s(\eta)$, and $r(\eta)$ [156]:

$$T = T_\mathrm{e} + T_\mathrm{e}\left[\left(\frac{u_\mathrm{w}}{u_\mathrm{e}} - 1\right)^2 \frac{u_\mathrm{e}^2}{2T_\mathrm{e}c_{p,\mathrm{w}}}\, r(\eta) + \left(\frac{T_\mathrm{w}}{T_\mathrm{e}} - \frac{T_\mathrm{r}}{T_\mathrm{e}}\right) s(\eta)\right] \tag{4.32}$$

$$T_\mathrm{r} = T_\mathrm{e} + T_\mathrm{e}\left[\left(\frac{u_\mathrm{w}}{u_\mathrm{e}} - 1\right)^2 \frac{u_\mathrm{e}^2}{2T_\mathrm{e}c_{p,\mathrm{w}}}\, r(0)\right] \tag{4.33}$$

Here, T_r is the so called recovery temperature, which represents the adiabatic wall temperature caused by dissipation. It is evident that the energy equation is strictly valid only for thermally perfect gases with constant c_p and constant Prandtl number. Nonetheless, the results have also been very promising in modeling boundary layers of calorically imperfect fluids. Solutions for $s(\eta)$, $r(\eta)$ can be obtained via the following high-order differential equations, once the solution is known for $f(\eta)$ and the derivatives of f:

$$\frac{\mathrm{d}^2 r}{\mathrm{d}\eta^2} + \mathrm{Pr}\, f(\eta)\frac{\mathrm{d}r}{\mathrm{d}\eta} = -\frac{2\,\mathrm{Pr}}{(u_\mathrm{w}/u_\mathrm{e} - 1)^2}\left(\frac{\mathrm{d}^2 f}{\mathrm{d}\eta^2}\right)^2 \tag{4.34}$$

$$r(\infty) = 0, \quad \frac{\mathrm{d}r}{\mathrm{d}\eta}(0) = 0 \tag{4.35}$$

$$\frac{\mathrm{d}^2 s}{\mathrm{d}\eta^2} + \mathrm{Pr}\, f(\eta)\,\frac{\mathrm{d}s}{\mathrm{d}\eta} = 0 \tag{4.36}$$

$$s(0) = 1, \quad s(\infty) = 0 \tag{4.37}$$

The acquired solutions not only allow to describe the internal structure of laminar boundary layers, moreover, other key quantities can be derived immediately. These include the vertical displacement velocity v_e, the wall shear stress τ_w, and the wall heat flux q_w:

$$\frac{v_\mathrm{e}}{u_\mathrm{e}} = \frac{\rho_\mathrm{w}}{\rho_\mathrm{e}}\sqrt{\frac{\nu_\mathrm{w}}{2xu_\mathrm{e}}}\left[\lim_{\eta\to\infty}(\eta - f) + \left(\frac{u_\mathrm{w}}{u_\mathrm{e}} - 1\right)^2 \frac{u_\mathrm{e}^2}{2T_\mathrm{e}c_{p,\mathrm{w}}}\int_0^\infty r\,\mathrm{d}\eta + \left(\frac{T_\mathrm{w}}{T_\mathrm{e}} - \frac{T_\mathrm{r}}{T_\mathrm{e}}\right)\int_0^\infty s\,\mathrm{d}\eta\right] \tag{4.38}$$

$$\tau_\mathrm{w} = \mu_\mathrm{w}\left(\frac{\partial u}{\partial y}\right)_\mathrm{w} = \mu_\mathrm{w}u_\mathrm{e}\sqrt{\frac{u_\mathrm{e}}{2x\nu_\mathrm{w}}}\,\frac{\mathrm{d}^2 f}{\mathrm{d}\eta^2}(0) \tag{4.39}$$

$$q_\mathrm{w} = -\lambda_\mathrm{w}\left(\frac{\partial T}{\partial y}\right)_\mathrm{w} = -\frac{\mathrm{d}s}{\mathrm{d}\eta}(0)\,(T_\mathrm{w} - T_\mathrm{r})\sqrt{\frac{u_\mathrm{e}\rho_\mathrm{w}\mu_\mathrm{w}}{2x}}\,\frac{c_{p,\mathrm{w}}}{\mathrm{Pr}_\mathrm{w}} \tag{4.40}$$

4.2.2 Turbulent Boundary Layer

For the description of a fully turbulent boundary layer, other approaches must be used. First, a turbulent boundary layer is entirely unsteady and there is no unique solution for temperature and velocity profiles. Instead, it is assumed that the time-averaged profiles of axial velocity component u and temperature T follow power laws. Thus, the structure of the time-averaged turbulent boundary layer is self-similar, leading to the following expression for velocity:

$$\xi = \frac{y}{\delta(x)} \tag{4.41}$$

$$\left|\frac{u - u_\mathrm{w}}{u_\mathrm{e} - u_\mathrm{w}}\right| = \begin{cases} \xi^{1/7} & \text{if} \quad 0 \le \xi \le 1, \\ 1 & \text{else.} \end{cases} \tag{4.42}$$

Here, ξ is the self similarity variable of the turbulent boundary layer. Under the assumption of a unity Prandtl number, the following profiles for temperature and density have been proposed by Mirels [156]:

$$\frac{\rho_\mathrm{e}}{\rho} = \frac{T}{T_\mathrm{e}} = \begin{cases} \frac{T_\mathrm{w}}{T_\mathrm{e}} \left(1 + b\,\xi^{1/7} - c\,\xi^{1/7}\right) & \text{if} \quad 0 \leq \xi \leq 1, \\ 1 & \text{else.} \end{cases} \tag{4.43}$$

$$b = \frac{T_\mathrm{r}}{T_\mathrm{w}} - 1, \quad c = \left(\frac{T_\mathrm{r}}{T_\mathrm{e}} - 1\right) \frac{T_\mathrm{e}}{T_\mathrm{w}} \tag{4.44}$$

In order to determine the vertical displacement velocity v_e and the boundary layer thickness $\delta(x)$, integral methods are used for the boundary layer equations (Eq. 4.21 - 4.23). The mass and momentum equations now read:

$$\frac{\mathrm{d}\delta^*}{\mathrm{d}x} = \frac{\mathrm{d}}{\mathrm{d}x} \int_0^\infty \left(1 - \frac{\rho u}{\rho_\mathrm{e} u_\mathrm{e}}\right) \mathrm{d}y \tag{4.45}$$

$$\frac{\mathrm{d}\Theta}{\mathrm{d}x} = \frac{\mathrm{d}}{\mathrm{d}x} \int_0^\infty \frac{\rho u}{\rho_\mathrm{e} u_\mathrm{e}} \left(1 - \frac{u}{u_\mathrm{e}}\right) \mathrm{d}y = \frac{\tau_\mathrm{w}}{\rho_\mathrm{e} u_\mathrm{e}^2} \tag{4.46}$$

Equation 4.45 and 4.46 feature the boundary layer displacement thickness δ^* and boundary layer momentum thickness Θ. Both equations can be integrated using the power law expressions for velocity, temperature, and density:

$$\frac{\delta^*}{\delta(x)} = 1 - 7\frac{T_\mathrm{e}}{T_\mathrm{w}} \left[\frac{u_\mathrm{w}}{u_\mathrm{e}} I_6 + \left(1 - \frac{u_\mathrm{w}}{u_\mathrm{e}}\right) I_7\right] \tag{4.47}$$

$$\frac{\Theta}{\delta(x)} = 7\frac{T_\mathrm{e}}{T_\mathrm{w}} \left(1 - \frac{u_\mathrm{w}}{u_\mathrm{e}}\right) \left[\frac{u_\mathrm{w}}{u_\mathrm{e}} I_6 + \left(1 - 2\frac{u_\mathrm{w}}{u_\mathrm{e}}\right) I_7 - \left(1 - \frac{u_\mathrm{w}}{u_\mathrm{e}}\right) I_8\right] \tag{4.48}$$

$$I_N = \int_0^1 \frac{z^N}{1 + bz - cz^2}\,\mathrm{d}z \tag{4.49}$$

This leaves the boundary layer thickness $\delta(x)$ as remaining unknown. Applying the chain rule to the LHS of Eq. 4.46 yields:

$$\frac{\mathrm{d}\Theta}{\mathrm{d}\delta}\frac{\mathrm{d}\delta}{\mathrm{d}x} = \frac{\Theta}{\delta}\frac{\mathrm{d}\delta}{\mathrm{d}x} = \frac{\tau_\mathrm{w}}{\rho_\mathrm{e} u_\mathrm{e}^2} \tag{4.50}$$

Because Θ/δ is no function of x, the expression can be integrated, if the wall shear stress is known. Thus, empirical descriptions of wall shear stress as function of δ are required. These are usually obtained from measurements of compressible flows over semi-infinite plates. In the original work of Mirels [156], however, the Blasius friction coefficient [157] for incompressible flow has been used:

$$\frac{\tau_\mathrm{w}}{\rho_\infty u_\infty^2} = 0.0225 \left(\frac{\nu_\infty}{u_\infty \delta}\right)^{1/4} \tag{4.51}$$

The subscript “∞” denotes a free flow quantity. In order to improve the accuracy for compressible flow, those quantities evaluated for free flow conditions are replaced by quantities representing an average state within the boundary layer:

$$T_\mathrm{m} = 0.5\,(T_\mathrm{w} + T_\mathrm{e}) + 0.22\,(T_\mathrm{r} + T_\mathrm{e}) \tag{4.52}$$

$$\frac{T_\mathrm{r}}{T_\mathrm{e}} = 1 + \left(\frac{u_\mathrm{w}}{u_\mathrm{e} - 1}\right)^2 \frac{u_\mathrm{e}^2\, Pr_\mathrm{m}^{1/3}}{2\, T_\mathrm{e} c_{p,\mathrm{m}}} \tag{4.53}$$

Here, the mean temperature T_m and the recovery temperature T_r are mutually dependent, and can be determined by an iterative algorithm. In order to apply the derived skin friction coefficient in a coordinate system propagating with the shock, the free flow velocities must be replaced by the velocity difference between external flow and the wall:

$$\frac{\tau_\mathrm{w}}{\rho_\mathrm{e} u_\mathrm{e}^2} = 0.0225\, \varphi \left(1 - \frac{u_\mathrm{w}}{u_\mathrm{e}}\right) \left|1 - \frac{u_\mathrm{w}}{u_\mathrm{e}}\right|^{3/4} \left(\frac{\nu_\mathrm{e}}{u_\mathrm{e}\delta}\right)^{1/4} \tag{4.54}$$

$$\varphi = \left(\frac{\mu_\mathrm{m}}{\mu_\mathrm{e}}\right)^{1/4} \left(\frac{T_\mathrm{e}}{T_\mathrm{m}}\right)^{3/4} \tag{4.55}$$

Here, φ is a correction value for the mean state.

Despite the corrections for compressible flow by using an average state, much better suited expressions for the skin friction coefficient are available. Thus, Mirels original model has been generalized by Petersen and Hanson [158], with the aim to allow the use of different skin friction coefficient models in a straightforward manner. The skin friction correlation in a generalized form reads [158]:

$$\frac{\tau_\mathrm{w}}{\rho_\mathrm{e} u_\mathrm{e}^2} = \beta\, \varphi \left(1 - \frac{u_\mathrm{w}}{u_\mathrm{e}}\right) \left|1 - \frac{u_\mathrm{w}}{u_\mathrm{e}}\right|^{1-\alpha} \left(\frac{\nu_\mathrm{e}}{u_\mathrm{e}\delta}\right)^{\alpha} \tag{4.56}$$

$$\varphi = \left(\frac{\mu_\mathrm{m}}{\mu_\mathrm{e}}\right)^{\alpha} \left(\frac{T_\mathrm{e}}{T_\mathrm{m}}\right)^{1-\alpha} \tag{4.57}$$

Equation 4.56 features the coefficients α and β, which determine the respective skin friction correlation. The originally used Blasius model is recovered for $\alpha = 0.25$ and $\beta = 0.0225$, while the correlation of Spalding and Chi [159], corresponding to model coefficients $\alpha = 0.14$ and $\beta = 0.0077$, has been recommended by Petersen and Hanson [158] and was therefore used in this work. After substituting Eq. 4.56 in Eq. 4.50 and subsequent integration, the equations for boundary layer thickness, vertical displacement velocity, and wall shear stress as function of x can be derived:

$$\delta = c_1\, x \left(\varphi \frac{1 - u_\mathrm{w}/u_\mathrm{e}}{\Theta/\delta}\right)^{1-n} \left|1 - \frac{u_\mathrm{w}}{u_\mathrm{e}}\right|^{\frac{1-\alpha}{1+\alpha}} \left(\frac{\nu_\mathrm{e}}{u_\mathrm{e} x}\right)^{n} \tag{4.58}$$

$$\frac{v_\mathrm{e}}{u_\mathrm{e}} = c_2\, \frac{\delta^*}{\delta} \left(\varphi \frac{1 - u_\mathrm{w}/u_\mathrm{e}}{\Theta/\delta}\right)^{1-n} \left|1 - \frac{u_\mathrm{w}}{u_\mathrm{e}}\right|^{\frac{1-\alpha}{1+\alpha}} \left(\frac{\nu_\mathrm{e}}{u_\mathrm{e} x}\right)^{n} \tag{4.59}$$

$$\frac{\tau_\mathrm{w}}{\rho_\mathrm{e} u_\mathrm{e}^2} = c_2\, \frac{\Theta}{\delta} \left(\varphi \frac{1 - u_\mathrm{w}/u_\mathrm{e}}{\Theta/\delta}\right)^{1-n} \left|1 - \frac{u_\mathrm{w}}{u_\mathrm{e}}\right|^{\frac{1-\alpha}{1+\alpha}} \left(\frac{\nu_\mathrm{e}}{u_\mathrm{e} x}\right)^{n} \tag{4.60}$$

The model parameters c_1, c_2, and n can be calculated as functions of α and β, as follows [158]:

$$c_1 = [\beta\,(1 + \alpha)]^{\frac{1}{1+\alpha}} \tag{4.61}$$

$$c_2 = \frac{c_1}{1 + \alpha} \tag{4.62}$$

$$n = \frac{\alpha}{1 + \alpha} \tag{4.63}$$

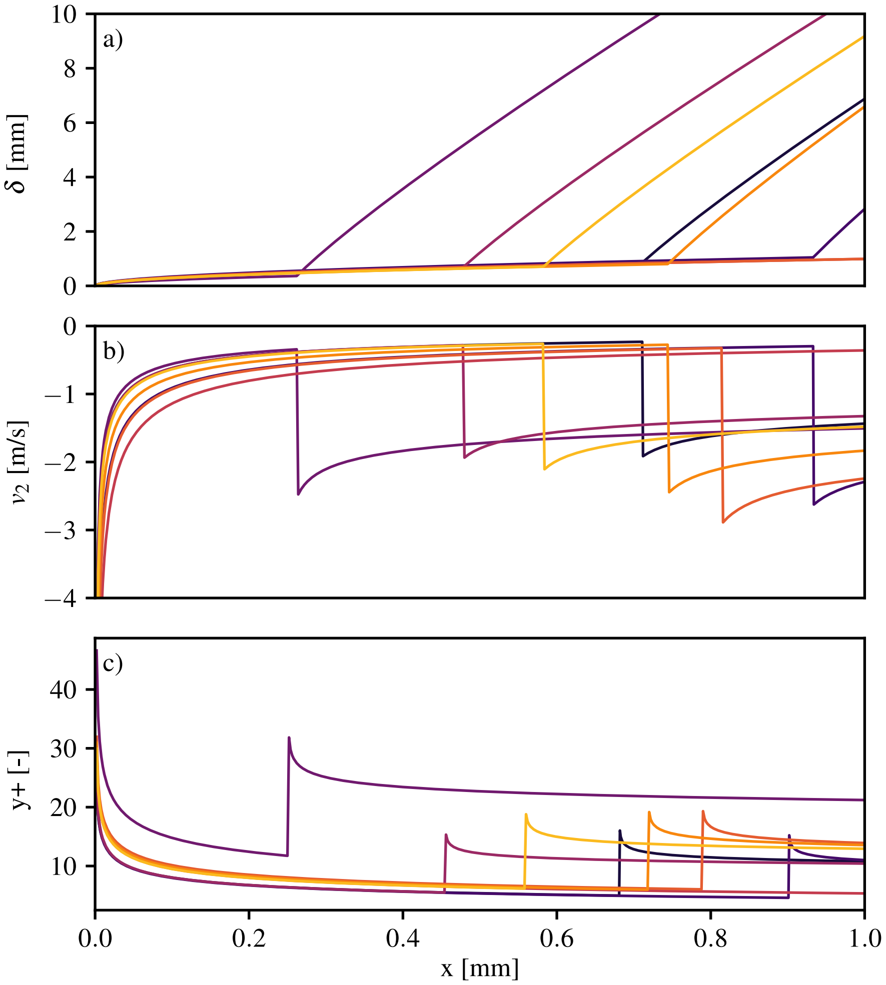

Figure 4.1: (a) Boundary layer thickness δ, (b) vertical displacement velocity v_2 (in region 2), and (c) dimensionless wall distance $y+$ of the first numerical cell for shock-tube experiments performed in Duisburg and listed in Chapter 6 Tab. 6.1. Each line represents the boundary-layer solution for simulated shock-tube experiments in no particular order.

Figure 4.1 shows results for boundary layer thickness δ, vertical displacement velocity v_2 and dimensionless wall distance $y+$ as function of distance x to the shock front, whereby boundary layer transition from laminar to turbulent is considered using the definition of Hartunian et al. [154]. Each color indicates a specific case from Chapter 6 Tab. 6.1. in no particular order. The pressures behind the incident shock of the respective shock-tube experiments are considered low or moderate, thus, the assumption of a fully turbulent boundary layer cannot be made and the laminar boundary layer is present in all cases. It is also evident that turbulent boundary layers are characterized by larger growth rates, higher displacement velocities and a higher demand regarding grid resolution to resolve the boundary layer sufficiently. Therefore, jumps appear at the location of transition.

4.3 Nonuniformities

The presence of a boundary layer behind the incident shock acts as a mass sink term and causes the fluid in the core flow to expand. This results in a core flow that has no axially homogeneous profile as in the inviscid adiabatic case, but instead features axial distributions of the thermodynamic state variables, which are referred to as *nonuniformities* following Mirels and Braun [160].

The small perturbation theory has been used [160, 161] to calculate the nonuniformities, where the pressure perturbation at any location x behind the shock equals the sum of a left and a right running perturbation-pressure wave. The particle-velocity perturbation Δu can be determined likewise, using acoustic relations:

$$\Delta p = \Delta p^+ + \Delta p^- \tag{4.64}$$

$$\Delta u = \frac{1}{\rho c}\left(\Delta p^+ - \Delta p^-\right) \tag{4.65}$$

The computation of the pressure perturbation requires an approximation of the mass flux that is exchanged between the core flow (external) and the boundary layer. A pressure perturbation from a right-running wave, for example, can be calculated as [161]:

$$\Delta p = c^2 \Delta\rho \tag{4.66}$$

$$\Delta p^+ = c^2 \, \frac{1}{2\,(c+u)} \int_{-\infty}^{x} \dot{m}\,(\xi, \tau)\, \mathrm{d}\xi \tag{4.67}$$

$$\tau = t - \frac{x-\xi}{c+u} \tag{4.68}$$

Here, ξ and τ are integration variables for x and t, and $\dot{m}$ is the mass flux entering the boundary layer per unit cross sectional area and per unit x. Equation 4.67 can be rewritten in terms of the vertical boundary-layer displacement velocity v_e and hydraulic diameter d_h [161]:

$$\dot{m}(x,t) = \frac{4}{d_\mathrm{h}} \rho v_\mathrm{e}(x,t) \tag{4.69}$$

$$\Delta p^+ = p \, \frac{2\gamma}{c\, d_\mathrm{h}} \left(\frac{1}{2\,(1+M)} \int_{-\infty}^{x} v_\mathrm{e}\,(\xi,\tau)\, \mathrm{d}\xi \right) \tag{4.70}$$

Equations that compute the vertical displacement velocity at the edge of a boundary layer are provided in Sec. 4.2.1 and Sec. 4.2.2 for fully laminar and fully turbulent boundary layers, respectively.

The integration in Eq. 4.70 is carried out along characteristic line segments in the regions 2 and 3 and can be rewritten in a closed form without integrals [160], assuming a fully laminar or fully turbulent boundary layer. However, at low and moderate pressures, the distance from the incident shock to the point of transition can be significant and affect the variation of quantities. Therefore, instead of using analytical solutions, approximations are used, for which the characteristic lines are divided into segments, so that the integrals can be approximated by finite sums. This approach allows to consider boundary layer transition effects.

Apart from the pressure and particle-velocity variations, the temperature variation is required to fully describe the gas state at a certain location x_i. The temperature is not only affected by pressure waves in isentropic manner, but also by the reduction of the shock strength due to shock attenuation. Both lead to a variation of entropy s along the center line, whereby the entropy remains constant along the individual particle paths. Knowing the entropy perturbation Δs and the pressure perturbation Δp at location x_i for a given time t_i, allows to compute the temperature perturbation:

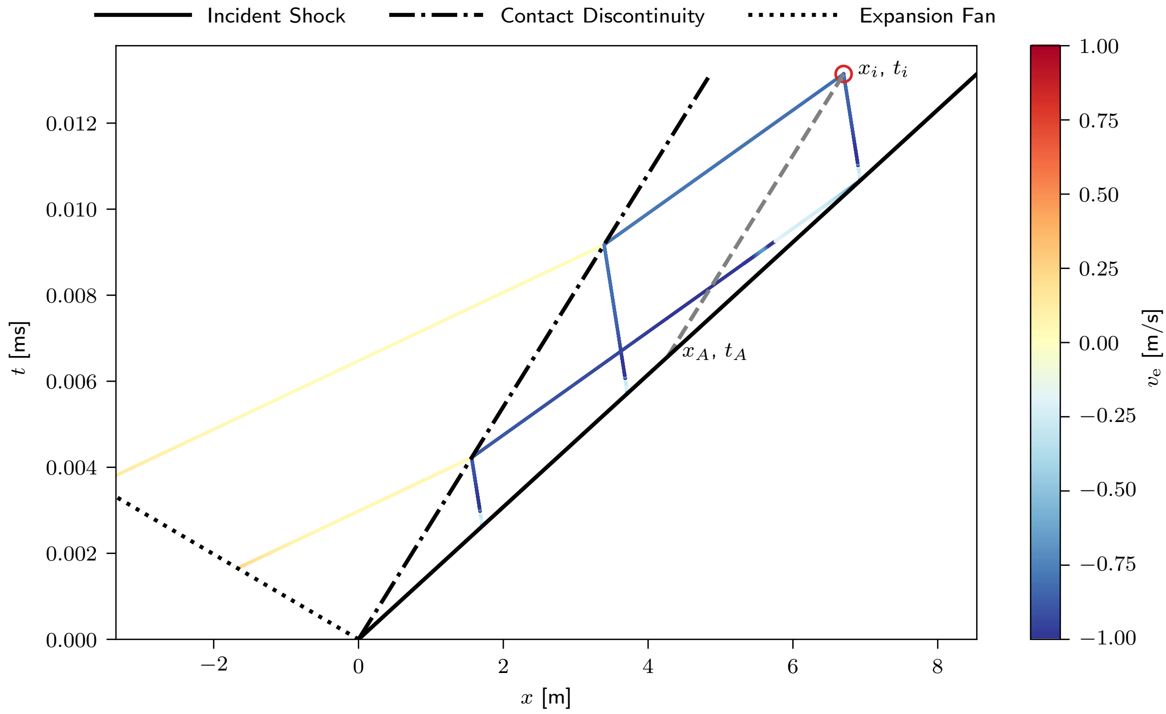

Figure 4.2: Characteristic line segments in regions 2 and 3 of a representative shock-tube simulation, colored by the local vertical displacement velocity at the edge of the boundary layer. The perturbations are evaluated for a specific point in time and space (represented by the open symbol), denoted as t_i and x_i, where x_i typically corresponds to the computational inlet. The location x_A at time t_A illustrates the path (gray dashed line) of a particle that was just shocked at time t_A and reaches the location x_i at time t_i.

$$\left(\frac{\Delta T_2}{T_2}\right)_{x_i,t_i} = \left(\frac{\gamma_1 - 1}{\gamma_1}\frac{\Delta p_2}{p_2} + \frac{1}{\gamma_1}\frac{\Delta s_2}{c_v}\right)_{x_i,t_i} \tag{4.71}$$

Since the entropy is constant along individual particle paths, the previous shock location x_A at time t_A is introduced (see Fig. 4.2), such that the particle path originating in x_A intersects with the location x_i at time t_i. The entropy perturbation can be related to the pressure perturbation behind the shock at time t_A, using the shock relations of a calorically perfect gas [160]:

$$\left(\frac{\Delta s_2}{c_v}\right)_{x_i,t_i} = \frac{(\gamma_1 - 1)\left(M_\mathrm{s}^2 - 1\right)^2}{M_\mathrm{s}^2\left[(\gamma_1 - 1)\,M_\mathrm{s}^2 + 2\right]}\left(\frac{\Delta p_2}{p_2}\right)_{x_\mathrm{A},t_\mathrm{A}} \tag{4.72}$$

4.4 Inlet Modeling

The typical length of shock tubes is up to several meters with diameters of 8 cm and more. If the boundary layer shall be resolved, experience shows that a grid resolution of $\Delta = 50\,\mu\mathrm{m}$ or finer is mandatory. This results in a number of 310 billion finite volumes for the discretization of a three-dimensional domain, if an equidistant grid is used. By today's standards, these computational efforts are unaffordable, especially since the demands on grid resolution at high pressures are still much higher. Even in 2D, the costs are still disproportionately high and at the same time the effects of 3D turbulence are not taken into account. For this reason, only a part of the shock tube near the end wall, where the shock is reflected, is simulated in

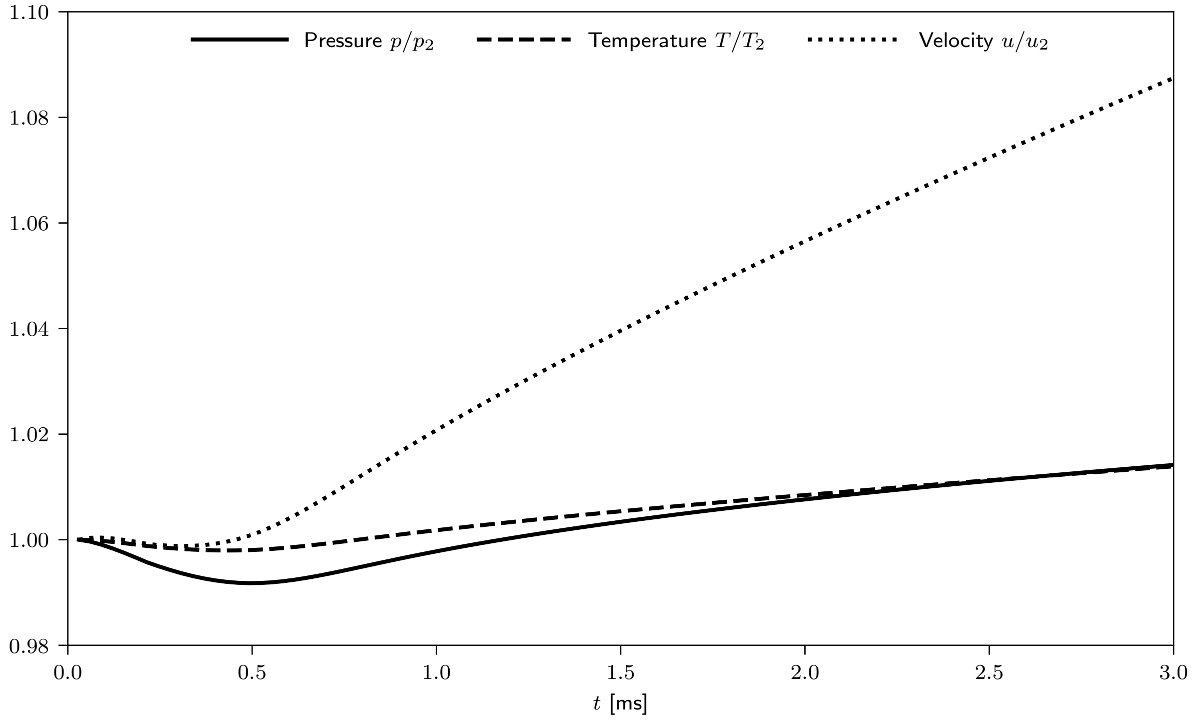

Figure 4.3: Evolution of pressure (solid line), temperature (dashed line), and axial velocity (dotted line) at the inlet for a representative shock tube simulation and normalized by the initial values behind the shock in region 2.

this work. However, simulations that only cover the end part of the shock tube, have the disadvantage that the evolution of the thermodynamic state variables and the velocity must be modeled at the inlet of the computational domain. This concerns not only the internal boundary layer structure and its growth rate, but also the variations in the core flow due to nonuniformities.

For this reason, at the start of each shock tube simulation in this work, the steady-state solutions of the fully laminar and the fully turbulent boundary layer behind the incident shock are calculated first. The results for the displacement velocity are then used to predict the time variation of pressure, axial velocity, and temperature in the core flow, where x_i is located at the computational inlet and boundary layer transition is taken into account. During boundary layer transition, the individual solutions of the laminar and turbulent boundary layer are smoothly blended using linear interpolation to avoid jumps. Figure 4.2 presents those characteristic line segments that intersect at the inlet of the numerical domain x_i at a given time t_i for a representative shock-tube simulation. The color of the characteristic lines indicates the local vertical displacement velocity at the edge of the boundary layer. A blue color of the lines in region 2 indicates negative displacement velocities and accordingly an accumulation of mass in the boundary layer, whereas a red color in region 3 indicates the exact opposite.

The resulting temporal evolutions of pressure, axial velocity, and temperature at the inlet are presented in Fig 4.3. It was pointed out in [160], that the values of pressure, temperature, and particle velocity are monotonically increasing, under the assumption of a fully laminar or fully turbulent boundary layer. However, as presented in Fig. 4.3, consideration of boundary-layer transition effects can lead to a qualitative different evolution of state quantities. Specifically at low pressure levels, a pronounced pressure minimum is observed, which approximately overlaps with the transition point. A similar observation is made for temperature, while temperature is also affected by shock attenuation and therefore reaches the minimum earlier in most of the cases. The deviations from the reference values are very large for low pressure cases and shock tubes that feature small diameters.

The combination of the boundary layer solutions and the time variations of the core flow at the inlet allow a two-dimensional description of the flow at the inlet. For this purpose, it is assumed, that the flow outside the boundary layer is exclusively a function of position x and is described by nonuniformities. Inside the boundary layer, the structure of the axial velocity component u and the temperature T is prescribed, whereby the profiles are scaled in such a way that the value at the boundary layer edge equals that of the core flow to avoid inconsistencies. The pressure inside the boundary layer also corresponds to the value of the core flow. The gas composition is further assumed to be frozen and density can be calculated using the equation of state. The two dimensional solution is stored in a table with wall distance y and simulation time t as look up parameters. Once the boundary layer has transitioned, artificial turbulence is applied within the boundary layer using the approach of Klein et al. [162] or Kempf et al. [163].

It should be noted that the vertical velocity component is not included in the solution, while it could be calculated using Eq. 4.25. Here, the value at the wall is zero (impermeability) and approaches a larger value at the boundary layer edge with a constant value outside the boundary layer. Therefore, this approach is only applicable for free flows over a flat plate but inappropriate in a domain closed by walls. Thus, the values for the vertical component are extrapolated using interior points instead. This inexact description of vertical velocity results in artifacts at the inlet, while no impact on the flow near the end wall has been observed. Nevertheless, the approach can be improved at this point and a Poisson-type algorithm could be used to determine a solution for both, the pressure and the vertical velocity field, such that the continuity equation is satisfied. Here, a Dirichlet boundary condition would be applied for the pressure directly behind the shock and on the center line, while a zero gradient boundary condition could be used at the wall.

Chapter 5
Analysis of mild ignition in a shock tube using a highly resolved 3D-LES and high-order shock-capturing schemes

Analysis of mild ignition in a shock tube using a highly resolved 3D-LES and high-order shock-capturing schemes [6]

Authors: J. T. Lipkowicz, I. Wlokas, A. M. Kempf

This chapter including all figures and tables was previously published in 'Shock Waves, 29, J. T. Lipkowicz, I. Wlokas and A. M. Kempf, Analysis of mild ignition in a shock tube using a highly resolved 3D-LES and high-order shock-capturing schemes, 511 - 521, Copyright ©Springer (2019)' and is reprinted with permission from Springer. The author J. T. Lipkowicz developed the codes for the CFD simulations and the post-processing tasks, performed all the simulations, wrote the paper and generated all figures and tables. The authors I. Wlokas and A. M. Kempf contributed corrections, discussions, and proof-reading.

Abstract

A highly resolved three-dimensional large-eddy simulation (LES) is presented for a shocktube containing a stoichiometric hydrogen-oxygen (H_2/O_2) mixture, the results are compared against experimental results. A parametric study is conducted to test the effects of grid resolution, numerical scheme, and initial conditions before the 3D simulations are presented in detail. An approximate Riemann solver and a high-order interpolation scheme are used to solve the conservation equations of the viscous, compressible fluid and to account for turbulence behind the reflected shock. Chemical source terms are calculated by a finite-rate model. Simultaneous results of pseudo-Schlieren, temperature, pressure, and species are presented. The ignition delay time is predicted in agreement with the experiments by the three-dimensional simulations. The mechanism of mild ignition is analysed by Lagrangian tracer-particles, tracking temperature histories of material particles. We observed strongly increased temperatures in the core region away from the end-wall, explaining the very early occurrence of mild ignition in this case.

5.1 Introduction

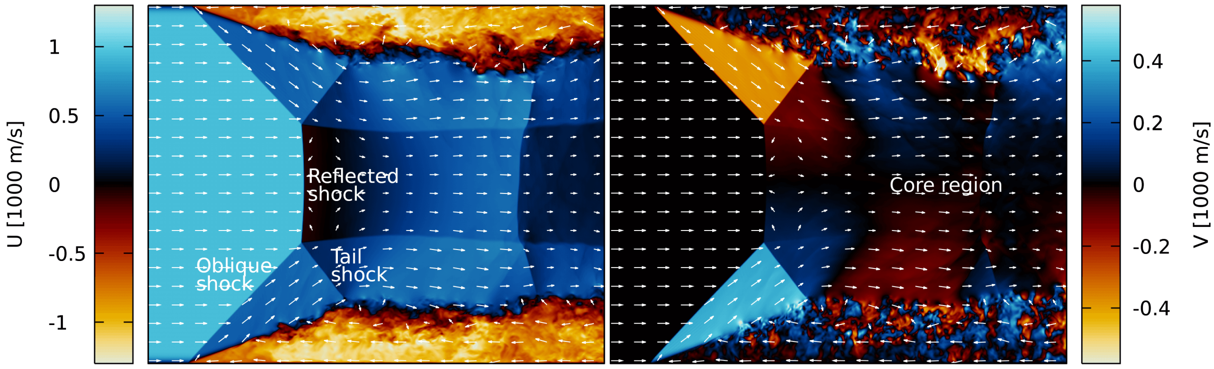

Figure 5.1: Instantaneous fields of axial velocity component U (left), vertical velocity component V (right) and velocity vector field from a 3D simulation (3Db) with a grid resolution of Δ = 50 µm.

5.1.1 Motivation

Shock-tube experiments are a classical technique to provide data for the development of accurate reaction mechanisms. A shock tube consists of a driver section with a pressurised (inert) gas and separated by a diaphragm, at lower pressure, the section filled with the test gas. At a sufficiently high pressure difference between the sections, the diaphragm bursts and a compression shock propagates into the test gas, followed by the contact discontinuity between the mixtures. After the reflection of the shock at the end wall, the temperature of the test gas is increased further by the reflected shock, initiating the chemical reactions and an auto-ignition delay time can be measured. Ideally, the test gas behind the reflected shock is at rest and homogeneous, under the assumption of an inviscid, adiabatic process. In reality, deviations from the ideal assumptions affect the system and hence the measured auto-ignition delay time. This deviation is negligible in some cases, but so large in other cases that the measurements must be discarded.

Such deviations have been examined and are caused by a diaphragm bursting in a finite time and by shock attenuation [161, 164, 165] due to the formation of a boundary layer, by mild ignition [5, 166, 167] and by shock-boundary interaction [168, 169]. This paper focuses on mild ignition, where the ignition takes place prematurely in small spherical hotspots away from the end wall, in contrast to strong ignition, where the mixture ignites simultaneously in a volume near the end wall, which is necessary for a meaningful measurement of auto-ignition delay time. The formation of the hotspots occurs due to inhomogeneities in the flow field behind the reflected shock caused by the interaction of the reflected shock with the boundary layer. Furthermore, in many cases, the shock-boundary layer interaction leads to a bifurcation phenomena, which has been first observed in a shock-tube experiment by Mark [168].

The bifurcation is characterized by a triple point connecting the reflected shock, the oblique shock, and the tail shock, as presented in Fig. 5.1 (left). Non-boundary-layer fluid entering the bifurcation is compressed first by the oblique shock and then by the tail shock, resulting in less entropy production and hence reduced temperatures behind the tail shock, compared to the core region. Due to the low Mach number of the fluid in the boundary layer, the pressure gradient between the undisturbed region and the boundary region behind the reflected shock reverses the boundary layer flow, resulting in a recirculation bubble. Using several simplifications, Mark [168] suggested that a bifurcation occurs if the stagnation pressure (in a shock-fixed frame) in the boundary layer is smaller than the static undisturbed pressure behind the reflected shock. Davies et al. [170] found good agreement between their experiments and the criterion proposed by Mark, for incident Mach numbers smaller than M = 3.6. A bifurcation always leads to a highly non-uniform velocity field, clearing the way for mild ignition.

5.1.2 Mild ignition

Voevodsky and Soloukhin [171] were the first to define a criterion for mild ignition in shock tubes after several mild-ignition observations [172–174] had been made in experiments. They found a curve in the p-T plane separating the mild- and strong ignition regimes, which was close to the curve of the upper explosion limit of H_2/O_2 mixtures. Meyer and Oppenheim [166] emphasized another criterion by relating the change of ignition delay time τ_{ig} to the change of temperature T and found a slightly better agreement for a threshold value of $\partial\tau_{\mathrm{ig}}$ / ∂T = -2 µs/K compared to the first criterion. This finding demonstrates the importance of temperature fluctuations in the region behind the reflected shock and was later confirmed by one-dimensional simulations of Oran et al. [175]. They found excellent agreement regarding simulations for strong ignition conditions and qualitative agreement in the case of mild ignition. Though one dimensionality cannot account for the effects of a non-uniform velocity field due to shock-boundary interaction, the numerics introduced temperature perturbations and variations in the velocity field, triggering a mild ignition. Since then, several numerical simulations [176–180] in 2D or 3D have focussed on ignition behind reflected shocks in shock tubes. Oran et al. [176] presented two-dimensional simulations of ignition events in a stoichiometric ethylene-air mixture. For M = 2.5, strong ignition occurred, while for M = 2.2 mild ignition was observed. Dzieminska and Hayashi [180] observed auto ignition behind the reflected shock in the boundary layer after the ignition occurred at the end wall. Ihme et al. [177] investigated ignition kernels in a three-dimensional simulation using an AMR (Adaptive Mesh Refinement) code with a smallest cell size of less than 10 µm. They observed ignition kernels between the tail shock and the stagnation point of the boundary layer fluid, when using adiabatic boundary conditions. Grogan et al. [178] performed 2D simulations and examined the effect of wall-boundary conditions and shock-tube diameter on ignition events. The wall-boundary condition had a significant impact on the result, since adiabatic boundary conditions resulted in mild ignition and isothermal boundary conditions in strong ignition. Additionally, a larger diameter of the shock tube led to an increased ignition delay time, providing further evidence that wall effects trigger the mild ignition. Khokhlov [179] used a 3D simulation of a stoichiometric H_2/O_2 mixture to explain the development of hot spots. The authors emphasized the role of entropy perturbations with regards to mild ignition.

5.1.3 Outline

In the first part of this work, the most important features and numerical methods of the LES-solver are presented. Part two describes the experiment and provides basic information about the simulations and the boundary conditions. The third part presents a parameter study and examines the mild ignition event in 3D. Temperature histories of Lagrangian particles are used for investigating the mechanism that leads to mild-ignition.

5.2 Numerical methods

The simulations were carried out with the LES-code “PsiPhi” [181–184], using the FVM (Finite-Volume-Method) approach on an equidistant, Cartesian grid, preserving the formal accuracy of the numerical schemes. In contrast to AMR methods, the high grid resolution was maintained after the shock, helping to reduce artificial numerical diffusion in the turbulent boundary layer and hence excessive numerical mixing that may strongly affect ignition. PsiPhi uses a distributed memory, domain decomposition approach for parallelization, utilizing MPI (Message Passing Interface) communication and was run on up to 78,334 cores for the present simulations. The flow was described by the filtered conservation equations for mass, momentum, energy (Eq. 5.1), and species (Eq. 5.2):

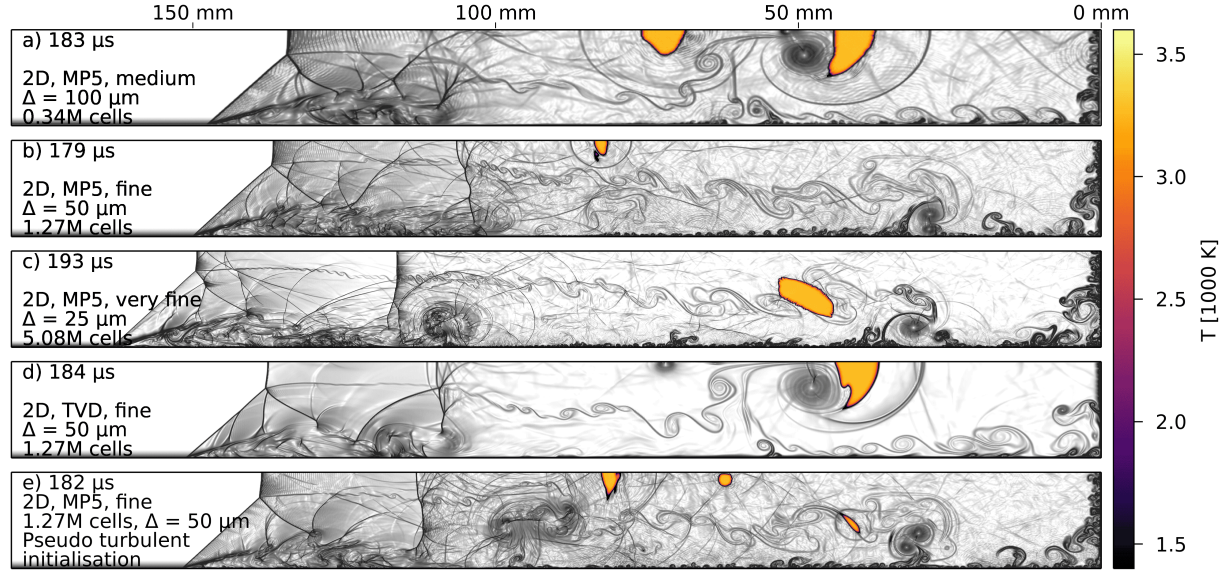

Figure 5.2: Instantaneous pseudo-Schlieren images superimposed with temperature T in the two-dimensional case for different grid resolutions, discretization, and turbulent initial conditions.

$$\frac{\partial \bar{\rho}\widetilde{e}_{\mathrm{t}}}{\partial t}+\frac{\partial \widetilde{u}_j\left(\bar{\rho}\widetilde{e}_{\mathrm{t}}+\bar{P}\right)}{\partial x_j}=\frac{\partial \widetilde{u}_j\widetilde{\tau}_{ij}}{\partial x_j}-\frac{\partial \widetilde{q}_j}{\partial x_j} \tag{5.1}$$

$$\begin{aligned}\frac{\partial \bar{\rho}\widetilde{Y}_k}{\partial t}+\frac{\partial \bar{\rho}\widetilde{u}_j\widetilde{Y}_k}{\partial x_j}&\\ &=\frac{\partial}{\partial x_j}\left(\rho\widetilde{Y}_k\left[\left(D_k+\frac{\mu_{\mathrm{t}}}{\mathrm{Sc}_{\mathrm{t}}}\right)\frac{\partial \widetilde{Y}_k}{\partial x_j}+V_{\mathrm{c},k}\right]\right)+\dot{\omega}_k\end{aligned} \tag{5.2}$$

The equations include the total chemical energy e_{t}, the tensor of frictional stresses $\widetilde{\tau}_{ij}$, the diffusive flux $\widetilde{q}_j$ of energy due to heat conduction and due to species diffusion and the correction velocity $V_{\mathrm{c},k}$ to ensure the conservation of mass. Further information is available from previous work [185].

$$e_{\mathrm{t}}=e+\frac{u_iu_i}{2}+\sum_{k=1}^{N}h^0_{\mathrm{f},k}Y_k \tag{5.3}$$

$$\begin{aligned}\widetilde{q}_j=&\left(\lambda+C_p\frac{\mu_{\mathrm{t}}}{\mathrm{Pr}_{\mathrm{t}}}\right)\frac{\partial \widetilde{T}}{\partial x_j}\\ &+\bar{\rho}\sum_{k=1}^{N}\left(\widetilde{h}_{\mathrm{s},k}\widetilde{Y}_k\left[\left(D_k+\frac{\mu_{\mathrm{t}}}{\mathrm{Sc}_{\mathrm{t}}}\right)\frac{\partial \widetilde{Y}_k}{\partial x_j}+V_{\mathrm{c},k}\right]\right)\end{aligned} \tag{5.4}$$

For time-integration, a third-order low storage Runge-Kutta scheme [186] is used and diffusive fluxes are discretized by central differencing. In order to capture shocks with minimal oscillations, the approximate Riemann solver "HR-Slau2" by Kitamura et al. [139] was used to calculate convective fluxes. The primitive quantities were interpolated to each cell face using the fifth-order, monotonicity preserving scheme by Suresh et al. [122]. Sub-filter fluxes are modelled with eddy-viscosity and eddy-diffusivity approaches for turbulent Schmidt- and turbulent Prandtl numbers of $\mathrm{Pr}_{\mathrm{t}} = \mathrm{Sc}_{\mathrm{t}} = 0.7$. The turbulent viscosity was computed with Nicoud's sigma model [55]. Thermochemical and transport properties, including binary diffusion coefficients, were tabulated for each species as a function of temperature using Cantera [187]. Molecular viscosity of the mixture was calculated according to the modified Wilke-model [188],

Indication	Δ	ni	nj	nk	N	Cost
-	μm	-	-	-	10^6	CPUh
3Da	100	2,520	315	231	183	316,800
3Db	50	4,992	624	442	1,377	3,760,000
2Da	100	2,016	168	1	0.3	784
2Db	50	4,992	315	1	1.6	7,000
2Dc	25	9,984	630	1	6.3	50,000
2Dd	50	4,992	315	1	1.6	7,000
2De	50	4,992	315	1	1.6	7,000

Table 5.1: Computational grids applied for the simulations, giving the grid resolution Δ in μm, the number of cells over the length (ni), height (nj) and depth (nk) of the domain, the total number of cells N (in millions), and the respective computational cost.

the mixture averaged heat conductivity was derived using the approach of Peters et al. [189] and the mixture averaged diffusion coefficient for species k was determined by applying the equation of Kee et al. [190]. CVODE [94, 191] was used to directly solve the reaction mechanism by O'Conaire et al. [192], featuring 10 species and 40 reactions. Subgrid modelling of the chemical source term in this context was not necessary, since the ratio of Taylor microscale to filter width was well above 1 throughout the domain and more than an order of magnitude larger where the ignition occurred, i.e. in the core region. (The Taylor microscale in that context is an important lengthscale, since Wang and Peters found ignition kernels to be of the same order [193].)

5.3 Setup

5.3.1 Experiment

We simulated the experiment by Meyer and Oppenheim [166] using an undiluted-, stoichiometric H_2/O_2 mixture as a test gas. The pressures p_5 and temperatures T_5 behind the reflected shock were between 0.2–2.1 bar and 900–1300 K respectively and incident Mach numbers ranged from 2.3 to 2.9. To distinguish weak and strong ignition, Schlieren images were taken during each experiment. The shock tube was unusual in featuring a rectangular cross-section of 31.75 mm × 44.45 mm therefore making the case particularly suitable for our high-order numerics on Cartesian grids.

5.3.2 Simulations

Five simulations were carried out in two dimensions to study the sensitivity of the results on grid size, numerical discretization scheme, and initial conditions. Two costly simulations (Tab. 5.1) were performed in three dimensions. To lower the computational cost, only one half of the end section (250 mm) of the rectangular shock tube was simulated for a single experiment, for which mild ignition was observed, leading to a still high computational cost of 3.8 million core hours for the largest simulation with 1.38 billion cells. Additionally, Lagrangian particles were utilized to monitor the temperature history of material (gas) particles in time.

For each main run, one or two smaller precursor simulations were required. The first one resembled the typical Riemann problem, simulating not only the shock, but also the rarefaction wave. At the end of the first simulation, the shock front was located and three-dimensional profiles with approximately 10 cells before the shock-front and 50 cells behind the shock-front were stored. Those profiles contained realistic and thermodynamically compatible fields of temperature, pressure, velocities and species and were used as initial solution in the following runs. Channel flow simulations, initialised with the state behind the incident shock and periodic inlet/outlet, were executed partly to provide inlet (the open end of the domain, opposite to the end wall) conditions and to pre-calculate the boundary layer. However, tests showed negligible differences between these inlet conditions and a zero-gradient inlet condition applied to

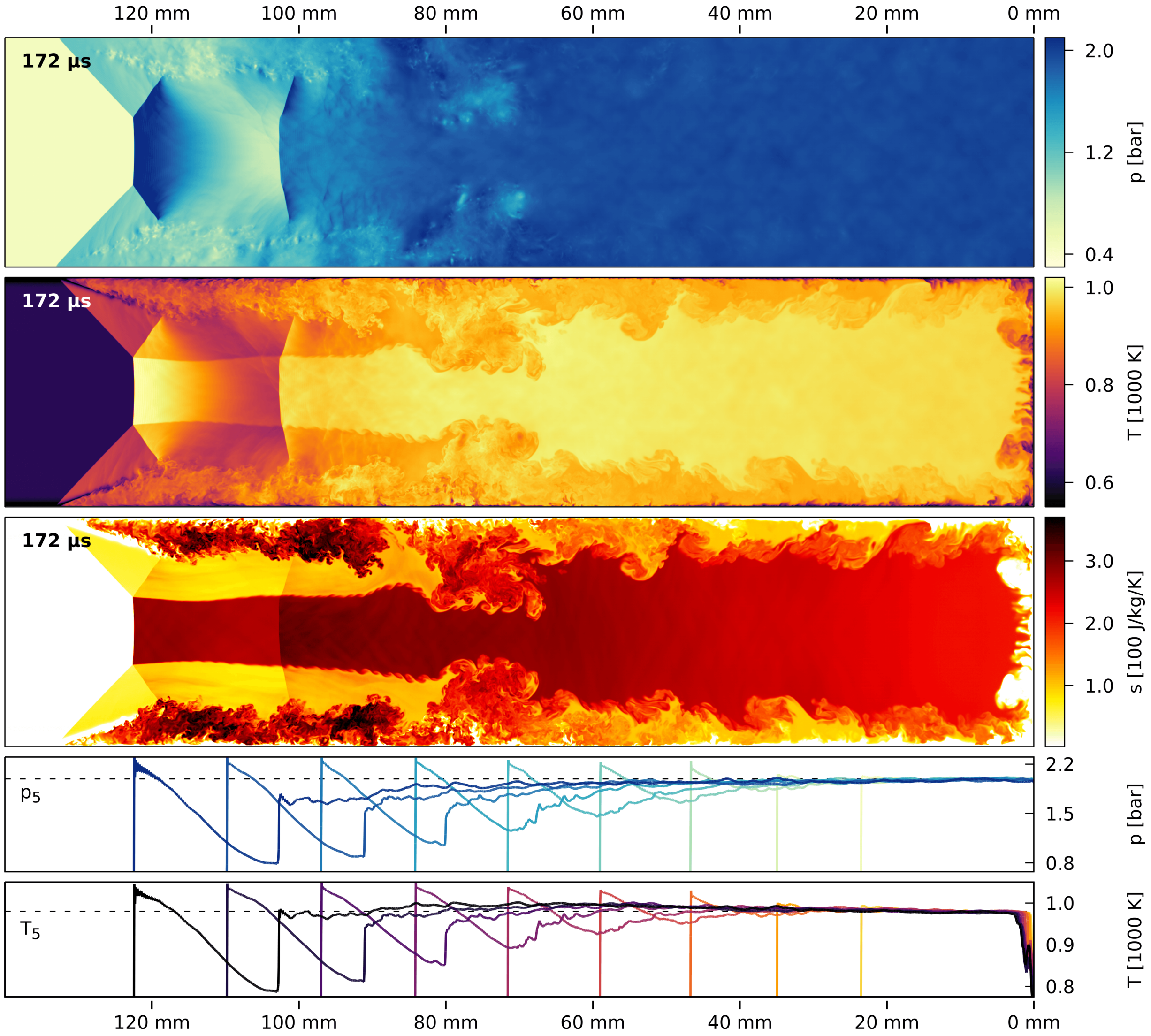

Figure 5.3: Instantaneous fields of pressure p, temperature T and specific entropy s at the top from a 3D simulation (3Db). Centreline profiles of pressure p and temperature T at the bottom coloured by respective timestep. Ignition will occur at approximately 70 mm from the end wall.

the primitive quantities for laminar boundary layers. It is important to note that incident shock attenuation outside the computational domain was not considered at the inlet. Hence, the effect of incident shock attenuation is highly reduced in our simulations and other effects contributing to mild ignition can be investigated.

5.4 Results

5.4.1 Checking the numerical treatment in 2D

Results from tests in 2D are presented first. Figure 5.2 shows pseudo-Schlieren images and the ignition kernels, visualized by superimposed fields of temperature above 1100 K. To investigate the effect of grid resolution on ignition delay time τ_{ig} (defined as time until maximum temperature in the simulation exceeds 1200 K), tests were conducted in two dimensions on grids with cell sizes of 100 µm (2Da), 50 µm (2Db), and 25 µm (2Dc), yielding ignition delay times of 170 µs, 175 µs, and 177 µs, respectively, so that all grid resolutions can be seen as sufficient to simulate the auto-ignition delay time. It seems that the

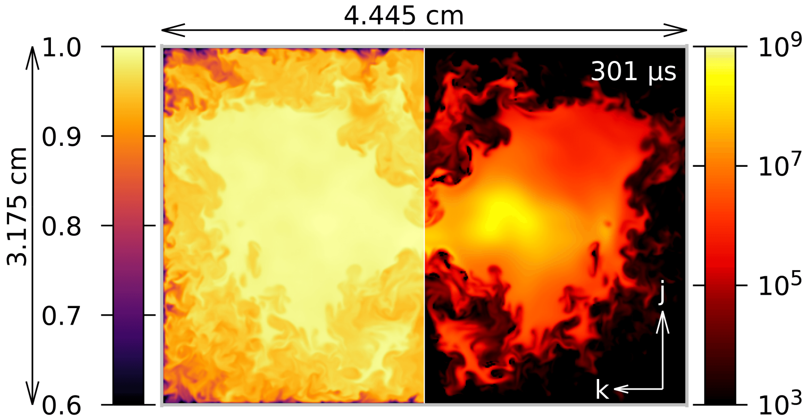

Figure 5.4: Instantaneous, mirrored plot of temperature T [1000 K] on the left and instantaneous plot of heat-release rate $\dot{\omega}_\mathrm{H}$ [W/m^3/s] on the right in a cross-section of the 3D-simulation (3Da) at 75 mm from the end wall at 301 µs.

underlying mechanism responsible for mild ignition in the investigated case does not heavily depend on grid resolution (at least in 2D), as long as the developing boundary layer behind the incident shock is sufficiently resolved. Figures 5.2 a-c illustrate the ignition event for the three grid resolutions. The locations of the ignition kernels appear to vary, though there is a consistent distance between the end wall and the nearest ignition kernels, suggesting a minimum distance at which ignition will occur. Overall, all ignition kernels presented in Fig. 5.2 appear between 40 and 70 mm from the end wall. In addition, similarities are observed with respect to the geometry of the bifurcation and the most important shock features for the three cases.

To check the effect of the discretization, a simulation was performed with a common TVD-scheme instead of the fifth-order, monotonicity preserving scheme at a grid resolution of 50 µm (2Dd). The ignition delay time was almost as before (τ_ig = 173 µs). Figure 5.2 shows that the result of this simulation is very similar to the solution of the higher order scheme at medium resolution. This is the case not only for the ignition delay time, but also for the location of the ignition kernel and the most notable vortex and shock structures. One might therefore consider the improvement achieved by the higher order scheme to be comparable to a refinement by a factor of two in each direction.

To test the impact of initial conditions, velocity perturbations were added to the initial velocity field with a standard deviation of 1 m/s. The perturbations were small and damped quickly after the start of the simulation and one might therefore expect no change of the results. However, when comparing the second (Fig. 5.2 b) and fifth plot (Fig. 5.2 e) at the very same timestep, it is striking that the initial conditions had a significant effect on the locations of ignition, demonstrating a very strong sensitivity. It should be noted though, that in the simulation without perturbations, further ignition kernels were visible shortly after and that ignition delay time was hardly affected. These observations lead to the conclusion that a meaningful simulation of the process in three dimensions is possible.

5.4.2 Mild ignition in 3D-LES simulations

Only three-dimensional simulations can consider realistic turbulence, but are far more expensive. Fields of the axial and vertical velocity component of the higher resolved, three-dimensional simulation (3Db) are depicted in Fig. 5.1 to provide a general idea of the flow fields in a bifurcated shock. Figure 5.3 presents instantaneous fields of pressure, temperature and entropy as well as profiles of pressure and temperature on the centreline from the same simulation. To illustrate fields in a cross-section of the shock tube, Fig. 5.4 presents temperature T on the left and heat-release rate $\dot{\omega}_\mathrm{H}$ on the right for the three-dimensional simulation (3Da) at a cell size of 100 µm and at a distance of 75 mm from the end wall. For convenience, the temperature field is mirrored according to the symmetry boundary condition in the middle plane. The yellow region in the plot of heat-release rate indicates the location of the mild ignition.

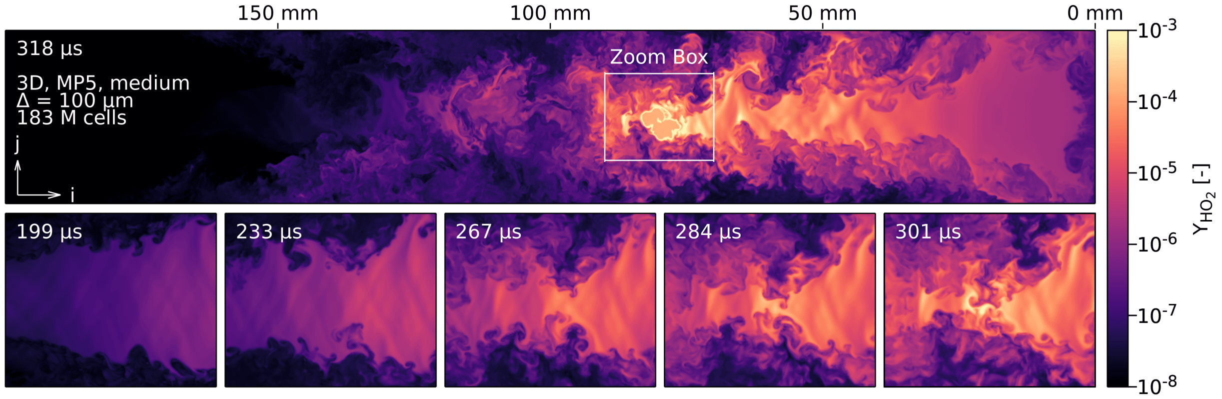

Figure 5.5: Instantaneous volume-rendered fields of species mass fraction Y_{HO_2} in the 3D simulation (3Da) shortly after ignition (first row) and prior to ignition inside the zoom-boxes (second row).

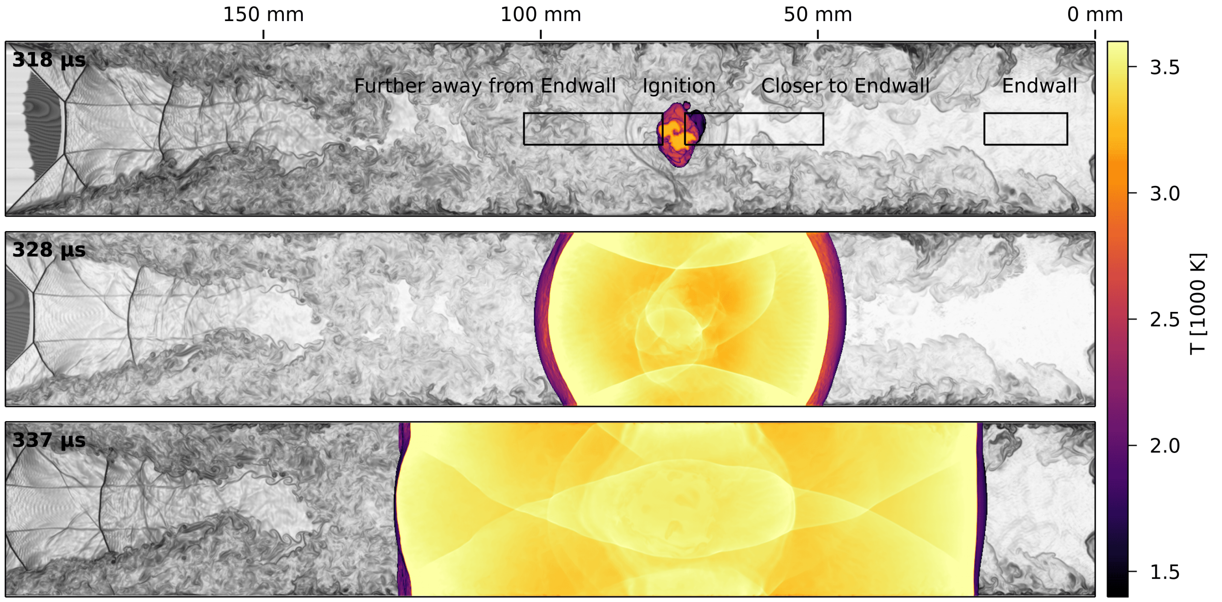

Figure 5.6: Ignition in 3D (3Da). Instantaneous plots of volume-rendered pseudo-Schlieren in the background and volume-rendered temperature T above 1100 K. Rectangles indicate the regions of Lagrangian particles that are discussed in the further analysis.

A striking feature of Fig. 5.3 is the expansion region behind the normal reflected shock, followed by a second normal shock. Interestingly, the observed flow field is reminiscent of the flow downstream of an overexpanded jet, leading to the formation of a shock-cell – here between the first and second normal shock. A fine description of the flow field physics has been provided by Weber et al. [194], who did numerical investigations of reflected shock/boundary-layer interaction in two dimensions with air as driven gas. The leading shock has formed the classical lambda foot so that the fluid that is adjacent to the boundary layer and that passes the oblique shock is deflected upwards. Afterwards, the fluid is compressed a second time by the tail shock, after which the static pressure equals the static pressure behind the normal reflected shock, as observed in Fig. 5.3. The boundary layer adjacent fluid maintains vertical momentum across the tail shock, as seen in Fig. 5.1, although the expansion fan behind the tail shock redirects it to the wall within a short distance. As a result, the fluid that passes the normal reflected shock, is initially forced towards the centreline by the boundary layer adjacent fluid, before it "follows" the boundary layer adjacent fluid outwards. Hence, the boundary layer adjacent fluid forms a Laval-nozzle shaped tube around the core fluid. This is well illustrated by the slip line (in Fig. 5.3), which indicates the interface between the fluids that have passed through the normal and the oblique shock. Initially, when the bifurcation structure is small, the subsonic fluid (in a shock-fixed frame) is accelerated in the convergent part without reaching a Mach number of $M = 1$. Subsequently it is compressed in the divergent part. But at some point, after the bifurcation structure grew further, the fluid in the smallest cross section of the "Laval nozzle" reaches a critical state and the supersonic fluid is further accelerated in the divergent part. Pressure waves originating from the elevated pressure reservoir at the end wall cannot travel upstream any more. As a result, a non-linear wave forms, which finally becomes the second normal shock. Since the bifurcation structure keeps growing after the smallest cross section reached a critical value, the flow is choked and the state behind the reflected shock changes accordingly. The axial profiles (Fig. 5.3) of this simulated flow are well in line with the results of Weber et al. [194]. The axial profiles of temperature and pressure (Fig. 5.3, bottom) reveal peaks behind the normal reflected shock, which are significantly higher than the values of T_5 and p_5, calculated the by the shock tube theory of Mark [168]. While the pressure decreases monotonically with end-wall distance, the temperature increases and reaches a maximum at a distance of approximately 60 mm. It is apparent that pressure and temperature are not connected by isentropic relations in this case with strong shock bifurcation. The snapshot of specific entropy s in Fig. 5.3, illustrates the increase of entropy with end-wall distance and the entropy production resulting from the second normal shock.

Preceding 0D reactor simulations with the same reaction mechanism revealed a peak of the mass-fraction of HO_2 immediately before auto-ignition. For that reason, it is a worthwhile indicator for the auto-ignition progress. Figure 5.5 presents the mass fraction of HO_2 shortly after ignition in the first row. It is remarkable that the HO_2 mass fraction on the centreline is up to 3 orders of magnitude higher than near the end wall. It is clear that mild ignition must occur near the middle plane of the shock tube, at least for this setup. The images in the second row show the ignition region at previous timesteps, implying that local turbulent structures and temperature fluctuations might affect ignition here.

In three dimensions, an ignition delay time of 305 µs (3Da) and 256 µs (3Db) is observed, which agrees with the experimental evidence [166] (250 µs $< \tau_{\mathrm{ig}} <$ 500 µs) and that is much faster than the ignition delay time obtained from 0D reactor simulations, initialised with the theoretical, idealised values T_5 and p_5 (see Table 5.2). However, care must be taken when comparing auto-ignition delay times from simulations with those of the experiments, due to uncertainties of the reaction mechanisms at the investigated low temperatures behind the reflected shock. Auto-ignition delay times from the 2D simulations are clearly shorter than those from the 3D simulations. This is mainly caused by a less pronounced incident shock attenuation in the 2D simulations during runtime, resulting in a higher temperature behind the reflected shock of T_5 = 985 K. Besides, mild ignition in 2D simulations often took place in high strain regions next to vortex structures that cannot survive in 3D, due to break-up of eddies into smaller eddies. Table 5.2 summarizes the auto-ignition delay time results from the simulations.

Figure 5.6 shows the ignition in the 3D case (3Da) by pseudo-Schlieren images superimposed with high temperatures. The "mild" ignition kernel appears in a highly turbulent region where a detonation wave develops and quickly expands, as presented in the second row of Fig. 5.6, leading to a "global ignition"

Indication	Dimensions	T_5	p_5	τ_{ig}	$\tau_{\mathrm{ig,ideal}}/\tau_{\mathrm{ig}}$
-	-	K	bar	µs	-
Experiment	-	980	1.80	> 250	-
0Da	0	980	2.00	1020	1.00
3Da	3	980	2.00	305	3.34
3Db	3	980	2.00	256	3.98
Experiment	-	990	1.80	150	-
0Db	0	985	2.02	638	1.00
2Da	2	985	2.02	170	3.75
2Db	2	985	2.02	175	3.65
2Dc	2	985	2.02	177	3.60
2Dd	2	985	2.02	173	3.69
2De	2	985	2.02	175	3.65

Table 5.2: Auto-ignition delay times τ_{ig} from simulations and the experiment for an initial state p_5/T_5 behind the reflected shock.Also given is the ratio of ideal ignition delay time $\tau_{\mathrm{ig,ideal}}$ to observed ignition delay time τ_{ig} to illustrate auto ignition delay time reduction, due to mild ignition.

long before strong ignition would be expected after 1020 µs. The observed wave speed is 2500 m/s, which is well in line with the theoretical result of 2600 m/s following Chapman-Jouguet theory.

5.4.3 Analysis with tracer particles

To investigate the temporal evolution of the thermochemical state of material fluid elements, Lagrangian tracer particles were utilized. In order to reduce the number of list entries (storing the temporal evolution of the tracked quantities), only one particle per Rank was initialised after the reflected shock reached the location of the Rank. This corresponds to a typical particle spacing of 1 particle / 2.1 mm. The local state was stored by the particles every few timestep achieving a high temporal resolution. For the further discussion, only certain particles were considered, which can be categorized as i) the particle to first exceed a threshold value of 1.0E-3 of the mass fraction of HO_2; this particle is labelled “Ignition particle”, and ii) particles that were located near the *ignition particle* but closer to the end wall at the time of ignition (labelled “Closer to Endwall”), and iii) particles that were located near the *ignition particle* but further away from the end wall at the time of ignition (labelled “Further away from Endwall”), and iv) particles that were located in a region near the end wall at the time of ignition (labelled “Endwall-region”). The boxes in Fig. 5.6 indicate the three regions and the approximate location of the *ignition particle*. Particles located in the colder boundary layer near the walls ignited late and were excluded from the analysis.

Time-histories of temperature and pressure are presented in Fig. 5.7 a)-c) for the four particle classes. The particle data show peak temperatures and pressures significantly above the expected values of T_5 and p_5 in accordance with the axial profiles of Fig. 5.3. After passing the “Laval nozzle” like flow, the temperatures of the *ignition particle* and nearby particles, settle at a higher level compared to the temperature level of particles near the end wall. Fig. 5.7 b) illustrates this temperature offset of the particles in more detail. Particles further away from the end wall and the *ignition particle* sensed local temperatures typically between 995 and 1000 K, while the particles closer to the end wall sensed temperatures between 985 K and 995 K. This is an important observation, since higher temperatures behind the reflected shock are usually attributed to shock attenuation of the incident shock, where a subsequent change of pressure can be observed as well and be linked to the change of temperature via isentropic relations, as reported by Petersen et al. [165]. However, the effect of incident shock attenuation outside of the computational domain is not modelled at the inlet, hence the reason for the temperature offset is likely to be different and caused by the gas dynamics behind the reflected shock. The temperature peaks of the observed particles overall increase with the distance of the particles from the end wall. However, specifically the *ignition particle* seems to reach a higher peak temperature, compared to neighbouring particles, which also reflects in the evolution of local heat release in Fig. 5.7e) . Here, the local heat release of the *ignition particle* is clearly greater compared to neighbouring particles. Since the second normal shock does not appear in the

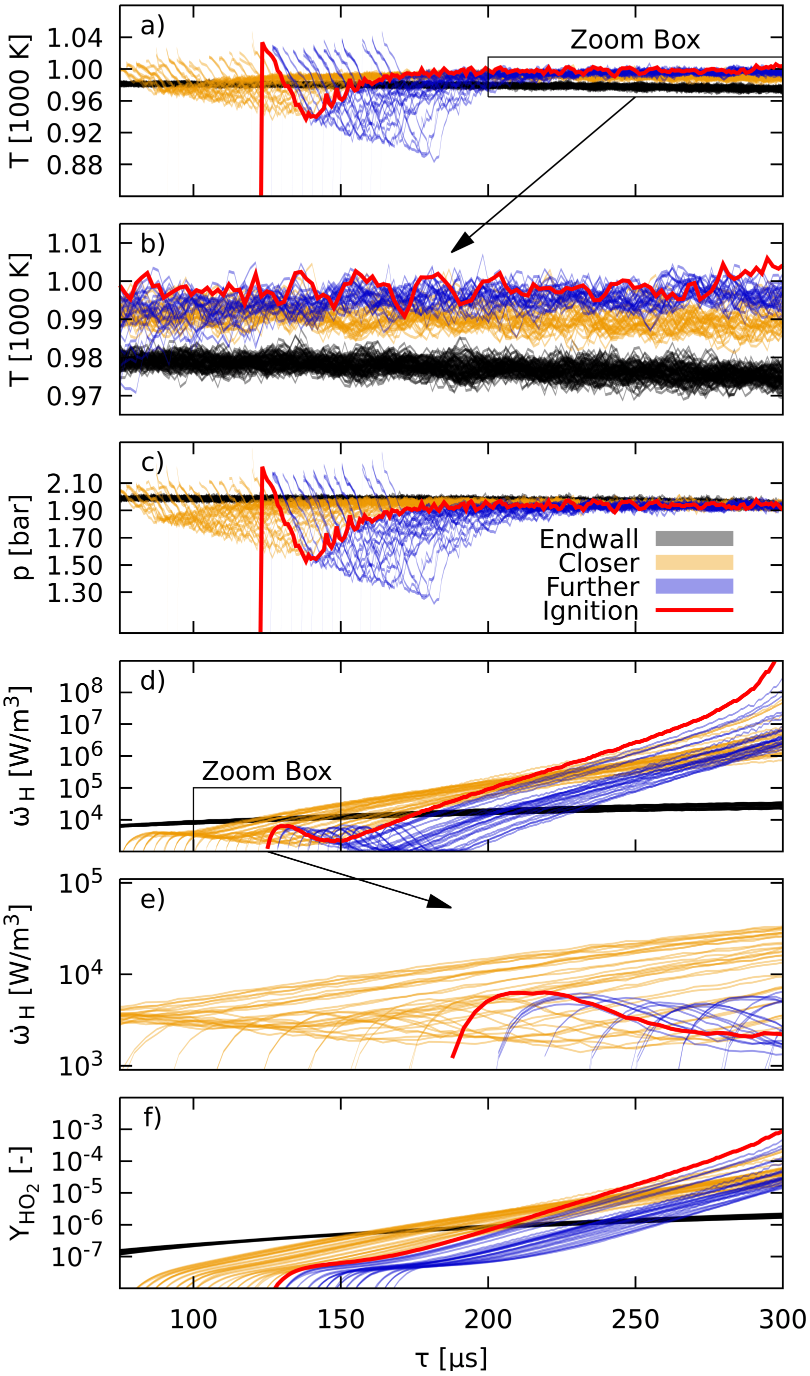

Figure 5.7: Histories of temperature T, pressure p, heat-release rate $\dot{\omega}_\mathrm{H}$ [W/m^3] and species mass fraction Y_{HO_2} from Lagrangian particle data. The trajectory of the *ignition particle* is red, particles closer to the end wall are shown in orange, further from the end wall in blue and particles near the end wall in black.

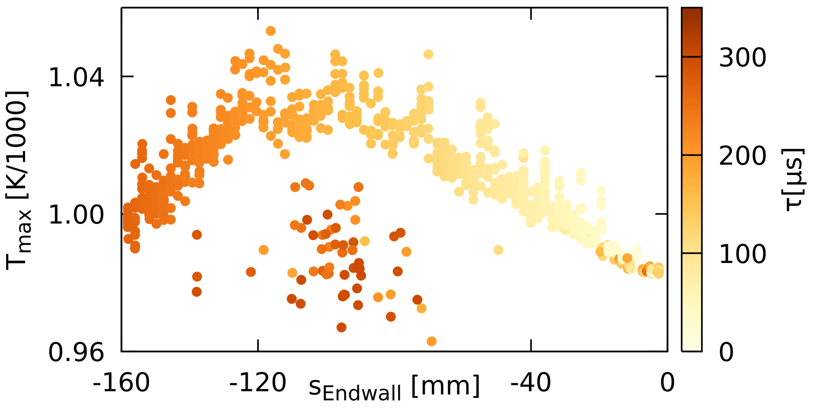

Figure 5.8: Temperature peaks $T_{\max}$ of Lagrangian particles with respect to the end wall distance, coloured by time τ, after the reflection of the shock.

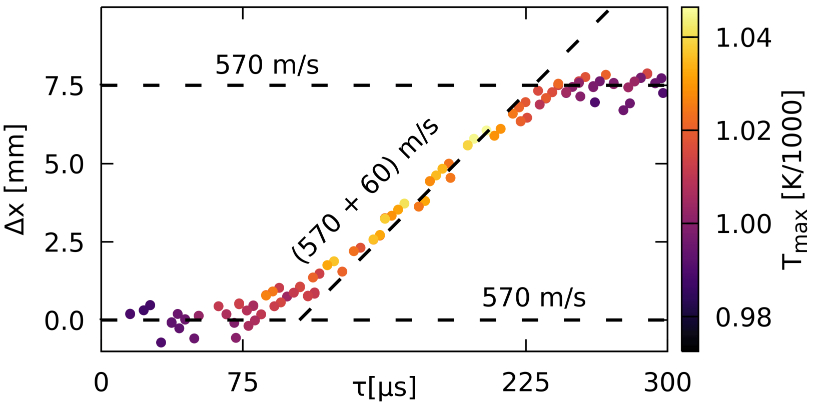

Figure 5.9: Deviation Δ x between position of reflected shock-front, reconstructed by Lagrangian particles, and position of shock-front at constant speed, coloured by maximum temperature $T_{\max}$. The slope of the inflectional tangent is 60 m/s.

data of the *ignition particle*, we notice that the second shock did not trigger the ignition. Nevertheless, the ignition location is nearly identical to the location, where the second shock appeared first, at a distance of approximately 70 mm from the end wall, as can be seen in Fig. 5.3.

At 125 µs after the compression, the HO_2 concentration of the *ignition particle* exceeds that of a particle that experienced the compression 50 µs earlier but which is located in a slightly cooler region. This illustrates the sensitivity of auto-ignition delay time τ_{ig} with respect to temperature, which is a prerequisite for the event of mild ignition according to the criterion of Meyer and Oppenheim [166]. The temperature offset of the *ignition particle*, compared to the temperature in the vicinity of the end wall (approximately $\Delta T = 20$ K), results in higher conversion rates and is responsible for the mild ignition according to the particle data.

Figure 5.8 shows the peak temperatures of the Lagrangian particles (near the centreline) and their corresponding end-wall distance at peak temperature, coloured by the time of peak temperature. First, the maximum temperatures on the centreline increase with the distance from the end wall. At 110 mm, a maximum is reached after which the maximum particle temperatures decrease again. The varying temperature observed in Fig. 5.8 implies that the strength and speed of the reflected shock must vary, since the state is nearly constant in front of the reflected shock.

The particle data can be used to reconstruct the reflected shock-front in space and time and to compare the location to a reflected shock, travelling at constant initial speed. Figure 5.9 illustrates the displacement Δx between the observed reflected shock and an ideal reflected shock propagating at a constant speed of 570 m/s.

Around 100 μs after the reflection of the shock at the end wall, the shock accelerates by 60 m/s, resulting in the observed shock leading the ideal shock by 7.5 mm. The increased Mach number of the reflected shock leads to higher temperatures behind it and hence faster ignition. It appears likely that the acceleration of the shock-front is a result of the bifurcation growth. Weber et al. [194] also observed an increase of reflected shock speed in two-dimensional simulations, while Matsuo et al. [195] measured a change of reflected shock speed in their experiments.

Hot spots as a source for mild ignition have been investigated already by Lamnaouer et al. [196] in a non-reactive, axisymmetric simulation covering the whole shocktube as well as by Khokhlov [179] in a three-dimensional reactive simulation. However, Lamnaouer et al. observed hot spots in the vicinity of the end wall, travelling towards the centreline in time, which we do not observe in our setup due to cold boundary layer fluid. Khokhlov [179] on the other hand, observed mild ignition near the corner of the shocktube, triggered by non-linear perturbations. We noted similar mild ignition locations at higher Mach numbers, but which is not in the scope of this paper.

Hence, this observation of varying reflected shock speed, which is consistent with previous results, enables us to link the increased speed of the reflected shock and remote ignition. We hope that our paper contributes to the understanding of such phenomena. Hanson et al. [197] for example, reported on repeatable remote ignition events at a constant distance away from the endwall, using $H_2/O_2/Ar$ mixtures at nearly the same temperature (T_5 = 990 K) that we had in our simulations. Interestingly, the "...exact mechanism leading to the remote ignition phenomenon is generally unknown ..." according to Hanson et al. [197].

5.5 Conclusions

Two-dimensional simulations and three-dimensional highly resolved large eddy simulations of shock-tube experiments have been presented. The results emphasize the importance of the role that gas dynamic effects and turbulence play for mild ignition in shock tubes, specifically for bifurcated shocks.

The simulations in three dimensions predicted realistic ignition delay times in line with the experiment, whereas simulations in two dimensions had less incident shock attenuation during runtime, resulting in shorter ignition delay times.

The particle histories in time led to the conclusion that mild ignition results from an initial peak in temperature and a sustained offset in temperature behind the expansion region in addition to local temperature variations due to wave phenomena and turbulence. The *ignition particle* in particular was set apart from neighbouring particles by an even higher temperature.

The observed increase of temperature behind the reflected shock, partially results from a "Laval-nozzle" shaped core flow, caused by the displacement due to the bifurcation. This reflects in a varying speed of the reflected shock and is consistent with earlier observations [194, 195].

Modern shock tubes have larger diameters compared to the shock tube investigated in this paper, hence the required time until the observed flow field and the resulting effects would have an impact, is significantly longer. However, since low temperature kinetics need to be looked after, where typical ignition delay times can exceed several ms, the observed phenomena could explain ignition events far from the endwall (e.g. Fieweger et al. [198] or Hanson et al. [197]) even nowadays.

Acknowledgements

The authors gratefully acknowledge the financial support by DFG grant KE 1751/8-1, the computing time on magnitUDE granted by the Center for Computational Sciences and Simulation of the Universität of Duisburg-Essen through DFG INST 20876/209-1 FUGG, INST 20876/243-1 FUGG at the Zentrum für Informations- und Mediendienste and the computing time on the supercomputer HazelHen (ACID 44116).

Chapter 6
Numerical Investigation of Remote Ignition in Shock Tubes

Numerical Investigation of Remote Ignition in Shock Tubes [7]

Authors: J. T. Lipkowicz, I. Wlokas, A. M. Kempf
This chapter including all figures and tables was previously published in 'Flow, Turbulence and Combustion, 106, J. T. Lipkowicz, D. Nativel, S. Cooper, I. Wlokas, M. Fikri, E. Petersen, C. Schulz and A. M. Kempf, Numerical Investigation of Remote Ignition in Shock Tubes, 471 - 498, Copyright ©Springer (2019)' and is reprinted with permission from Springer. The author J. T. Lipkowicz developed the codes for the CFD simulations and the post-processing tasks, performed all the simulations, wrote the paper and generated all figures and tables. The author D. Nativel conducted all experiments at the university of Duisburg-Essen and S. Cooper conducted all experiments at the university of Texas. The authors I. Wlokas, M. Fikri, E. Petersen, C. Schulz and A. M. Kempf contributed corrections, discussions, and proof-reading.

Abstract

Highly resolved two- and three-dimensional computational fluid dynamics (CFD) simulations are presented for shock-tube experiments containing hydrogen/oxygen (H_2/O_2) mixtures, to investigate mechanisms leading to remote ignition. The results of the reactive cases are compared against experimental results from Meyer and Oppenheim (*Proc. Combust. Inst.* 13 (1971) 1153-1164) and Hanson *et al.* (*Combust. Flame* 160 (2013) 1550-1558). The results of the non-reactive case are compared against shock tube experiments, recently carried out in Duisburg and Texas. The computational domain covers the end-wall region of the shock tube and applies high order numerics featuring an all-speed approximate Riemann scheme, combined with a 5$^{\text{th}}$ order interpolation scheme. Direct chemistry is employed using detailed reaction mechanisms with 11 species and up to 40 reactions, on a grid with up to 2.2 billion cells. Additional two-dimensional simulations are performed for non-reactive conditions to validate the treatment of boundary-layer effects at the inlet of the computational domain. The computational domain covers a region at the end part of the shock tube. The ignition process is analyzed by fields of localized, expected ignition times. Instantaneous fields of temperature, pressure, entropy, and dissipation rate are presented to explain the flow dynamics, specifically in the case of a bifurcated reflected shock. In all cases regions with locally increased temperatures were observed, reducing the local ignition-delay time in areas away from the end wall significantly, thus compensating for the late compression by the reflected shock and therefore leading for first ignition at a remote location, i.e., away from the end wall where the ignition would occur under ideal conditions. In cases without a bifurcated reflected shock, the temperature increase results from shock attenuation. In cases with a bifurcated reflected shock, the formation of a second normal shock and shear near the slip line is found to be crucial for the remote ignition to take place. Overall, the two- and three-dimensional simulations were found to qualitatively explain the occurrence of remote ignition and to be quantitatively correct, implying that they include the correct physics.

6.1 Introduction

6.1.1 Shock Tubes

Shock tubes have been an important tool for many years to investigate fast reaction kinetics and to support the development of reaction mechanisms. A membrane initially separates a pressurized inert gas in the driver section (denoted as region 4) at an elevated pressure from the test mixture in the driven section (denoted as region 1). The experiment starts in the instant the membrane bursts, after which a shock (incident shock) quickly evolves due to the pressure difference. A contact discontinuity forms at the place where the driven and driver gases touch, creating a zone of compressed driven gas between contact discontinuity and incident shock (referred to as region 2) and a zone of expanded driver gas between contact discontinuity and expansion fan (region 3). Eventually, the incident shock wave will reach the end wall of the shock tube having accelerated all driven gas towards the end wall. The shock is then reflected (reflected shock), running back towards the driver gas, and bringing the driven gas to rest, thus increasing pressure and temperature (designated as region 5). The initial conditions are usually chosen such that the temperature T_5 behind the reflected shock exceeds 800 K, initiating chemical reactions, so that an ignition-delay time τ_{ig} can be measured [199]. It must, however, be ensured that the ignition-delay time is sufficiently short compared to the possible test time that is limited by the arrival of the contact discontinuity. At high temperatures and accordingly short ignition-delay times ($\tau_{\text{ig}} < 1$ ms), a nearly homogeneous thermodynamic state establishes (until the mixture ignites) behind the reflected shock and the problem can be modeled as inviscid and adiabatic [200]. These well defined initial boundary conditions allow to compare the measurements to those of a perfectly mixed reactor at constant volume.

At longer test times, several phenomena, most of them directly related to the formation of a boundary layer initiated by the motion of the incident shock, can severely impact the results and lead to huge deviations of measured ignition-delay time and the expected ignition-delay time at constant volume. The effect of the boundary layer is well known: It decelerates the (near-wall) flow behind the incoming shock and thus “removes” mass from the core flow and therefore affects the state in the core flow outside of the boundary layer. The change of state in the core-flow has been modeled by Mirels [201–203], using perturbation theory and has been successfully applied to compute the attenuation of the incident shock or the change of state at a given location in time. According to perturbation theory, the pressure can be approximated by the superposition of the ideal pressure from an adiabatic, inviscid process and weak pressure perturbation waves. This leads to a spatially and temporally changing distribution of state quantities behind the incident shock (non-uniformities) and also affects the change of state behind the reflected shock, as the pressure variations are amplified across the reflected shock [204]. Assuming a purely laminar or purely turbulent boundary layer, Mirels found that the state quantities are constantly increasing between the incident shock and the contact discontinuity. While pressure and temperature fall short compared to the ideal values, the particle velocity behind the shock front decreases due to the reduced shock strength, but accelerates near the contact discontinuity. Hence, the distance between the incident shock wave and the contact discontinuity decreases and the maximum test time is reduced. In some cases, *e.g.*, at very low pressures, the contact discontinuity can even reach the speed of the incident shock [205]. Typically, the boundary-layer induced variations of state lead to a slow, continuous rise of pressure ($\partial p_5/\partial t$) at the end wall.

Another boundary-layer effect is due to the interaction with the reflected shock under conditions that promote the formation of a shock-bifurcation structure. Mark [168] developed a simple model to predict the occurrence of the shock bifurcation and to describe the geometry and size of this structure. A brief summary is given below.

For his analysis, Mark examined the Mach number of the fluid in the boundary layer M_{bl} and in the main flow M_2 in reflected-shock coordinates. Mark made the assumptions that the fluid in the boundary layer is in thermal equilibrium with the wall and has no velocity relative to laboratory coordinates. He found that the boundary layer Mach number M_{bl} (as one would expect due to the velocity deficit) is below the Mach number of the main flow M_2 at moderate Mach numbers M_1 of the incident shock, as presented in Fig. 6.1. However, if the Mach number M_1 further increases, a critical point M_1^* is reached

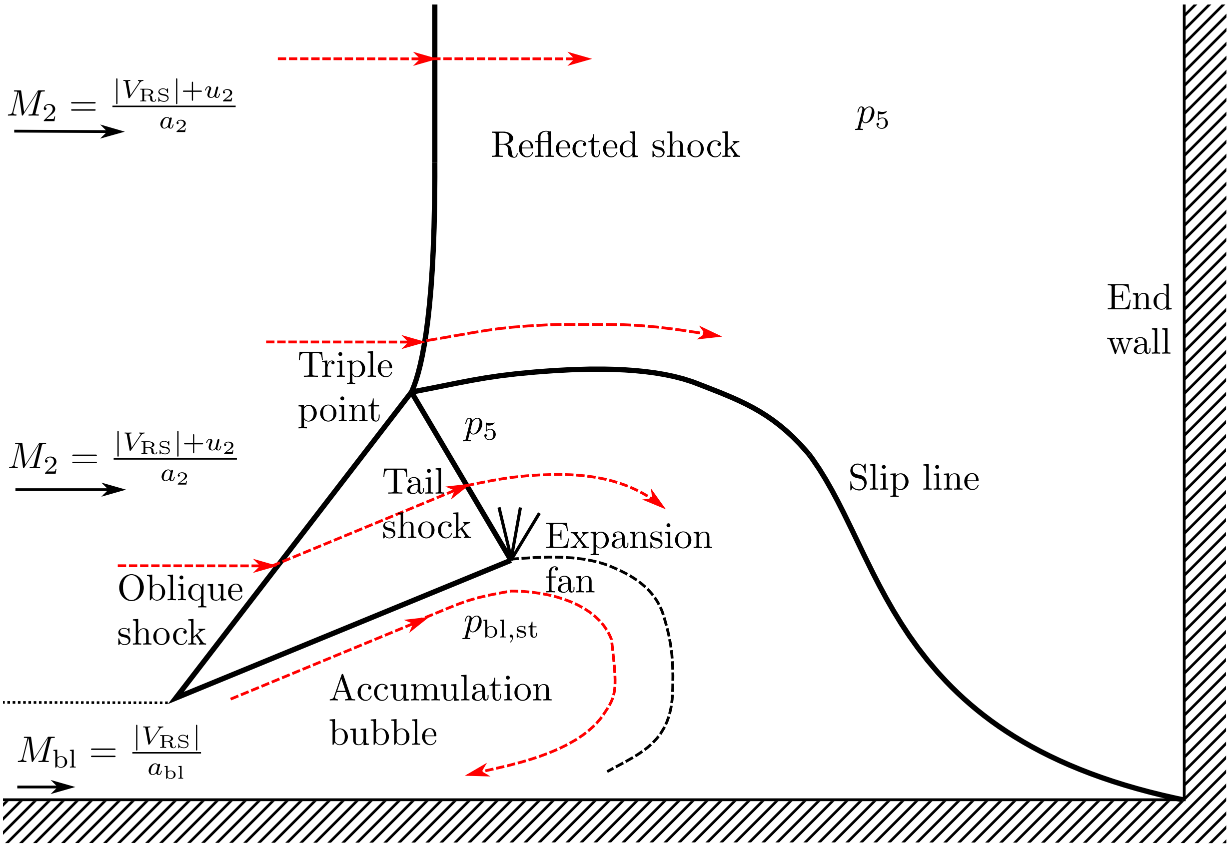

Figure 6.1: Sketch of a bifurcation structure, showing the speed of the reflected shock V_{RS} in laboratory coordinates, the particle speed u_2 in region 2 in laboratory coordinates, the speed of sound a_2 in region 2, and the speed of sound a_{bl} in the boundary layer. M_2 and M_{bl} are Mach numbers in reflected shock coordinates. Solid lines indicate locations with high density gradients. Dashed lines show particle paths. The sketch shows the bifurcation structure under flow conditions such that the Mach number of the boundary layer is less than 1 and thus no shock occurs in the boundary layer.

after which the boundary-layer Mach number M_{bl} exceeds the Mach number M_2 of the main flow. This phenomenon is due to the cooling effect of the wall. It is also worth noting that the ratio of specific heats γ has a very large influence. The point at which the Mach number of the boundary layer exceeds that of the main stream is reached earlier for large values of γ (*e.g.*, $M_1^* = 7.4$ for $\gamma = 1.4$, $M_1^* = 3.8$ for $\gamma = 1.67$). In addition, the stagnation pressure of the boundary layer $p_{\mathrm{bl,st}}$ and the static pressure of the main flow p_5 behind the reflected shock were investigated and compared. At an incident Mach number M_1 close to 1, the stagnation pressure $p_{\mathrm{bl,st}}$ is higher than the static pressure p_5 of the main flow and the boundary layer fluid can pass the reflected shock into the end-wall region. At higher incident shock Mach numbers, a lower crossover point $M_{1,\mathrm{L}}$ is reached, where the static pressure of the main flow p_5 exceeds the stagnation pressure $p_{\mathrm{bl,st}}$ instead. The interaction of shock and boundary layer is expected to be fundamentally different at Mach numbers M_1 larger than the lower cross-over point $M_{1,\mathrm{L}}$. If the stagnation pressure in the boundary layer is below the static pressure in the main flow, the boundary layer fluid cannot match the static pressure even after stagnating. Instead, as it works against the static pressure of the main flow, it is decelerated until stagnation and reversely accelerated in the direction of the reflected shock, causing the fluid to accumulate. This phenomenon is referred to as bifurcation of the reflected shock. At even higher Mach numbers of the incident shock, the Mach number of the boundary layer surpasses that of the main flow at the Mach number M_1^*. As a result, an upper cross-over point $M_{1,\mathrm{U}}$ exists, after which the boundary-layer fluid can pass the reflected shock again and no bifurcation emerges. It is important to note that the two crossover points are closer together in the case of large ratios of specific heats, while the ratio $p_{\mathrm{bl,st}}/p_5$ is higher at the same time (*e.g.*, $M_{1,\mathrm{L}} = 1.33$, $M_{1,\mathrm{U}} = 6.45$ and $p_{\mathrm{bl,st}}/p_5 \geq 0.5$ for $\gamma = 1.4$, $M_{1,\mathrm{L}} = 1.57$, $M_{1,\mathrm{U}} = 2.8$ and $p_{\mathrm{bl,st}}/p_5 \geq 0.9$ for $\gamma = 1.67$). Furthermore, the assumptions that are made to calculate the limits of this phenomenon are very conservative. In fact, shock-tube experiments containing a gas or a mixture with large values of γ (*e.g.*, Argon) are very unlikely to suffer from reflected shock bifurcation [206].

A bifurcation structure is characterized by a triple point, where the oblique shock, the normal reflected shock and the tail shock meet. A slip line emerges from the triple point, which separates fluid from the oblique shock and the normal reflected shock. While the fluid behind the shock and along the slip is mechanically in balance, the difference in entropy provokes instabilities and triggers the formation of vortices. The flow field behind a bifurcated reflected shock is always inhomogeneous and the variations in temperature can provoke the ignition from small ignition kernels (mild-ignition) [6].

6.1.2 Remote Ignition

Under ideal conditions and corresponding homogeneous fields of pressure and temperature behind the reflected shock, the reactive mixture will always ignite at the end wall of the shock tube, as the ignition process depends exclusively on the time that passed after the compression by the reflected shock wave. This type of ignition is commonly referred to as strong ignition. Under real conditions, however, ignition processes were frequently observed that start from small ignition kernels at various positions in the test section [172–174] and often transition into a detonation. These ignition kernels can be located near the end wall (*e.g.*, along the slip line in case of a bifurcated shock, which will be denoted as mild ignition) or further away, which we will refer to as remote ignition. For mild ignition to occur, the ignition-delay time in general must exceed a certain, yet unknown, limit so that flow-induced inhomogeneities can evolve in the flow field, which significantly reduces the local ignition-delay time. One criterion by Meyer and Oppenheim [166] states that the change of ignition-delay time with respect to the change of temperature $(\partial\tau_{\mathrm{ig}}/\partial T)_p$ must be below a critical value (*e.g.*, $\partial\tau_{\mathrm{ig}}/\partial T = -2$ µs/K for stoichiometric hydrogen/oxygen mixtures) such that mild ignition occurs. Many numerical studies were published studying the mild ignition phenomenon in shock tube-simulations in 2D [176–178] and 3D [179]. The studies focussed on the impact of the incident shock Mach number [176], the evolution of ignition kernels due to velocity fluctuations [177], the effect of wall treatment on mild ignition [178], and the development of hot spots in 3D [179]. However, all these studies featured cases with bifurcated reflected shocks, while remote ignition was also observed in the absence of bifurcated reflected shocks [197]. The present paper aims to shed light on the physics of remote ignition in cases with and without bifurcated reflected shocks.

6.2 Numerical Details

6.2.1 Code

The simulations are carried out with the in-house code *PsiPhi* that has been developed at Imperial College in London and at the university of Duisburg-Essen by Kempf and co-workers [6, 183, 207, 208]. PsiPhi solves the fully compressible set of Favre-filtered conservation equations for mass, momentum, total absolute internal energy and partial densities to simulate reactive flow problems:

$$\frac{\partial \bar{\rho}}{\partial t} + \frac{\partial \bar{\rho}\tilde{u}_\mathrm{i}}{\partial x_\mathrm{i}} = 0 \tag{6.1}$$

$$\frac{\partial \bar{\rho}\tilde{u}_\mathrm{i}}{\partial t} + \frac{\partial \bar{\rho}\tilde{u}_\mathrm{i}\tilde{u}_\mathrm{j}}{\partial x_\mathrm{j}} = -\frac{\partial \bar{p}}{\partial x_\mathrm{i}} + \frac{\partial \bar{\tau}_\mathrm{ij}}{\partial x_\mathrm{j}} \tag{6.2}$$

$$\frac{\partial \bar{\rho}\tilde{E}}{\partial t} + \frac{\partial \bar{\rho}\tilde{u}_\mathrm{i}\left(\tilde{E} + \bar{p}/\bar{\rho}\right)}{\partial x_\mathrm{i}} = \frac{\partial\left(\bar{q}_\mathrm{j} + \tilde{u}_\mathrm{i}\bar{\tau}_\mathrm{ij}\right)}{\partial x_\mathrm{j}} \tag{6.3}$$

$$\frac{\partial \bar{\rho}\tilde{Y}_\mathrm{k}}{\partial t} + \frac{\partial \bar{\rho}\tilde{u}_\mathrm{i}\tilde{Y}_\mathrm{k}}{\partial x_\mathrm{i}} = \frac{\partial\left(\bar{j}_\mathrm{i,k} + \bar{\rho}\tilde{Y}_\mathrm{k}V_\mathrm{i,c}\right)}{\partial x_\mathrm{i}} + \bar{\dot{\omega}}_\mathrm{k} \tag{6.4}$$

$$\bar{\tau}_\mathrm{ij} = (\bar{\mu} + \mu_\mathrm{t})\left[\frac{1}{2}\left(\frac{\partial \tilde{u}_\mathrm{j}}{\partial x_\mathrm{i}} + \frac{\partial \tilde{u}_\mathrm{i}}{\partial x_\mathrm{j}}\right) - \frac{1}{3}\delta_\mathrm{ij}\frac{\partial \tilde{u}_\mathrm{k}}{\partial x_\mathrm{k}}\right] \tag{6.5}$$

$$\bar{q}_\mathrm{j} = \left(\bar{\lambda} + \frac{\mu_\mathrm{t}\bar{c}_\mathrm{p}}{\mathrm{Pr}_\mathrm{t}}\right)\frac{\partial \bar{T}}{\partial x_\mathrm{j}} \tag{6.6}$$

$$\bar{j}_{i,k} = \left(\bar{\rho}\bar{D}_\mathrm{k} + \frac{\mu_\mathrm{t}}{\mathrm{Sc}_\mathrm{t}}\right)\frac{\partial \bar{Y}_\mathrm{k}}{\partial x_\mathrm{i}} \tag{6.7}$$

The equations feature the Favre-filtered velocity components $\tilde{u}_\mathrm{i}$ in the ith direction, the Favre-filtered total absolute internal energy $\tilde{E}$, the viscous stress tensor $\bar{\tau}_\mathrm{ij}$, the heat-flux density $\bar{q}_\mathrm{i}$ due to heat conduction and due to enthalpy fluxes caused by mass diffusion, the Favre-filtered mass fraction $\tilde{Y}_\mathrm{k}$ of the kth species, the source term $\bar{\dot{\omega}}_\mathrm{k}$ of species k, the mixture-averaged diffusion $\bar{j}_\mathrm{i,k}$ of species k, and the correction velocity $V_\mathrm{i,c}$ to achieve consistency between partial densities and the transported density.

Applying a LES (large-eddy simulation) filter operation to the Navier-Stokes equations leaves unclosed terms that need to be modeled. In this work, sub-filter fluxes are modeled with the eddy-viscosity approach for momentum and the eddy-diffusivity approach for scalars with a turbulent Schmidt- and turbulent Prandtl number of $\mathrm{Sc}_\mathrm{t} = \mathrm{Pr}_\mathrm{t} = 0.7$, where the sub-grid viscosity is computed using the σ-model proposed by Nicoud *et al.* [55]. (The sigma model has been tested extensively against the static and dynamic Smagorinsky model, using the in-house code *PsiPhi* [209].)

No modeling is required with regards to the filtered chemical source term, since gradients of scalars are small in the ignition regions. (This assumption is generally valid until combustion waves lead to strong spatial gradients of the scalars. However, this work focuses on the period up to the ignition only.)

The finite-volume method (FVM) is utilized to discretize the equations on an equidistant, cartesian grid, where no local refinement or coarsening is applied to ensure a high level of consistency, even in the region behind the reflected shock, where transport and mixing must be resolved to predict weak ignition. *PsiPhi* uses a distributed memory domain decomposition approach, utilizing the message passing interface (MPI) and a non-blocking implementation for simultaneous computations and exchange of data, yielding high parallel efficiency. Diffusive fluxes are discretized using a 2nd order accurate central-difference scheme. The solution is advanced in time, using a low-storage explicit Runge-Kutta scheme [186] of 3rd order.

A wide range of velocities is present in simulations of shock-tube experiments. Hence, the all-speed approximate Riemann solver HR-Slau2 [210] developed by Kitamura, is used for the computation of convective fluxes, which reduces the contribution of the numerical dissipation term regarding the computation of the interface pressure in the low Mach-number limit. The states left and right to a cell interface are determined by a 5th order accurate monotonicity-preserving reconstruction scheme (*MP5*) by Suresh and

Huynh [211] that either reconstructs the local, one-dimensional characteristic variables or the set of primitive variables. The five-point stencil of the reconstruction scheme is also used to distinguish discontinuities from extrema such that the accuracy reduces to first order only next to discontinuities. The reconstruction scheme of Suresh and Huynh has been tested against the classical weighted essentially non-oscillatory (*WENO5*) scheme by Scandaliato *et al.* [212], where it proved to be more efficient and more accurate. Both of the reconstruction schemes have also been tested in a publication by Zhao *et al.* addressing the wave propagation errors of smooth waves, when interacting with discontinuities [213], where the *MP5* scheme turned out to be a good compromise regarding wave propagation errors and was slightly more efficient than other schemes with a formal accuracy of 5th order. Further publications have dealt with the properties and defects of shock-capturing schemes. The reader is referred to the works of Pirozzoli [214], Larsson [215], Quirk [216], and LeVeque [217].

One of the disadvantages of using a high-order scheme and characteristic variables is the occurrence of strong oscillations under special circumstances, for example when two discontinuities interact [218]. This can manifest in negative values of density and pressure. In order to avoid these unphysical solutions, recursive-order reduction (ROR) is partially applied [143]. A completely different problem concerns the numerical dissipation of a Riemann solver at low speeds, for example in a boundary layer. The jump of normal velocity components across a cell interface is the main contribution to numerical dissipation in the context of high-order, shock-capturing schemes, according to Thornber *et al.* [219]. He proposed a simple fix [220] that relaxes the normal velocity components towards the arithmetic average as the low Mach-number limit is reached.

Thermochemical and transport properties of individual species and reaction-rate constants are first determined for each species with the aid of Cantera [187] and tabulated as a function of temperature to reduce computational effort. Reaction rates are computed during runtime, using the tabulated reaction-rate constants and the effective local concentrations. Furthermore, reaction-rate constants of fall-off reactions that depend on pressure, are tabulated not only as a function of temperature, but also as a function of effective concentration. The mixture-averaged molecular viscosity, heat conductivity, and molecular diffusion are determined by models of Wilke *et al.* [221], Peters *et al.* [189], and Kee *et al.* [190] respectively. Direct chemistry is used, where the system of ordinary differential equations, is implicitly solved by CVODE [191] within a Strang [91] operator-splitting framework. The reaction model FFCM-1 by Smith *et al.* (foundational fuel chemistry model, 29 reactions / 11 species) [222] and alternatively the model by O'Conaire (40 reactions / 11 species) [223] are used to simulate auto-ignition in hydrogen-oxygen mixtures.

6.2.2 Simulation Setup and Experimental Facilities

Simulations are conducted with non-reactive mixtures (*NR*) and reactive hydrogen-oxygen mixtures (*R*) at low pressure. The results are compared to shock-tube experiments from Berkeley (*B*) [166], Duisburg (*D*), Stanford (*S*) [197], and from Texas A&M (*T*), as summarized in Tab. 6.1 and 6.2. Argon is used as the main component of the test gas throughout the non-reactive cases to suppress the occurrence of a reflected shock bifurcation. The addition of small amounts of carbon monoxide (CO) in the experiments (*NRD3-NRD6*) allowed the measurement of temperature using a two-color fixed-wavelength thermometry technique. The experiments in the (small) Berkeley shock tube with a rectangular cross section ($31.75 \times 44.45\,\mathrm{mm}^2$) are simulated in 3D, the experiments in the other (larger) shock tubes in 2D only, due to the high computational cost.

The numerical domain of the main simulations covers the end part of the shock tube (13.5-132 cm) to allow a higher numerical resolution. In order to have realistic profiles of scalar quantities and velocities behind the incident shock wave in terms of a suitable initial solution, precursor simulations from the time of membrane rupture are performed. After the Mach number of the incident shock has reached the target value, a part of the solution behind the incident shock is stored and applied as an initial condition for the following main run. An isothermal no-slip boundary condition is used at all boundaries, except for the inlet of the numerical domain, located on the "left" of the numerical domain.

Simulations that cover only the end part of the shock tube require that the evolution of the state variables

Table 6.1: Overview of two-, and three-dimensional simulations performed in the scope of this work. D and W depict the geometry, where D is the diameter (or the height regarding ducts) and W is the width of the numerical domain in k-direction. The numerical grid resolution is denoted by Δ with the number of cells n_I, n_J, and n_K in the corresponding directions.

	Case	D	W	Δ	n_I	n_J	n_K
		mm	mm	µm			
2D	NRT1	162	-	50	15,600	3,240	-
	NRT2	162	-	50	15,600	3,240	-
	NRD1	80	-	50	15,600	1,600	-
	NRD2	80	-	50	15,600	1,600	-
	NRD3	80	-	50	15,600	1,600	-
	NRD4	80	-	50	15,600	1,600	-
	NRD5	80	-	50	15,600	1,600	-
	NRD6	80	-	50	15,600	1,600	-
2D	RS1	141.3	-	100	13,200	1,400	-
	RS2	141.3	-	100	13,200	1,400	-
	RS3	141.3	-	100	13,200	1,400	-
3D	RB1	31.75	44.45	50	3,978	624	884
3D	RB1	31.75	44.45	50	3,978	624	884
	RB2	31.75	44.45	50	2,704	624	884

Table 6.2: Overview of two-, and three-dimensional simulations performed in the scope of this work. The shock Mach number M refers to the value just before the reflection. p_1 is the pressure of the initial quiescent gas in the driven section with the pressure p_5 and T_5 behind the reflected shock. The ideal ignition-delay time $\tau_{\mathrm{ig},0}$ is the result of zero-dimensional reactors at constant volume/energy and τ_ig is the result from the two-, and three-dimensional simulations. To compute the source terms of individual species caused by chemical conversion, either the O'Conaire mechanism or the foundational fuel chemistry model are used.

	Case	Mixture	M	p_1	p_5	T_5	$\tau_{\mathrm{ig},0}$	$\tau_\mathrm{ig}/\tau_{\mathrm{ig},0}$	Mechanism
		vol%		mbar	mbar	K	ms		
2D	NRT1	100 Ar	2.19	74.7	1481	1204	-	-	-
	NRT2	100 Ar	2.51	48	1408	1539	-	-	-
	NRD1	100 Ar	2.43	120	3210	1441	-	-	-
	NRD2	100 Ar	2.20	75	1490	1198	-	-	-
	NRD3	95 Ar / 1 CO / 4 H_2	2.82	44.3	1810	1845	-	-	-
	NRD4	95 Ar / 1 CO / 4 H_2	2.67	57.9	2030	1665	-	-	-
	NRD5	95 Ar / 1 CO / 4 H_2	2.46	72	1990	1432	-	-	-
	NRD6	95 Ar / 1 CO / 4 H_2	2.30	86	1960	1269	-	-	-
2D	RS1	94 Ar / 4 H_2 / 2 O_2	2.01	240	3632	992	3.750	0.61	FFCM-1
	RS2	94 Ar / 4 H_2 / 2 O_2	2.00	240	3592	986	5.780	0.53	FFCM-1
	RS3	94 Ar / 4 H_2 / 2 O_2	2.00	240	3592	986	6.370	0.46	O'Conaire
3D	RB1	66.67 H_2 / 33.33 O_2	2.46	70	2053	980	1.092	0.26	O'Conaire
	RB2	66.67 H_2 / 33.33 O_2	2.45	35	1015	974	0.142	0.99	O'Conaire

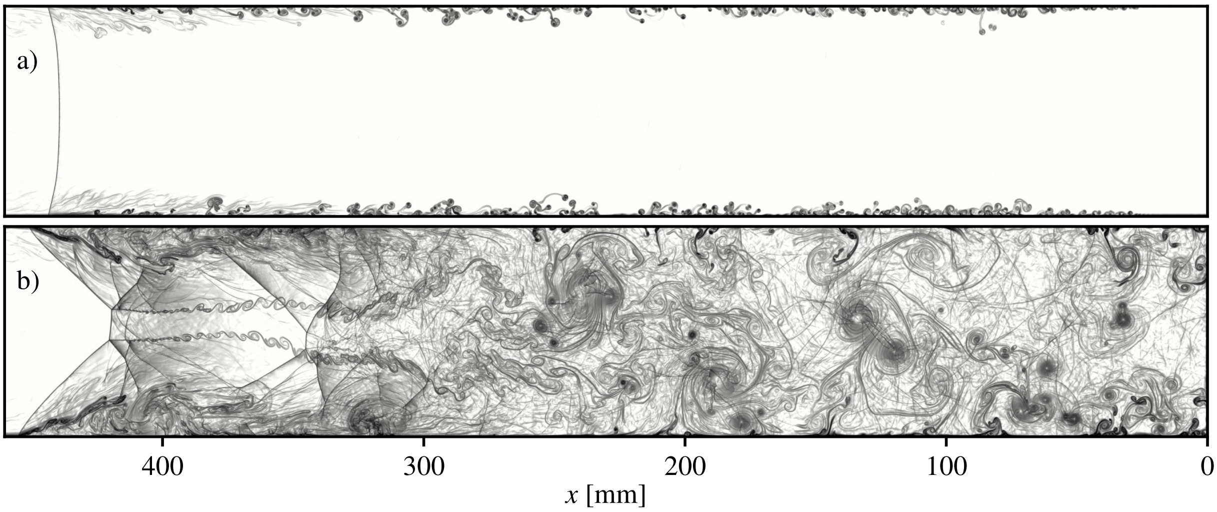

Figure 6.2: Instantaneous numerical schlieren visualizations from two-dimensional simulations *NRD1* (a) and a two-dimensional simulation with nitrogen as driven gas (b), to illustrate the effect of shock bifurcation on the region behind the reflected shock. The reflected shock is moving to the “left”, away from the end wall on the “right”. The schlieren visualizations are generated by computing the absolute gradient of density, followed by division with the maximum value and subsequent application of the decadic logarithm. The end wall of the shock tube is located on the right ($x = 0\,\mathrm{mm}$).

and the velocity at the inlet must be modeled. This concerns both the variation within the boundary layer and its growth, but also the variation of the state variables in the core flow. The perturbation theory by Mirels [202, 203] is used to compute the variation of quantities outside the boundary at the location of the inlet of the computational domain as a function of time. The solution for a laminar boundary layer is calculated according to Mirels [155] by solving the Blasius differential equations in a shock-fixed frame, while the solution for the turbulent boundary layer is computed according to the equations by Petersen and Hanson [165]. The resulting profiles of the axial flow field and the temperature field are tabulated as function of time and are applied in terms of a Dirichlet boundary condition.

6.3 Results

6.3.1 Non-Reactive Cases

Non-reactive cases are simulated to compare the temporal pressure variation at the end wall to experimental measurements, thus validating the code and the modeling of boundary-layer effects. Figure 6.2 shows numerical schlieren visualizations after the reflection of the shock with argon (Fig. 6.2a) and with nitrogen (Fig. 6.2b) as test gases, by evaluating the absolute gradient of density. When nitrogen is used, a pronounced bifurcation of the reflected shock is present.

The shear layer between reversed fluid and fluid that passes the oblique shock, produces turbulent kinetic energy, while vortices form along the slip line. As a result, the fields of state and velocity are highly inhomogeneous and the conditions are not ideal for shock-tube experiments. Argon, on the other hand, typically suppresses bifurcation. The reflected shock is then curved due to a higher propagation speed of the reflected shock within the turbulent boundary layer. The absence of the bifurcated shock-induced vortices and shear layers leads to much smoother distributions of state quantities, which is a prerequisite for meaningful results from shock-tube experiments. However, the variation of state variables along the center line, introduced by the development of the boundary layer, still affects the state behind the reflected shock in space and time, especially because the variations are amplified by the reflected shock [204].

Figure 6.3 compares the evolution of pressure at the end wall for all non-reactive simulations against the respective measurements. The cases cover initial pressures from 44-120 mbar with pressures behind the reflected shock ranging from 1600-3200 mbar at Mach numbers of the incident shock from 2.3-2.8.

Very good agreement is achieved in most of the cases, especially in terms of shock tubes with a large diameter (Fig. 6.3a,b) or at high pressure (Fig. 6.3c). At low pressure or small shock-tube diameters (*e.g.*, Fig. 6.3d), deviations appear after 1 ms. Deviations however are expected, as the perturbation theory relies on the assumption that the thickness of the boundary layer is negligible compared to the height/diameter of the shock tube. At low pressure and/or small shock-tube diameters, these assumptions are easily violated. Nevertheless, the results are initially consistent with those of the experiments, which would not have been the case with a primitive inflow condition neglecting the evolution of the boundary layer. The remaining deviations can be partially attributed to shock-contact surface interaction or the arrival of the expansion wave, effects that are not considered in the simulations. Strikingly, simulations and experiments (Fig. 6.3a,b,e-g) both show an initial decrease of pressure followed by a linear increase, which is in contrast to the usual expectation of a purely linear increase of pressure. This assumption of a linear increase of pressure is also incorporated in many low-order models for reactors that are used for the validation of reaction mechanisms, thus neglecting the observed behaviour could lead to large errors. It is obvious to attribute the unexpected drop of pressure to transition effects of the boundary layer. Therefore, the observed characteristic evolution of pressure is only expected at low pressures behind the incident shock, when the laminar boundary layer can not be neglected.

Figure 6.4 presents stacked center-line profiles of both pressure and temperature for simulation *NRD1*, which is in excellent agreement with the experiment. The normalized pressure increase at the end of the shock tube is linear at a value of $\partial p_5/\partial t/p_5 \approx 3.6$ %/ms and presents the only simulation with a linear pressure evolution in this study. In contrast to the results shown in Fig. 6.3, the surfaces illustrate the entirety of changes in time and space, where the profile for $x = 0\,\mathrm{cm}$ (end wall) in the lower panel refers to the solution in Fig. 6.3c. According to the results, the strength of the reflected shock increases, while travelling upstream (away from the end wall), which is reflected in higher pressures and temperatures behind the shock. However, the evolution of temperature and pressure at a fixed location is very different directly at the end wall, compared to locations further away. This is well illustrated by the fact that for a fixed time of $t = 2.5\,\mathrm{ms}$, the pressure decreases with the distance from the end wall whereby the temperature increases. While pressure and temperature are connected by isentropic relations at the end wall, this is clearly not the case further away from the end wall, a circumstance which is to be led back among other things to the variation of entropy by shock attenuation. The temperature increases continuously with distance and time such that the temperature maximum of the presented data is reached for $x = 40\,\mathrm{cm}$ and $t = 2.5\,\mathrm{ms}$ and is significantly larger ($\approx 50\,\mathrm{K}$) than the temperature at the end wall at the same time. Such a temperature distribution could lead to a remote ignition, if a reactive mixture were used instead.

Figure 6.5 also presents stacked center-line profiles, but for simulation *NRD3*, a simulation that matches the experimental results although the initial pressure is considered very low. The differences of pressure and temperature surfaces from the previous case (Fig. 6.4) are apparent. In this case, a characteristic valley forms both in pressure and in temperature, independent of the end-wall distance. While the evolution at a fixed location is qualitatively similar, the strength of the changes (gradients) decreases with the wall distance. As in the previous case, pressure decreases with wall distance at a simulation time of $t = 2.5\,\mathrm{ms}$, whereas the temperature increases, while the distribution of both the quantities along the center line is much more homogeneous compared to the previous case. The pressure and temperature distributions at these low pressure levels are over all very complex and the values vary strongly in time. At this point we want to emphasize that it will be very important to quantify such effects in low-pressure experiments to be able to interpret the measurement results.

Slice-integrated profiles of the mass flux per unit depth, are presented in Fig. 6.6 for the cases *NRD1* and *NRD3* and for different times. Without viscous effects and heat losses, a reflected shock of constant strength forms, such that the fluid behind the reflected shock wave is instantly at rest. The local distribution of the state variables of the investigated cases in contrast leads to a change in shock strength and, for example, to a change in the momentum of the fluid behind the reflected shock, as presented in the panels a) and b) of Fig. 6.6. In the case of *NRD1*, this means that the fluid behind the reflected shock wave

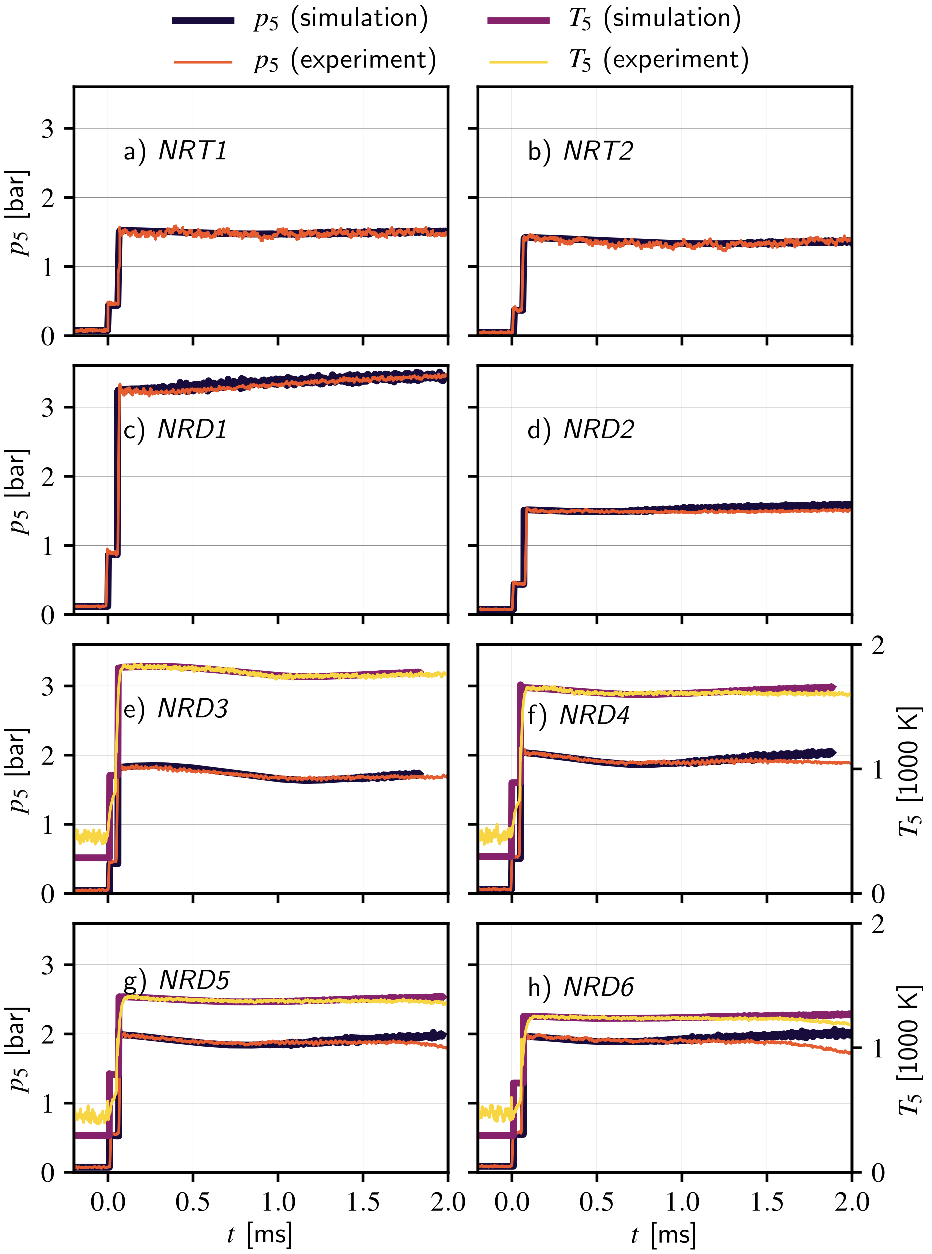

Figure 6.3: Pressure histories from the non-reactive cases (dark black) and from the corresponding experiments (light orange), as well as temperature histories from simulation (dark purple) and from experiments (light yellow), evaluated at the end wall of the shock tube.

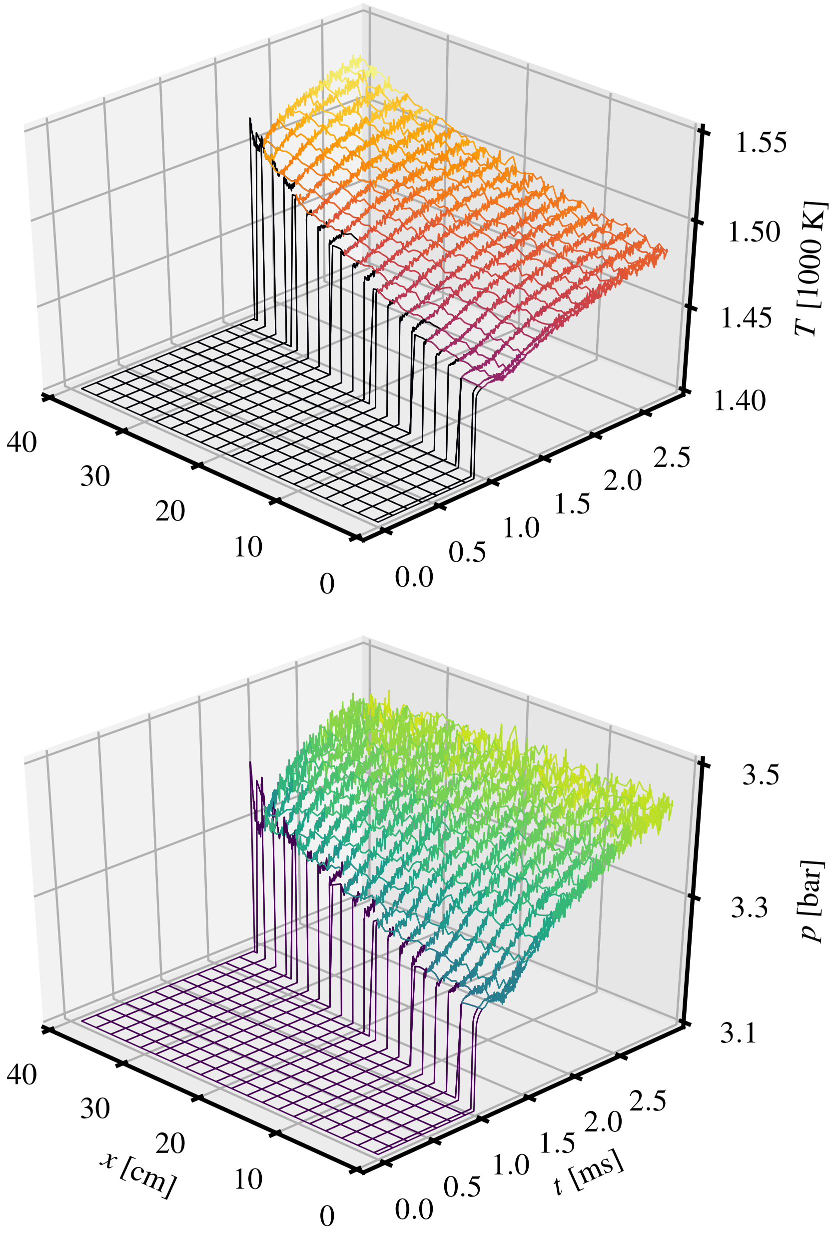

Figure 6.4: Stacked center-line profiles of simulation *NRD1* of temperature (top) and pressure (bottom), illustrated as a function of end-wall distance x and time after shock reflection t. The end wall of the shock tube is located on the right ($x = 0\,\text{cm}$).

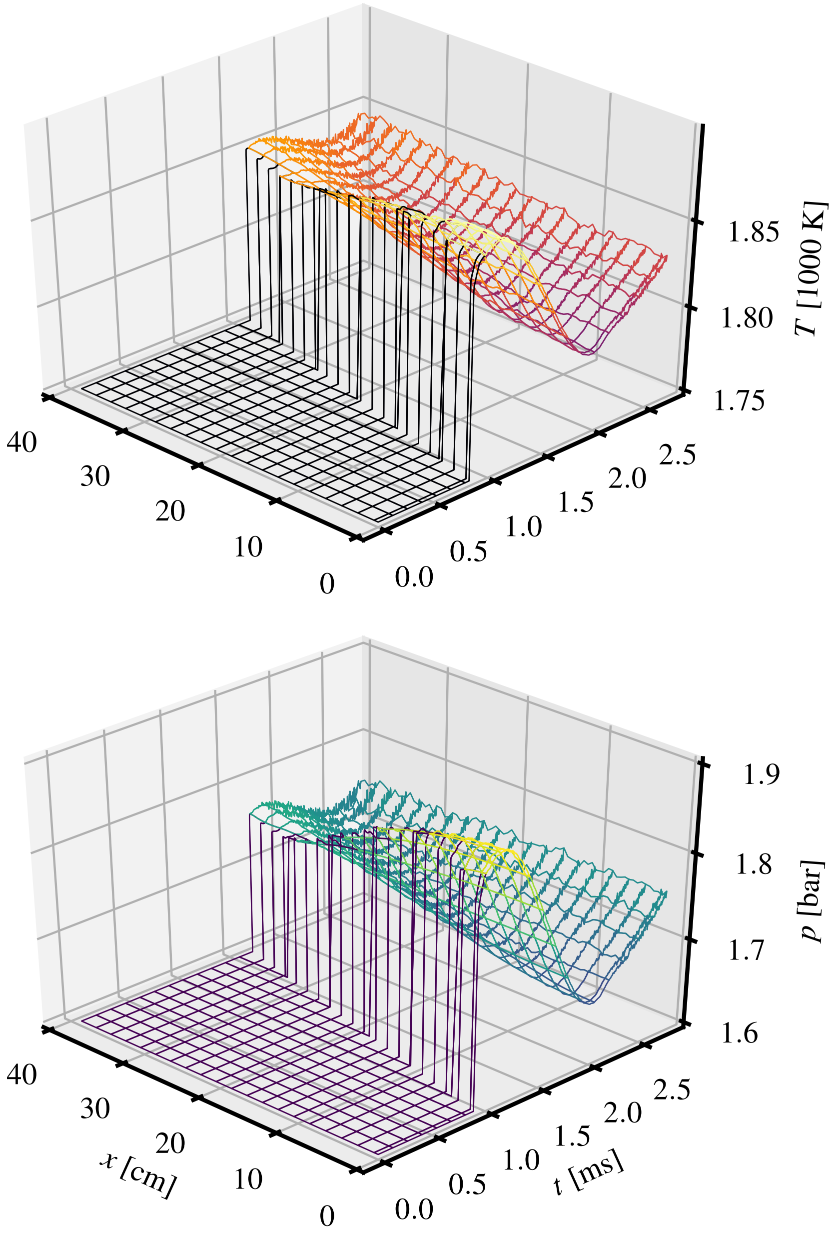

Figure 6.5: Stacked center-line profiles of simulation *NRD3* of temperature (top) and pressure (bottom), illustrated as a function of end-wall distance x and time after shock reflection t. The end wall of the shock tube is located on the right ($x = 0\,\mathrm{cm}$).

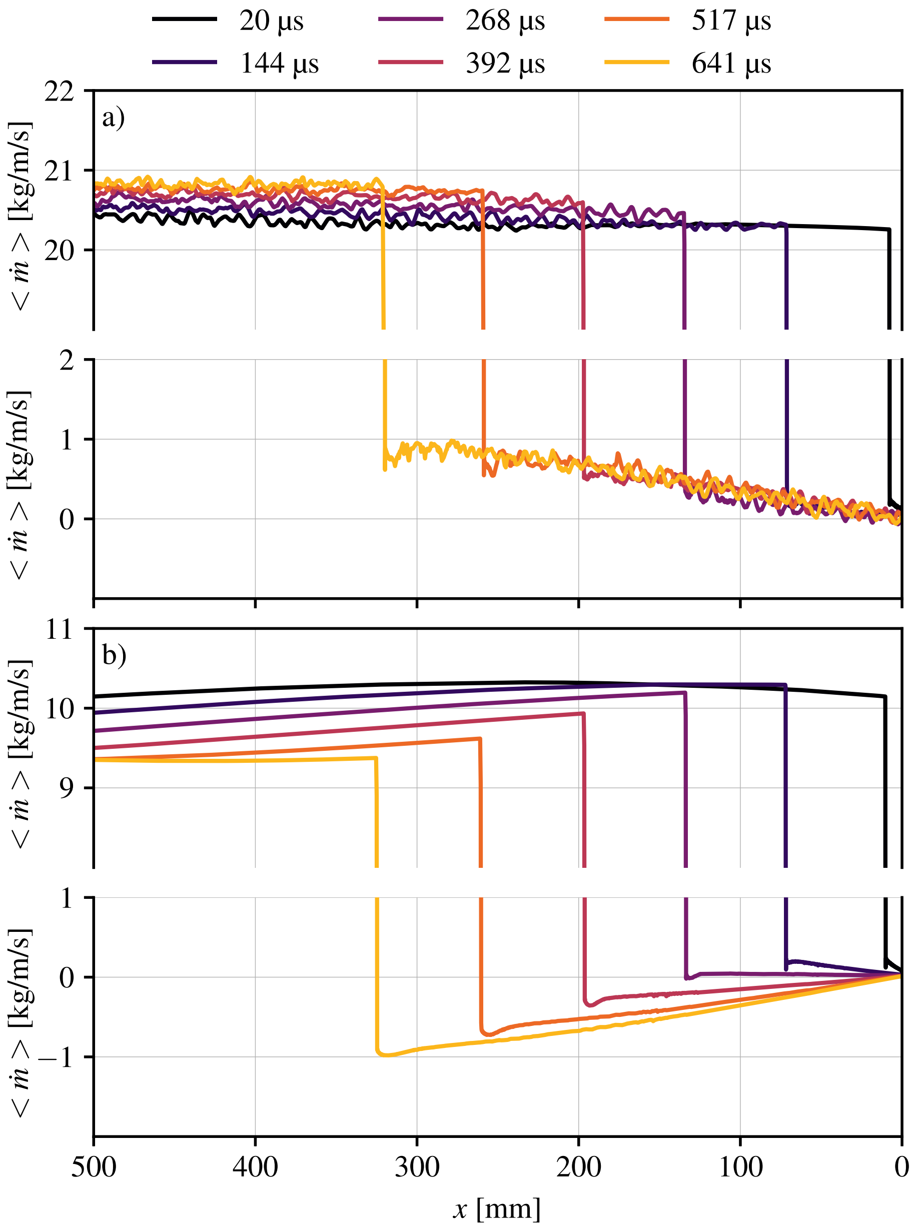

Figure 6.6: Slice-integrated values of mass flux per unit depth of simulation *NRD1* (a) and *NRD3* (b). Colors indicate the time that has passed since the reflection of the shock wave. The end wall of the shock tube is located on the right ($x = 0$ mm).

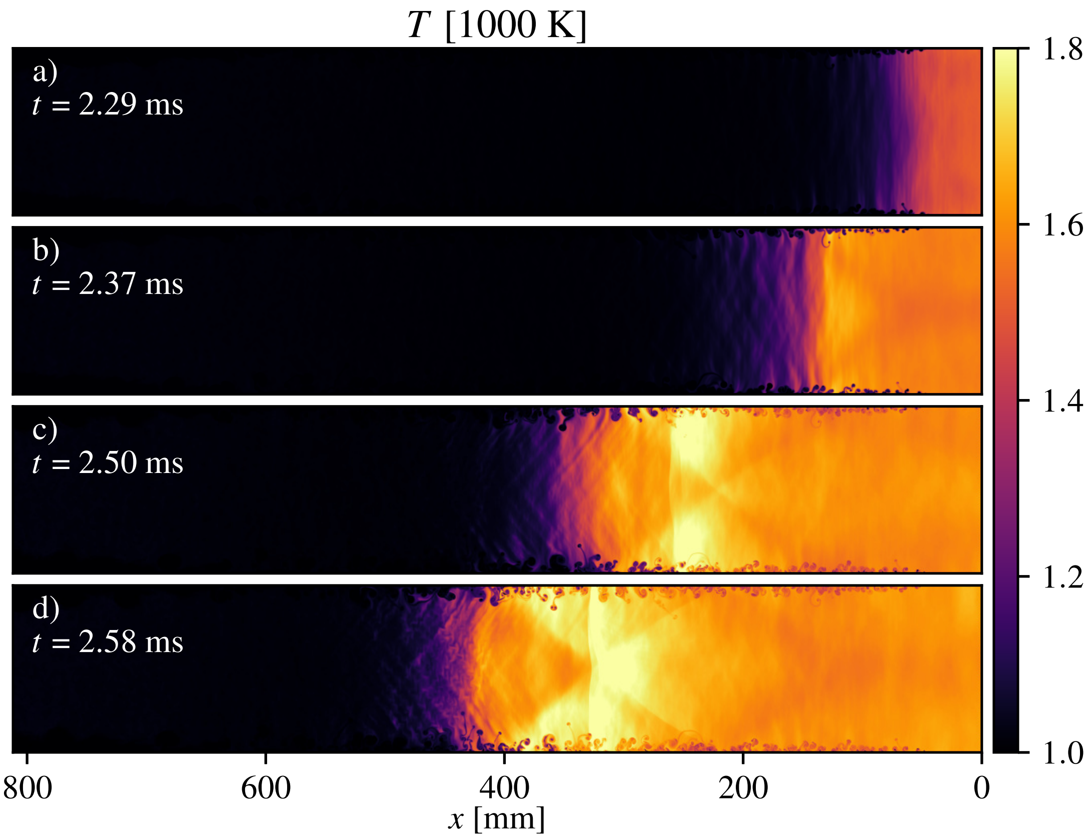

Figure 6.7: Instantaneous temperature fields of simulation *RS1* at different times after the reflection of the shock wave, illustrating strong ignition and the subsequent formation of a strong wave. The end wall of the shock tube is located on the right ($x = 0$ mm).

still has a residual momentum. It is eventually brought to a rest, accompanied by an increase in pressure and temperature. In the case of *NRD2*, however, the fluid behind the reflected shock has a negative momentum, hence moving in the direction of the reflected shock. The gas behind the reflected shock thus expands, decreasing the temperature. A one-dimensional inviscid simulation of case *NRD1*, presented in supplementary material (Sec. 6.5), confirms that the fluctuations visible in panel a) do not stem from the applied algorithms, but instead are linked to the transition from the laminar to the turbulent boundary layer and occur first at the inlet, where artificial turbulence is created in the boundary layer. The much higher pressure in case *NRD1*, in contrast to that of case *NRD3*, causes a very early transition, which is why no fluctuations are visible in panel b), since the boundary layer has not yet turned over at this point.

6.3.2 Remote Ignition Simulated in 2D

The observed agreement of experiments and simulations, both qualitative and quantitative, indicates that the most important phenomena including boundary-layer effects have been simulated successfully. Therefore the code can be used to also examine remote ignition events. Figure 6.7 presents temperature fields at different instances of simulation *RS1*. Since the mixture ignites simultaneously in a region near the end wall, this ignition can be classified as a strong ignition. The pressure increase resulting from the combustion is particularly strong due to the closed end of the shock tubes, and a strong “left”-running wave is formed.

As highlighted in Tab. 6.2, the Mach number in case *RS2* and case *RS3* is slightly lower than that in case *RS1*, but this small difference is sufficient for the ignition to take a different course of events, as shown in Figs. 6.8 and 6.9. Both simulations (*RS2, RS3*) use the same initial- and boundary conditions and differ only in the mechanism used for solving the chemistry (FFCM-1 in terms of simulation *RS2* and

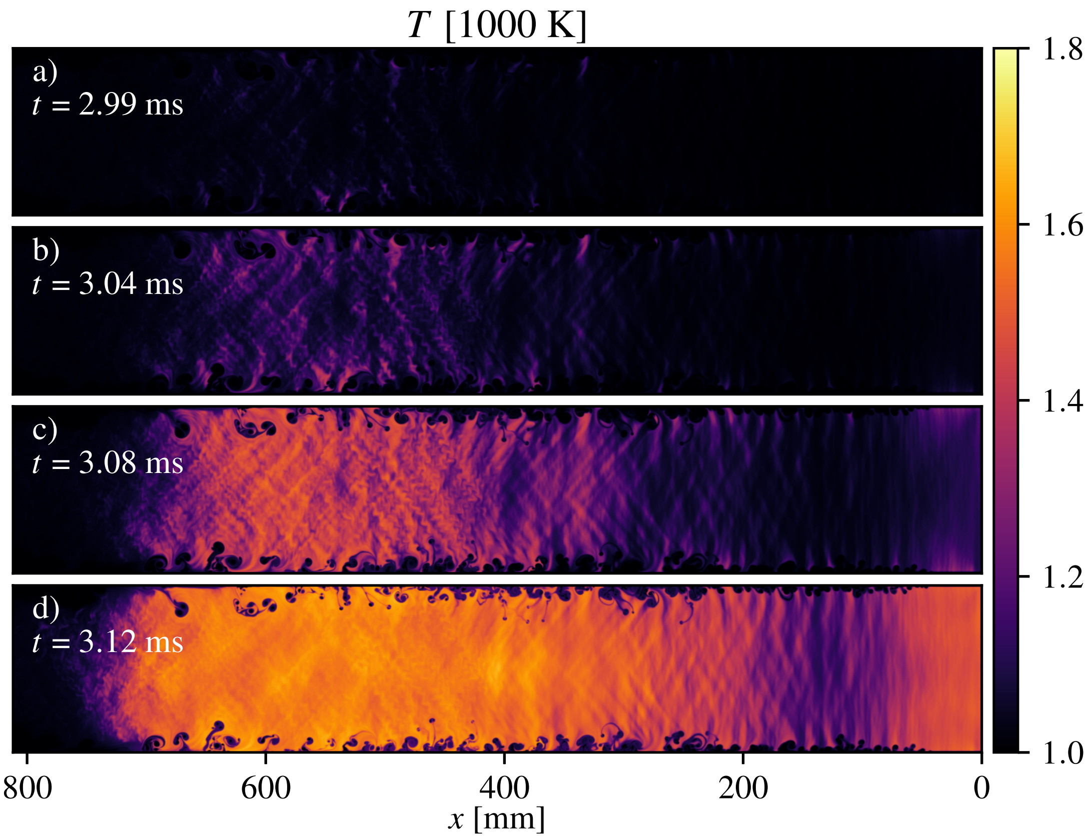

Figure 6.8: Instantaneous temperature fields of simulation *RS2* at different times after the reflection of the shock wave, illustrating mild ignition remotely from the end wall. The end wall of the shock tube is located on the right ($x = 0$ mm).

O'Conaire in terms of *RS3*).

According to Fig. 6.8a, the ignition starts from small ignition kernels, located at a distance of approximately 500 mm away from the end-wall. More ignition kernels appear at $t = 3.04$ ms between end-wall distances of 400 and 600 mm before the whole mixture ignites remotely at $t = 3.08$ ms. Also, an increase of temperature is observed at the end wall, which suggests that these conditions mark the transition from a strong to a remote ignition. This means that the reduction of the ignition-delay time caused by fluid dynamics away from the end wall just compensates for the delayed compression by the reflected shock away from the end wall.

If the reaction mechanism of O'Conaire is used instead, the ignition event slightly deviates from the previous result, as can be seen in Fig. 6.9, and attributed to uncertainties of the reaction mechanisms at low temperatures. This time, ignition kernels are already visible after 2.93 ms and are located even further away from the end wall at a distance of 600 mm, while the mixture is consumed more rapidly. However, the largest deviation in comparison to simulation *RS2* concerns the region near the end wall, where no significant temperature increase is observed. Hence, the competition of the characteristic time scales favors the remote ignition event. According to Tab. 6.2, boundary-layer effects in each of the simulations (*RS1,RS2,RS3*) greatly reduce the ignition-delay time τ_{ig} compared to the ideal ignition-delay time $\tau_{\mathrm{ig,0}}$ as obtained from low-order simulations. The reduction is particularly pronounced in cases *RS2* and *RS3*, where remote ignition occurs.

The local heat-release rate $\dot{\omega}_{\mathrm{HR}}$ plays an obvious and important role in the ignition process as it results from chemical conversion and accelerates it at the same time. Figures 6.10 and 6.11 present scatter plots of local heat-release rate over temperature, colored with the end-wall distance. Figure 6.10 shows the result for simulation *RS1* and thus for the case of a strong ignition. As expected, the heat-release rates are initially highest at the end wall. Nothing changes subsequently in this overall picture despite higher

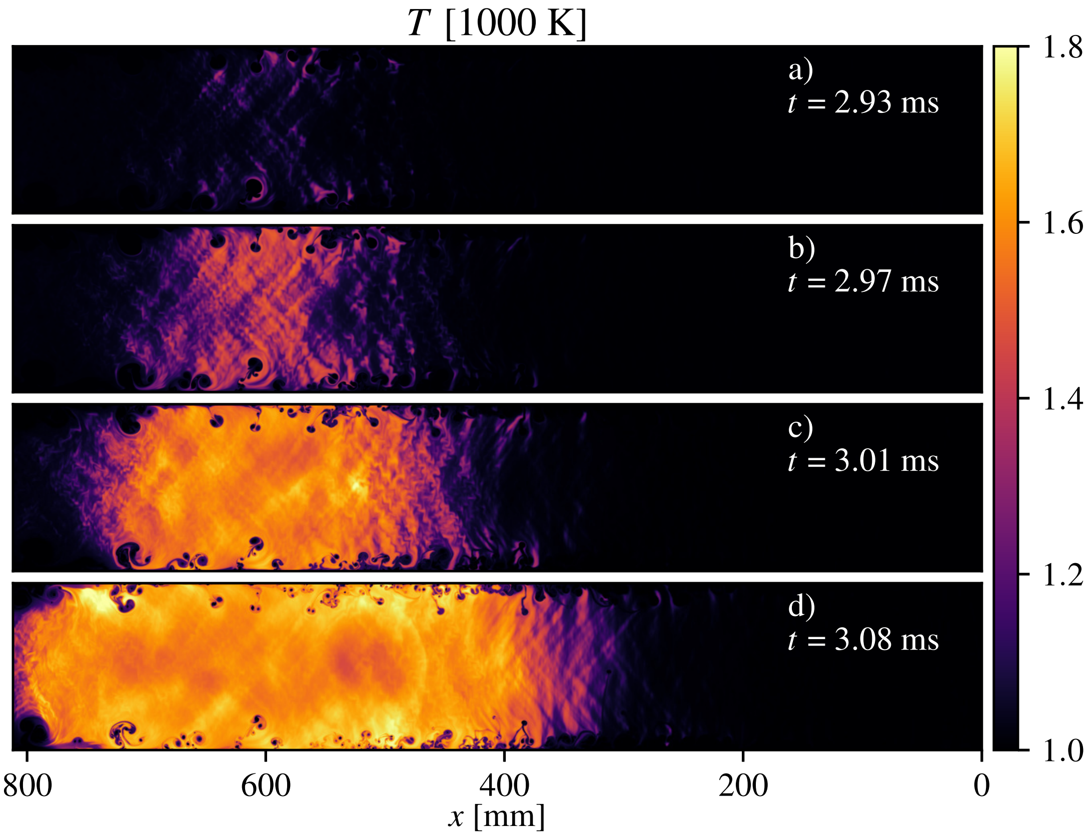

Figure 6.9: Instantaneous temperature fields of simulation *RS3* (carried out with the reaction mechanism by O'Conaire [223]) at different times after the reflection of the shock, illustrating mild ignition remotely from the end wall. The end wall of the shock tube is located on the right ($x = 0$ mm).

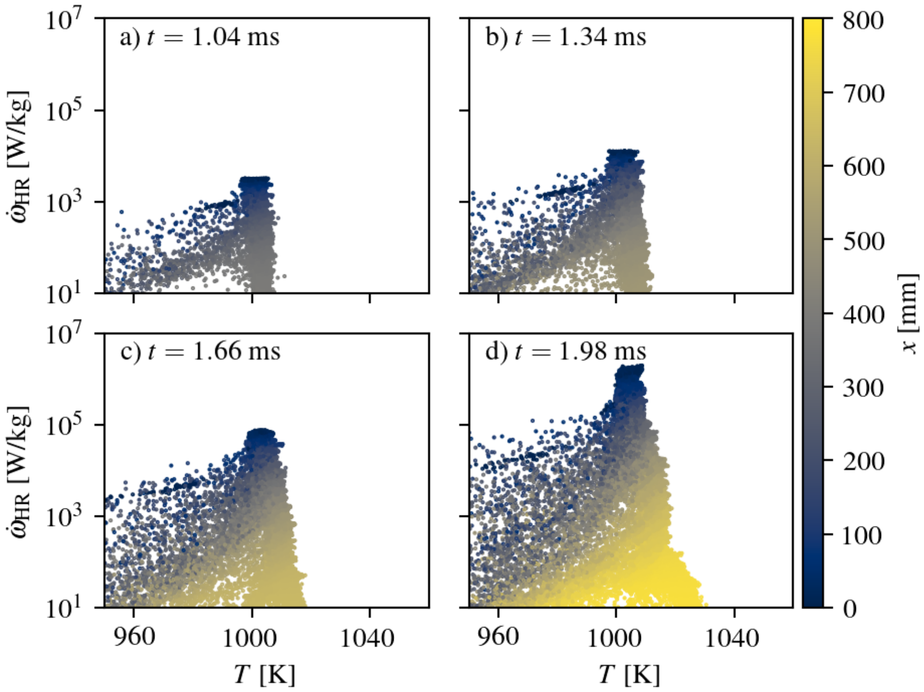

Figure 6.10: Scatter plot of local heat-release rate $\dot{\omega}_{\mathrm{HR}}$ over temperature T and colored with the respective end-wall distance x for simulation *RS1*.

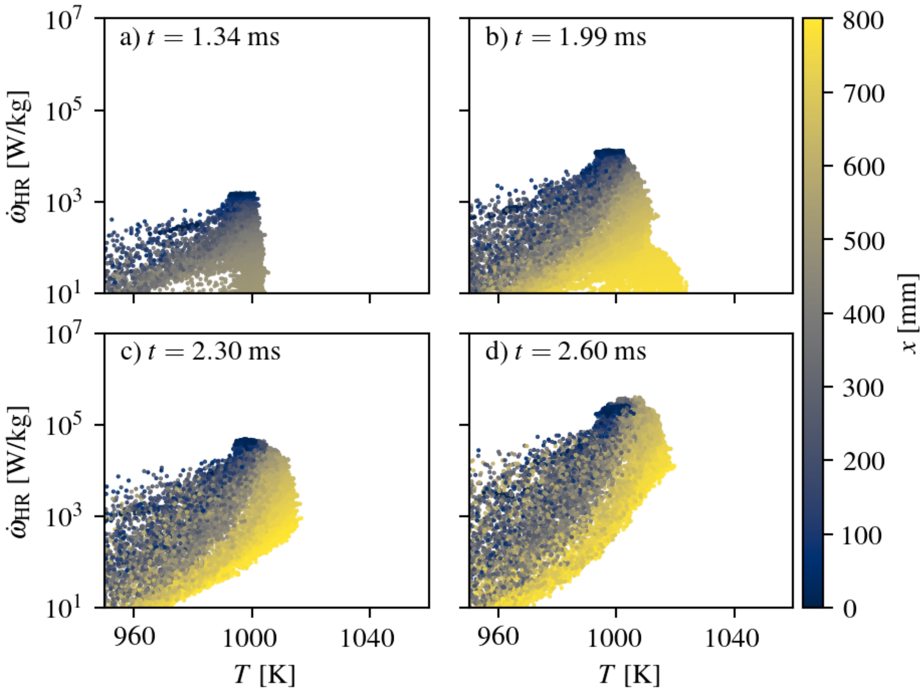

Figure 6.11: Scatter plot of local heat-release rate $\dot{\omega}_{\mathrm{HR}}$ over temperature T and colored with the respective end-wall distance x for simulation *RS2*.

temperatures at greater distances from the wall. A completely different picture emerges for Simulation *RS2*. Figure 6.11b presents the distribution of local heat-release rate of simulation *RS2* at the same time as Fig. 6.10a for simulation *RS1*. The heat-release rates at the end wall in this case are an order of magnitude below those observed in simulation *RS1*. At a time of 2 ms after the reflection of the shock, this gap has further increased, and the heat-release rates at the end wall of simulation *RS1* now exceed those of simulation *RS2* by two orders of magnitude. In contrast to simulation *RS1*, simulation *RS2* shows more concentrated distributions of heat-release rates prior to ignition, again emphasizing that flow-induced temperature inhomogeneities upstream made up for the delayed compression.

In order to illustrate how these temperature variations affect the localization of ignition, we determine the expected time of ignition after shock-wave reflection (i.e., a ”local” ignition delay time) in a post-processing step. For each numerical cell of the computational domain, the instantaneous thermochemical state is utilized to estimate the related ignition-delay time based on the assumption of isochoric 0D reactors. The results are therefore decoupled from convection and diffusion. The first panel of Fig. 6.12 presents the field of expected time of ignition, 0.75 ms after the reflection of the shock for simulation *RS1*. A general spatial gradient of the expected time of ignition is recognizable in axial direction, favouring ignition near the end wall, whereby the expected ignition times vary strongly, specifically near the walls of the shock tube. As the process progresses, these local gradients disappear at the end wall, so that the ignition is globally initiated instead of an ignition from smaller kernels. Results of the same type of post-processing, but for simulation *RS2*, are shown in Fig. 6.12d-f. In contrast to the results from simulation *RS1*, it is not possible to predict where the ignition will take place based on the result 0.34 ms after the reflection of the shock. The field of expected ignition times remains heterogeneous until the point of ignition, with deviations between the shortest and highest expected ignition time of about 0.3 ms. The small kernels with the shortest expected ignition times dictate the subsequent ignition process, starting at a distance of 500 mm.

In order to facilitate the interpretation and to quantify the flow-induced reduction of expected ignition time as a function of axial location, the fields of expected ignition time are averaged in the vertical direction ($< \cdot >$), followed by a filter operation ($\hat{\cdot}$) to eliminate fluctuations. Figure 6.13 presents the results for simulation *RS1* on the left and *RS2* on the right. Solid lines in the upper panels show the averaged and

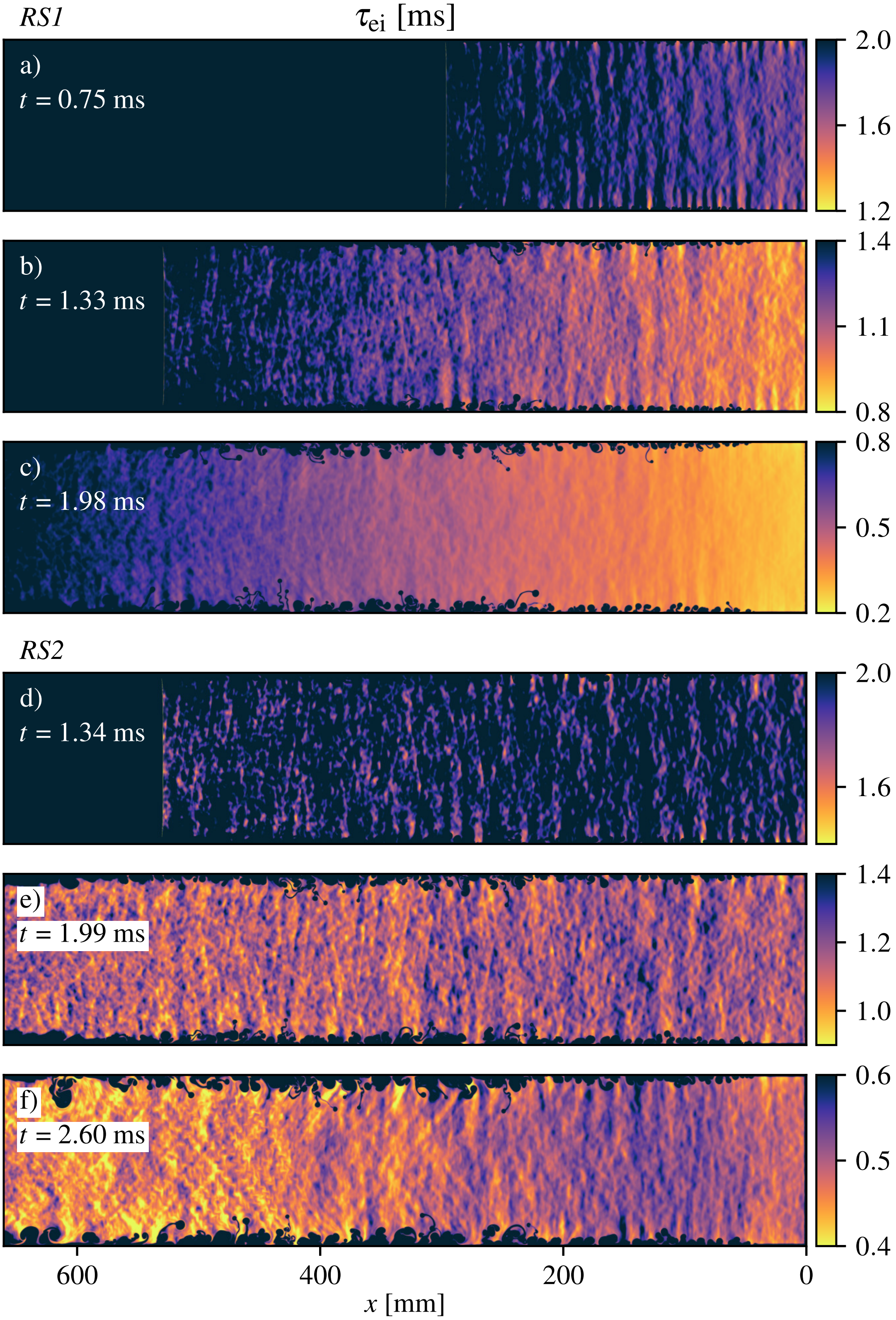

Figure 6.12: Expected time of ignition, using instantaneous values from simulation *RS1* (a-c) and from simulation *RS2* (d-f) as initial condition for isochoric 0D-reactors. The end wall of the shock tube is located on the right ($x = 0$ mm).

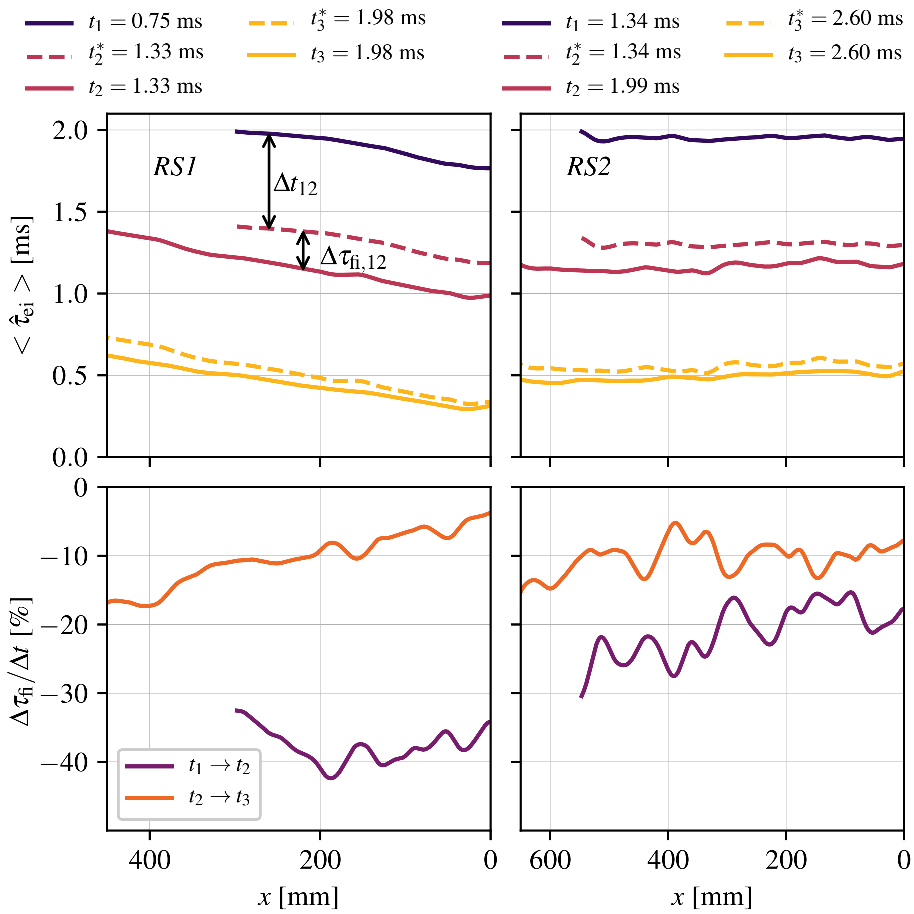

Figure 6.13: Upper panels show vertically averaged and filtered profiles of expected ignition time $<\hat{\tau}_{\mathrm{ei}}>$ (solid lines). Dashed lines present projected profiles. Lower panels present approximated flow-induced reductions of ignition time $\Delta\tau_{\mathrm{fi}}$ over a given time interval and normalized by the simulation-time difference between the samples Δt. Data before compression of the reflected shock is excluded from the plots.

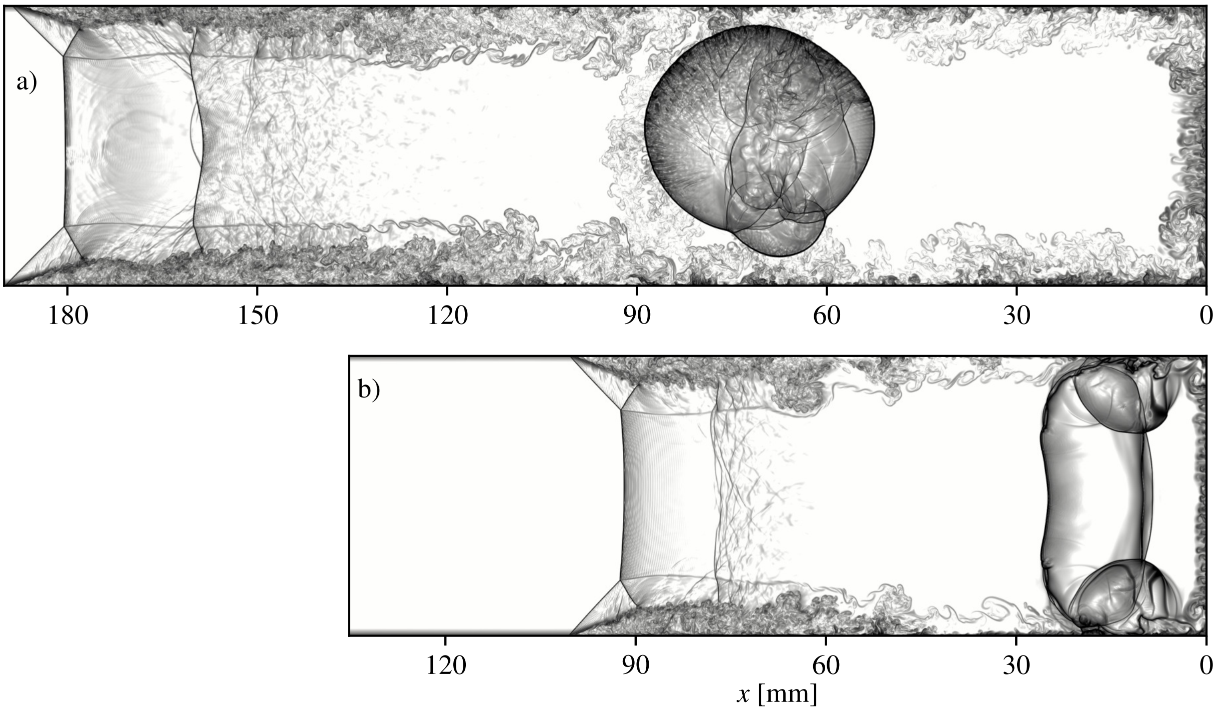

Figure 6.14: Instantaneous numerical schlieren visualizations from simulation *RB1* (a) and simulation *RB2* (b), illustrating the ignition locations. The end wall of the shock tube is located on the right (x = 0 mm).

filtered profiles of expected ignition time at time t_n. The dashed lines show projected profiles t^*_n resulting from shifting the previous profile $t_\mathrm{n-1}$ by the difference in simulation time between the samples, i.e., by $\Delta t = t_\mathrm{n} - t_\mathrm{n-1}$. In this discussion, it is worth pointing out that the expected time of ignition increases monotonically with x for *RS1*, whereas it is almost constant for *RS2*, making the location of ignition a lot more sensitive to small perturbations. A flow-induced reduction of ignition time $\Delta\tau_\mathrm{fi}$ is introduced by subtracting the computed profile of expected ignition time from the projected profile. This variable approximates the reduction of ignition time due to fluid dynamics within a given time interval. It is interesting to note that fluid dynamics reduce the ignition time independent from the axial location. Nevertheless, the trend can be observed that the expected ignition time is reduced more at greater distance to the end wall. In case of simulation *RS2*, the initially flat profile of expected ignition time thus gets altered by the fluid dynamics such that remote ignition occurs.

6.3.3 Remote Ignition Simulated in 3D

While remote ignition in the previous cases is governed by effects due to the formation of a boundary layer, remote ignition can also be related to the flow field evolving behind bifurcated shocks. In contrast to the simulations in 2D, no complex inlet treatment is applied with regards to simulations *RB1* and *RB2*, as the bifurcation-induced effects are studied exclusively. Instead, the solution resulting from the ideal shock relations is applied. Numerical schlieren visualizations, shortly after the ignition, are presented in Fig. 6.14.

The upper image shows the result of simulation *RB1*, where the mixture ignites in the core of the shock tube at a distance of approximately 70 mm away from the end wall. Reasonable agreement with the experiments by Meyer and Oppenheim [166] has been achieved with an ignition-delay time of 281 µs (approximated by the time, when the maximum temperature surpasses 1600 K) in the simulation and one that exceeded 250 µs in the experiment. Compared to the ideal ignition-delay time $\tau_\mathrm{ig,0}$ of 1092 µs (Tab. 6.2), the ignition-delay time from this simulation is reduced by a factor of four by taking into account

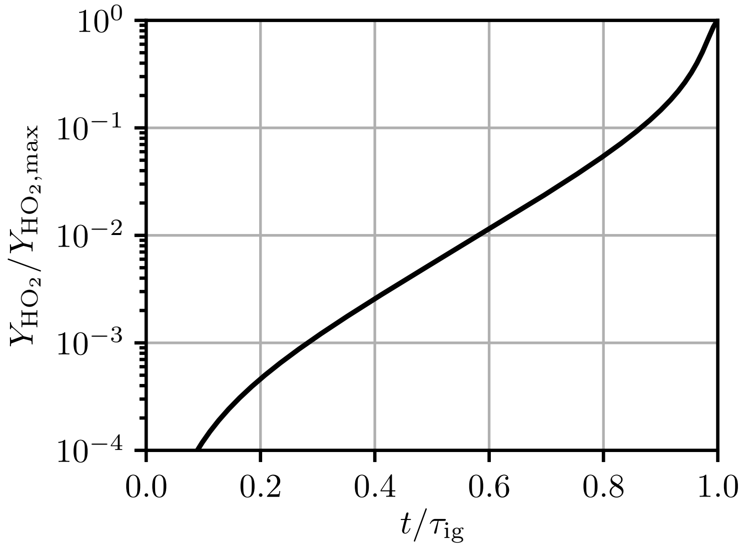

Figure 6.15: Evolution of mass fraction of hydroperoxyl (HO_2) normalized by the maximum value at the point of ignition to present the behaviour of the auto-ignition marker. Results have been obtained with Cantera using the O'Conaire reaction mechanism. The initial conditions match the values (p_5, T_5) of Tab. 6.2 in terms of case *RB1*.

the shock-boundary layer interaction.

The ignition locations in simulation *RB2* are very different, as the ignition starts near the corners close to the slip line before a larger volume spanning the entire cross section of the shock tube ignites. Many of the schlieren photographs by Meyer and Oppenheim [166] showed very similar ignition locations at comparable temperatures behind the reflected shock. The reasons for the remote ignition in case *RB1* were discussed in detail before [6], but are described briefly again for the sake of completeness.

One of the striking features is the formation of a second normal shock after the bifurcation structure has grown significantly. The second shock is clearly visible in the upper panel of Fig. 6.14 at a location of 165 mm from the end wall, while it is not fully developed in the lower panel. Instead, many strong waves can be observed at a location of 75 mm, each of which are increasing the local temperature and are thus moving at a higher speed than the waves upstream. Eventually, they will catch up with other waves and form the second shock wave. Similar shock-wave patterns were observed in two-dimensional simulations as reported by Weber *et al.* [194].

Figure 6.16 introduces instantaneous fields of pressure, temperature, and hydroperoxyl (HO_2) complemented by center-line plots of pressure and temperature before the ignition has taken place, to fully understand the physics. According to Fig. 6.15, hydroperoxyl can be used as an auto-ignition marker, since the mass fraction increases monotonically while the growth is almost perfectly exponential over a wide range. In contrast to the previously demonstrated auto-ignition marker, where the expected time of ignition is evaluated based on instantaneous fields, this marker and the use of a logarithmic scale reveals features that are not visible in the other marker field.

The existence of the second normal shock (travelling at a similar speed compared to the reflected shock) implies an acceleration of the fluid behind the reflected shock (referred to as the core fluid) to supersonic speeds in a coordinate frame that is fixed to the reflected shock. The flow field behind the reflected shock is determined by displacement effects of outer-core fluid and pressure variations within the bifurcation structure. The displacement effect of the outer-core fluid is caused by the oblique shock, as the fluid that passes the oblique shock gains momentum in vertical direction. Combined, these effects force the fluid in the core to follow a convergent-divergent streamline pattern which forms a Laval-nozzle shaped stream tube, which is in fact well illustrated by the interface between core- and outer fluid along the slip line in the temperature field. Initially, when the bifurcation structure is small and the cross-section areas, characterizing the Laval-nozzle like flow and which are bounded by the slip line, are correspondingly

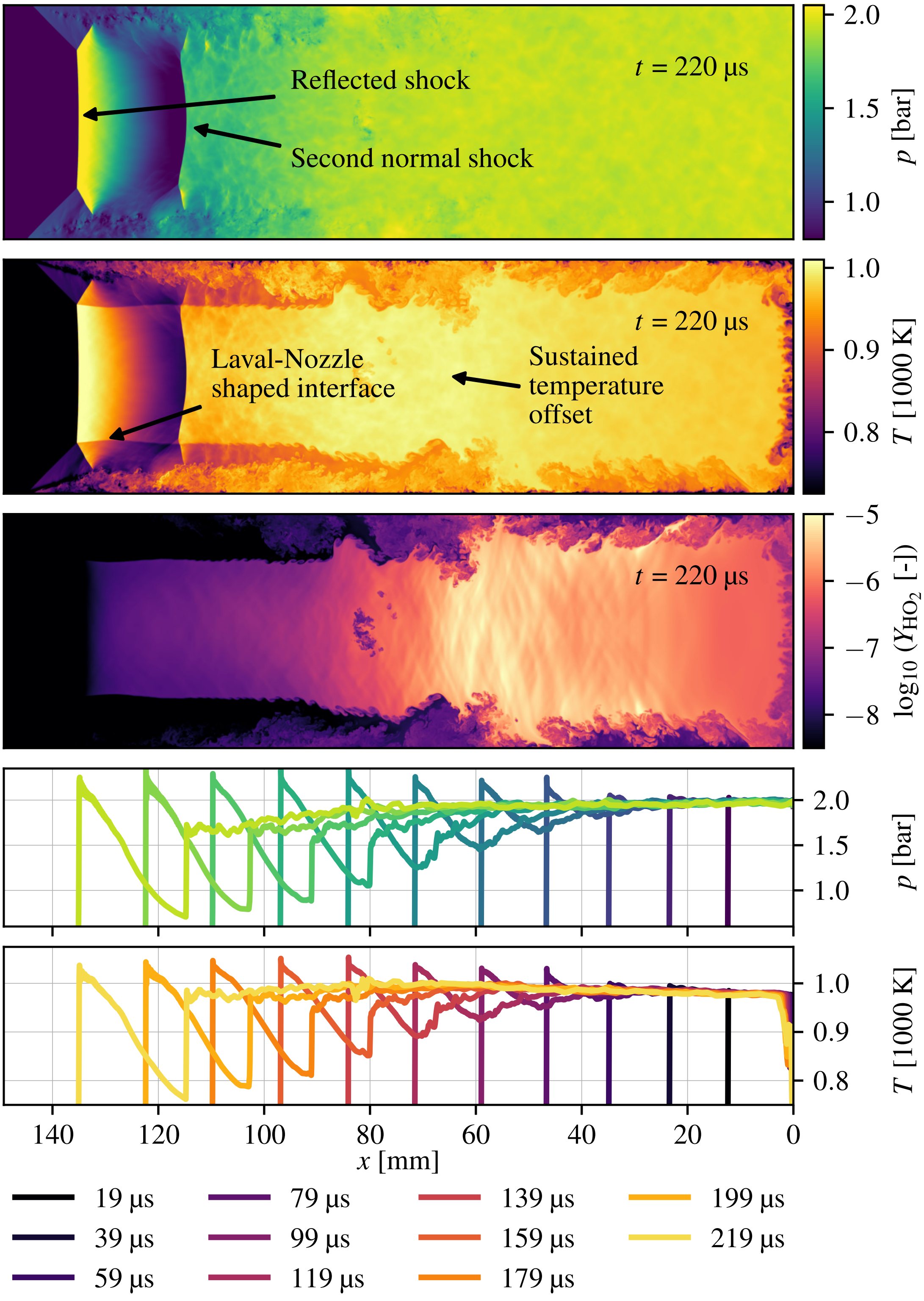

Figure 6.16: Instantaneous fields of pressure, temperature and HO_2 species mass fraction from simulation *RB*1, as well as center-line plots of pressure and temperature at different times from simulation *RB*1. The end wall of the shock tube is located on the right ($x = 0\,\mathrm{mm}$).

large, the variations of velocity and state are also small. However, due to the growth of the bifurcation, these variations will increase. Since the pressure drops in the core flow, as a result of the velocity gain, fluid will be also accelerated from the end wall towards the reflected shock. Once the velocity in the core-flow has nearly reached super sonic speed, these pressure waves will start to "pile up" and eventually form the second shock. This evolution is well captured by the history of center-line plots in Fig. 6.16. The additional production of entropy, caused by the second shock, is clearly evident by a sustained offset of temperature compared to the temperature at the end wall.

Apparently, this temperature variation has huge implications regarding the distribution of ignition-delay times, as presented in Fig. 6.17. Comparing these results to those without the occurrence of a bifurcation, it is noticeable that the values now differ greatly from each other, namely between 0.3 and 0.9 ms in the first panel, which presents the result 99 µs after the reflection of the shock. The smallest values are within a range of 20 to 40 mm from the end wall. After another 80 µs, the minimum has shifted further to the "left", now in a distance of about 70 mm to the end wall. Due to the high sensitivity of the ignition-delay time to temperature changes, the increased temperature in this region compensates for the delay regarding the compression of the reflected shock. Further away from the end wall (around 70 mm), a constriction is visible (also present in Fig. 6.16), where fluid is forced from the walls towards the core. The location coincides approximately with the formation of the second normal shock. In the following, the cold fluid from the walls mixes with that from the core and prevents ignition in this region, as can be seen in the third panel of Fig. 6.17. According to Fig. 6.16, the temperature to the "left" of the constriction is even higher, while this temperature difference does not compensate for the time elapsed for the shock wave to process the gas upstream. Therefore, the mixture ignites to the "right" of the mixing zone and much earlier than the ignition at the end wall would have occurred.

The flow characteristics of simulation *RB2* are very similar to those of simulation *RB1*. However, since the second normal shock has not even formed at the time of ignition in case of simulation *RB2* and since the ignition starts first from small kernels near the slip line, the gas dynamics responsible for remote ignition in this case must be very different. Figure 6.18 presents the expected time of ignition for simulation *RB2*.

Here, the conditions behind the reflected shock promote a faster ignition compared to simulation *RB1*. Moreover, the field in the first panel appears much more homogeneous, and the results are overall more comparable with the results of a strong ignition from simulation *RS1*. A wave pattern is also conspicuous, whereby the orientation of the waves suggests that their origin lies in the bifurcation structure.

In order to investigate the physics of the ignition mechanism in this particular case, Fig. 6.19 shows instantaneous fields of the dissipation rate of kinetic energy, as well as entropy of the mixture. Aside from the expected high dissipation rates within the bifurcation and within the boundary layer, high values are also observed along the slip line and in close proximity to the slip line. Especially after the break up of the slip line and the subsequent formation of vortices, a broad region with very high dissipation values of more than 10^7 W/kg is present. The high dissipation rates are also reflected in the field of entropy, where the values are particularly high in the zones of the following ignition kernels. Assuming that a fluid element in close proximity to the slip line is affected by shear with a dissipation of $5 \cdot 10^7$ W/kg, over a period of 100 µs, the estimated temperature increase based on these values would be 5 K, enough to explain a slightly earlier ignition according to the temperature sensitivity of ignition-delay times. Compared to the ideal ignition-delay time $\tau_{\mathrm{ig},0}$ of 142 µs (Tab. 6.2), the ignition-delay time of 140 µs from this simulation turns out to be almost identical, which is also supported by the strong ignition in the entire volume shortly after. However, it is conceivable that the ignition mechanism proposed here could lead to a more significant reduction in other cases.

6.4 Conclusion

Two-dimensional computational fluid dynamics simulations of shock-tube experiments with non-reactive mixtures, as well as two- and three-dimensional simulations of shock-tube experiments with hydrogen-oxygen mixtures were carried out using high-order numerics and detailed chemistry.

The non-reactive cases confirmed the measurements of pressure and temperature at the end wall in a

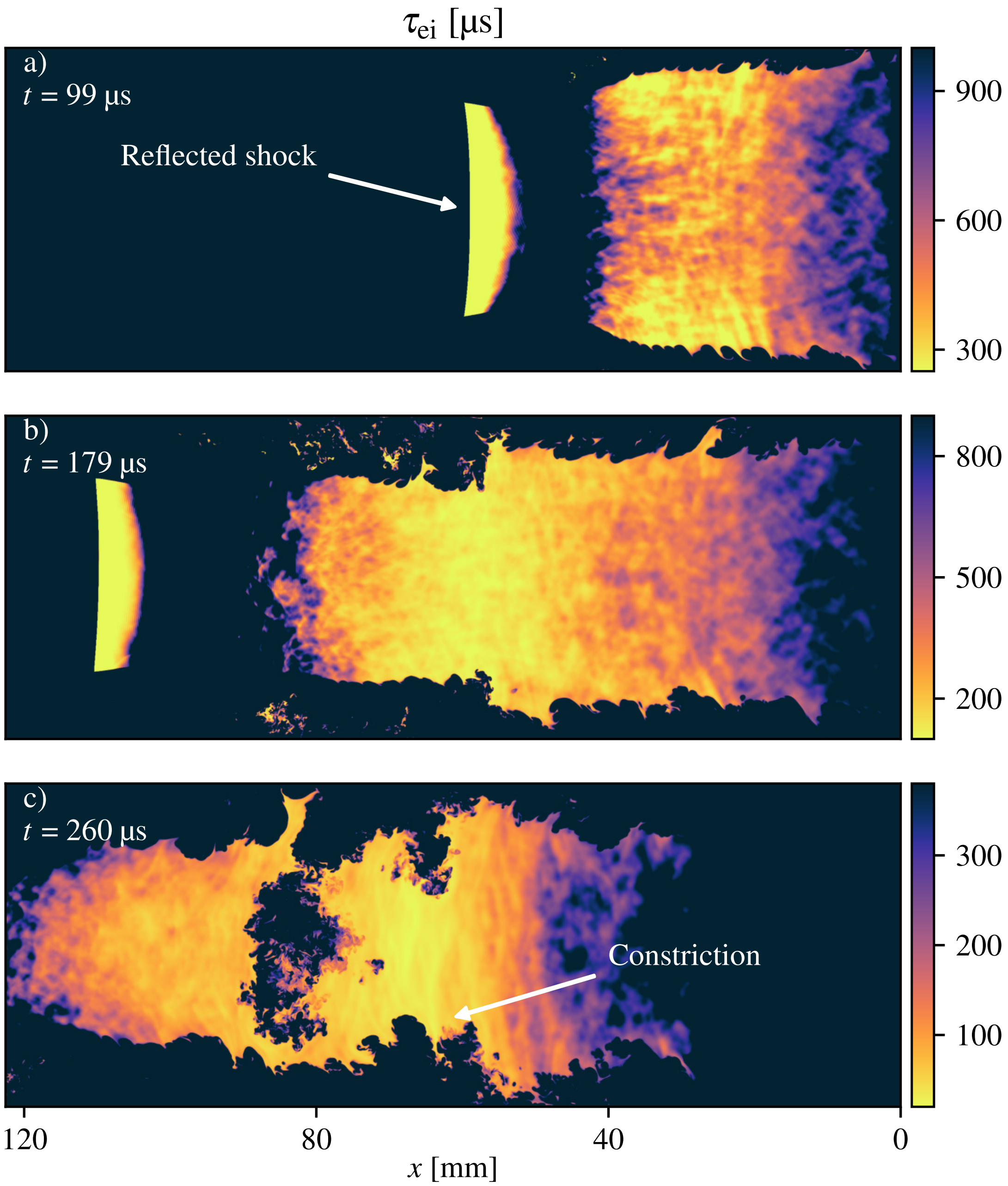

Figure 6.17: Expected time of ignition, using instantaneous values from simulation *RB1* as initial condition for isochoric 0D-reactors. The end wall of the shock tube is located on the right ($x = 0$ mm).

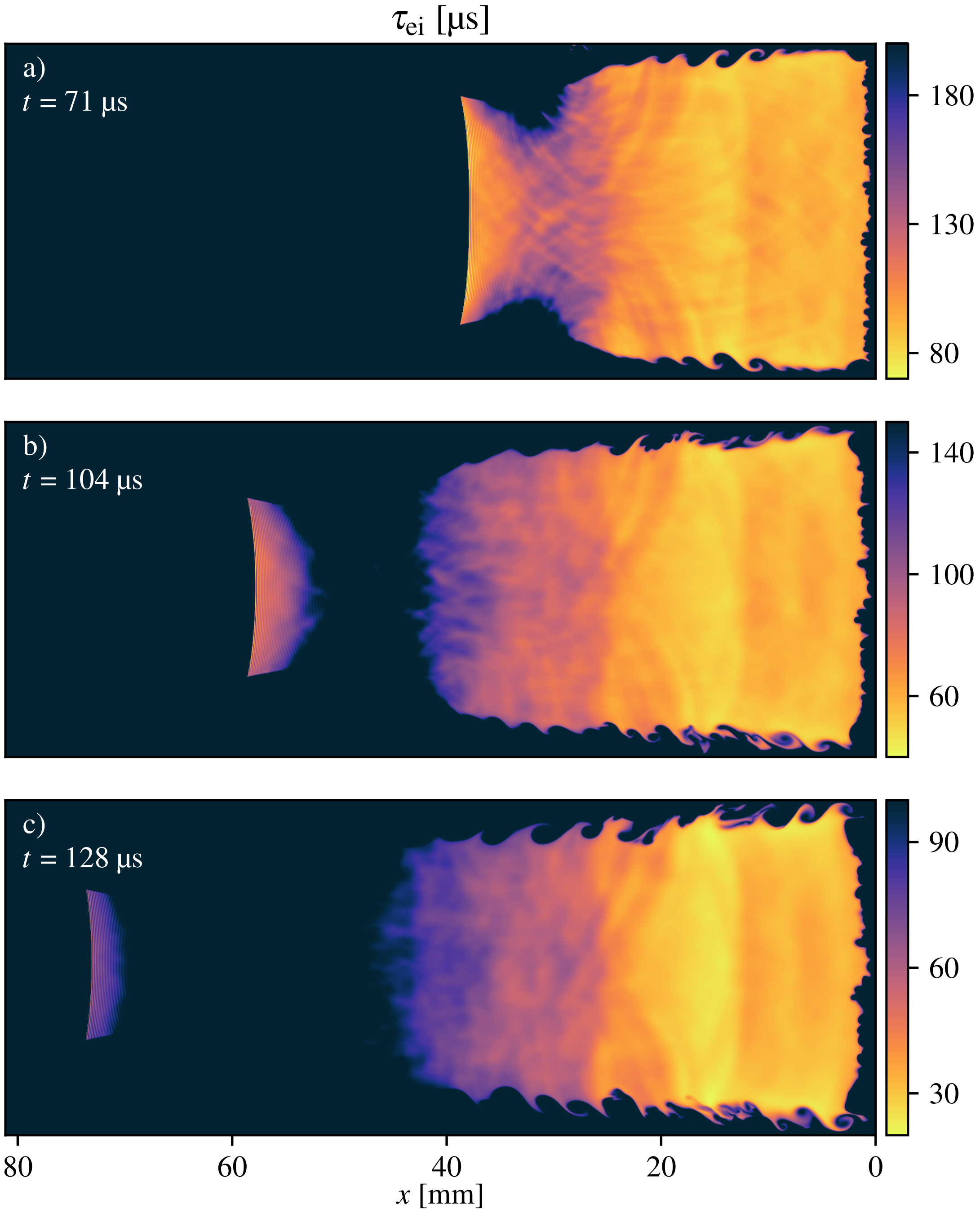

Figure 6.18: Expected time of ignition, using instantaneous values from simulation *RB2* as initial condition for isochoric 0D-reactors. The end wall of the shock tube is located on the right ($x = 0$ mm).

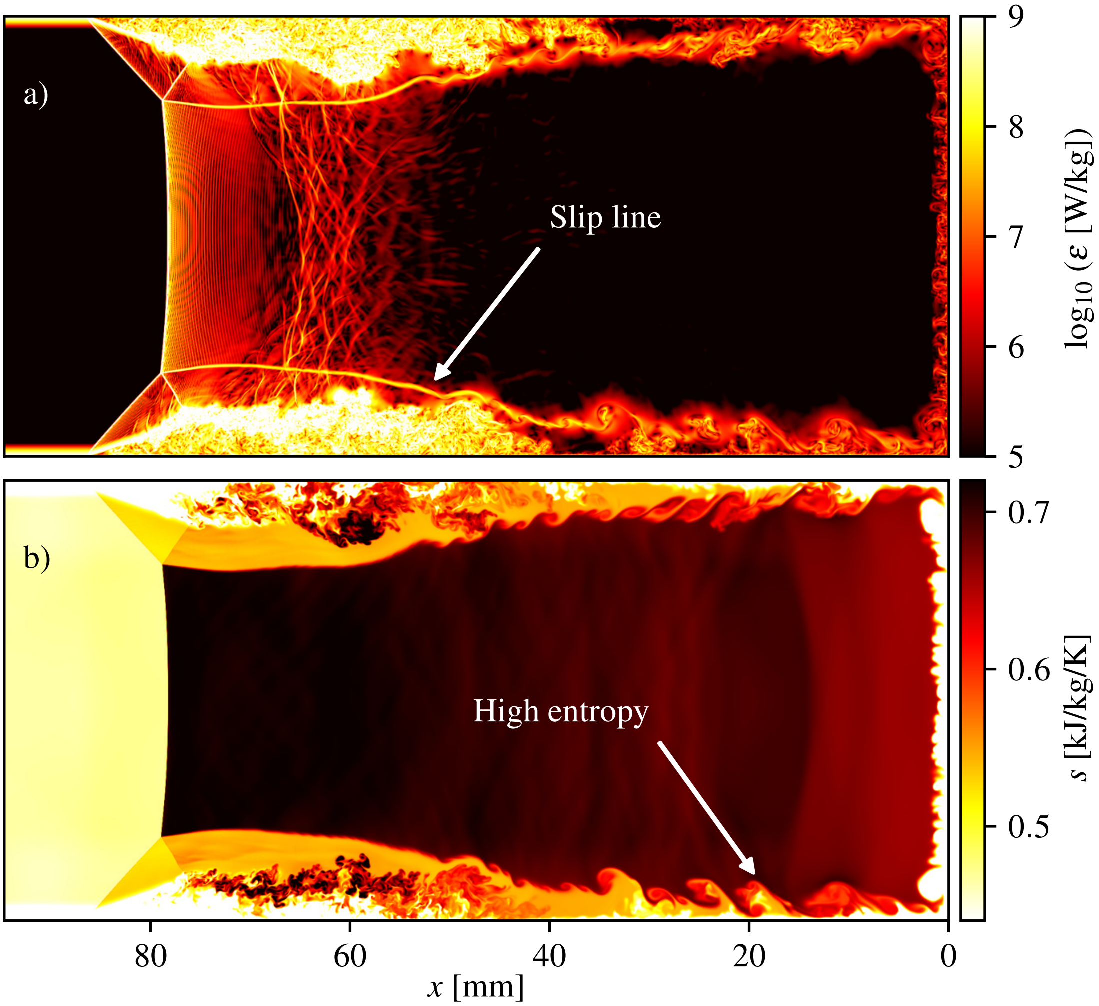

Figure 6.19: Instantaneous fields of dissipation of kinetic energy (a) and entropy (b) from simulation *RB2*. The end wall of the shock tube is located on the right ($x = 0\,\mathrm{mm}$).

case with a linear increase of pressure and in several cases, where the pressure initially decreased. This phenomenon of a decreasing pressure, followed by the transition into a linear increase, can be clearly attributed to the transition of the boundary layer, whose effects were modeled at the inlet of the computational domain. Taking these effects into account will be very important for low-order models to provide reliable results at low pressure. A strong increase of temperature with wall distance was observed, likely resulting from shock attenuation and decoupled from the pressure.

The event of remote ignition in an argon-diluted hydrogen-oxygen mixture was reproduced using two different reaction mechanisms, while another simulation at a slightly higher Mach number showed ignition in strong ignition mode. Differences of the results (using different reaction mechanisms) qualitatively and quantitatively underline the large uncertainties of reaction mechanisms at low temperatures and the need for improvement. Clearly, the remote ignition phenomenon in these cases was caused by the variation of temperature along the center line, resulting from the attenuation of the incident shock.

The remote ignitions, observed in the three-dimensional simulations, however, were caused exclusively by the complex fluid dynamics behind the reflected shock, as boundary layer effects were not modeled at the inlet of the computational domain. If the ignition-delay time is sufficiently long, a second normal shock might evolve before ignition takes place, leading to additional formation of entropy and regions of higher temperature, thus reducing the local ignition-delay time. In the first case investigated, this mechanism led to remote ignition, whereas remote ignition was initiated in the second case, before the second normal shock had formed. Instead, shear in close proximity to the slip line caused a temperature increase, sufficient for a premature ignition from small kernels.

Acknowledgements

The authors from Duisburg gratefully acknowledge the financial support by DFG (project number 279056804) and the computing time on magnitUDE (Universität Duisburg-Essen, through DFG INST 20876/209-1 FUGG, INST 20876/243-1), the Gauss Centre for Supercomputing e.V. (www.gauss-centre.eu) for funding this project by providing computing time on the GCS Supercomputer SUPERMUC-NG at Leibniz Supercomputing Centre (www.lrz.de) and on the GCS Supercomputer HazelHen at Höchstleistungsrechenzentrum Stuttgart (www.hlrs.de). The work at Texas A&M University was supported by the Texas A&M Engineering Experiment Station.

Conflict of interest

The authors declare that they have no conflict of interest.

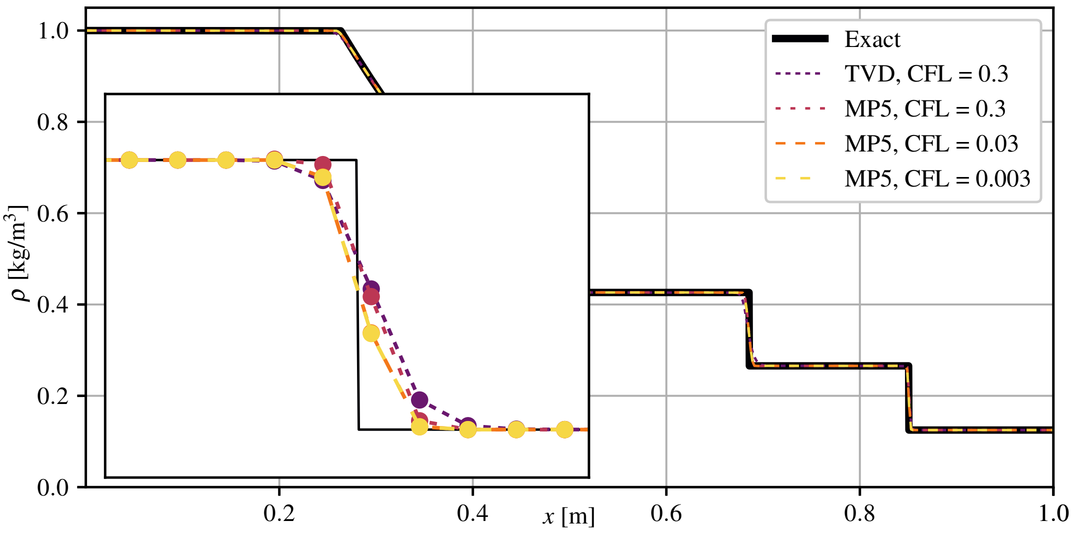

Figure 6.20: Results from simulations of the SOD shock-tube benchmark. Presented are density profiles at a simulation time $t = 0.2$ s and the analytical solution. The close-up presents the solution in the vicinity of the shock wave.

6.5 Supplementary Material

The in-house code *PsiPhi* has been extensively tested against one- and two-dimensional benchmarks of inviscid flow. A small selection of results from one-dimensional simulations is presented below to demonstrate how the shock-capturing numerical schemes used in this work perform in terms of their shock-capturing properties.

Figure 6.20 presents results from inviscid one-dimensional simulations of the SOD shock-tube benchmark [224] to test reconstruction schemes and their impact on shock location and shock resolution, as well as the effect of the time-step size by varying the CFL number. The simulations were performed on a computational grid with 500 cells.

The results show that the location of the shock coincides with that of the analytical solution at a simulation time of $t = 0.2$ s, regardless of the reconstruction scheme or the CFL number (and therefore regardless of numerical viscosity) emphasizing that all implemented methods are time accurate. At a CFL number of 0.3 the scheme is less dissipative, while the solution converges with decreasing step size. The shock itself is captured by the same three numerical cells in terms of the *MP5* scheme and is captured by four numerical cells with regards to the *TVD* scheme.

Figure 6.21 presents results from inviscid one-dimensional simulations of the Shu-Osher benchmark [225] testing the interaction of a shock wave with smooth waves, where the shock propagates into stagnant fluid with a sine-wave density distribution. The simulations were performed on a computational grid with 500 cells.

The respective benchmark is very challenging due to the simultaneous presence of smooth waves and a discontinuity, where the accuracy of the reconstruction scheme reduces to first order. Shock-capturing reconstruction schemes typically introduce amplitude and phase errors, as reported by Zhao et al. [213]. The advantages of higher-order methods are obvious, with the *MP5* scheme most closely matching the reference solution.

Figure 6.22 shows results from an inviscid one-dimensional simulation of case *NRD1* to test the shock speed and to quantify numerical fluctuations that stem from the numerical schemes. The simulation was performed on a computational grid with 2,400 cells. The reference values for the shock speed of the incident shock wave and the pressure behind the reflected shock are obtained from the shock-tube equations for a calorically perfect gas [168]. Since the position and speed of the shock are tracked continuously during the simulation, those values can be compared with the reference values.

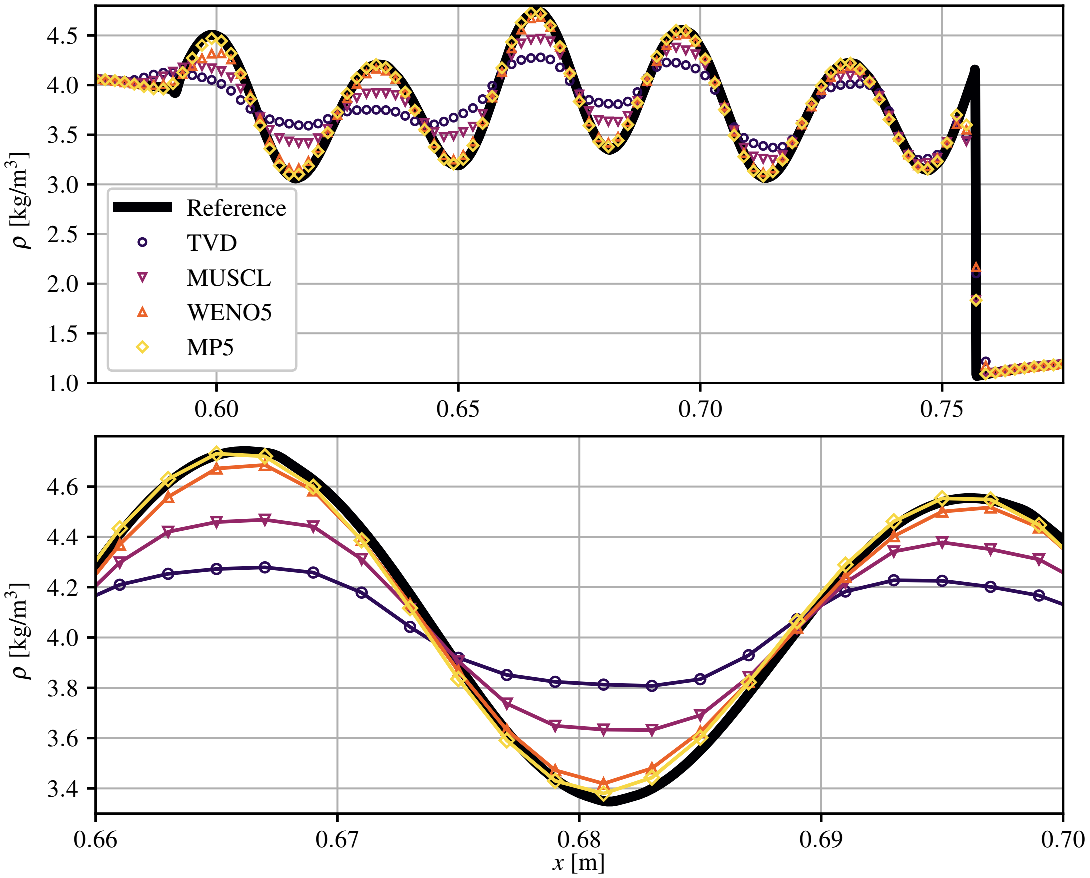

Figure 6.21: Results from simulations of the Shu-Osher benchmark. Presented are density profiles at a simulation time $t = 0.178$ s and a reference solution.

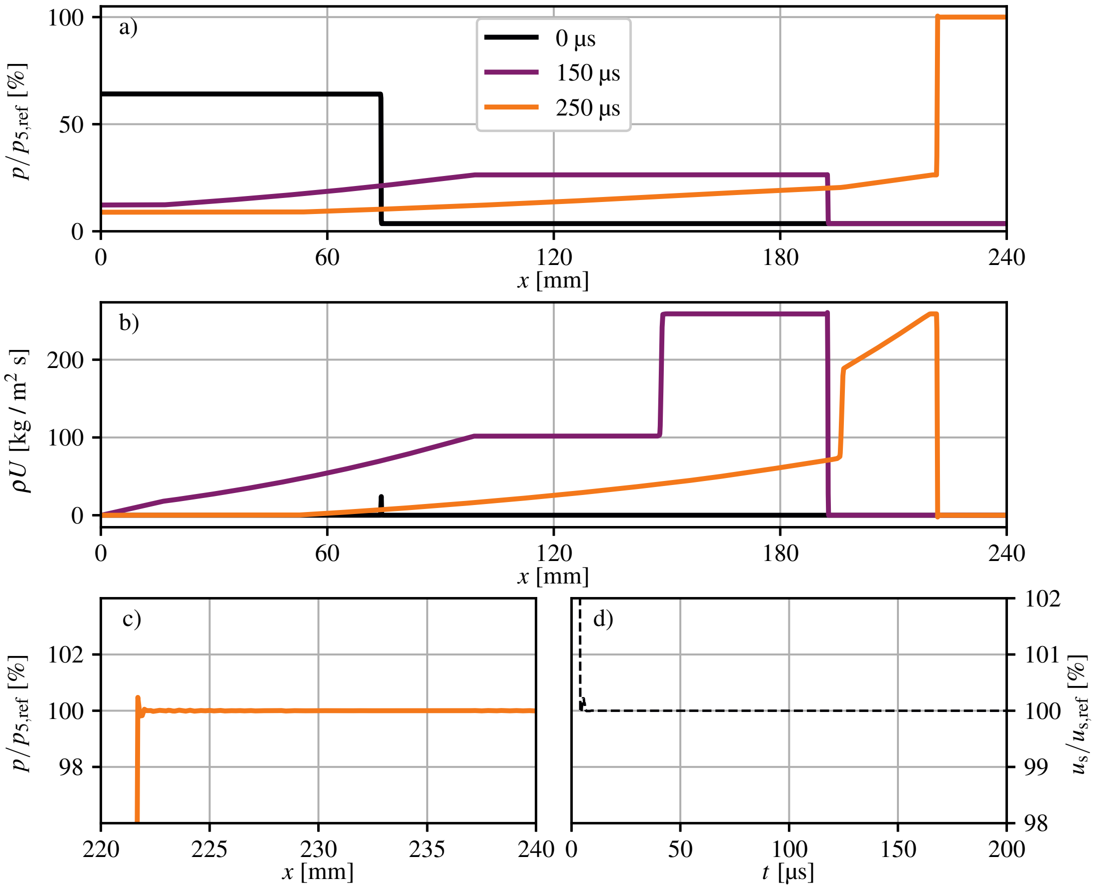

Figure 6.22: Results from a one-dimensional simulation of experiment *NRD1*, using Euler Equations. Presented are profiles of density (a), profiles of momentum (b), the density profile behind the reflected shock (c), and the propagation speed of the incident shock wave normalized by the reference speed (d).

Panel a) and b) of Fig. 6.22 show the pressure profiles and density profiles respectively at different simulation times. A small overshoot is visible ($< 1\%$) behind the reflected shock, while the fluctuations are not lasting and are quickly damped as shown in the close up in panel c). The overshoot behind the discontinuity is more pronounced in the case of the reflected shock compared to the incident shock, a circumstance which, according to Quirk [216], is due to the lower propagation speed relative to the numerical grid. After a short period, during which the incident shock develops, the propagation speed of the incident shock wave u_s matches the reference speed $u_\mathrm{s,ref}$, according to the results presented in panel d). The correct speed of the incident shock wave is also a prerequisite to match the predicted pressure p_5 behind the reflected shock wave, which again is the case as presented in panel c).

Chapter 7
Cellular Stability of Hydrogen-Oxygen Detonation

Cellular Stability of Hydrogen-Oxygen Detonation (Under review)

Authors: J. T. Lipkowicz, J. Crane, X. Shi, H. Wang, I. Wlokas and A. M. Kempf
This chapter was submitted to the 'Journal of Fluid Mechanics' but was rejected. A shortened version of the manuscript was sent to the journal 'Combustion and Flame' and is under review at the time of printing. The author J. T. Lipkowicz wrote the code for the CFD simulations and ran all the simulations. The authors J. T. Lipkowicz and J. Crane generated all figures and tables. The authors J. T. Lipkowicz, J. Crane, and X. Shi wrote the paper. The authors I. Wlokas, H. Wang, and A. M. Kempf contributed corrections, discussions and proof-reading

Abstract

A detonation cellular stability mechanism based on the dynamics of reactive decaying blasts is examined through detailed analyses of two-dimensional (2D) numerical simulations of hydrogen-oxygen detonations. Different from previous blast-based examinations, we resolve the transient process of decoupling between shock and reaction fronts in decaying blasts, and correlate the size of unburnt gas mixtures behind decaying shocks to that of the subsequent blast kernels. The impact on the stability mechanism of 1) chemical kinetics, 2) diffusive processes, and 3) boundary conditions are examined through a series of simulations. At a dopant level, ozone is known to reduce ignition delay without altering thermodynamic properties of the mixture, enabling investigation of the impact of ignition kinetics on the cellular stability. The addition of ozone leads to a stronger coupling between shock and reaction fronts and stabilizes the blast kernel to a smaller size. The resulting global cell size reduction in the ozonated detonation is well described by the stability analysis and in agreement with experimental cell measurements reported in Crane *et al.*, *Combust. Flame* 200 (2019) 44–52. The inclusion of diffusive physics marginally affects the detonation cellular structure, but causes a global propagation speed deficit. Results from two channel heights show that cell size increases in the smaller channel due to mode-locking. A detailed grid convergence study is performed, which examines both kinetic and macroscopic structural features as a function of grid resolution. The results of the stability analysis is independent of numerical grid resolution.

7.1 Introduction

The detonation cellular structure, ever since its discovery [226, 227], has never left the central stage of modern detonation research. The size and shape of these detonation cells reveal useful information regarding the interplay between gas dynamics and chemistry and the cellular length scales also provide key information regarding the scale and geometry of practical detonation power devices [228], such as rotating detonation engines and pulse detonation engines. These engines are considered promising as a new generation of energy conversion devices due to their high theoretical energy efficiencies and simple mechanical design. Beyond power production, a basic understanding of propagation and cellular development of detonation is critical to mitigating safety problems in hydrogen storage and utilization [229], nuclear power plant operation [230], and all energy systems especially those that involve the use of hydrogen as the energy carrier [231]. In particular, the detonation cellular structure is essential to detonation safety evaluations [232].

Detonation propagation and structures are inherently multidimensional. A characteristic cellular structure emerges [233] as a result of shock bifurcation and the interactions among incident shock, Mach stem, and transverse wave [234]. Along with chemical reactions and heat release, these processes form the cellular structure. Within a cell, complex, coupled dynamics evolve over its life cycle, as described experimentally using PLIF images [235]. To illustrate these dynamics, figure 7.1 presents four sequential snapshots of a detonation wave from a two-dimensional detonation simulation, showing the evolution of reactive gas dynamics starting from a *blast kernel* at the end of a previous detonation cell cycle (panel a), leading to an overdriven shock wave at a speed in excess of the theoretical Chapman-Jouguet (CJ) speed (panel b), the decay in the shock speed to below the CJ speed (an underdriven wave) and the separation of the shock front from reaction front (panel c), and lastly, the birth of a new cell cycle from a new blast kernel (panel d). Each cell cycle interacts with its neighboring cells, and these interactions produce a sequence of spatially distributed, autonomously propagating energy centers that ensure the burned gas to be globally choked, thus enabling the global propagation of the detonation wave.

Although the cellular structure can be easily measured experimentally, a clear picture of the relationship between the detonation cellular structures and mixture properties is still lacking at a fundamental level. In terms of cell size, a widely adopted approach is to relate experimental cell size to computed induction length from one-dimensional, steady-state calculations, e.g., the Zel'dovich-Neumann-Döring (ZND) detonation, through a proportionality factor. However, the factor is known to vary significantly among different mixtures and conditions. Over the past few decades, the proportionality factor has evolved from a single constant [236], to a function of mixture conditions, e.g., equivalence ratio and dilution [237, 238], and to a multi-parameter fitting involving stability parameters [239, 240]. The correlation between cell size and induction length is sensitive also to how induction and chemical lengths are defined, all of which is heuristic by nature [241]. Despite the varying degrees of success in using these empirical approaches, a quantitative theory is yet to be established.

In terms of cell regularity, a wide range of regular (figure 7.1) or irregular structures have been observed. Radulescu and coworkers [242–244] noted that the cellular regularity is governed by both gas-dynamic and chemical effects; and to the first order, these two factors may be characterized by the ratio of specific heats at the von Neumann state, γ_{VN} [243, 244], and the effective activation energy of mixture ignition, ϵ_i [245, 246]. High γ_{VN} and low ϵ_i mixtures tend to yield regular cell structures, whereas low γ_{VN} and/or high ϵ_i mixtures produce irregular cells with a wide range of cell size distribution [242, 243]. To clearly isolate the gasdynamic and chemical kinetic effects, a recent study used ozone as a trace additive [247] and demonstrated, by experiment and numerical simulation, that the theory advanced by Radulescu to be correct.

At a detailed level, however, *what modulates cell size for detonation with a regular cellular structure* remains to be an open question. Previously, we examined the cellular stability using a semi-empirical geometric model [248]. In this model, shock-reaction interactions within a detonation cell cycle are described through unsteady one-dimensional cylindrical detonation simulations. The evolving detonation structure was then modeled in a confined space with specified boundary conditions and the assumption that the

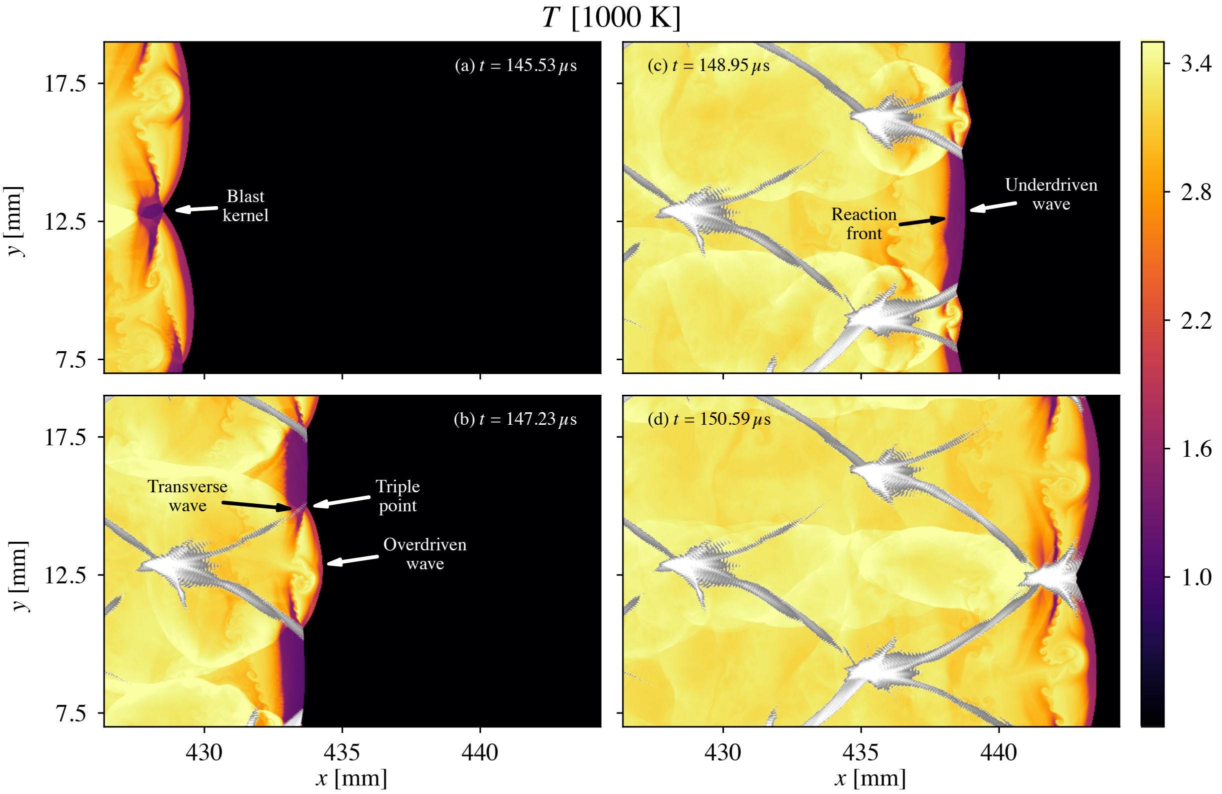

Figure 7.1: Snapshots of temperature fields (in lab coordinates) computed for a stoichiometric H_2-O_2 mixture at 15 kPa and 300 K, showing the evolution from **(a)** the blast kernel to **(b)** an overdriven detonation wave, **(c)** an underdriven wave and the decoupling of shock front and reaction front, and finally **(d)** the onset of a subsequent detonation cell cycle. The temperature fields are superimposed by numerical soot foils for pressure ≥ 9 bar. The detonation wave travels from left to right.

mean shock speed within a cell is equal to the CJ speed. The model predicts that the size of the blast kernel, defined by the spatial gap between the shock and reaction fronts at the end of a cell cycle, dictates the size of the subsequent cell. Stable cell size emerges through the feedback control of the blast kernel sizes in two sequential cells. The stable size is unique to a particular fuel/oxidizer mixture, and hence it explains the notable difference in cell size in detonations of non-ozonated and ozonated hydrogen-oxygen mixtures [241]. Not only does the proposed stability mechanism have the potential to predict stable detonation cell sizes for any given mixture, it provides a physics-based context to investigate the possibility of multiple stable cell sizes for a given mixture, and the effect of various physical processes, e.g., diffusion, on detonation cellular structure. Nevertheless, question remains as to whether the semi-empirical geometric model is capable of revealing detonation dynamics at a fundamental level. Indeed the model relies on assumptions that are related to initiation of cylindrical 1D detonations and global propagation speed.

The other long standing issue, in the area of numerical simulation, is the inability to reproduce cellular features that satisfactorily agree with experimental measurements. The discrepancy may be caused by a variety of factors. For example, many numerical detonation simulations rely on one-step or several-step global chemistry models to reduce the computational cost. The use of detailed chemistry yielded results that can be significantly different from those computed with one-step chemistry [249, 250]. Also observed in numerical simulations is a dependency between cell size and initial conditions, which has not, at least not clearly, been observed in experiments [251]. Many detonation simulations were performed using the Euler equations [252–254], although recently researchers noted that using the Navier-stokes (NS) equations can produce qualitatively different results [255–258]. Quantitatively, however, there is little information about the role of diffusive physical processes on cellular structure, detonation velocity, and boundary layer development.

In this study, we seek to address the above two issues through a set of high-resolution, two-dimensional simulations of detonations with detailed chemistry and a quantitative test of the kinetics-resolved detonation cellular stability mechanism using the simulation results. Simulations of hydrogen-oxygen mixtures without and with ozone addition are made to provide insight into the role of chemical kinetics, diffusive processes, and confining geometry on detonation cellular stability and propagation.

7.2 Numerical details

7.2.1 Numerical solver

Simulations are performed using the in-house code *PsiPhi* [6, 183, 207, 208] that utilizes the finite-volume method (FVM) on a Cartesian, equidistant grid. A non-blocking message passing interface (MPI) based domain decomposition parallelization is implemented and yields a high scaling efficiency. The set of fully compressible conservation equations for momentum, total internal energy, and species is solved to simulate detonation wave propagation:

$$\frac{\partial \rho u_i}{\partial t} + \frac{\partial \rho u_i u_j}{\partial x_j} = -\frac{\partial p}{\partial x_i} + \frac{\partial \tau_{ij}}{\partial x_j}, \tag{7.1}$$

$$\frac{\partial \rho E}{\partial t} + \frac{\partial \left(\rho E + p\right) u_i}{\partial x_i} = -\frac{\partial q_i}{\partial x_i} + \frac{\partial \tau_{ij} u_i}{\partial x_j}, \tag{7.2}$$

$$\frac{\partial \rho Y_\alpha}{\partial t} + \frac{\partial \rho Y_\alpha u_i}{\partial x_i} = -\frac{\partial j_{i,\alpha}}{\partial x_i} + \dot{\omega}_\alpha. \tag{7.3}$$

These governing equations feature the mass density of the mixture ρ, the velocity components u_i in the i^{th} coordinate, the static pressure p obtained from the equation of state, the viscous stress tensor τ_{ji}, the total internal energy E of the mixture, the absolute enthalpy h of the mixture, the heat flux q_i due to heat conduction and molecular diffusion, the partial mass density ρY_α of species α, the diffusion flux $j_{i,\alpha}$ of species α, and the source term $\dot{\omega}_\alpha$. Key quantities just discussed are calculated as:

$$\tau_{ij} = \mu \left[\left(\frac{\partial u_i}{\partial x_j} + \frac{\partial u_j}{\partial x_i} \right) - \frac{2}{3} \frac{\partial u_k}{\partial x_k} \delta_{ij} \right], \tag{7.4}$$

$$q_i = -\lambda \frac{\partial T}{\partial x_i} + \sum_{\alpha=1}^{N_\mathrm{s}} h_\alpha j_{i,\alpha}, \tag{7.5}$$

$$j_{i,\alpha} = -\rho D_\alpha \frac{\partial Y_\alpha}{\partial x_i} + \rho V_{i,\mathrm{c}} Y_\alpha, \tag{7.6}$$

$$h_\alpha = \Delta h^0_{\mathrm{f},\alpha} + \int_{T_0}^{T} c_{p,\alpha} \, \mathrm{d}T, \tag{7.7}$$

$$h = \sum_{\alpha=1}^{N_\mathrm{s}} Y_\alpha h_\alpha, \tag{7.8}$$

$$E = h - \frac{p}{\rho} + \frac{u_i u_i}{2}. \tag{7.9}$$

The above auxiliary equations feature the mixture-averaged dynamic viscosity μ, the mixture-averaged heat conductivity λ, the total enthalpy h_α of species α, the mixture averaged diffusivity D_α of species α, the correction velocity $V_{i,\mathrm{c}}$ to achieve consistency between partial mass densities and the transported mass density, the standard enthalpy of formation $\Delta h^0_{\mathrm{f},\alpha}$ of species α, and the constant-pressure heat capacity $c_{p,\alpha}$ of species α.

Thermochemical and transport properties of individual species and chemical reaction rate constants are calculated using Cantera [187] and tabulated as a function of temperature. For pressure fall-off reactions, the rate constants are tabulated also as a function of "effective" concentration [11], computed as the sum of the products of collision efficiency β_α and corresponding concentration $[\mathcal{X}_\alpha]$ of all species considered. The resulting tables are then used by *PsiPhi* during runtime to reduce the computational cost. The mixture-averaged viscosity, heat conductivity, and species diffusivities are determined using models by Wilke [221], Peters and Warnatz [189], and Kee et al. [11], respectively. Species production rates are evaluated using the tabulated reaction rate constants and the local species concentrations. A Strang [91] operator-splitting framework, 2nd-order accurate in time, is implemented to treat chemistry and transport separately. The solution of chemistry is advanced in time by CVODE [191]. For transport, the approximate Riemann solver HR-Slau2 [210] is used for the computation of convective fluxes. The states on the left and right sides of a numerical cell interface are determined by a 5th-order accurate reconstruction scheme [211], which reconstructs the local, one-dimensional characteristic variables. The five-point stencil of the reconstruction scheme is also used to distinguish discontinuities from extrema so that the accuracy reduces to first order only near discontinuities. One of the disadvantages of using a high-order scheme with characteristic variables is the occurrence of strong oscillations under some circumstances, for example when two discontinuities interact [218]. In order to avoid nonphysical solutions, recursive-order reduction (ROR) is applied [143]. Diffusive fluxes are calculated using the 2nd-order central difference scheme. The solution of transport is advanced in time by a low-storage, 3rd-order explicit Runge-Kutta scheme [186].

7.2.2 Numerical setup

Simulated mixtures are stoichiometric hydrogen-oxygen mixtures at 300 K and 15 kPa, with or without 3000 ppm ozone doping, as in the experiment [241]. Detailed reaction kinetics are used for the simulation using the hydrogen sub-model of the Foundational Fuel Chemistry Model Version 1.0 (FFCM-1) [222, 259] complemented by the Princeton ozone sub-model [260]. Table 7.1 summarizes the key thermodynamic and kinetic properties of the simulated mixtures, including the theoretical CJ speed V_CJ, the

X_{O_3} (ppm)	V_{CJ} (m/s)	T_{CJ} (K)	L_i (mm)	L_{hr} (mm)	τ_{ig} (µs)	$\tilde{E}_a$
0	2732	3314	0.44	0.43	0.85	4.39
3000	2734	3317	0.25	0.24	0.48	2.92

Table 7.1: Characteristic properties of the simulated hydrogen-oxygen mixtures (300 K and 15 kPa). X_{O_3} is the molar fraction of ozone in the unburned mixture.

ID	N_x (10^6)	L_{hr}/Δ_x	L_x/L_{hr}	CPU (10^3h)
EU6O	2.2	24	152	31
NS6O	2.2	24	152	31
EU6	2.2	43	85	35
NS6	2.2	43	85	31
EU24O	8.6	24	152	152
NS24O	8.6	24	152	331
EU24	8.6	43	85	304
NS24	8.6	43	85	331

Table 7.2: Overview of the core simulations performed, using Euler EU) and Navier Stokes (NS) equations for the 6 mm narrow channel (6) and the 24 mm wide channel (24) with (O) or without ozone added. All simulations listed use a grid resolution of $\Delta_x = 10$ µm.

equilibrium temperature T_{CJ}, the ZND induction length L_i, the half-reaction length L_{hr}, the ignition delay time τ_{ig}, and the dimensionless activation energy $\tilde{E}_a$. Based on an assessment following Gamezo et al. [252], both $\tilde{E}_a$ values are considered low, thus regular detonation cellular structures are expected for both mixtures. Here, the ZND solution is obtained with the CalTech Shock & Detonation Toolbox from Browne et al. [261] using the thermochemical data of the same reaction model.

Simulations are conducted with the Navier-Stokes (NS) equations (7.1-7.3) and the Euler (EU) equations (the same equations but removing the shear stress and diffusion terms) in two channel widths: 6 mm (6) and 24 mm (24), with (O) and without ozone - resulting in a set of eight core simulations, as identified in table 7.2. A 10 µm grid resolution is used in all of the core simulations. In addition to the core simulations, four supplementary simulations are performed to examine the impact of grid resolution, convergence, and boundary conditions, as summarized in table 7.3. The first three supplementary simulations are identical to the core simulation NS24O at 10 µm resolution, except their grid resolutions are changed to 40, 20, and 5 µm. The final supplementary simulation (NS6-FS-A) uses free-slip and adiabatic boundary conditions (as in EU6) but with diffusive transport treated in the bulk gas.

The domain length, L_x, is kept at 36 mm for all simulations, which substantially exceeds the requirement of $L_x/L_{hr} \approx 20$ for mixtures with dimensionless activation energies of 10, as suggested by Mazaheri et al. [255]. For comparison, our smallest L_x/L_{hr} value is 85 in the case of the non-ozonated mixture.

ID	N_x (10^6)	Δ_x (µm)	L_{hr}/Δ_x	L_x/L_{hr}	CPU (10^3h)
NS24O-40	0.5	40	6	152	21
NS24O-20	2.2	20	12	152	83
NS24O-5	35	5	48	152	2,648
NS6-FS-A	2.2	10	43	85	31

Table 7.3: Overview of the supplementary simulations performed.

Additionally, the grid resolution of the core simulations ($\Delta_x = 10\,\mu\text{m}$) is expected to be sufficient for resolving detonation dynamics according to the $L_{\text{hr}}/\Delta \geq 25$ criterion for a dimensionless activation energy of $\tilde{E}_{\text{a}} \leq 10$ [255]. Nevertheless, a detailed grid resolution study will be presented in the next section considering both kinetic convergence and the convergence of all major macroscopic features.

A Dirichlet boundary condition is applied at the inlet for both transported quantities and pressure, while the Navier-Stokes Characteristic Boundary Condition (NSCBC) [145] is used at the exit. The NSCBC advances the full set of conservative variables by replacing the normal derivatives in the Navier-Stokes equations by characteristic expressions from the local one-dimensional inviscid (LODI) relations, while solving the transverse derivatives, as well as diffusive terms and source terms in accordance with the numerical schemes applied in the inner numerical domain. This boundary condition can be set to be either perfectly non-reflecting or partially reflecting by specifying a far field reference pressure and relaxing towards this pressure. In this work, a partially reflecting exit is used, where the far field pressure is set to the value of the equilibrium pressure p_{CJ}, while the amplitude of the incoming waves is computed by the equation of Rudy and Strikwerda [262] with a model constant of $\sigma = 0.15$. This setup allows a numerical domain that is moved at the theoretical CJ speed relative to the laboratory reference without wave reflection, if the flow is subsonic at the outlet. A no-slip, isothermal boundary condition is applied at both the bottom and top of the numerical domain when the Navier-Stokes equations are solved, while a free-slip, adiabatic boundary condition is used when the Euler equations are solved. Henceforth and unless otherwise stated, the solutions of Navier-Stokes equations impose no-slip and isothermal boundary conditions, while the Euler solutions imply free-slip and adiabatic boundary conditions. In all cases, a slightly inclined planar detonation wave according to the ZND solution is specified to initialize the simulation. This initial condition is selected to mitigate frequency biasing which could result in initial condition dependent cell sizing, as seen in previous work by Sharpe and Quirk [251].

Figure 7.2 presents numerical Schlieren images from Euler simulations EU6 and EU24 in the 6 mm and 24 mm channels. The images show the complete numerical domain, where the detonation wave travels from left to right. Many known features, such as wave fronts and vortices, are captured and resolved. Also visible is the performance of the non-reflecting exit boundary condition, which does not appear to introduce any numerical artifacts into the domain.

Computational soot foils are generated by tracking the local maximum pressure for each location through the simulation. Figure 7.3 presents the full-length soot foil from NS24, illustrating the transition from the initial inclined 1D detonation wave into a cellular detonation. At first, a wave evolves at the upper end of the domain as the oblique shocks are reflected off the top wall. This wave rapidly consumes fuel, as evidenced by the generation of an array of pressures in a broad region. The wave leaves perturbations in its wake, resulting in the formation of additional, weaker waves near the top of the domain. After the reflection of the initial wave off the bottom, the downwards propagating weaker waves interact with the reflected wave, thus promoting the initial detonation-wave kernels. Initially, cells of varying sizes start to develop in the channel until the wave has travelled a distance of about 400 mm, after which a regular constant-cell-size cellular pattern emerges.

7.3 Results and discussion

The goals of the numerical simulation analysis are threefold: (1) validate simulation results by comparing global cellular features to those from existing experimental measurements, (2) establish the kinetics-resolved stability mechanism by analyzing the local dynamics of the cell formation process, and (3) quantitatively evaluate the effect of chemical kinetics, diffusion, and boundary conditions on the stability mechanism and the associated detonation features. This section is divided into three sub-sections that coincide with the three goals.

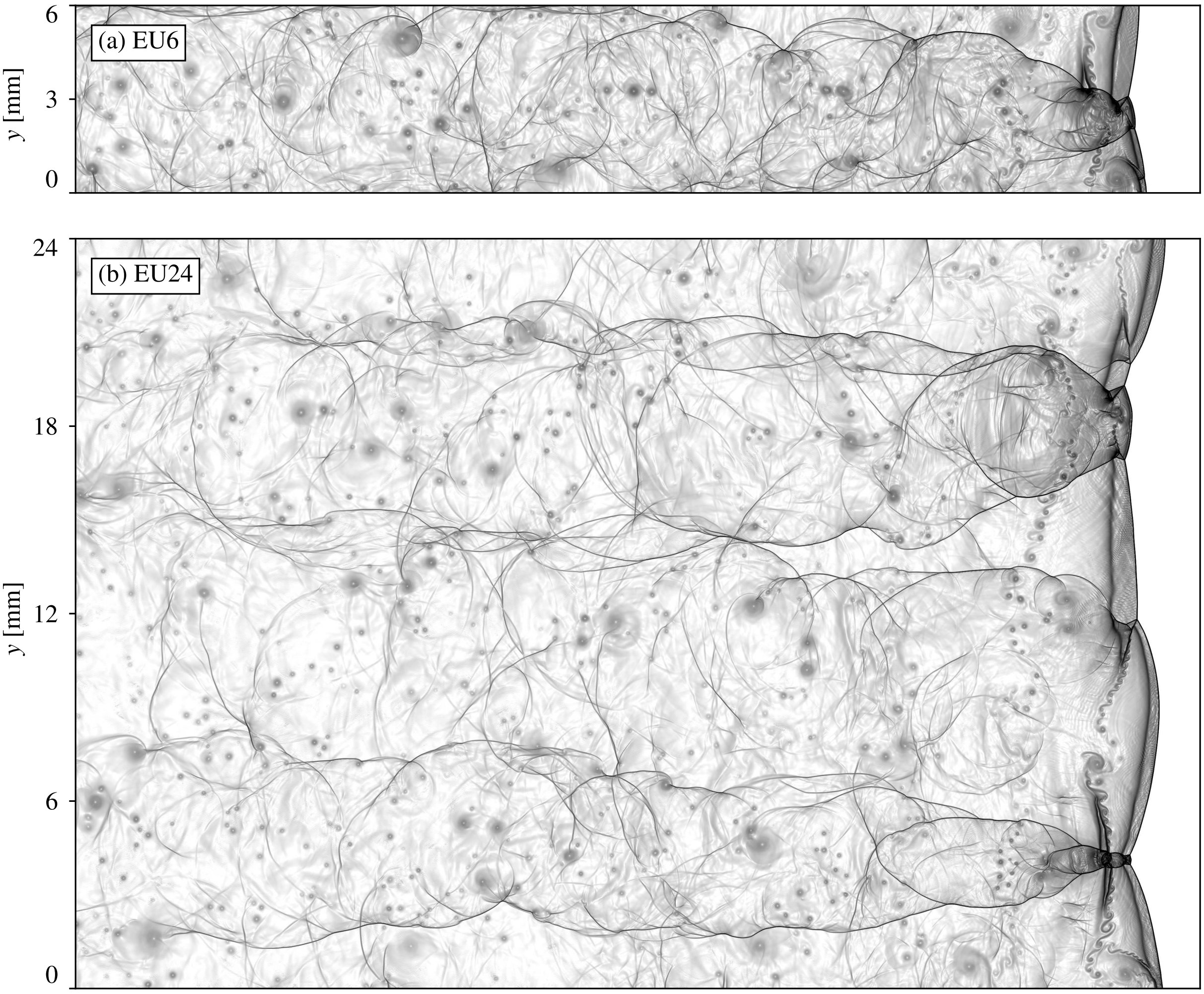

Figure 7.2: Numerical Schlieren images from two-dimensional simulations with channel widths of **(a)** 6 mm and **(b)** 24 mm (bottom). The two simulations are EU6 and EU24, respectively. The computational inlet is located on the right with walls at the top and at the bottom. The detonation wave travels to the right.

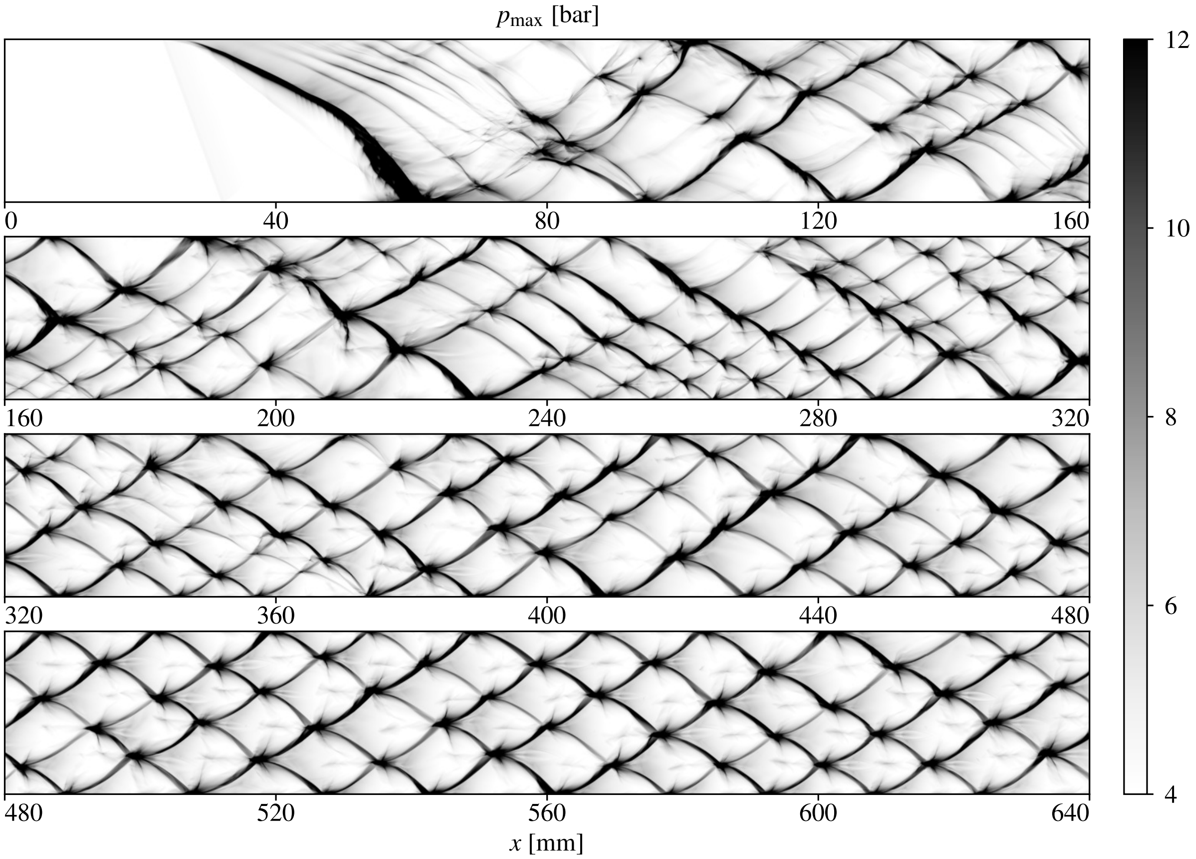

Figure 7.3: Numerical soot foil from Simulation NS24. The soot foil is broken into four parts with the right side of the upper image connecting with the left side of the image below.

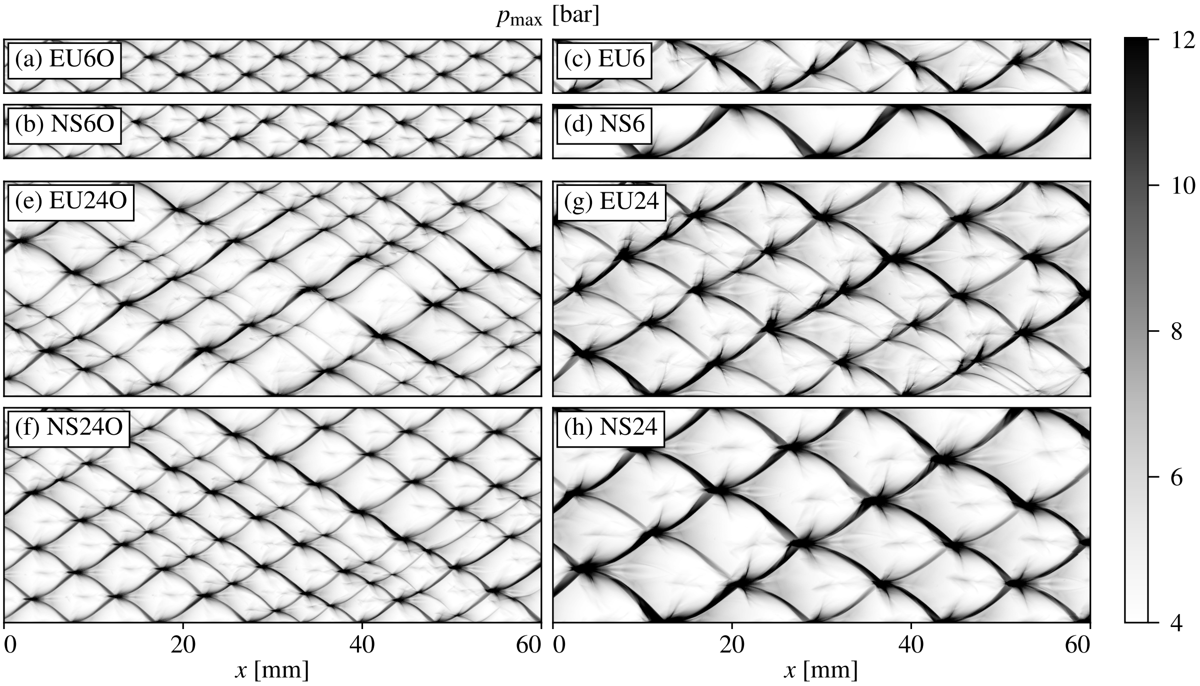

Figure 7.4: Numerical soot foils from simulations with **(a,b,e,f)** ozonated (3000 ppm) and **(c,d,g,h)** non-ozonated mixtures in channels with **(a,b,c,d)** heights of 6 mm and **(e,g,f,h)** 24 mm. Both Euler and NS results are presented. The lines represent the traces of triple points.

7.3.1 Global cellular features

We discuss first the general features of the detonation cell structure beyond its initial development for all eight core simulations. Cellular mode-locking plays a strong role in detonation in confined geometries [263, 264]. The confinement allows only discrete channel width (w)-over-cell width λ ratios owing to shock reflections off the walls. Despite the strong mode-locking effect, an inspection of the smoke foils of figure 7.4 shows universal reduction in cell size from non-ozonated mixture (right column) to the ozonated mixture (left column) under comparable conditions. The extent of cell-size reduction is in agreement with the experimental results [241] as will be elaborated later. Subtle differences exist between the Navier-Stokes and Euler simulations. In particular, comparing EU6 and NS6 (figure 7.4 panel b and d), we see that in the Euler simulation weak transverse waves are visible in addition to the strong transverse waves that are present in both EU6 and NS6 simulations. The single, strong transverse wave of the “Zig-Zag” pattern mirrors that of the single-headed spinning mode observed in three-dimensional detonations near the detonation limit [265, 266]. Weak transverse waves are also observed in the Euler simulation in the wider channel (24 mm) whereas such weak waves are absent in NS24. The supplemental simulation NS6-FS-A soot foil, using free-slip and adiabatic boundary conditions identical to those of EU6, matches closely that of NS6, as it also yields a simple “Zig-Zag” pattern (not shown here). Hence, the boundary conditions are not the direct cause of the weak transverse waves in EU6. Rather, the weak transverse waves are dampened or fully suppressed by viscous dissipation. The extent of such an effect depends on the reactive mixtures. For example, in ozonated mixtures, the weak transverse waves alternate with strong transverse waves in the 24 mm channel with and without the viscous transport terms.

The cells computed for the wider 24 mm channel are still mode locked, and hence, they are impacted by the channel size (figure 7.4h). Nevertheless, the large number of detonation cells available from the simulation enables a semi-quantitative comparison with experimental measurements of cell width [241] made in a tube of a comparable size. Figure 7.5 presents the distributions of cell widths, measured from the experimental and numerical soot foils. In spite of the difference in geometry (a 2D channel in simulations and a circular tube 32 mm in diameter in experiments), the experimental and simulated cell sizes and

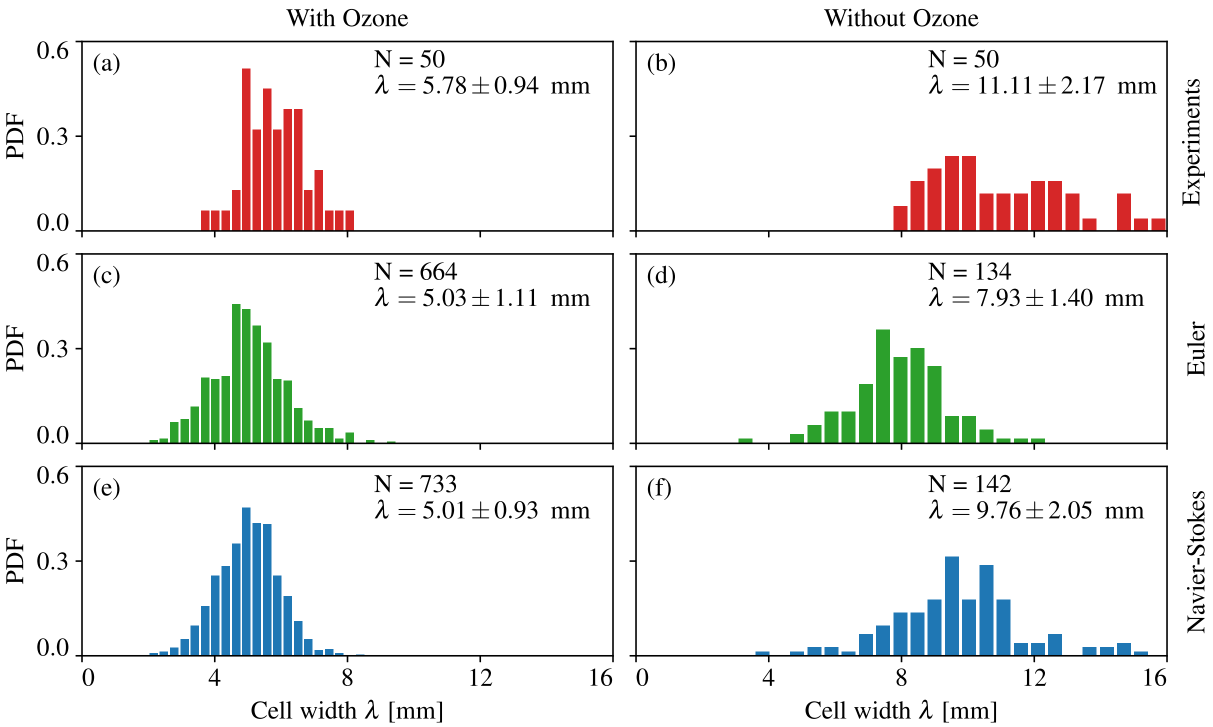

Figure 7.5: **(a,b)** Cell width probability density function from 32 mm round tube experiments [241], **(c,d)** Euler simulations, and **(e,f)** Navier-Stokes simulations with (*EU24O, NS24O*) and without ozone (*EU24, NS24*) in 24 mm channels.

their distributions agree well. For the ozonated mixture, cell size distributions between Euler and NS simulations are close to each other in both the mean values and standard deviations. For comparison, the average cell widths of the simulations (NS24: 5.03±1.11 mm, EU24: 5.01±0.93 mm) are about 13 % below the experimental value (5.78±0.94 mm), all with comparable standard deviations.

For the non-ozonated mixture (NS24 and EU24), the mean cell width is smaller in the Euler case than the NS case (NS24: 9.76±2.05 mm, EU24: 7.93±1.40 mm). This difference is consistent with the observation of weak transverse wave suppression due to viscous dissipation. The NS simulations show a generally better agreement with the experimental cell widths. We note that while it is tempting to conclude that this better agreement is expected because of the inclusion of diffusive physics leading to a more complete representation of the physical processes in the experiments, we caution that because of mode locking and the different geometry and size, the comparison shown may be fortuitous and is semi-quantitative at best. The key takeaway here is that the effect of 3000 PPM ozone doping, leading to the cell size reduction by about a factor of two as observed experimentally, is well captured by the simulations, thus suggesting that the overall detonation cellular dynamics is well captured by the simulations.

7.3.2 Cellular stability mechanism

In an earlier work, we proposed a detonation cellular stabilization mechanism whereby the propagation of detonation waves is controlled by local blast kernels [248], which provides the feedback required to modulate the cell size for detonations with regular cell sizes. The analysis, however, was subject to a major assumption: all cell cycles propagate at an average velocity of the CJ velocity. The current work seeks to generalize this stability mechanism through a validation of this assumption by analyzing the 2D simulation results.

We precede our analysis by illustrating first the dynamics of the cellular structure in the context of sequential local blasts. As figure 7.6 shows, a blast kernel is an unburnt post-shock gas pocket immediately following the collapse of transverse waves from neighboring blasts. The kernel is over compressed; and

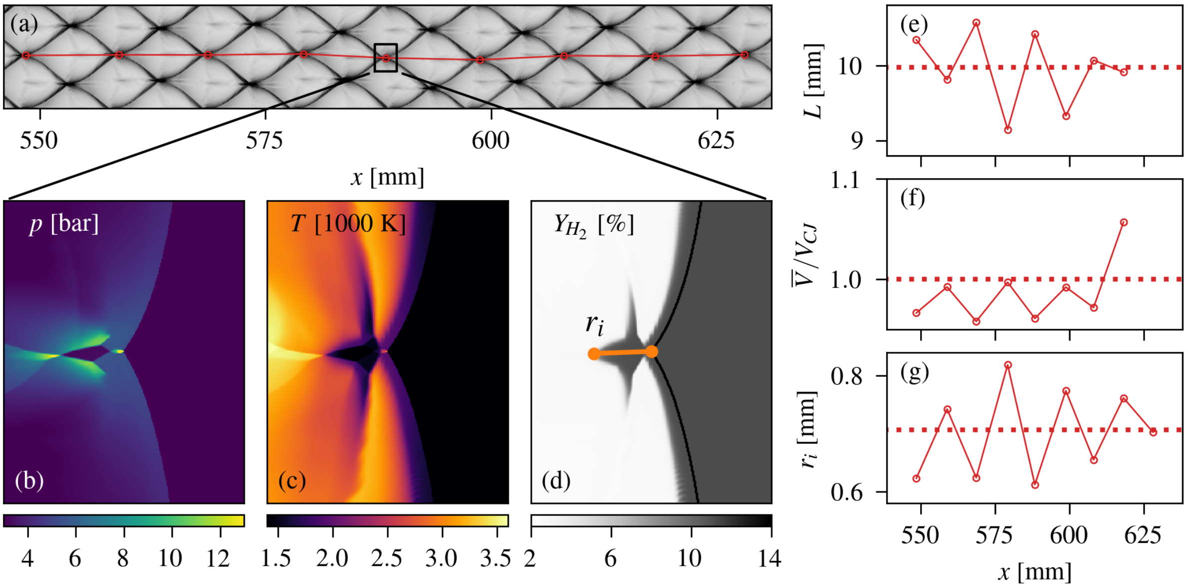

Figure 7.6: **(a)** A subsection of the soot foil for NS24O with a series of blast kernels labeled by circles and connected by the line. **(b, c, d)** Pressure (p), temperature (T), and hydrogen mass fraction (Y_{H_2}) snapshots of a blast kernel. **(e, f, g)** Cell length (L), normalized average cell velocity ($\overline{V}/V_{CJ}$) and blast kernel size (r_i), respectively, along blast kernel line with global averages noted as dashed lines. Lines in **(e, f, g)** are drawn to guide the eyes.

the ignition of this kernel is related to the generation of the overdriven wave. In figure 7.6(a), we mark these kernels by the array of small red circles. Each kernel represents the end of the previous cell and the birth of a new cell. Figure 7.6 (panel b, c, and d) present the pressure p, temperature T and H_2 mass fraction profiles Y_{H_2} around the blast kernel. In principle, the blast kernel marks the point of transition of the frontal propagation from an underdriven wave in a previous cell cycle to a strongly overdriven wave in a new cell. The size of the blast kernel r_i, labeled in figure 7.6(d), is expected to control the subsequent propagation dynamics. Plotted in figure 7.6(e), (f) and (g) are the evolution of cell length (L), normalized cell-average propagation velocity ($\overline{V}/V_{CJ}$) and blast kernel size (r_i), respectively, for the chain of detonation cells shown in figure 7.6(a). From this example, it is immediately evident that individual detonation cells do not propagate at an average velocity equal to the CJ velocity; and hence, the actual propagation dynamics are more complex than we assumed earlier [248]. Nonetheless, the cell length, normalized velocity, and kernel size exhibit a clear feedback behavior, as they oscillate close to their respective stable values.

7.3.2.1 Kernel-driven cellular propagation

In our previous work we showed (using 1D simulations) that larger detonation kernels yield more robust blasts which, when the average cell velocity is equal to the CJ velocity, yields larger detonation cells. Given the more complex dynamics evident from figure 7.6, we seek to use the present 2D simulations to statistically discern the role of detonation kernels on structure.

Figure 7.7(a) shows the velocity decay of a representative blast (from the NS24O simulation) along the centerline of the detonation cell. The velocity decay is calculated as the temporal derivative of the shock front position ($V_P = dR_P/dt$), where R_P is the wave location based on a pressure threshold. Also plotted is a fitted exponential decay function, which approximates the behavior of the velocity function. The form of the decay function is:

$$V(t) = (V_{\max} - V_\infty)e^{-t/\tau} + V_\infty, \tag{7.10}$$

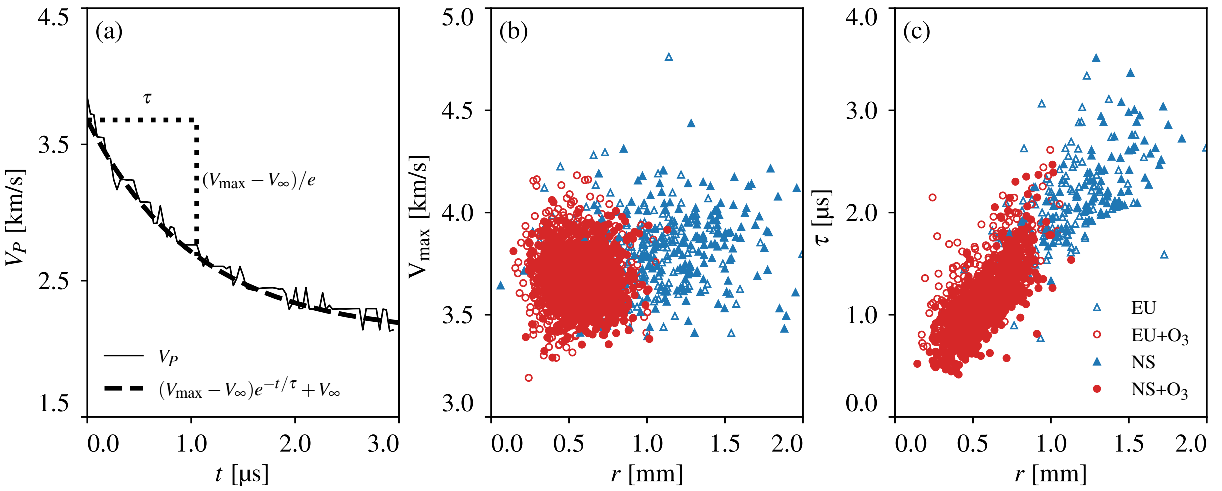

Figure 7.7: **(a)** Representative blast velocity profile with fitted exponential decay function, **(b)** fitted maximum velocity as a function of kernel size, **(c)** fitted decay time constant as a function of kernel size, legend in **(c)** also applies to **(b)**. Only kernels from the 24 mm simulation are included.

where $V_{\max}$ is fitted to be an average of the first five points in the velocity profile. V_∞ is set to a constant value (2000 m/s for non-ozone simulations and 2100 m/s for simulations with ozone), which is based on the stable velocity observed in the average profiles. We set V_∞ as a constant value instead of fitting it similarly to $V_{\max}$ because many blasts end before a steady state value is achieved due to neighboring blast dynamics. With $V_{\max}$ and V_∞ determined, τ is fitted with a least-squares minimization.

Shown in figure 7.7(b) is $V_{\max}$ as a function of blast kernel size for all four core simulations in the 24 mm channel. As shown in the figure, there is little correlation between the blast kernel size and the maximum overdriven velocity. Additionally, there is no discernible difference in the maximum overdriven velocity among the four simulations shown. Clearly, the maximum velocity is dictated not by the size of the blast kernel r_i. Rather, the exponential decay time constant, τ, shows a strong dependence on r_i, as seen in figure 7.7(c): increasing r_i leads to an increased exponential decay time scale. This result is, in fact, entirely consistent with results from our earlier work [248], in that larger kernels sustain more robust blast waves as the shock velocity decay is slower than smaller kernels. The more robust blast waves resultant from larger kernels lead to, on average, larger and/or faster detonation cells. Figure 7.8(a) and (b) show the correlations of cell length L and normalized cell averaged velocity $\overline{V}/V_{CJ}$ with the kernel size, respectively. Clearly shown in figure 7.8 is the monotonic relationships in spite of the statistical scatter. Highlighted with larger and more opaque symbols in (a) are cells which propagate within 2% of the CJ speed, and in (b) cells within 10% of the mean cell length. These cells are highlighted because they are less influenced by competing effects from other parameters. A large kernel may lead to a faster-than-CJ speed and mid-sized cell, a moderate speed and large cell, or some combination thereof. Given this evidence, it is clear that the detonation kernels are useful vehicles for us to analyze and better understand detonation cellular stability, as we shall discuss in what follows.

7.3.2.2 Cellular stabilization *via* kernels

Along the line of triple-point collisions (e.g., the red line shown in figure 7.6a), a larger kernel leads to a smaller kernel in the subsequent cell, and conversely a smaller kernel produces a larger kernel in the next cell. The chain of eight blasts in figure 7.6(f) clearly shows this phenomenon. Analysis of a large number of sequential blasts from the present simulations confirms this description. Shown in figure 7.9(a) is the kernel size evolution from a sequential chain of blasts in the NS24 (blue, top) and the NS24O (red, bottom), both over a longer simulation duration. Also plotted (dotted lines) are the average kernel sizes. Evident from the blast chains is the oscillatory behavior of the kernel size about its mean value. Also seen in figure 7.9(a) are the early transients in the NS simulation where the kernels are substantially smaller

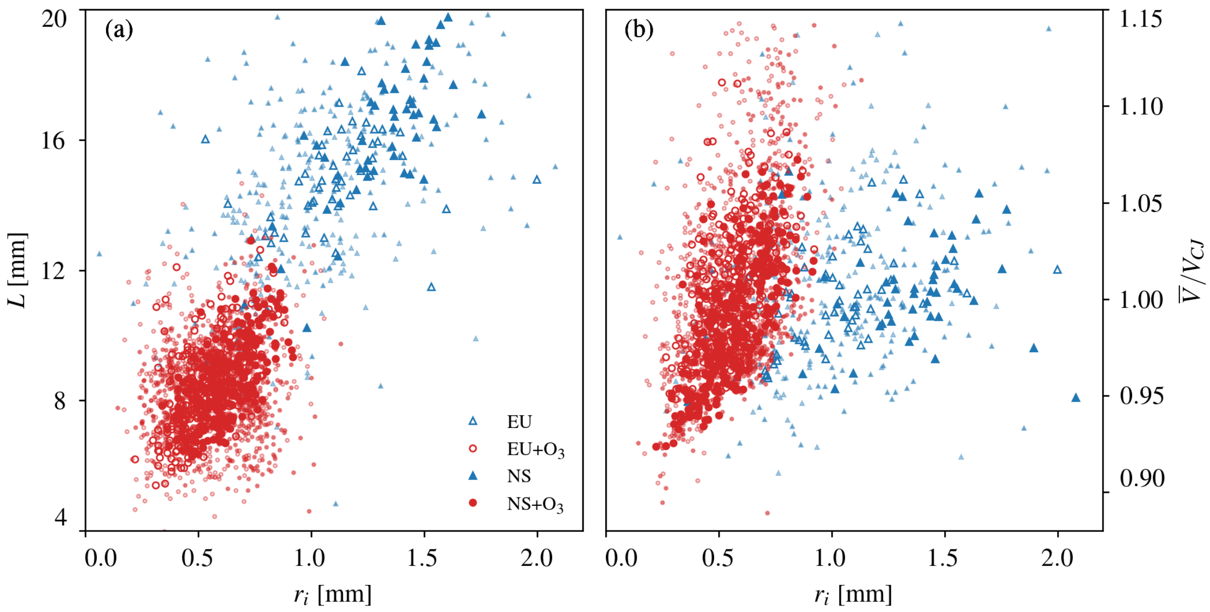

Figure 7.8: Relationship between kernel size r and detonation cell length L (a) and normalized cell averaged velocity $\overline{V}/V_{CJ}$ (b). Highlighted as larger and more opaque symbols in (a) are cells which propagate within 2% of the CJ speed, and in (b) cells within 10% of the mean cell length.

than the average kernel size and grow until they oscillate about the average size.

To confirm the kernel stabilization mechanism, figure 7.9(b) shows the correlations between the difference of subsequent and incident kernel sizes ($r_{i+1} - r_i$) as a function of the incident kernel size r_i for every blast in the converged section of the numerical soot foils of NS24 and NS24O. The relative sparsity of the NS24 data shown is due to the fewer number of detonation cells present in these simulations (as they are larger). Also shown in figure 7.9(b) is the best-fit to data for each of the simulations. It can be seen that despite some scatter, $r_{i+1} - r_i$ correlate negatively to r_i, indicating the feedback mechanism: blasts will tend toward a stable size and then oscillate around that stable size, as shown by the blast chains in figure 7.9(a). Furthermore, figure 7.9(b) is broken into four quadrants (divided by the respective vertical lines for each simulation and the same horizontal line of $r_{i+1} - r_i = 0$). The upper left and lower right quadrants indicate a stable phenomenon (kernels moving toward the average), and the upper right and lower left quadrants indicate an unstable phenomenon. Clearly, a majority of the points lie in the stable quadrants, and those that are in the unstable quadrants are near the stability boundary.

To further demonstrate the feedback control, we analyze the pressure front along with the chemical reaction front (as quantified by the temperature) of the incident shock in a cell cycle. Figure 7.10(a) shows the temporal radial positions of the shock and reaction fronts (R_P and R_T, respectively) of two representative blasts in NS24 and NS24O, in addition to a reference position (R_{CJ}) assuming a steady CJ propagation; note that the CJ velocity between the non-ozone and ozone simulations varies by $\sim$ 0.1 %, and so only one line needs to be plotted. The shock front position is defined as the position of the leading shock, and the reaction front is defined as the position behind the shock which first exceeds 1800 K, a reasonable proxy for the location of maximum heat release rate in these particular mixtures. It is evident that both blasts are initially overdriven, as seen by comparing the slopes of the R_P lines and the CJ line. Both blasts transition to be underdriven after approximately one half of the cell cycle. To magnify the separation dynamics, figure 7.10(b) illustrates the difference of pressure front and temperature front with respect to the CJ velocity (i.e., $R_P - R_{\text{CJ}}$ and $R_P - R_{\text{CJ}}$) of a sequence of representative blasts from NS24O. It is seen that the pressure and temperature fronts are strongly coupled during the early stage of the cell cycle, and they begin to decouple when the blast transitions from overdriven to underdriven propagation. Also labeled in figure 7.10(b) is the initial kernel size, r_i, and two subsequent kernel sizes, r_{i+1} and r_{i+2}. In this sequence, the kernel size oscillates between larger and smaller values as expected. Importantly,

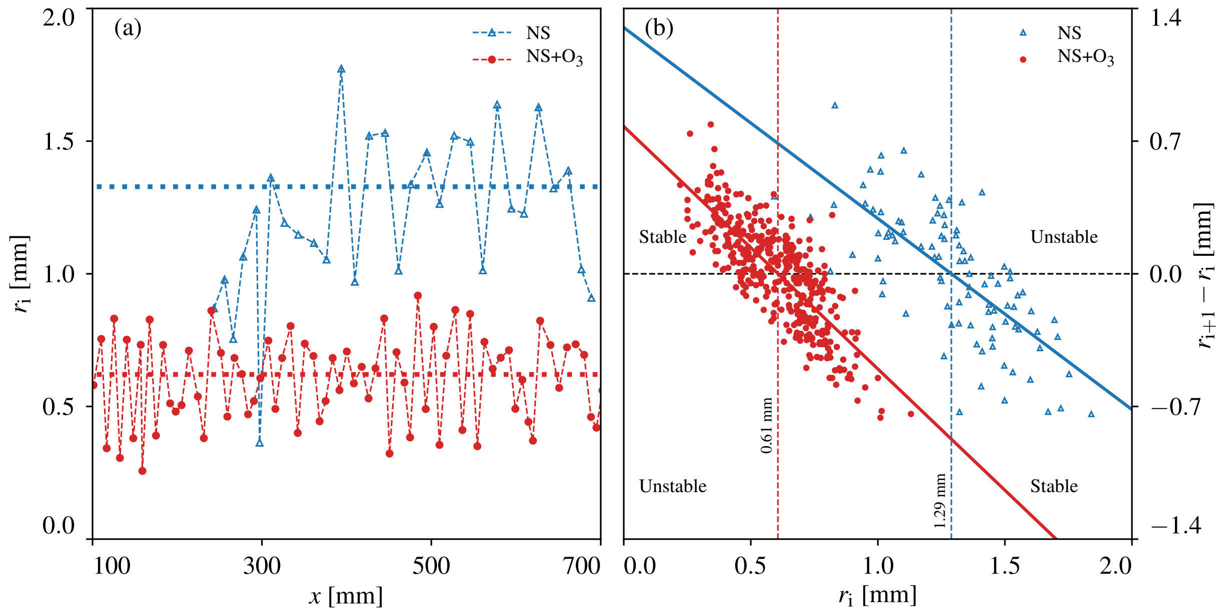

Figure 7.9: **(a)** Single chains of blasts (symbols) oscillate about their respective mean kernel sizes (dotted horizontal lines). The solid lines are drawn to guide the eyes. **(b)** Blast kernel size versus subsequent blast kernel size difference in NS24 and NS24O. The solid lines are fits to data for each mixture. The vertical dashed lines mark the zero-crossing values (stable kernel size). The horizontal dashed line in **(a)** corresponds to the location of the vertical dashed line in **(b)**.

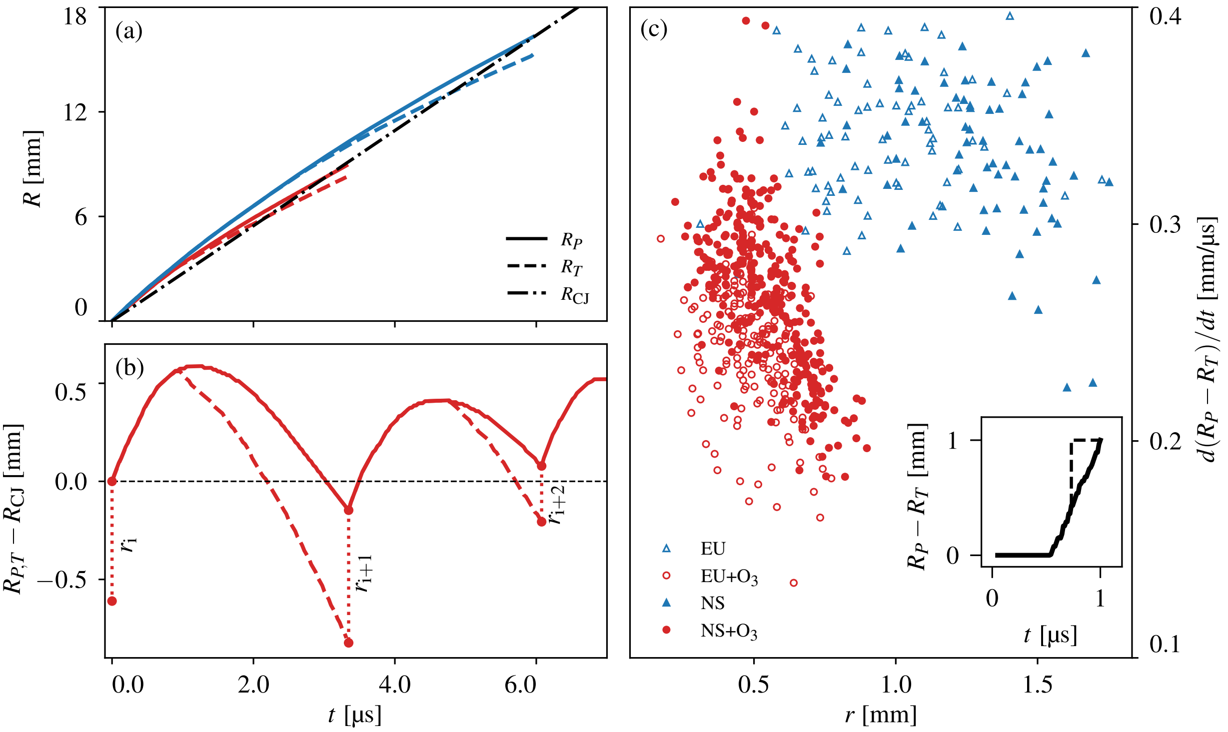

Figure 7.10: **(a)** Pressure (solid line) and temperature front (dashed line) evolution for two representative blasts from the NS24 (top, blue) and the NS24O (bottom, red) simulations. **(b)** Difference of pressure front (solid line) and temperature front (dashed line) for the representative blast and the subsequent two blasts from the NS24O simulation with regards to the location R_{CJ}. **(c)** Pressure and temperature front separation rate $d(R_P - R_T)/dt$ as a function of kernel size. The inset shows a representative temporal separation $(R_P - R_T)$ profile with fitted separation rate. Only kernels from the 24 mm simulations are included.

the shock and reaction front decoupling dictates the subsequent kernel size. Figure 7.10(b) illustrates the result of the kernel feedback mechanism on cell-averaged velocity: the first cell propagates slower than the average simulation speed; it yields a relatively large detonation kernel. The subsequent detonation cell propagates faster than the average CJ speed, yielding a cell propagation speed close to the CJ speed. Hence, the modulation of the detonation kernel size is also logically the mechanism by which sequential detonation cells adjust their speed in order to produce a global average velocity close to the CJ speed.

Given that the shock and reaction front decoupling dictates the kernel size, we analyze the decoupling rate as a function of kernel size. Figure 7.10(c) shows the average separation rate of the pressure and temperature fronts along the cell length, $d(R_P - R_T)/dt$, after they begin to separate (defined as a gap larger than $\frac{1}{2}$ the ZND induction length of the mixture). Inset on figure 7.10(c) is a temporal separation evolution for a representative blast. Evident is the nearly linear separation rate, once separation begins. For the ozonated mixtures, the separation rate is negatively correlated with kernel size: larger kernels correspond with a slower separation rate. A slow separation rate yields a subsequently smaller kernel. In the non-ozonated mixtures, the trend is less clear, perhaps due to the sparser number of samples, but its trend is still consistent with that observed in the ozonated mixtures. Again the current analysis provides strong support to what was proposed earlier [248], that the shock and reaction separation rate is the key mechanism that controls the kernel size and hence the cell size and its stability. Without a doubt, the separation rate is controlled by both chemical kinetics and gas dynamics.

7.3.3 Cellular stability sensitivity

7.3.3.1 Chemical kinetics

Chemical kinetics contribute to macroscopic structural changes in detonations [241]. To illustrate this point further, we compare the frontal propagation behavior, as first measured experimentally by Dormal et al. [267], between the ozonated and non-ozonated mixtures. The propagation velocity of the pressure front ($V_P = dR_P/dt$) is ensemble-averaged across all detonation cells in a given simulation. Results of this averaging from four different simulations are normalized by the CJ velocity and shown in figure 7.11. The time is also normalized by the average cell cycle time. One standard deviation in the velocity is plotted as error bars. Within the uncertainty, the velocity decay across the cell cycle is seen to be self-similar across all four simulations. The self-similarity is rather unexpected: past literature suggests that a change in reduced activation energy $\tilde{E}_\mathrm{a}$ results in a different shock velocity profile within a cell cycle [252]. Here, the addition of ozone yields a 34% reduction in $\tilde{E}_\mathrm{a}$ but a negligible change in the velocity profile. This result suggests that $\tilde{E}_\mathrm{a}$ is not a good predictor of cell velocity dynamics. Nonetheless, the self-similarity in velocity profiles among simulations enables an examination of the effect of kernel dynamics on structure in an isolated manner.

Combining the results shown in figures 7.7, 7.10, and 7.11 paint a clear picture of the mechanistic effect of ozonation and activation energy reduction on detonation cellular structure. The presence of ozone does not affect the shock front dynamics: with the same sized kernel the pressure front propagates nearly identically in the ozonated and non-ozonated mixture. This means that gas dynamics and heat release govern the shock front motion, neither is dependent on the ignition kinetics. Conversely, the separation rate between the shock and reaction fronts is dictated by the ignition kinetics: faster ignition time scales correspond with a slower separation of the shock and reaction fronts. And as a result, the blast kernel at the end of a cell cycle is smaller in the ozonated case as compared to the non-ozonated case. This gap, $r_{i+1} = R_P - R_T$, constitutes the subsequent blast kernel size. And so, starting with identically sized blast kernels, the ozonated case results in a smaller subsequent blast kernel as compared to the non-ozonated case. This leads to the steady state kernels to be smaller in the ozonated case eventually, and hence, denser and smaller detonation cells.

This detailed physical description explains why ZND induction length correlates with experimentally-observed detonation cell size: induction length is a reasonable proxy for the separation rate of the shock and reaction fronts. Furthermore, this physics also shows why a unified linear correlation between detonation cell size and induction length is unattainable: when mixtures change, the gas dynamics and heat

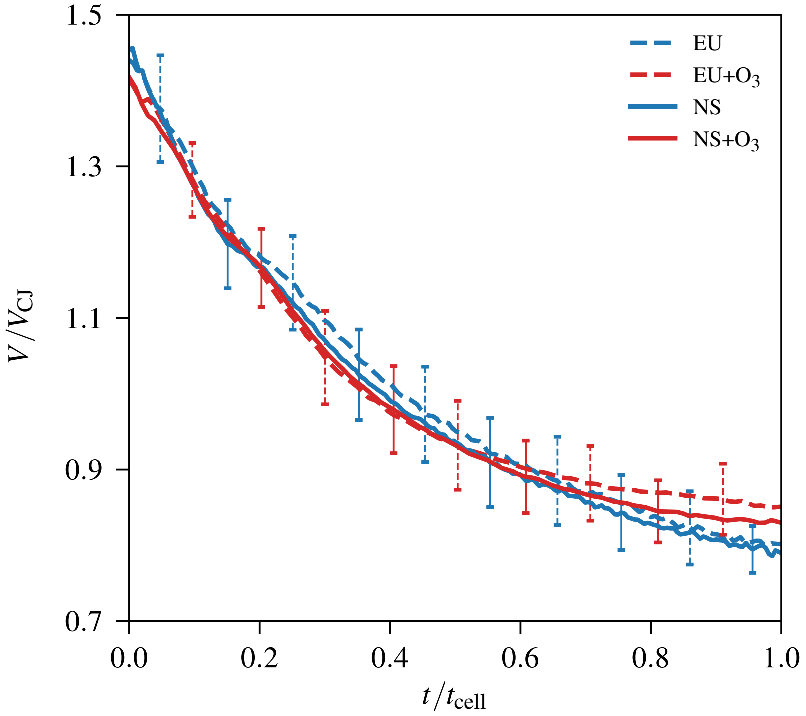

Figure 7.11: Normalized ensemble-averaged cellular frontal velocity for all EU24 (blue, dashed), EU24O (red, dashed), NS24 (blue, solid), NS24O red, solid). Error bars show one standard deviation variability across ensemble averaging.

release change, and thus the shock front propagation dynamics change in addition to just chemical kinetic rates. With changes to the shock front dynamics, the shock and reaction frontal separation rates would no longer have an identical effect on detonation cell size.

7.3.3.2 Diffusion and boundary conditions

To understand the effect of diffusive terms and boundary conditions on overall detonation cellular stability we examine the full set of simulations performed in the present work. Table 7.4 summarizes the stable kernel size $\bar{r}$ compared to the average cell width $\bar{\lambda}$, as well as the slope m of the best-fit lines for the r_i vs. $(r_{i+1} - r_i)$ stabilization plot (as seen in figure 7.9b) for all eight core simulations. The average kernel sizes $\bar{r}$ listed in table 7.4 show several clear trends.

The first is that $\bar{r}$ drops by approximately a factor of two when using ozone across all conditions. This is explainable physically because ozone slows the separation rate between the shock and reaction fronts, which yields a smaller stable kernel size.

The second trend is that the kernel sizes for viscous simulations are larger than their inviscid counterparts. Typically the kernels are larger by about 10%, although notably NS6 features kernels twice as large as EU6. This enlargement of detonation kernels is hypothesized to be due to (1) viscous effects retarding ignition, and thus growing the shock-reaction gap, and (2) isothermal and no-slip walls leading to a change of ignition dynamics near the walls. Similar observations regarding the role of viscous effects on cell structure, although with somewhat different boundary conditions, were made by Xiao et al. [268].

Thirdly, the ratio between cell size and kernel size $\bar{\lambda}/\bar{r}$ is relatively invariant across all simulations, varying from 7.40 to 9.15. The slope of the kernel stabilization mechanism m can be linked to qualitative cellular stability. EU6 has the largest slope of all simulations, and is strongly oscillatory between a one-cell and a half-cell propagation mode (figure 7.4c). Meanwhile, the strongly mode-locked simulations, EU6O, NS6O, and NS6, have relatively small slopes. In the middle are simulations in the larger channel which have moderate stability with less influence from the boundaries. Overall, the kernel stabilization

ID	$\bar{\lambda}$ mm	$\bar{r}$ mm	$\lambda/\bar{r}$	m
EU24	7.93	1.04	7.62	-1.09
EU6	6.58	0.77	8.55	-1.47
NS24	9.76	1.29	7.57	-1.01
NS6	11.91	1.61	7.40	-0.85
EU24O	5.03	0.55	9.15	-1.28
EU6O	3.99	0.51	7.82	-0.77
NS24O	5.01	0.61	8.21	-1.28
NS6O	4.09	0.55	7.44	-1.04

Table 7.4: Key results from cell stability analysis including the stable kernel size $\bar{r}$, the average cell width $\bar{\lambda}$, the slope m of the best-fit lines to the data clouds for all eight core simulations.

mechanism can explain changes in apparent cell size with respect to mixture and geometry. Note, however, that our analysis does not preclude an alternative stable kernel size developing, as in the cases observed by Sharpe and Quirk [251]. Although not observed in the present simulations, it is possible that multiple stable kernel sizes exist, each of which can have its own corresponding kernel thermodynamic state. This more detailed stability description, particularly regarding the possible non-uniqueness of cellular structure, is left to future work.

To investigate the effects of viscosity and boundary conditions on global detonation features, we performed spatial and temporal averaging of key scalars in the domain. Figure 7.12 presents space- and time-averaged profiles of p, T, and $Y_{\mathrm{H_2}}$ from NS (dashed lines) and EU (solid lines) simulations for the ozonated mixture in the two channels and in comparison to the profiles from the ZND solution (dash-dotted lines). The averaged profiles were computed by first finding the local shock front of each each point in the y-z plane, and then using the one-dimensional solution behind each local shock front for averaging. The averages are normalized by the frozen post-shock pressure p_{ps}, the CJ equilibrium temperature T_{CJ}, the fresh-gas fuel mass fraction $Y_{\mathrm{H_2,fg}}$, and the induction length L_{i}, all of which are obtained from ZND calculations based on the equilibrium CJ speed. In the Euler cases, the downstream temperature (T_{CJ}) and composition matches that of the ZND solution. The differences observed around the shock front are likely due to the two-dimensionality of the shock front. In the NS cases, a pressure deficit from the ZND solution is clearly visible, whereby the pressure deficit is up to 12 % in the 6 mm channel and 5 % in the 24 mm channel. A temperature deficit is also present in the NS cases, although the deficit is less significant in the 24 mm channel compared to the ZND solution. The temperature deficit has a small impact on fuel consumption, which we use as a measure of detonation wave thickness. The latter is approximated by the distance between the wave front and the intersection point where the fuel mass fraction reaches 95% of the equilibrium value, $Y_{\mathrm{H_2,eq}}$:

$$\frac{Y_{\mathrm{H_2,95}} - Y_{\mathrm{H_2,0}}}{Y_{\mathrm{H_2,eq}} - Y_{\mathrm{H_2,0}}} = 95\,\%. \tag{7.11}$$

This criterion is shown with horizontal and vertical dashed lines in figure 7.12. The detonation wave thickness is about two times the ZND thickness, irrespective of the transport equations used (*EU* and *NS*). The increase in thickness is caused by the transient nature of the detonation propagation: as a 2D detonation transitions from highly overdriven state to substantially underdriven state, the induction time also changes significantly. After decoupling, the shock and reaction fronts separate appreciably, causing the wave to thicken, on average, as compared to the ZND solution.

Understanding detonation propagation speed is important for the accurate prediction of detonation limit behavior. Substantial differences in propagation speed are observed between the inviscid and viscid simulations. An obvious reason for the differences is momentum and heat losses in the boundary layer. Thereby, mass accumulates in the boundary layer, which causes an expansion of the core flow [202].

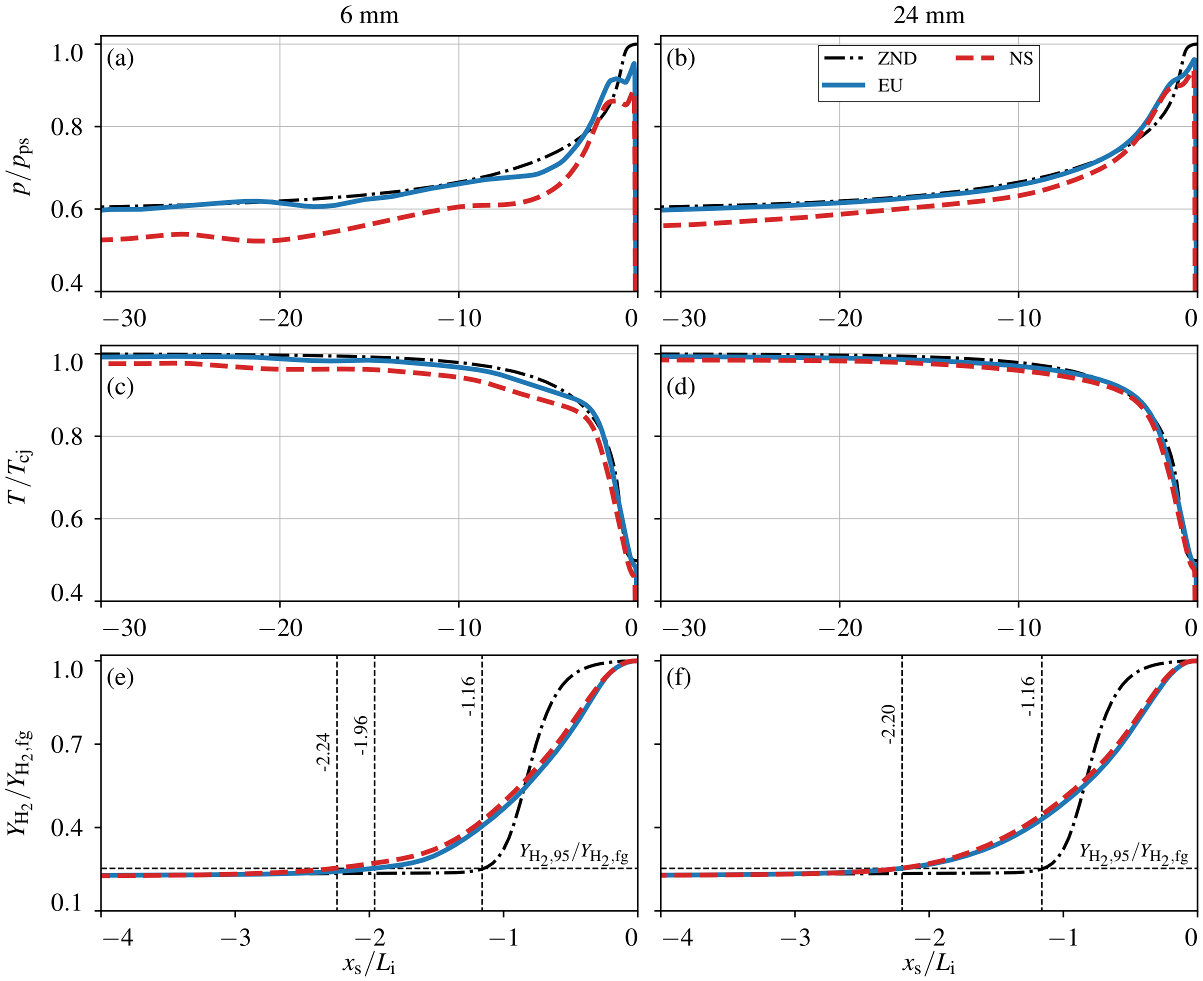

Figure 7.12: **(a,b)** Sample-averaged profiles of pressure normalized by the frozen post-shock pressure p_{ps}, **(c,d)** temperature normalized by the CJ equilibrium temperature T_{CJ}, and **(e,f)** hydrogen mass fraction normalized by the fresh gas value $Y_{H_2,fg}$ over axial space x normalized by the ZND induction length L_i. Presented are results from viscid simulations (dashed lines), from inviscid simulations (solid lines), and from the ZND solution (dashed-dotted lines).

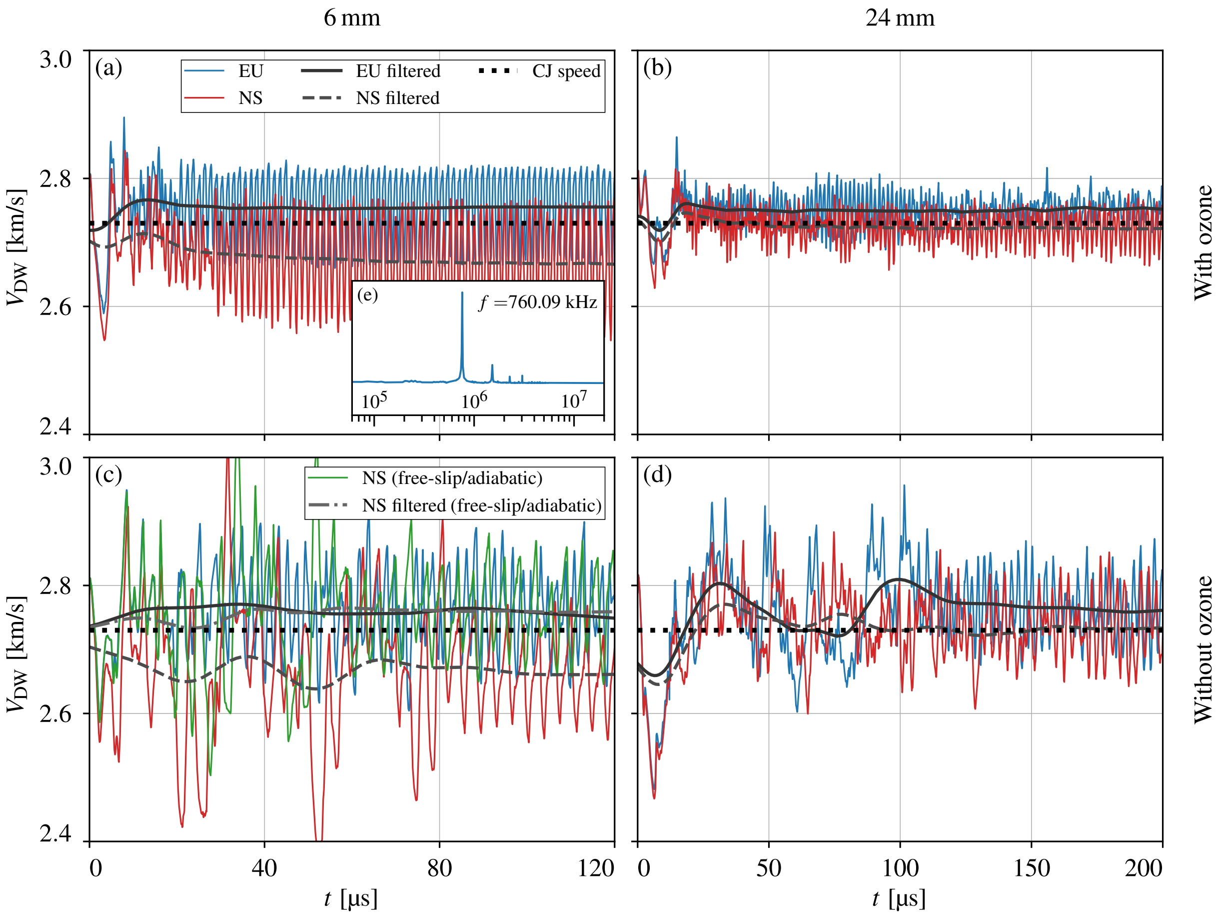

Figure 7.13: Detonation wave velocities V_{DW} computed by differentiating the cross-width averaged detonation wave front locations. The theoretical CJ speed is indicated by the horizontal dashed lines. Shown in the plots are results from the Euler simulations (solid lines) and from the Navier-Stokes simulations (dashed lines), and from a Navier-Stokes simulation with free-slip/adiabatic boundary conditions (dash-dotted line). Inset in panel (a) shows the dominant amplitudes as obtained from a fast Fourier transform using the velocity data from EU6O.

Since the flow in the wave frame is initially subsonic, pressure perturbations can propagate toward the wave front and thus weaken the detonation. Accordingly, the wall-induced losses lead to a velocity deficit that is absent in the simulations with the free-sliding and adiabatic boundary conditions. In addition to the boundary layer-induced losses, there is also a geometric coupling between the cell structure and the confining geometry, particularly in the 6 mm cases, potentially leading to macroscopic changes in velocity.

Figure 7.13 presents the temporal evolution of the detonation propagation speeds, computed as the time derivative of the location of the detonation wave front averaged across the channel width. The figure also shows smoothed profiles obtained from a Gaussian filter in time (the filter width is given as the standard deviation and was set approximately equal to the timescale of the formation of one cell). The fluctuations in the velocity signal are related to the cell density. The inset in figure 7.13(a) shows the result of a fast-Fourier transform with a dominant frequency of $f = 760\,\mathrm{kHz}$ in case EU6O. As expected, the oscillations of the velocity can be linked to the cellular cycle, with each complete cell cycle featuring two velocity spikes, the first for the incident kernel explosion, and the second peak corresponding to the two resultant kernel explosions on the top and bottom vertices of the cell. As such, the detonation cell size can be approximated by $L = 2\overline{V_{DW}}/f$, where $\overline{V_{DW}}$ is the average detonation wave velocity. For example, for EU6O, this results in $L = 7.2\,\mathrm{mm}$ which is in excellent agreement with the numerical soot foil at $L = 7.3\,\mathrm{mm}$.

Common to all Euler simulations is that the propagation speed is slightly larger than the corresponding

ID	V_{DW} m/s	V_{CJ} m/s	d_{h} mm	λ mm	$1 - \frac{V_{\mathrm{DW}}}{V_{\mathrm{CJ}}}$ [%]	$C_{\mathrm{m}}\left(\frac{d_{\mathrm{h}}}{\lambda}\right)^{-1}$ [%]
NS6O	2665	2734	12	4.09 (4)	2.49	2.46 (2.40)
NS24O	2722	2734	48	5.01 (4)	0.42	0.75 (0.60)
NS6	2661	2732	12	11.91 (6)	2.59	4.46 (2.23)
NS24	2733	2732	48	9.76 (8)	-0.04	0.91 (0.74)
NS6-FS-A	2759	2732	12	11.94 (6)	-0.99	4.44 (2.23)

Table 7.5: Propagation speeds V_{DW}, hydraulic diameter d_{h}, cell width λ, normalized velocity deficit $1 - V_{\mathrm{DW}}/V_{\mathrm{CJ}}$ and expected velocity deficit based on correlations $C_{\mathrm{m}}\,(d_{\mathrm{h}}\lambda)^{-1}$ for all NS simulations. Values in brackets indicate cell widths and expected velocity deficits for the next stable configuration. The constants C_{m} are mixture dependent, where $C_{\mathrm{m}} = 0.0446$ is used for hydrogen-oxygen mixtures and $C_{\mathrm{m}} = 0.0720$ for hydrogen-oxygen mixtures with ozone.

theoretical CJ equilibrium speed, as sometimes observed in hydrogen oxygen mixtures [269]. The Navier-Stokes simulations, in contrast, typically yield propagation speeds below the theoretical CJ equilibrium speed. The detonation wave in a 6 mm channel with ozone, for example, propagates at 2665 m/s in the NS case as compared to the CJ speed of 2734 m/s. In the Euler case, the speed increases to 2756 m/s, 3.3 % higher than the NS case. In the wider channel (24 mm), the increase between Euler and NS cases is only 1.1 %. The same trend is observed for the non-ozonated mixtures, although notably, the propagation speed in NS24 is still slightly above the CJ equilibrium value. For the present 2D setups, a direct comparison with the velocity deficits observed in the 32 mm tube experiments is not possible due to the different hydraulic diameter d_h (ratio of wetted perimeter to flow-through-area) between the 2D channel and tube. The hydraulic diameter for a 3D round tube is $d_h = d$, while the hydraulic diameter for a 2D channel, considering an infinite width, is $d_h = 2h$, where h is the channel height. To compare the present simulations and experiments, the correlation ($1 - V_{\mathrm{DW}}/V_{\mathrm{CJ}} = C_{\mathrm{m}}\ \lambda/d$) provided in Shi et al. [265] can be used to estimate the expected velocity deficit based on the ratio of hydraulic diameter d_{h} to cell width λ. This correlation is shown to be valid for $d/\lambda > 2/\pi$, the loss-dominated branch, as opposed to the cell-structure dominated branch. All values of d_h/λ in this work are larger than $2/\pi$. C_{m} is a mixture-dependent constant and is provided by Shi et al. [265] for the two mixtures considered in the work, with $C_{\mathrm{m}} = 0.0446$ for stoichiometric hydrogen-oxygen mixtures and $C_{\mathrm{m}} = 0.0720$ for hydrogen-oxygen mixtures with 3000 ppm ozone. The propagation speeds, velocity deficits and expected velocity deficits based on the correlation for the NS simulations are summarized in table 7.5.

The correlation predicted value for the velocity deficit is 2.46 % for the NS6O case and 0.75 % for the NS24O case. Hence, in the 6 mm channel, the empirically predicted value agrees with that of the simulation but is somewhat higher than the numerically determined value in the 24 mm channel. The 6 mm case without ozone complicates the interpretation of an appropriate cell size λ in the correlation due to the effect of strong mode locking. Evident from the comparison between EU6 and NS6, the detonation appears to be ‘close’ to transition to a one-cell mode. We have thus added, in brackets, the predicted value for the next stable cellular configuration (i.e., for NS6, one cell across, where $\lambda = 6$ mm). For the NS6 case, the numerically measured value (2.59 %) falls between the empirically predicted half-cell (4.46 %) and one-cell (2.23 %) configuration. In terms of simulation NS24, we observe a velocity decrease of 1.03 % by adding viscous terms. The resulting propagation velocity, however, is slightly above the CJ value and the velocity deficit is thus under predicted. All numerically predicted velocity deficits are within 1% of the predicted values from the experimentally-derived correlation.

To determine if insufficient domain length is leading to small discrepancies in observed versus predicted velocity deficit, the wave-frame Mach number is analyzed. Figure 7.14 shows sample averaged contours of Mach number of the ozonated mixture in the 6 mm and 24 mm channel. Note that the Mach number in the ZND calculations as well as the Mach number evaluated in the 2D simulations are based on the frozen speed of sound, with the term $1 - M_{\mathrm{f}}^2$ appearing as denominator in the ZND equations for

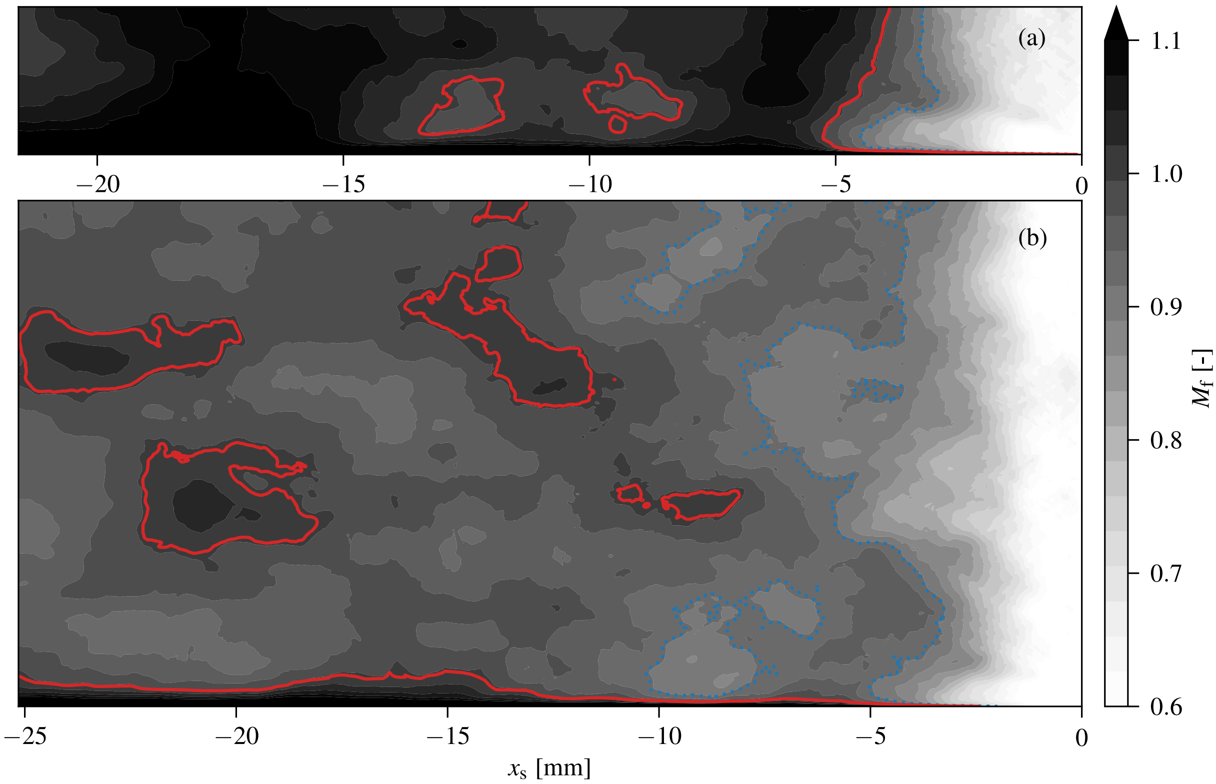

Figure 7.14: Sample averaged (approximately 50 samples per case) contour surfaces of frozen Mach number for simulations NS6 in panel (a) and NS24 in panel (b). Isolines are presented for the frozen Mach number approached in the ZND calculation (blue, dotted) and for a frozen Mach number of 1 (red). Note that due to a larger velocity deficit in the small channel and a subsequent shift of detonation wave location, the post shock region is shortened in the small channel.

detailed chemistry [269]. Consequently, if the CJ speed from the equilibrium solution is used as the input shock speed in the ZND calculations, the Mach number will asymptotically approach a Mach number smaller than 1, with $M_{f,\infty} = 0.95$ for the present mixture with and without ozone using FFCM-1. Isolines of Mach number are drawn for the value of $M = 0.95$ (blue, dotted) and for a Mach number of 1 (red, solid). We note that using the frozen sound speed, as opposed to the equilibrium sound speed, represents the upper limit of pressure wave propagation speed [269, 270]. It is evident that the post shock flow in the 6 mm channel quickly approaches a Mach number of 1 in the wave frame, which is typically denoted as the sonic locus. The sonic locus divides the post flow region into a subsonic region in which the characteristics C^+ and C^- point in opposite directions and a supersonic region where the characteristics point in the same direction. As has been outlined by Kasimov and Stewart [271], the supersonic region has no effect on the detonation wave, suggesting that the region able to weaken the detonation wave has been fully resolved in the numerical domain of the 6 mm configurations. This explains the satisfactory agreement between experimental correlations and numerically derived velocity deficit. In the 24 mm channels on the other hand, pockets of supersonic flow are present, while the averaged Mach number on the outlet boundary is still subsonic (N2S24: 0.975, NS24O: 0.982). We thus speculate that the somewhat smaller velocity deficit as compared to experiment in the 24 mm channels could be due to an insufficient domain length.

In order to analyze the effect of viscous terms, isolated from boundary layer losses, an additional viscid simulation of the mixture without ozone, denoted NS6-FS-A, was conducted in the 6 mm channel but with free-slip and adiabatic boundary conditions. It can be seen in figure 7.13(c) that the filtered velocity of NS6-FS-A converges towards the same value observed in the Euler simulation EU6. At the same time, however, the mode locked cell size equals that of the viscid simulation NS6 with half a cell size across

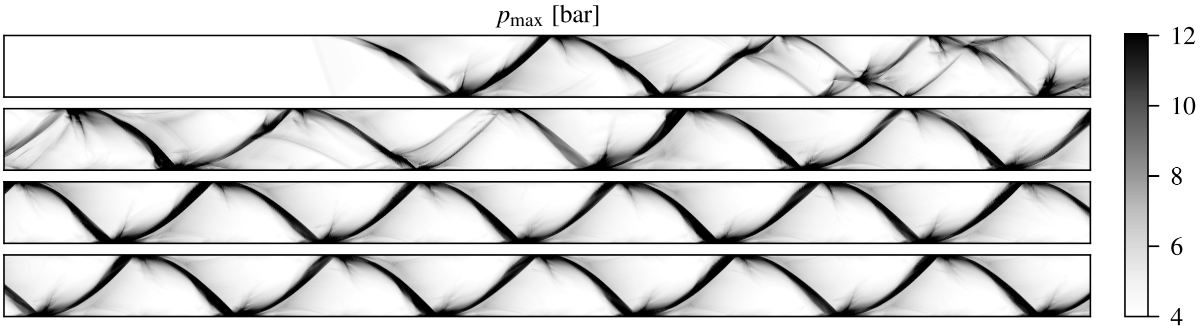

Figure 7.15: Numerical soot foil from Simulation NS6-FS-A. The soot foil is broken into four parts with the right side of the upper image connecting with the left side of the image below.

the channel height, as presented in figure 7.15. This finding is interesting, as velocity deficit and cell enlargement are usually linked [268]. Yet, in this case, cell enlargement is observed without the presence of a global velocity deficit. We conclude that a) local viscous effects, i.e., diffusion of momentum and heat as well as conversion of kinetic energy into heat, can also lead to a change in induction time and, as a consequence, cell enlargement and b) cell enlargement in absence of boundary layer losses does not impact propagation speed in this case. This observation does not necessarily contradict previous observations, where the simulations did not independently vary local viscous effects and boundary layer losses.

To visualize the magnitude of local viscous effects, we have conducted a budget analysis of each viscous simulation. Six individual terms are investigated for this analysis, and are denoted by $\mathcal{T}_i$:

$$\mathcal{T}_1 = \frac{\partial \rho u u_i}{\partial x_i}, \qquad \mathcal{T}_2 = -\frac{\partial p}{\partial x}, \qquad \mathcal{T}_3 = \frac{\partial \tau_{1i}}{\partial x_i},$$

$$\mathcal{T}_4 = \frac{\partial \rho h u_i}{\partial x_i}, \qquad \mathcal{T}_5 = \frac{\partial \tau_{ji} u_j}{\partial x_i}, \qquad \mathcal{T}_6 = \frac{\partial}{\partial x_i}\left(\lambda \frac{\partial T}{\partial x_i}\right).$$

$\mathcal{T}_1$, $\mathcal{T}_2$, and $\mathcal{T}_3$ capture the rate of change of axial momentum from convection, pressure, and diffusion, respectively. $\mathcal{T}_4$, $\mathcal{T}_5$, and $\mathcal{T}_6$ are terms determining the rate of change of total internal energy due to convection, dissipation, and heat conduction, respectively. Figure 7.16 presents the fields present in the Euler equations ($\mathcal{T}_1 + \mathcal{T}_2$ for momentum, $\mathcal{T}_4$ for energy) in the left column. The middle column is terms present only in the Navier-Stokes equations ($\mathcal{T}_3$ for momentum, $\mathcal{T}_5 + \mathcal{T}_6$ for energy), and the right column is the ratio between the second and first columns. In figure 7.16, the top row plots terms from the momentum equation, and the bottom row plots terms from the energy equation. As expected at high Mach numbers, the flow is dominated by convection and pressure gradients with amplitudes that are two orders of magnitude above those of the viscous contributions. There are regions, however, where the magnitudes are similar, indicating the local viscous contributions are comparable to the convective contributions. These viscous contributions are suspected to cause cell enlargement in simulation NS6-FS-A. High magnitudes of viscous terms are generally observed in proximity to strong waves, pronounced vortices and, as expected, in the boundary layer. Note that only the bottom part of the channel is plotted, and so the boundary layer is visible only on the bottom of the plots. To isolate the mean effect that the boundary layer has on the flow, the main loss terms ($\mathcal{T}_3$,$\mathcal{T}_6$) have been volume-integrated ($1/\Delta_x \int_V \mathcal{T}_i dV, V = H\,\Delta_x\, 1\text{m}$) in each slice normal to axial direction and averaged in time. According to the Gauß divergence theorem, the result of volume integrated divergence equals that of integrating the fluxes over the closed surface of the volume. Since the normal gradients in the axial direction are small compared to the normal gradients adjacent to the wall, the integration is expected to reveal the impact of the boundary layer. The resulting profiles are presented in figure 7.17. It can be seen that the averaged effects of the loss terms are identical among all NS simulations. We thus hypothesize that the observed losses are neither influenced by the channel width nor by the detonation structure, e.g., cell size and cell density, supporting the previous assumption

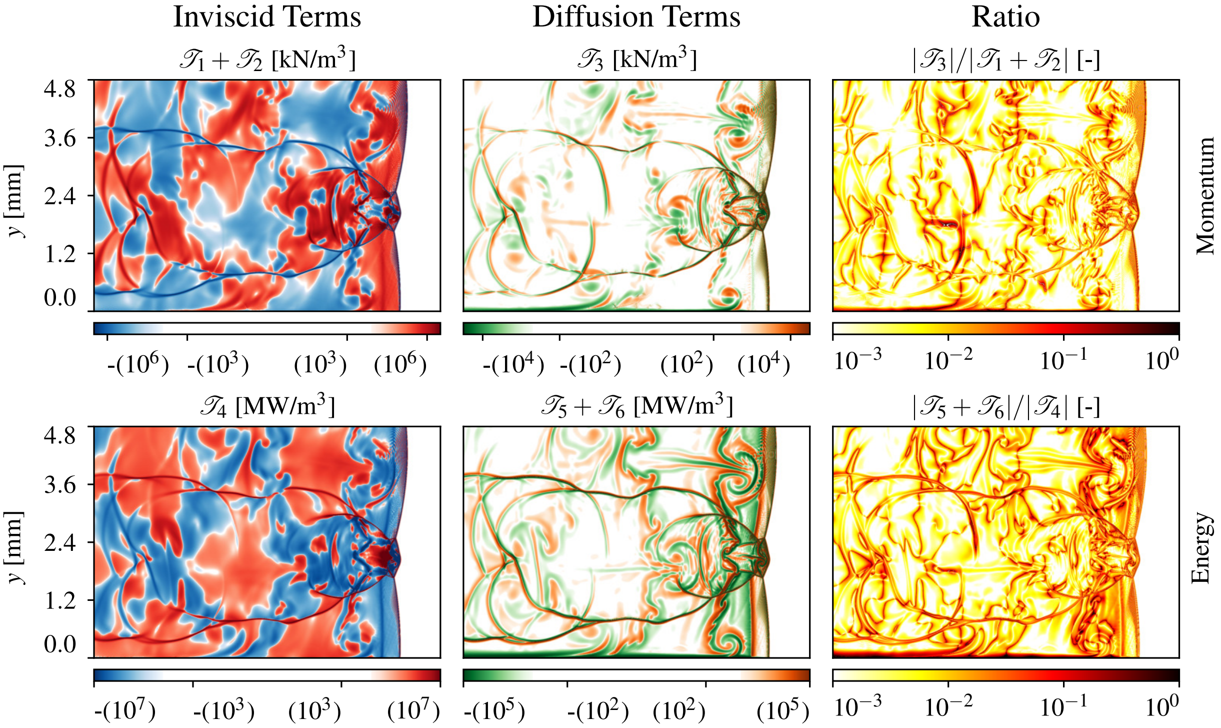

Figure 7.16: Fields of the individual terms to illustrate the rate of change of axial momentum and internal, total energy caused by convection ($\mathcal{T}_1$,$\mathcal{T}_4$), pressure gradients ($\mathcal{T}_2$), tangential stresses ($\mathcal{T}_3$), dissipation ($\mathcal{T}_5$) and thermal conduction ($\mathcal{T}_6$) with the ratio of the respective magnitudes on the right. The fields are generated from a single time-step in NS24O-5. $y = 0mm$ represents the lower wall boundary, and only the bottom part of the wall region is plotted.

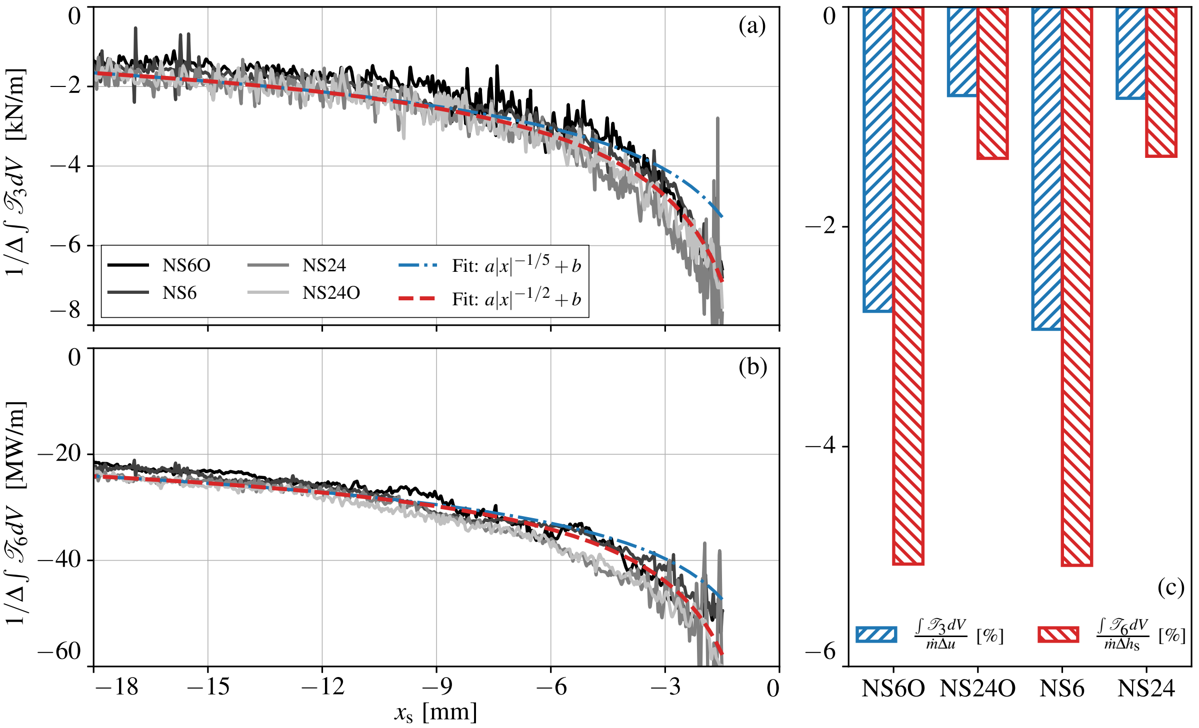

Figure 7.17: **(a)** Cross-width integrated values of tangential stresses (T_3), **(b)** cross-width integrated values of thermal conduction (T_6), and **(c)** volume integrated values of both terms, normalized by the change of momentum flux and enthalpy flux respectively. Functions of type $a|x|^{-1/5} + b$ and $a|x|^{-1/2} + b$ are fitted, using data in the range $x_s = [-18, -12]$ mm.

of the loss based regime reported in Shi et al. [265]. Here, x_s is the averaged location behind the shock wave. Data points that are close to the shock front ($|x_s| < 1.5$ mm) were excluded from the analysis due to large noise in the averaged profiles. Analytical solutions for laminar and turbulent boundary layers behind shock waves moving into stationary fluid have been added and were obtained by Mirels [272], who solved the Blasius boundary-layer equations in a frame fixed to the shock wave for a laminar boundary layer using integral methods and expressions for skin friction in a shock-fixed frame for a turbulent boundary layer. The theoretical laminar boundary-layer height is proportional to the square root of shock distance x, while the turbulent boundary layer height is proportional to the fifth root of x. The wall-heat flux and wall friction are anti proportional to distance x with the same exponent. Functions of type $a|x|^{-1/2} + b$ and $a|x|^{-1/5} + b$ are fitted to both the friction term ($\mathcal{T}_3$) and to the heat conduction term ($\mathcal{T}_6$), as presented in figure 7.17. Clearly visible is the excellent agreement of the fitted laminar boundary layer function for both the friction and heat conduction terms. It must be noted that turbulence is intrinsically different in 2D and 3D flows. Therefore, agreement with the turbulent boundary profiles should not be expected, but instead deviations from the laminar function fit once transition is happening. Nonetheless, the present results indicate that the mean effect of the loss terms can be related to the evolution of a laminar boundary layer in the simulations.

The observation of a laminar boundary layer with no evidence of boundary layer transition may be surprising given the high velocity and pressure. Apart from the obvious explanation to relate this circumstance to the known dissipative nature of upwind schemes, there is also experimental evidence to put the results into context. Hartunian et al. [273] measured boundary layer transition behind shock waves and found that the Reynolds number $\mathrm{Re}_{\mathrm{tr}}$, at which boundary layer transition occurs, is initially constant for weak to medium strength shocks. However, once the shock waves approach a strength with temperature ratios of $T_1/T_2 \approx 0.5$, the transition Reynolds number starts to increase significantly. The authors attributed this behavior to high wall heat fluxes, which would stabilize the laminar boundary layer. For a shock wave with identical propagation speed to the detonation wave studied here, the transition distance behind the wave front can be estimated using the relations presented in the paper (see appendix 7.9). Accordingly, the transition distance is between 29 mm and 44 mm and thus near the outlet or even outside the numerical domain. Because the mentioned transition Reynolds number is strictly valid only for shock waves, this finding can only be used as an estimate and boundary layer transition behind detonation waves is left to future work.

To show that the determined mean effect of the loss terms is large enough to explain a reduction in propagation speed, figure 7.17(c) presents the loss terms integrated over the entire domain and normalized by the change of momentum flux $\dot{m}\Delta u$ and sensible enthalpy flux $\dot{m}\Delta h_s$ obtained from the ZND equilibrium solution. Because the mass flux $\dot{m}$ is 4 times larger in the 24 mm channel and since the integrated loss terms are similar for all channel heights, the normalized losses between simulations in 24 mm and 6 mm channels deviate approximately by a factor of 4, as expected. The difference observed between the channel widths is of similar magnitude to the observed differences in propagation speed. Furthermore, this analysis confirms the observation from the simulation with the Navier-Stokes equations with the free-slip and adiabatic walls (NS6-FS-A): a nearly identical velocity behavior from NS6-FS-A and EU6 shows that the velocity deficit behavior is due to the boundary layer.

7.4 Conclusion

A detonation cell stability mechanism was studied in detail using 2D numerical simulations. Simulations of propagating detonations in channels (6 mm and 24 mm in width) were performed using detailed chemistry and both Euler and Navier-Stokes formulations. Stoichiometric hydrogen-oxygen mixtures with and without ozone doping (3000 PPM) were tested. The following conclusions were drawn:

1) Numerical soot foils confirm the experimental observation that ozone reduces the characteristic cell size of detonation structure. The reduction stems from the reduced separation rate between shock and reaction fronts of a local blast, leading to a smaller blast kernel size thus smaller cell size. Simulated cell size distributions agree well with the experimental data, in spite of the difference between simulation and experiment in the geometries in which detonations propagate.

2) We confirm that the blast kernel and its size at the end of a detonation cell cycle controls the growth of the shock/reaction gap in the next cycle, which ultimately determines the blast kernel size for a new blast. We show that the kernel size dictates the propagation characteristics of the resultant new blast. Each mixture has a unique stable point it tends to, resulting in a characteristic cell size for that mixture. The stable point is controlled strongly by ignition kinetics (highlighted by the difference between ozonated and non-ozonated mixtures), and weakly by diffusion terms (shown by the increase in stable kernel size for NS simulations vs Euler simulations).

3) The viscous terms in the Navier-Stokes simulations have a minor impact on the blast dynamics and thus the cellular structure: Consistently among all cases, smaller stable kernel sizes establish in the Euler simulations, which typically translates into smaller detonation cell sizes unless geometric mode locking prevents such a solution. In the 6 mm channel without ozone, the diffusion terms increase the cell size by nearly a factor of 2, in the 24 mm channel without ozone, the diffusion terms increase the cell size by 25%. No such increase in cell size was observed in the ozonated mixtures. Cell enlargement was also observed in absence of a velocity deficit, presumably due to local effects from viscous terms.

4) In the Navier-Stokes simulations, a drop in propagation speed was observed (compared to Euler simulations), specifically in the narrow channel. This velocity deficit is conclusively shown to be due to the development of a laminar boundary layer.

Lastly, we caution, however, that the 2D simulations conducted here neglect the role of transverse waves in the third dimension of any real detonation waves, that are shown to modify the resultant cellular structure [274] and thermodynamic state and resultant cellular velocity within detonation cells [8].

All conclusions in this work are shown to be grid independent.

Acknowledgements

The authors from Duisburg gratefully acknowledge the Gauss Centre for Supercomputing e.V. (www.gauss-centre.eu) for funding this project by providing computing time on the GCS Supercomputer SUPERMUC-NG at Leibniz Supercomputing Centre (www.lrz.de) and the financial support by DFG (KE 1751/8-1) and the computing time on magnitUDE (Universität Duisburg-Essen, through DFG INST 20876/209-1 FUGG, INST 20876/243-1). The authors from Stanford University gratefully acknowledge funding from the Air Force Office of Scientific Research (FA9550-16-1-0486) with Dr. Chiping Li as Program Manager and the Office of Naval Research (N00014-22-1-2606) with Dr. Steven Martens as Program Manager. J. Crane also acknowledges the fellowships from the National Science Foundation (DGE-1656518) and Stanford University Vice Provost of Graduate Education.

Declaration of interests

The authors report no conflict of interest.

7.5 Grid resolution study

Simulation of highly-compressible reacting flows is often particularly sensitive to grid resolution. To confirm that the core simulations are satisfactorily converged, additional viscid simulations of the ozonated case in the 24 mm channel are performed at Δ_x = 40, 20, and 5 µm. The ozone case was chosen due to its smaller characteristic length scales, therefore being the more demanding case of the two mixtures considered in this work.

7.5.1 Cell sizes

Numerical soot foils of NS24O and the supplementary simulations at the other three resolutions are presented in figure 7.18, together with the statistical distribution of the cell widths. Cell width λ is measured for every complete cell in the converged portion of the soot foil using an automated script (details of the algorithmic approach are presented in appendix 7.8). Also plotted is the distribution of experimental cell size measurements [241] for direct comparison.

In contrast to previous grid studies for mixtures with highly irregular detonation cell structures [257], the impact of grid resolution on cell size is less distinct in our work; there is no statistical difference in the computed cell sizes over the range of the numerical resolutions studied. As shown in figure 7.18, the mean cell sizes are 5.18±1.08 mm, 4.48±0.74 mm, 5.01±0.93 mm and 5.02±0.88 mm for 40, 20, 10, and 5 µm resolutions. Qualitatively, the cell shape appears somewhat different in the 40 µm simulation, with triple point paths lighter in color (i.e., lower pressure) and less curved, while there is no discernible differences among the other three simulations. Within the range of grid resolution tested, other macroscopic properties, including kernel stabilization (*cf.* section 7.3.2) and velocity deficit (section 7.3.3), are shown to be also grid independent in appendix 7.6.

7.5.2 Heat release rates and species concentrations

To provide a quantitative estimate of the effect of finite resolution simulations on local heat release rates, we evaluated the inaccuracy when approximating Arrhenius kinetics with discrete computational cells over a domain with continuous gradients. The kinetic error for a given computational cell is estimated by calculating the net production rate of each species as well as the heat release rate, and comparing them with the respective rates from a group of sub-cells corresponding to the original cell with a ten-fold increase in resolution. To determine the thermodynamic states and composition for the sub-cells with the increased resolution, a linear interpolation is performed based on the immediately adjacent computational cells. This is equivalent to applying a Large Eddy Simulation (LES) sub grid model with an assumed top hat filtered density function (FDF), as proposed by [275], and testing if the sub grid model still has an

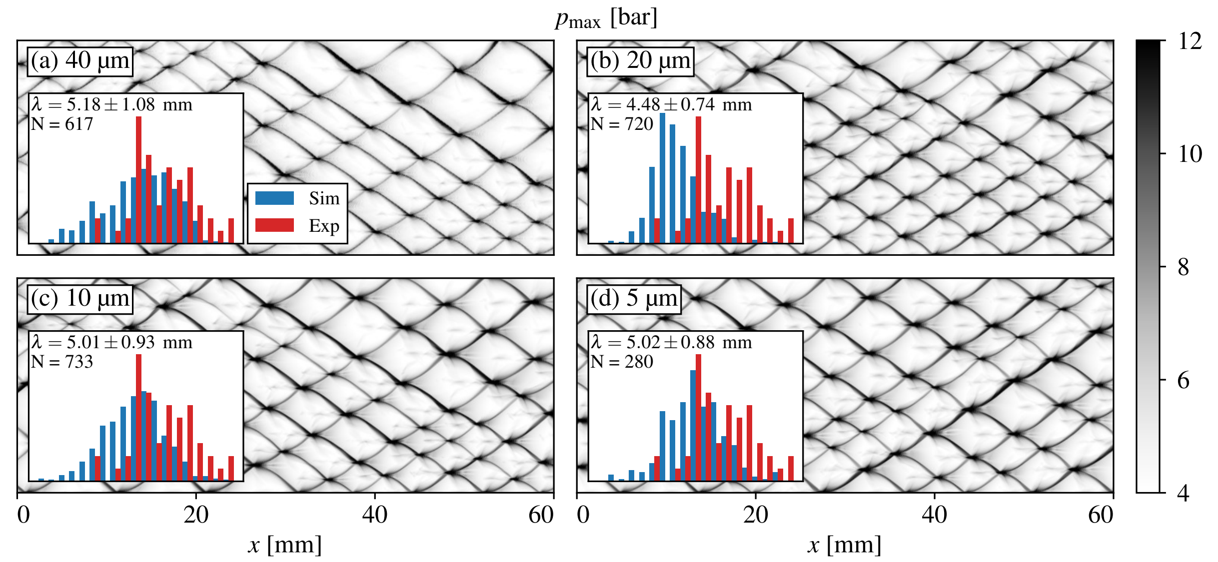

Figure 7.18: Grid resolution study showing converged numerical soot foils and cell-size distributions for grids of **(a)** 40, **(b)** 20, **(c)** 10, **(d)** 5 µm resolution. The simulation parameters are those of case NS24O. The cell width λ computed for each case is shown as the mean value averaged over N cells and its one standard deviation.

effect on the results. The normalized absolute deviation of the source term $\dot{\omega}$ (either species production or heat release rate) computed on the original grid and the sum of the source terms $\dot{\omega}_i$ computed on the interpolated grid is then used as an error measure ϵ:

$$\epsilon = \left| \frac{\dot{\omega} - \frac{1}{n^D} \sum_{i=1}^{n^D} \dot{\omega}_i}{\dot{\omega}} \right|$$

This equation considers the number n of sub cells in each of D dimensions, with $D = 2$ and n set to 10 for the present work. It is important to note that this method will likely predict relatively large errors for computational cells at shock fronts due to large gradients. Because the characteristic length scales associated with shocks are much smaller than the grid scale (i.e., $\ell_{\text{shock}} \ll \Delta_x$), a linear interpolation inside a cell with a shock is physically under resolved. This inevitable inaccuracy is considered when analyzing the results.

To account for computational cells of different states within the entire domain, we used a Monte Carlo sampling method to calculate the errors of heat release rates in 10 000 randomly chosen cells within a single temporal snapshot. The distribution of these errors is shown in figure 7.19 in 1% increment. The inset of figure 7.19 panel (c) shows the H_2 consumption rate error distribution at $\Delta_x = 10$ µm also in 1% increment. At $\Delta_x = 40$ µm, the heat release rate error is already insignificant, with over 60 % of the cells showing less than 1 % error. In comparison, at 10 µm resolution, over 80 % of cells show less than 1 % error in heat release rate; and the error in H_2 consumption rates is similar to that of the heat release rate, as expected. The inset of figure 7.19 panel (d) shows the fraction of cells with heat release rate errors ¿ 5 % for each grid resolution. Large errors occur primarily in shock-containing computational cells. For a well-converged simulation, however, the number of cells with large errors decreases by approximately one half as grid resolution doubles. In the 10 µm simulation, 3 % of cells contain errors greater than 5 %, while in the 5 µm simulation, 1.3 % of cells contain such errors, both showing a reasonable convergence behavior. Importantly, the uncertainty of the reaction model employed is around 5% in the laminar flame speed and 10-20% in ignition delay times [259]. Hence, the errors introduced by the finite resolution are at least comparable to or smaller than the reaction model uncertainty.

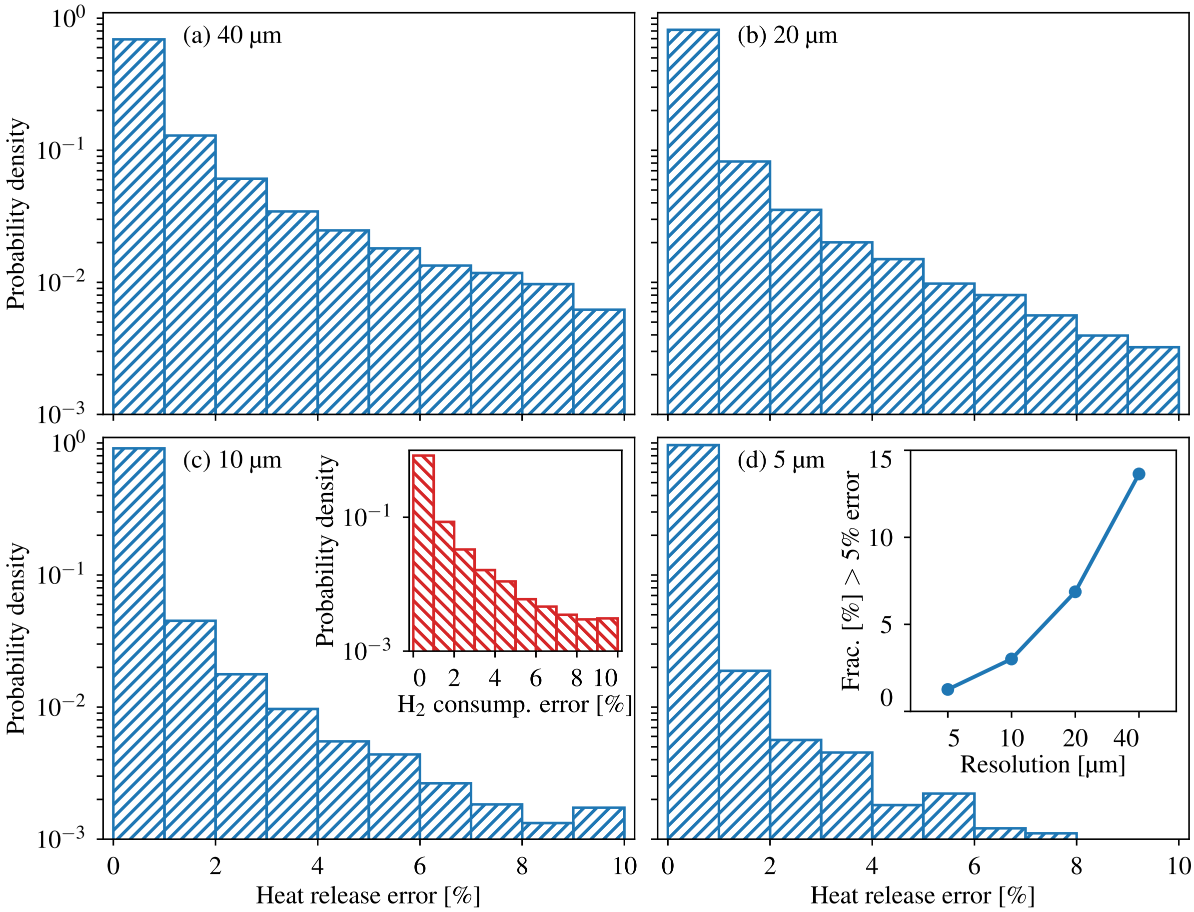

Figure 7.19: Distributions of error in heat release rate from Monte Carlo sampling (n = 10 000) of computational cells at the four grid resolutions **(a)** 40 µm (NS24O-40), **(b)** 20 µm (NS24O-20), **(c)** 10 µm (NS24O), **(d)** 5 µm (NS24O-5). Insets in panel (c) and panel (d) are the error distributions of the H_2 consumption rate and the fraction (in %) of cells with heat release rate errors larger than 5% as a function of grid resolution, respectively.

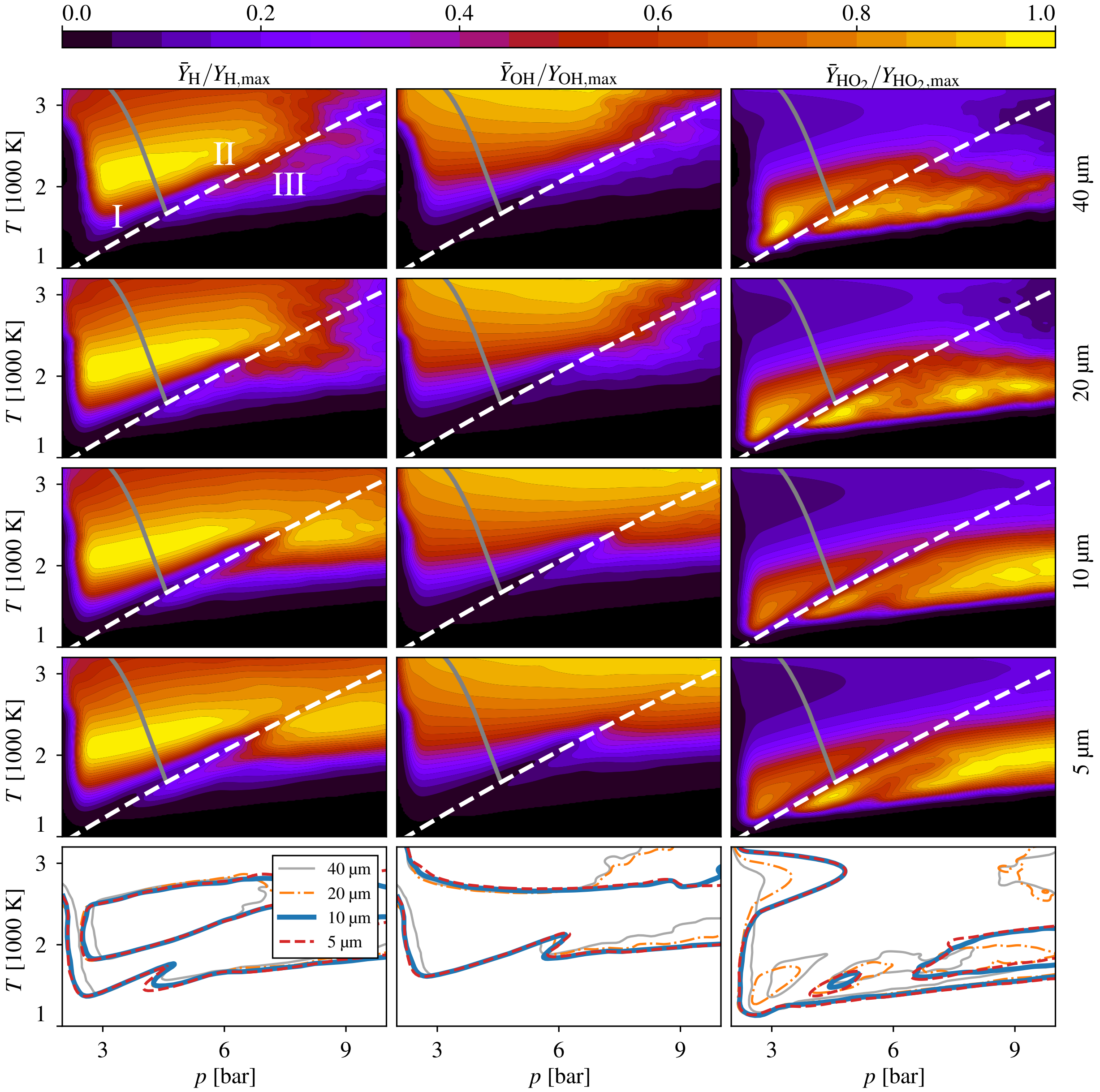

Figure 7.20: Time-averaged distributions of free radical intermediates (H, OH and HO_2) in $p - T$ space, whereby the first row shows the results at the coarsest grid resolution of 40 µm, while the fourth row shows the results for the finest grid resolution tested (5 µm). The last row presents isolines at values of 0.1 and 0.8.

Convergence of the chemical species concentrations is examined next by comparing computed intermediate species mass fractions. The highly non-linear dependence of reaction rates on temperature and compositions renders this convergence criterion more stringent than that of heat release rates. Specifically, mass fractions of selected intermediate species are sampled as a function of the local temperature and pressure. Samples are taken in a region behind the shock-wave front that excludes the boundary layer, and from 25 snapshots among all available time steps. Figure 7.20 presents the sample-averaged distributions of the mass fractions of Y_{H}, Y_{OH}, and $Y_{\mathrm{HO_2}}$ from 1000-3200 K and 2-10 bar. In each panel, the white dashed line illustrates the relation of the frozen post-shock pressure and post-shock temperature over a range of Mach numbers of a normal shock. The grey solid line illustrates the evolution of pressure and temperature from the ZND solution; its top endpoint corresponds to the equilibrium (CJ) condition of the reactive mixture. With these dividing lines, the solution can be classified roughly into three regions (labeled in the top left panel). Region I is dominated by fluid samples that are compressed by underdriven waves. Region II is dominated by fluid samples compressed by overdriven waves. Region III features high pressures with temperatures below the corresponding post-shock values; the states in this region are likely to stem from fluid samples that are compressed by two (or more) weaker shocks (e.g., underdriven detonation waves and/or transverse waves) instead of one strong shock. For atomic hydrogen, distributions in region I are similar at all grid resolutions. The distributions in regions II and III from the finer resolutions (10 μm and 5 μm) are similar to each other, but differ notably from those of the coarser resolutions (20 μm and 40 μm). The agreement between the distributions at grid resolutions of 10 μm and 5 μm is particularly well demonstrated in the last row of figure 7.20, which presents the isolines at mass fractions of 0.1 and 0.8 for all species considered. For the two finer grids the isolines match closely for all four species and in all three regions, while the isolines for the two coarser grids deviate notably from those of finer grids even in region I. This is most noticeable for the $\mathrm{HO_2}$ radical. Nevertheless, the analysis just presented provides a reasonably support for achieving grid convergence at $\Delta_x = 10$ μm resolution; the results from $\Delta_x = 10$ μm agree very well with those of 5 μm.

7.6 Invariance of conclusions based on grid resolution

To ensure that the conclusions of this work are unaffected by grid resolution, the major post-processing tasks are repeated for three grid resolutions: 20, 10, and 5 μm for the NS24O case. Already shown in the main text in figure 7.18 is the comparison of the soot foils for different grid resolutions. There is little or no quantitative or qualitative difference in the cellular structure between the 20, 10, and 5 μm simulations.

The blast kernel dynamics conclusions are also unaffected by grid resolution. Figure 7.21(a) shows the statistical description of the stabilizing mechanism for the three numerical resolutions (mirroring figure 7.9 a). Evident is that the stabilizing mechanism is present at all grid resolutions, and shows similar slopes. The blast propagation decay behavior as a function of numerical resolution is shown in figure 7.21(a) (mirroring figure 7.7 c) as the dependence between kernel size, r, and exponential decay constant, τ. Evident is that the 5 and 10 μm simulations display nearly identical behavior, showing that the 10 μm simulation is well converged. The 20 μm simulation show slightly different behavior, where the values of τ are slightly lower than the other simulations for the same kernel size, but the overall trend is the same. The final quantity analyzed for all three grid resolutions are the pressure and temperature front separation rates ($d(R_P - R_t)/dt$) as a function of kernel size. All three simulations appear to display similar behaviors, with separation rate inversely proportional to kernel size, again showing excellent convergence.

The propagation velocity behavior for the three grid resolutions is shown in figure 7.22(a). All three simulations show nearly identical initial transients, and the steady velocity among the three simulations is within 0.5 %. The 5 and 10 μm simulations have particularly close propagation velocities, showing that stable propagation velocity is well-converged in these simulations.

The average pressure behind the shock is also analyzed for each of the three simulations shown in figure 7.22(b). The nearly identical profiles again indicate excellent convergence.

The grid resolution requirements to resolve boundary layer are particularly high. Figure 7.23 presents the loss term analysis, in the same format as figure 7.17 in section 7.3.3, for the 40, 20, 10, and 5 μm

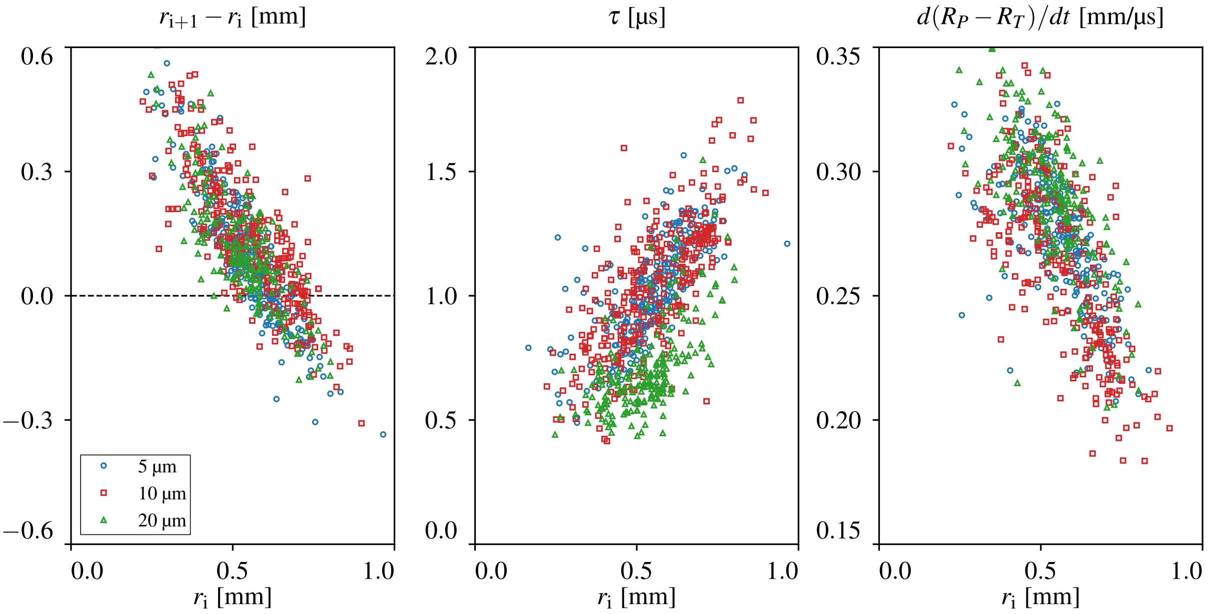

Figure 7.21: (a) Kernel stabilization mechanism for the three grid resolutions, (b) dependence of pressure front propagation on kernel size for the three grid resolutions, and (c) pressure-temperature front separation rate as a function of kernel size for three grid resolutions. Legend in (a) also applies to (b) and (c).

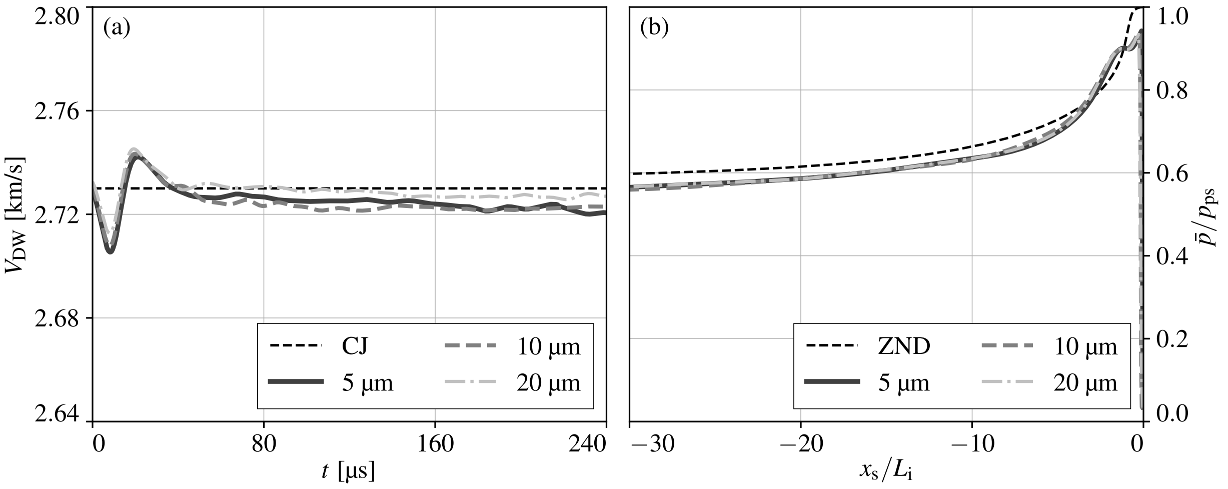

Figure 7.22: Gaussian-smoothed detonation wave velocity for simulation duration for the NS24O simulation for three grid resolutions, 5, 10, and 20 µm (left). Average pressure behind shock wave for the three grid resolutions, plotted with ZND profile.

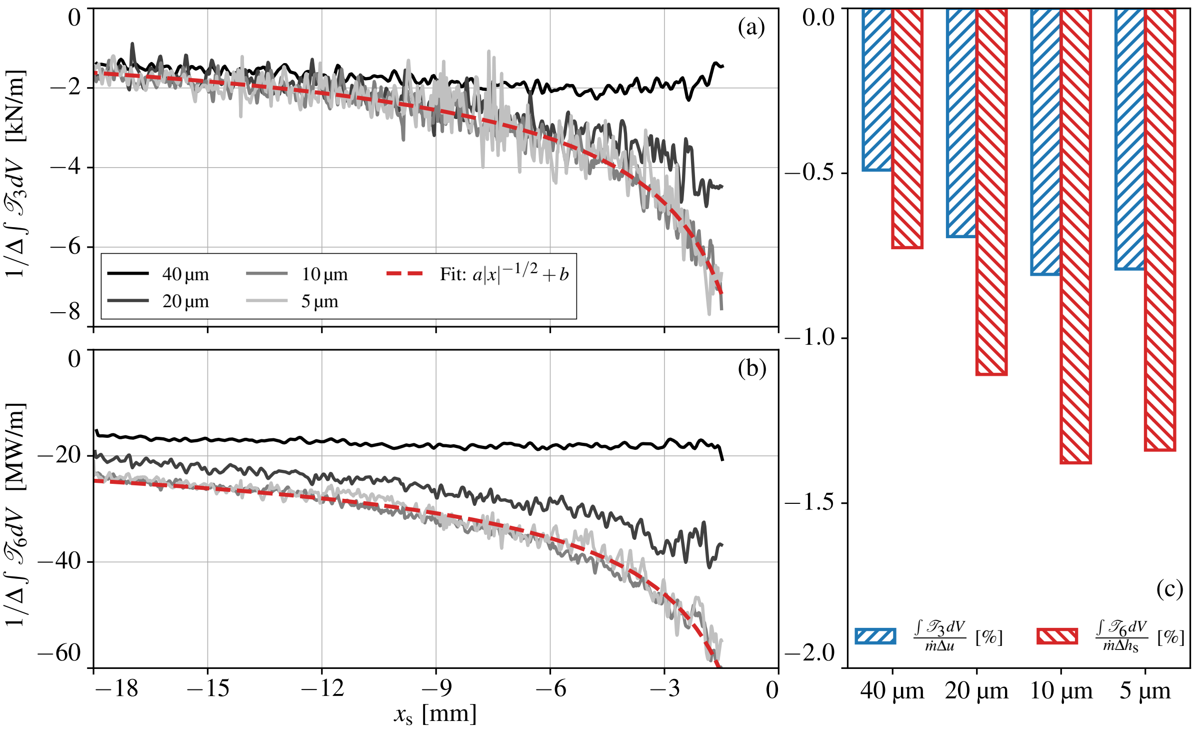

Figure 7.23: **(a)** Cross-width integrated values of tangential stresses ($\mathcal{T}_3$), **(b)** cross-width integrated values of thermal conduction ($\mathcal{T}_6$), and **(c)** volume-integrated values of both terms, normalized by the change of momentum flux and enthalpy flux respectively at different grid resolutions.

simulations. While the results of the integrated loss term for momentum in panel (a) from the 20, 10, and 5 µm simulations agree at some distance from the wave front, large discrepancies are observed for the 40 µm simulation, suggesting that the boundary layer is not captured. Similar conclusions are made for the cross-width integrated loss term of energy in panel (b), although deviations are observed for the 20 µm simulation. The excellent agreement between the 5 µm and 10 µm simulations show that the boundary layer conclusions are not affected by the resolution, once a sufficient resolution is reached.

All macroscopic properties analyzed show that the 10 µm simulation is well-converged, and furthermore that the conclusions made in this work are insensitive to numerical resolution.

7.7 Sensitivity to kinetic mechanism

Several kinetic mechanisms for modeling the finite-rate kinetics of hydrogen combustion exist. Recently developed mechanisms include Konnov's of Lund University [276], HP-MECH [277], the UCSD mechanism [278], and the Foundational Fuel Chemistry Model Version 1.0 (FFCM-1) [222, 259] used in this work. To understand the sensitivity of the results to the given kinetic mechanism, ZND calculations are performed with each of the four mechanisms listed above. The resultant ZND temperature and pressure profiles are plotted in Figure 7.24. While not identical, calculated induction lengths from the four mechanisms are within 11% of one another, which is within the typical 2 sigma experimental uncertainty of combustion measurements (e.g., shock tube ignition delay time) constraining the mechanisms [279]. FFCM-1 was chosen because the reaction model was subject to a rigorous optimization and uncertainty minimization analysis against a wide range of data (see, [222]). No other available model has gone through that level of quantitative scrutiny.

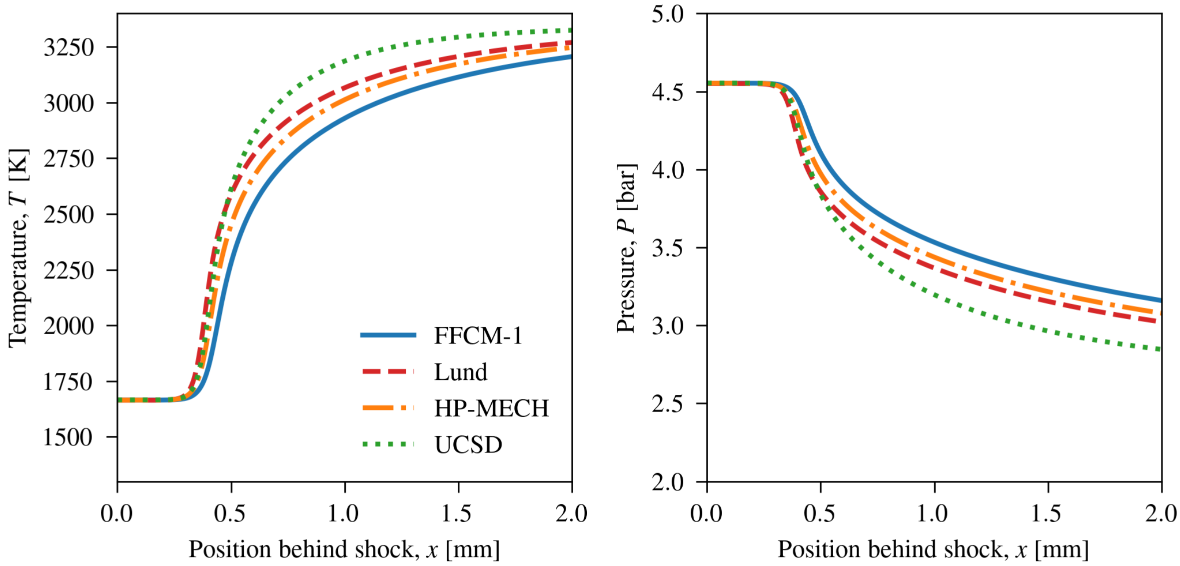

Figure 7.24: Computed ZND profiles for FFCM1, Lund mechanism (Konnov), HP-MECH, and the UCSD Mech. Plotted is temperature (left) and pressure (right) as a function of position behind the shock wave. Conditions are stoichiometric hydrogen-oxygen at 15 kPa initial pressure (same conditions as non-ozonated simulations). Legend applies to both figures.

7.8 Kernel post-processing

Extracting statistics from individual detonation cells and ignition kernels requires extensive post-processing. The first step in this post-processing is calculating the numerical soot foil, as described in section 6.2. The locations of individual blast kernels are then approximated from the soot foil by finding regions of local maxima, exceeding 8 bar in pressure, in the soot foil. The local maxima correspond to the highest pressure zone in a single cell cycle, and typically is close to the location of the blast kernel initiation. After this automated step, the soot foil, with the local maxima superimposed, is manually inspected to ensure accuracy of the algorithm. A soot foil will typically have 0-10 errors for kernel locations which are manually removed. Note that this process does not exclude somewhat fainter ignition kernels, like those found in the EU24 and EU24O simulations (see Figure 4).

Once the approximate locations of kernels are determined (their locations called p_a), then the exact locations of the kernels are found. This is achieved by loading 10 frames prior to the approximate kernel location and time, and searching for a condition where a large pressure rise occurs (found to perform well as 60 times the initial pressure, p_0) directly behind the shock wave. This pressure rise corresponds to two Mach stems colliding, and indicates the start of the collapse of the transverse waves. The point at which this occurs is defined to be the end of the cell cycle, and one end of the blast kernel, and we shall call this point p_r. The other end of the blast kernel is found to be the maximum Euclidean distance between p_r and the isoline of $Y_{H_2} = 0.04$ (corresponding to burned gas) within 15-degrees with respect to the x-direction. Snapshots of the regions around the approximate kernel location (p_a) and the exact kernel locations, p_r and p_ℓ, are shown in figure 7.21. The Euclidean distance between points p_r and p_ℓ is the kernel size r. We note that calculating the area of the kernel as opposed to the Euclidean distance between the front and back of the kernel does not impact the overall conclusions of the work. The kernel size is chosen for consistency with past work [248].

To determine the cell width, as shown in figures 7.5 and 7.18, the set of all points p_r in the domain is analyzed. For every point $p_{r,i}$, the nearest neighboring point $p_{r,i\neq j}$ is calculated, conditioned that the angle between $p_{r,i}$ and $p_{r,i\neq j}$ is less than 30 degrees in the y-direction, and conditioned that the x-position of $p_{r,i\neq j}$ is greater than that of p_r. The resultant cell widths are then superimposed on a numerical soot foil,

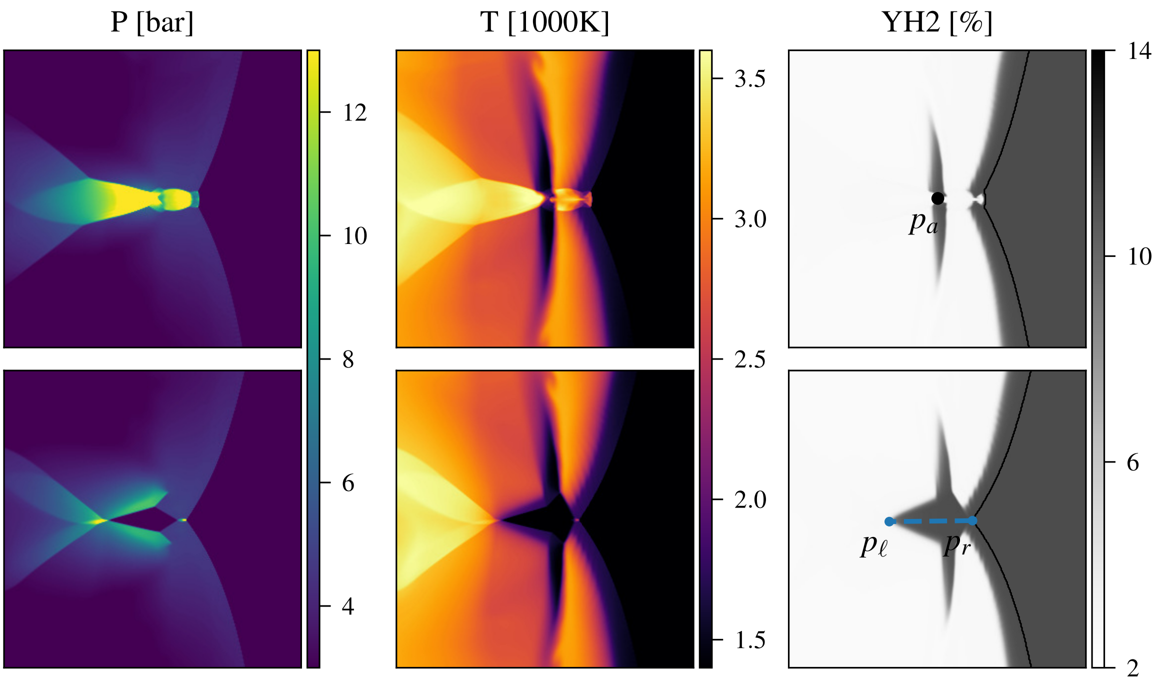

Figure 7.25: Top row: pressure, temperature, and hydrogen mass fraction of the approximate kernel location as determined from soot foil local maxima analysis from representative kernel, with approximate kernel location, p_a, labeled. Bottom row: exact kernel location with left (p_ℓ) and right (p_r) kernel points labeled on the hydrogen mass fraction plot. Also superimposed on both Y_{H_2} plots is the location of the shock front.

and verified manually.

To determine the velocity distribution of individual cells, which are used to determine the quantities displayed in figures 7.7-7.10, a line is drawn from $p_{r,i}$ to the subsequent kernel, $p_{r,i+1}$, defined as ℓ_i. The intersection point, defined as $p_{\text{int},i}$ between the shock front and the line ℓ_i is found for every time step. The temporal radial position of the blast wave is then the distance between $p_{r,i}$ and $p_{\text{int},i}$. An identical process is performed with the temperature front to determine the temperature front radial position.

7.9 Boundary layer transition distance

The definitions and syntax of Hartunian et al. [273] are used in the following. The transition Reynolds number Re_{tr} is a function of the wall temperature T_w (equal to the temperature of the quiescent gas) and the temperature of the compressed gas T_e (external in reference to the gas within the boundary layer). The ratio of these temperatures in the present case equals $T_\text{w}/T_\text{e} = 1667/300 = 0.18$, which corresponds to a transition Reynolds number of $\text{Re} = 2\,000\,000$ to $3\,000\,000$. The length scale chosen to characterize the Reynolds number is that of the distance a particle travels from its initial position until it reaches the transition location $L = (U_\text{s} - U_\text{e})/U_\text{e}\ U_\text{s}t_\text{tr}$ in reference to flow over a flat plate. Here, U_s is the shock speed (in our case equal to the detonation wave speed) and U_e denotes the speed of the compressed gas in wave coordinates, while t_tr represents the time that passes until the onset of turbulence is measured at a fixed location. The kinematic viscosity ν_e is based on the state of the compressed gas. Accordingly, the value of transition time can be determined to $t_\text{tr} = 10.61\,\mu\text{s}$ to $15.92\,\mu\text{s}$. During that time, the shock wave travels a distance $x_\text{tr} = U_\text{s}t_\text{tr} = 28.97$ mm to 43.46 mm.

Chapter 8

Three-dimensional detonation structure and its response to confinement

Three-dimensional detonation structure and its response to confinement [280]

Authors: J. Crane, J. T. Lipkowicz, X. Shi, I. Wlokas, A. M. Kempf and H. Wang
This chapter including all figures and tables was previously published in 'Proceedings of the Combustion Institute, 39(3), J. Crane, J. T. Lipkowicz, X. Shi, I. Wlokas, A. M. Kempf and H. Wang, Three-dimensional detonation structure and its response to confinement, 2915 - 2923, Copyright ©Elsevier' and is reprinted with permission from Elsevier. The author J. T. Lipkowicz wrote the code for the CFD simulations, ran all the simulations and developed post-processing tasks to generate head on animations. The author J. Crane wrote the paper and generated all figures and tables. The authors J. T. Lipkowicz, X. Shi, I. Wlokas, A. M. Kempf, and H. Wang contributed corrections, discussions and proof-reading.

Abstract

Three-dimensional (3D) detonation simulations solving the compressible Navier-Stokes equations with detailed chemistry are performed in both square channel and round tube geometries. The simulations are compared with each other and with two-dimensional (2D) channel simulations and round tube experiments of identical mixture and conditions (stoichiometric hydrogen-oxygen with 3000 PPMv ozone at 300 K and 15 kPa) with the goal of understanding the effect of confinement and boundaries on detonation structure. Results show that 3D detonations propagate with highly inhomogeneous blast dynamics, where blasts emerge not only from intersections of two transverse waves (similar to 2D propagation) but also from intersections of many transverse waves (unique to 3D detonations in the confinements tested). Intersections of many transverse waves lead to extreme thermodynamic states and highly overdriven wave velocities, well in excess of those seen in the ZND model and in 2D simulations. 3D simulations in the square tube show highly regular blast latticing, smaller detonation cells, and highly oscillatory velocities when compared to the round tube simulations. Round tube simulations show more spatially non-uniform blast dynamics. The conclusions reached in the current work are found irrespective of numerical grid resolution.

8.1 Introduction

Developing a better description of realistic multi-dimensional detonations hinges on understanding their structural features. Multi-dimensional detonations exhibit a characteristic cellular structure that results from the interaction of Mach stems, incident shocks, and transverse shocks [227, 281]. As one of the most measured and observed features of detonations, detonation cells appear to correlate with a variety of propagation properties [282] including deflagration to detonation transition (DDT) length [283, 284], critical diameter [285], and detonation limits [286, 287].

It is well-known that detonation confinement has a strong influence on its propagation characteristics. Indeed, if a geometry is substantially smaller than the characteristic cell size, detonations fail [288]. But confinement, or lack thereof, can also influence the cellular structure itself: partially unconfined detonations exhibit a cellular structure qualitatively different from those propagating in channels or tubes [289]. Detonations of practical interest (*i.e.*, those in engines, accident scenarios, etc.) propagate in a wide variety of geometries, including unconfined spaces, but more often tubes and channels of various types [290, 291]. Therefore, understanding how detonation structure responds to various confinements is of both fundamental and practical significance.

Most experimental work observing detonation cellular structure relies on bulk, 2D representations of the structure as measured on tube walls or in thin channels (*i.e.*, soot foils or optical diagnostics), or, occasionally, as measured head-on. Meanwhile, computational studies are typically limited to 2D studies of detonation, or 3D simulations in small, simple domains due to the high simulation cost along with the challenge in post-processing large 3D simulations [227]. The most complete description, from both experiments and simulations, of 3D cellular propagation in literature exists for rectangular channels [292–301], which generally describe a highly regular structure with rectangular or diagonal shocks strongly coupled to the confining geometry. Some time-resolved 3D simulations also exist for tube geometries, primarily in spinning, near-spinning, or strongly geometry-locked modalities [302–305]. More time-resolved 3D measurements, with detailed quantification, of detonation propagation in various types of confinements are needed to develop a comprehensive understanding of how 3D detonation structures evolve. More specifically, head-on and soot foil measurements of detonation propagation in round tube geometries suggests a substantially different propagation mode compared to the propagation in rectangular geometries, but little information exists on the details or implications of these differences [306].

This study aims to better understand and quantify detonation structural response to confinement by performing side-by-side 3D detonation simulations with two different geometries commonly used in experiments: square channels and round tubes, as well as a 2D companion simulation in a channel. We will also contrast the 2D and 3D results from this study to experimental results in tubes. The aims of this work are then (1) to build an improved understanding of the 3D cellular propagation mechanism, and in doing so, to understand how this differs from the well-developed description from 2D studies (as described, for example, in [307, 308]), and (2) to describe how the 3D propagation is affected by confinement. We examine, in particular, the velocity evolution and the thermodynamic states encountered in blast waves in 3D simulations with varying confinement and contrast the results to 2D simulations. Quantifying maximum pressure and temperature has important implications for future modeling in terms of predicting real gas effects [309, 310], the role of vibrational relaxation on detonation structure [311, 312], and the applicability of chemical kinetic models [222]. Understanding the range of thermodynamic states also has important implications for heat transfer rates [313] and material requirements [314] for real devices. This work relies on well-resolved 3D cellular detonation simulations. Specifically, we solve the compressible Navier-Stokes equations with detailed chemistry (shown to be important by Taylor [250]) with isothermal and no-slip boundary conditions to provide the highest fidelity simulations possible. The mixture simulated is stoichiometric hydrogen-oxygen at 300 K and 15 kPa, with 3000 PPMv ozone doping. This mixture is chosen because it has been experimentally studied in some detail [315] and it has a relatively stable cellular structure.

8.2 Numerical solver and setup

The simulations are performed with the in-house code *PsiPhi* [6, 183] that solves the fully compressible set of conservation equations for mass, momentum, total internal energy, and partial densities. The equations are discretized on an equidistant Cartesian grid utilizing the Finite Volume Method. An approximate Riemann solver computes convective fluxes at cell interfaces with the aid of a monotonicity preserving reconstruction scheme featuring a theoretical accuracy of 5th order, while a 2nd order central difference scheme is used for diffusive fluxes. A Strang Operator Splitting framework allows an explicit time integration of convection and diffusion with a 3rd order accurate Runge-Kutta scheme, and an implicit time integration of chemical kinetics using CVODE. Sub-filter dynamics are modeled with an eddy viscosity/diffusivity approach. The filtered chemical source term is computed based on the resolved fields of pressure and mass fractions with a presumed tophat PDF [76] of temperature for the purely temperature dependent reaction rate constants to account for non-linear behavior similar to the approach given in [72]. More details of the solver can be found in [6, 183].

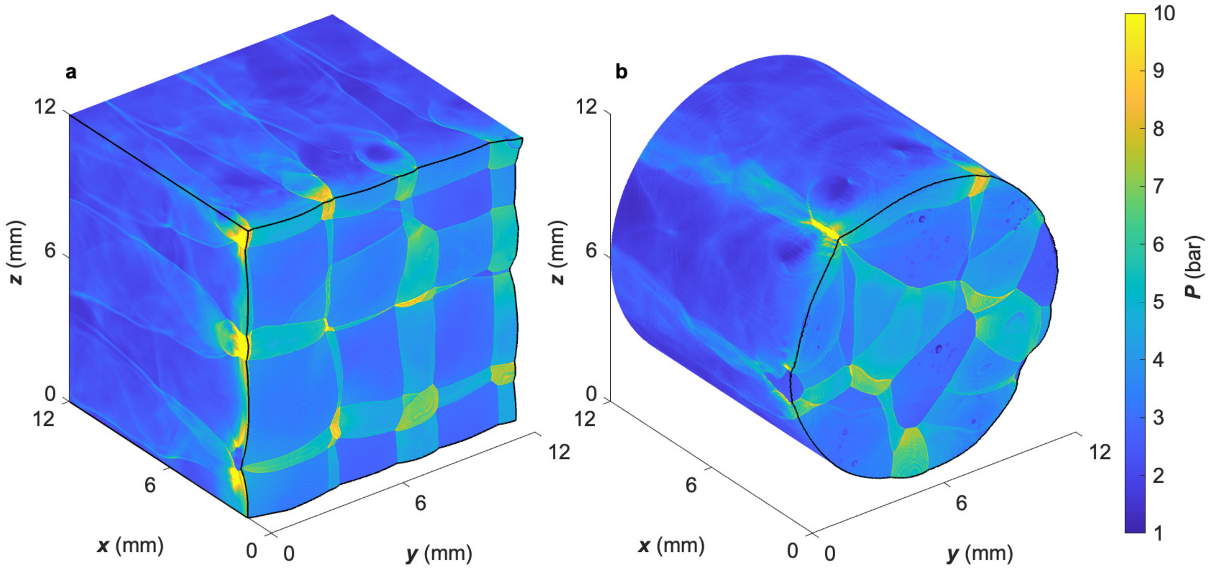

Figure 8.1: Isometric snapshots of the 3D square channel simulation (**a**) and the 3D round tube simulation (**b**) at the 20 µm grid resolution. Both are taken from the well-converged portions of the simulations. Plotted is pressure pseudocolor; the colorbar applies to both figures. Mixture and conditions of both simulations are stoichiometric hydrogen-oxygen with 3000 PPMv ozone additive at 15 kPa initial pressure.

The chemical kinetics model used is the hydrogen sub-model of the Foundational Fuel Chemistry Model Version 1.0 (FFCM-1) [222, 259] with the Princeton ozone model [260]. Two 3D geometries are considered: a square channel 12 x 12 x 12 mm, and a round tube 12 mm in diameter and 12 mm in length. A 2D simulation 24 mm in channel width and 36 mm in length is also performed. The round tube simulation is set up in a rectangular domain, where the effects of walls are modeled with the efficient immersed boundary technique. The boundary conditions used are no-slip and isothermal (300 K) for the walls, a Dirichlet boundary condition for the inlet, and a partially reflecting boundary condition for the outlet [145]. This setup allows the numerical domain to be moved at CJ speed relative to the laboratory reference without wave reflection. Three simulations are performed using three different numerical grid resolutions for each 3D geometry: 40 µm, 20 µm, and 10 µm, while the 2D simulation is performed at 10 µm. The finest simulation contains 24 numerical grid points per half reaction length, approximately the minimum criterion established for low activation energy mixtures (like ozonated hydrogen-oxygen) by Mazaheri et al. [255]. The coarsest simulations are initialized with an inclined ZND detonation wave, while the finer simulations are initialized with a converged solution from the coarser resolutions. The finest 3D simulations (10 µm) are run on 64,000 cores for approximately 150 wall-clock hours, equating to a total cost of approximately 10 million CPU-hours per simulation. Each grid coarsening reduces the computational cost by roughly an order of magnitude.

8.3 Results and discussion

Snapshots of a pressure pseudocolor are shown for both the 3D square channel (**a**) and round tube (**b**) simulations in Fig. 8.1. These snapshots are chosen in the well-converged portion of the simulations to exclude any memory effects from initial conditions. The two snapshots clearly show a substantial difference in the detonation structure between the two simulations. As other researchers have observed in the past [294, 299], the square channel exhibits a highly regular structure with ignition kernels occurring on a nearly perfectly spaced square grid. Although there are some deviations from the dominant structure (see upper right corner of Fig. 8.1a), the dominant structure is highly stable as evidenced by the fact that this structure is maintained throughout the entire simulation despite these deviations. The tube simulation, on the other hand, has no clearly discernible regular structure. Local shock waves of varying strength are observed throughout the detonation frontal structure, including reflections off the wall.

8.3.1 Cellular structure

Numerical soot foils are calculated, based on maximum pressure history, for the 3D channel and tube simulations and compared to those from 2D simulations and round tube experiments. The soot foils from the 3D simulations are calculated exclusively using the pressure data near the shock front for computational simplicity, and are thus an approximation of the full numerical soot foil. Nonetheless, they exhibit the characteristic cellular features expected, and are useful to analyze and compare with 2D numerical soot foils and experimental soot foils. Figure 8.2 shows the soot foils for the 3D square channel (**a**) and round tube (**b**) simulations as well as the 2D simulation (**c**) and the experiment (**d**), all with the same mixture and conditions (and in the case of the 3D and 2D simulations, at the same grid resolution of 10 μm). The experimental soot foil is a sub-section of the full foil obtained from a detonation tube experiment with tube inner diameter of 32 mm [315]. Clearly seen from Fig. 8.2 are the differing cellular structures among the various geometries. The square channel produces detonation cells which appear narrower but as long or longer as compared to those from the tube geometry. Meanwhile, the 2D simulation produces cells more characteristic of the tube simulation, and the experimental soot foil and the 3D tube simulation also appear qualitatively similar. Notably missing from the 2D simulation is the white banding which appears transverse to the dominant cellular structure and shows out of plane transverse waves that collide with the wall. The square channel shows highly regular banding, while the 3D tube simulation and tube experiment show similarly more random banding.

Cell structure statistics, recorded from hand-measured cells, are shown in Fig. 8.3. As observed qualitatively, the aspect ratio (cell length divided by width) from the square channel simulation is notably larger than that of the round tube simulation, which is primarily due to a smaller average cell width. The 2D simulation has both an aspect ratio and mean cell width somewhat in between the two 3D geometries. Meanwhile, the agreement in aspect ratio between the 3D tube simulation and tube experiments is good, although the distribution is somewhat wider in the case of the experiments. This is expected: more perturbations may exist in the experiments as compared to simulation (*e.g.*, rough walls, mixture inhomogeneities) which can broaden the distribution of cell morphologies.

8.3.2 Blast dynamics

To better understand the nature of the detonation structures, and shed light on the differences between the 3D square channel and round tube simulations, we analyze the blast dynamics resultant from detonation kernel ignitions. Detonation kernels (pockets of post-shock unburnt gas which experience rapid ignition after transverse wave collapse), and their resultant blasts, are key to understanding cellular structure [308]. Figure 8.4 shows isosurfaces (6 bar and 10 bar) from sub-domains (4 x 4 x 4 mm) of the square channel

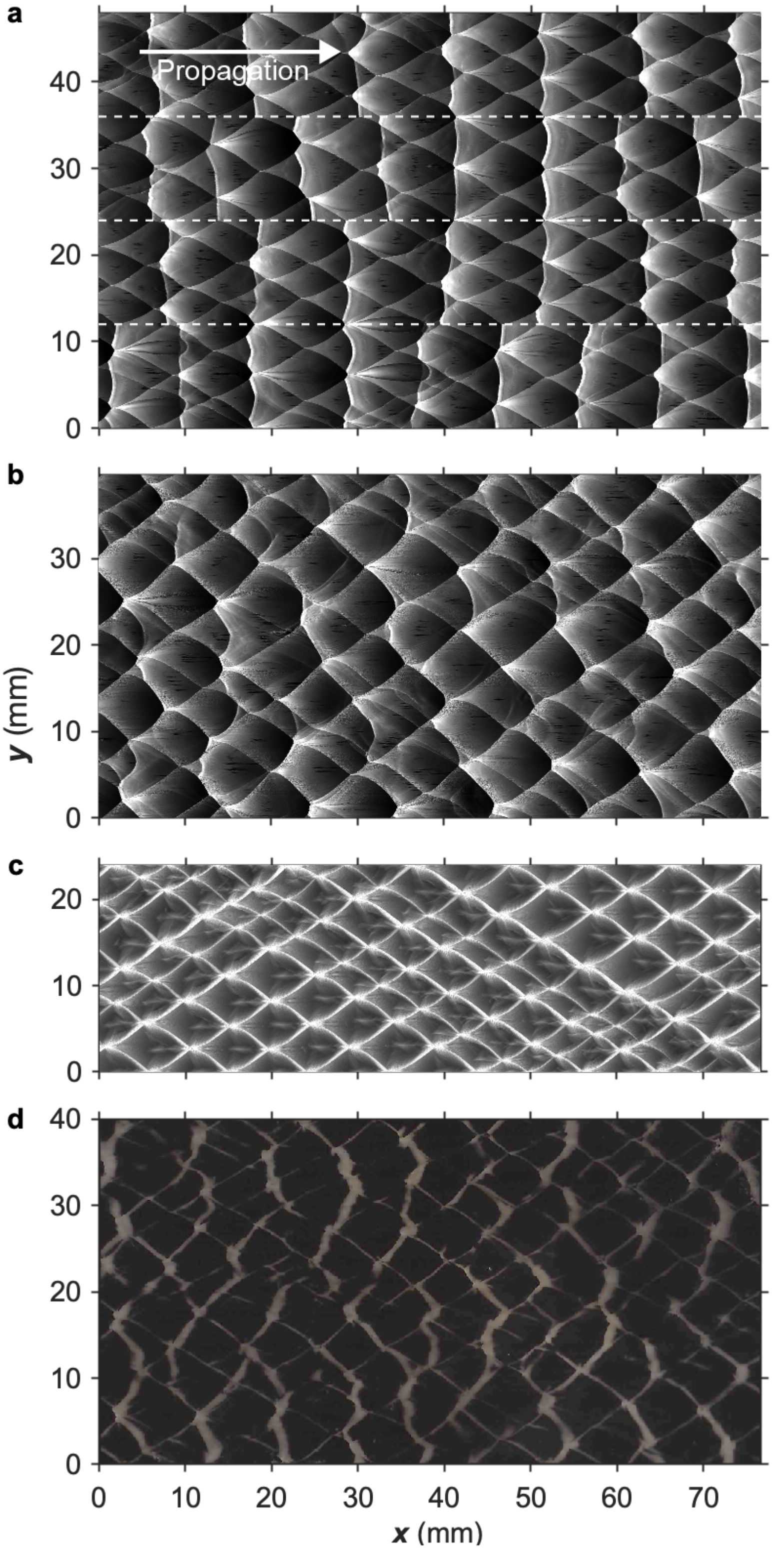

Figure 8.2: Numerical (**a, b, c**) and experimental (**d**) soot foils for identical mixture and conditions in different geometries: 3D square channel simulation (**a**), with dashed white lines showing channel corners, 3D tube simulation (**b**), 2D simulation (**c**), and tube experiments (**d**). All simulations at 10 µm grid resolution. All numerical soot foils have the same color bounds with a maximum of 10 bar (white) and minimum of 2 bar (black). Propagation is from left to right.

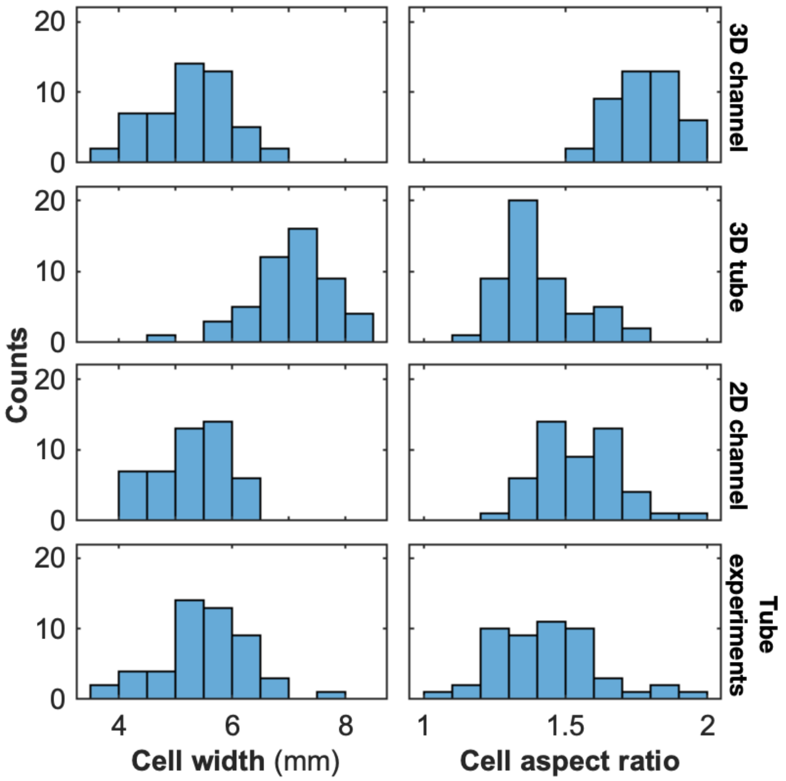

Figure 8.3: Soot foil statistics measured from Fig. 8.2. The left column contains cell width statistics, and the right column cell aspect ratio (cell length divided by cell width). The length and width of 50 cells were measured from each soot foil.

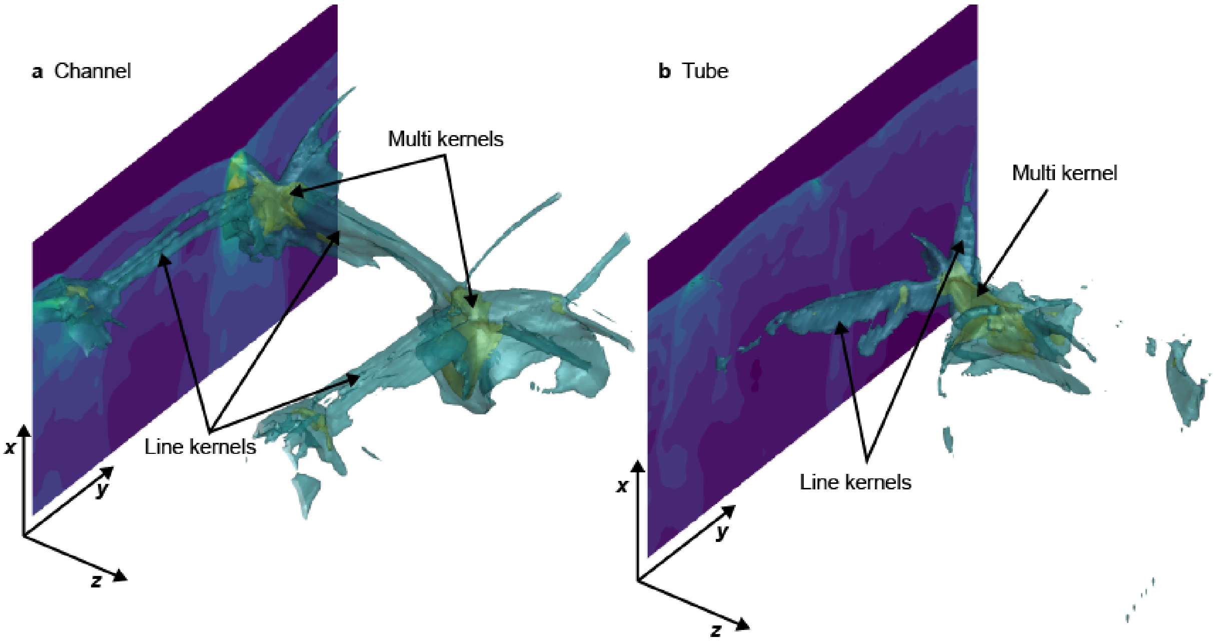

Figure 8.4: Isosurfaces of 6 bar (green) and 10 bar (yellow) from snapshots of the 3D square channel (**a**) and round tube (**b**) simulations at 40 μm grid resolution. Snapshots were selected to highlight kernel formation structure in each geometry. Detonation waves in both simulations propagate in the x-axis direction.

(**a**) and round tube (**b**) simulations, with specific snapshots chosen to highlight the detonation kernels shortly after transverse wave collapse. Apparent in Fig. 8.4 are the different appearances of the kernels between the two simulations. Both simulations contain what we term as ‘line’ kernels, which result from two transverse waves intersecting, and ‘multi’ kernels, which result from more than two transverse waves intersecting. The multi kernels, as expected, generally have more extreme states (as shown by the higher values of pressure in Fig. 8.4) as compared to the line kernels. The wave alignment from the boundaries of the square channel lead to a highly regular kernel structure which contain square lattices of line kernels and multi kernels. In the square channel, the multi kernels are almost always the result of the nearly simultaneous intersection of four waves. Meanwhile, in the round tube, a more irregular kernel structure is observed (see Figs. 8.1b, 8.4b, S1 of the Supplementary Material). In the round tube the multi kernels are often the result of three transverse waves collapsing, but sometimes are the result of up to five waves collapsing, although not always at exactly the same time.

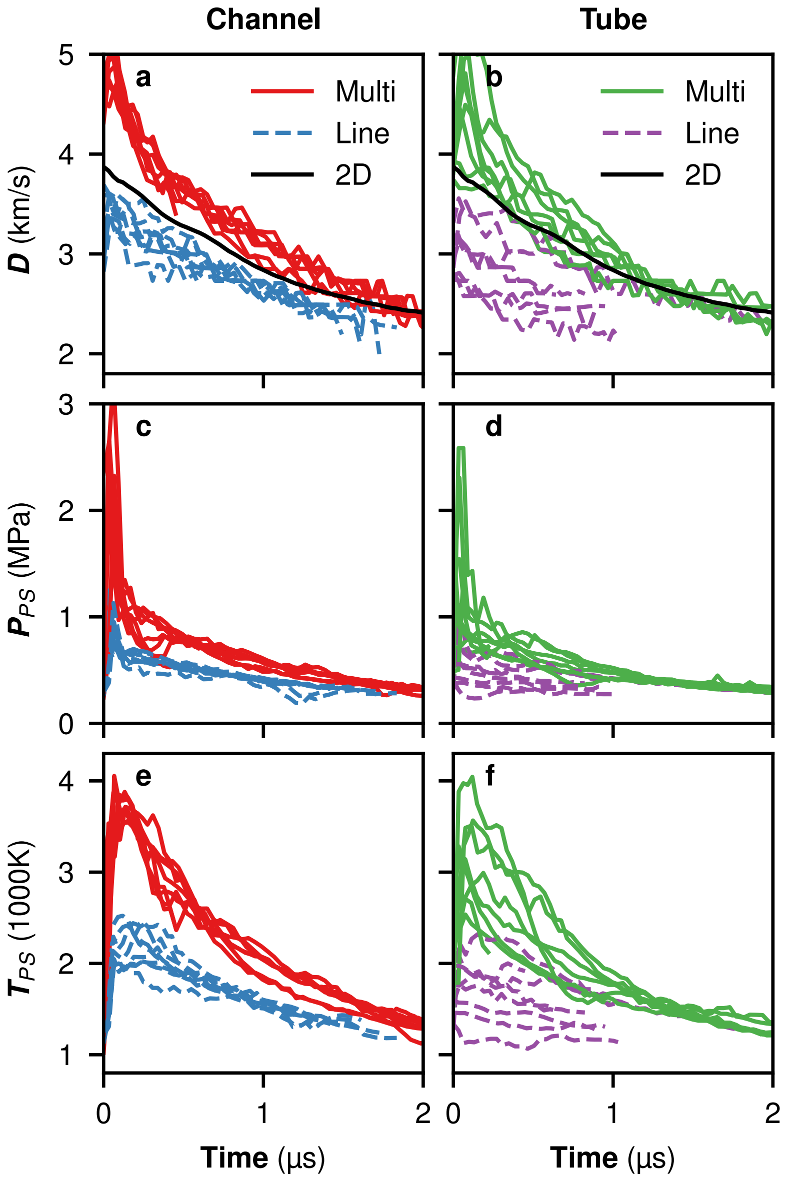

Figure 8.5: Wave velocity D (**a, b**), post-shock pressure P_{PS} (**c, d**), and post-shock temperature T_{PS} (**e, f**) for eight blasts from line (dashed lines) and multi (solid lines) blasts for detonations in the 10 μm grid resolution 3D square channel (**a, c, e**) and 3D round tube (**b, d, f**).

The different kernel structures between detonations in these geometries lead to differing subsequent blast propagation dynamics. To better understand this behavior, we consider the propagation characteristics of blasts resultant from line kernels and multi kernels from each geometry. Figure 8.5 shows the shock velocity D, the post-shock pressure P_{PS}, and the post-shock temperature T_{PS}, as a function of time for eight examples of line and multi blasts from each geometry. The blast dynamics are calculated by selecting, by hand, the center of a line kernel or multi kernel (a particular y, z location) at inception and tracking the shock location and post-shock properties of this y, z location for 2 µs (or until another shock intersects this location). Blasts are selected that occur both on the walls and in the center of the domain. In general, no major difference in the resultant propagation characteristics are observed between the wall and central blasts.

Consistent between both geometries is that multi kernels (solid lines in Fig. 8.5) have higher velocities and more extreme states when compared to line kernels. The multi kernels yield blasts which propagate initially at upwards of 5 km/s (about 1.8 times the CJ speed) while the line kernels propagate around 3.5 km/s (about 1.3 times the CJ speed). Both decay to an underdriven wave after about 1.5 µs. Meanwhile, the multi blasts lead to more extreme post-shock pressures (up to 3 MPa) and temperatures (almost 4000 K), while the line kernels yield more modest conditions (1 MPa and 2500 K). We note that even the line kernel blasts contain states substantially more extreme than the ZND Von Neumann state (P_{VN} = 0.45 MPa, T_{VN} = 1667 K for this mixture).

Also plotted in Fig. 8.5a and b is the averaged velocity of blasts in the 2D simulation (averaged across over 50 blasts in the well-converged portion of the simulation). Interestingly, the propagation velocity of the 2D blasts is somewhat in between the multi and line blasts from 3D. 2D blasts are the result of two transverse waves intersecting, and so it may be expected that the propagation velocity would be more similar to the line blasts. The deviation between line blasts and 2D blasts is possibly explained by the stronger geometric confinement of the 2D blasts (*i.e.*, cylindrical blasts versus spherical blasts) [316].

Between the square channel and the round tube simulations, the most notable difference in the blast dynamics is the blast-to-blast variability. In the channel simulation, each line kernel and multi kernel exhibit notably consistent dynamics, as seen in Fig. 8.5a, c, e. This consistency is presumably because the highly regular structure leads to similar transverse wave strengths and post-shock unburnt gas pocket size among all line and multi blasts. Furthermore, all multi blasts are the result of exactly four blasts. As a result, the blast dynamics in the channel geometry can be classified as a bimodal distribution, depending on whether it is a multi blast or a line blast. In contrast, the round tube dynamics are more widely spread. The multi blasts still contain velocities and states more extreme than the line blasts, but a variety of manifestations of blasts exist for both categories. Generally, the multi blasts in the round tube are as strong or weaker than the multi blasts from the square channel, likely because they can be the result of three, four, or five blasts, while the line blasts are somewhat stronger to somewhat weaker than those from the square channel. From the limited sample size presented here, the blast dynamics in a round tube follow a uniform, but broad distribution, with a variety of blast strengths observed.

8.3.3 Bulk detonation velocity

The difference in blast dynamics manifests in differing bulk velocity characteristics between the channel and tube geometries. Bulk velocity is calculated by differentiating in time the furthest point forward in the x-direction of the shock wave for each simulation. The averaged propagation velocity $\overline{u}$, shown in lower-left corner of Fig. 8.6, between the two simulations is nearly identical, with propagation around 97% of the CJ speed. The magnitude of this propagation velocity is in good agreement with experimental measurements of detonations of the same mixture propagating in geometries larger than its characteristic cell size [287, 315]. Notably different between the simulations, however, is the magnitude of velocity fluctuations. The channel contains bulk velocity excursions nearly three times in magnitude compared with the tube (114 m/s versus 44 m/s). The more strongly overdriven waves, and more significantly, the temporal coupling of the overdriven waves, lead to the much stronger oscillations in the square channel as compared to the round tube. This difference in velocity behavior further shows that detonations in the square channel exhibit a highly regular, oscillating structure, while detonations in the tube geometry contains a variety of modes, temporally misaligned, which leads to the more stable velocity behavior.

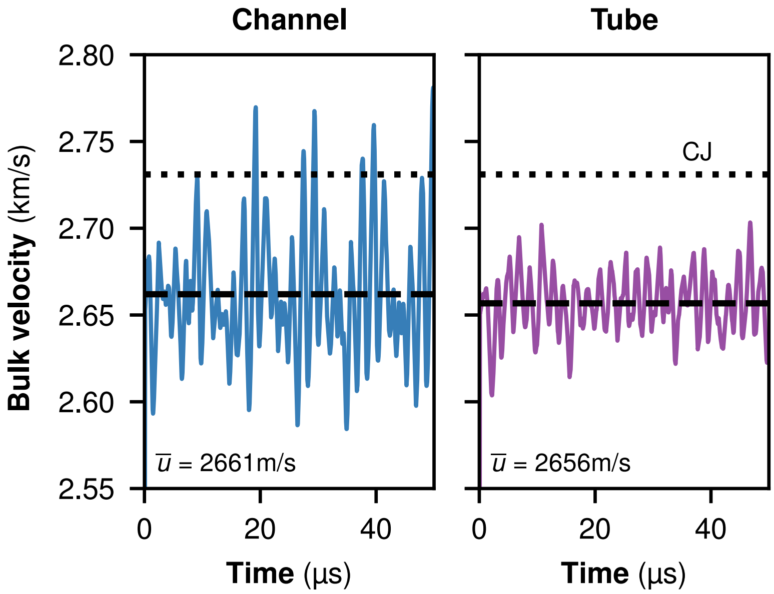

Figure 8.6: Bulk detonation velocities for the final 50 µs of the 10 µm grid resolution 3D square channel (left) and 3D circular tube (right) simulations. Dashed line shows averaged propagation velocity ($\overline{u}$) while dotted line shows CJ velocity.

8.3.4 Role of 3D confinement in detonation

Comparing cellular structure, blast dynamics, and bulk velocity of detonation in the square channel versus the round tube leads to a clearer picture of the role confinement plays on detonation propagation. Square confinement leads to a highly regular shock structure composed of square lattices (see Figs. 8.1, 8.4, S1). This regular structure leads to bimodal blast dynamics, depending on whether two or four shocks intersect to initiate a blast (*i.e.*, line versus multi kernels). The regularity of the structure leads to multi kernels which are both very strong and also temporally aligned with other multi kernels in the domain. The strong ignitions along with the highly regulating boundaries likely lead to the narrower detonation cells in the square channel (as compared to the round tube) and the temporal alignment leads to a highly oscillatory bulk velocity. Meanwhile, round boundaries do not lead to discernibly regular head-on structure, and analysis of blast dynamics show highly variable dynamics for both line and multi kernel blasts. From this perspective, the detonation propagation in square channels versus round tubes is substantially different. Moreover, the square channel propagation is the result of a strong coupling between perfectly smooth and straight boundaries and blast formation and propagation. In engineering situations where boundary irregularities and mixture inhomogeneities exist, this coupling may be disrupted and detonations in channels may more closely resemble those in round tubes.

8.3.5 Computational grid convergence

To ensure the numerical grid resolution used is sufficient to fulfill the aims of this work, we simulated detonation propagation in both 3D geometries at 40 µm, 20 µm, and 10 µm grid resolutions. Qualitatively, all three resolutions in the square channel exhibit the same highly regular propagation behavior described above while all three resolutions in the round tube show a similarly irregular behavior. Snapshots of head-on pressure pseudocolor plots for each geometry and resolution combination are shown in Fig. S1 of the Supplementary Material (SM), supporting this observation. Noted in Fig. S1, however, is that the different resolutions can yield differing quantities of shock structures within the domain. Notably, fewer shocks are observed in the 10 µm simulations (for both the square channel and round tube) as compared to the 20 µm and 40 µm simulations. The differences in number of shocks among resolutions translates directly to different detonation cell sizes. The side-wall soot foils for each simulation are shown in Fig. S2 of the SM, while the mean and one standard deviation of cell width and cell aspect ratio are shown in Fig. 8.7. The

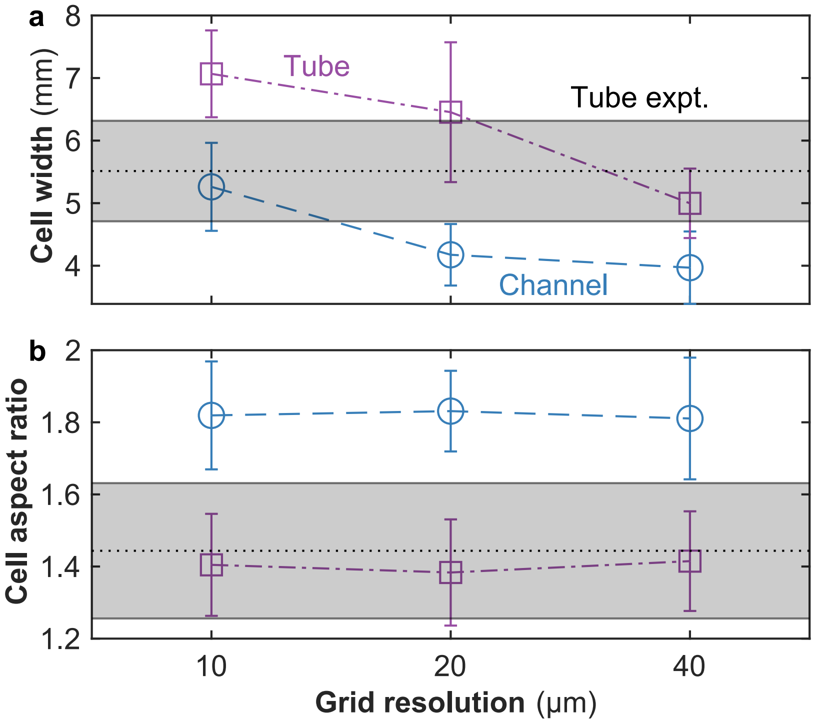

Figure 8.7: Cell width (**a**) and cell aspect ratio (**b**) as a function of numerical grid resolution for the round tube (purple squares) and the square channel (blue circles) simulations, and tube experiments (dotted black line and shaded bands). Error bars and shaded bands denote 1 standard deviation.

statistics are measured from 50 cells in the well-converged portion of each simulation. Also plotted in Fig. 8.7 are the mean and one-standard deviation of the cell width and cell aspect ratio from experiments in a 32 mm round tube [315] with an identical mixture. Clearly, the cell width is a function of grid resolution for both geometries, as shown in Fig. 8.7a, with finer resolutions yielding larger detonation cells (as also observed in [303]). At the finest resolution considered in the current work, the cell size may not have been fully converged, and so we treat the absolute values of quantities derived with some caution. The reasonable agreement in cell width between the tube simulation (7.1±0.7 mm for 10 μm resolution) and the tube experiment (5.5±0.8 mm) give confidence in the simulations, at least in terms of the purposes of this work: to derive mechanistic insight into the propagation characteristics of 3D detonations of the two geometries. To ensure convergence in the analyses of interest, analyses are repeated for all grid resolutions, including cell aspect ratio, blast propagation characteristics, and bulk velocity. As shown in Fig. 8.7b, cell aspect ratio is largely invariant across grid resolutions and in terms of aspect ratio an excellent agreement is observed between the tube simulation and tube experiment. Conclusions which result from analyses of other quantities of interest (blast propagation, shown in Fig. S3 and discussed in SM, and bulk velocity, shown in Fig. S4 and also discussed in SM) are also consistent across the grid resolutions tested, which indicate that the conclusions drawn in this work are not sensitive to grid resolution.

8.4 Conclusions

In this work, we performed detailed simulations of detonation propagation in a 3D square channel and a 3D round tube, along with a 2D channel, and compared the simulations with results from a tube experiment. By analyzing and comparing the cellular structure, blast dynamics, and bulk velocity, we conclude:

1. Three-dimensional detonation propagation consists of complexes of shock waves yielding line (two blasts intersecting) and multi (more than two blasts intersecting) kernels. The multi kernels contain substantially more extreme states, and lead to much faster local wave velocities, as compared to

the line kernels. These multi-dimensional features lead to more complex detonation dynamics as compared to 2D simulations.

2. Detonations in square tubes lead to a highly regular structure containing square lattices of shocks, while tubes lead to substantially more complex and distributed blasts.
3. Two-dimensional detonations exhibit blast characteristics which are in between the behaviors of the line kernel blasts and the multi kernel blasts, likely due to the difference in dimensional confinement of these blasts.
4. Spatial confinement plays a strong role in detonation propagation. This raises the question whether detonation cells and their sizes can be described as fundamental properties of an unburnt mixture without considering the impact of boundary conditions on their measurement and analysis.

These conclusions are found irrespective of the numerical grid resolution used.

Acknowledgments

The authors from Duisburg gratefully acknowledge the Gauss Centre for Supercomputing e.V. (www.gauss-centre.eu) for providing computing time on the GCS Supercomputer SUPERMUC-NG at Leibniz Supercomputing Centre (www.lrz.de), the financial support by DFG (KE 1751/8-1) and the computing time on magnitUDE (Universität Duisburg-Essen, through DFG INST 20876/209-1 FUGG, INST 20876/243-1). The authors from Stanford gratefully acknowledge funding from the Air Force Office of Scientific Research (FA9550-20-1-0398), the fellowships from the National Science Foundation (DGE-1656518) and Stanford University Vice Provost of Graduate Education to J. Crane.

Chapter 9
Summary and Outlook

9.1 Summary

The presented work investigates reactive supersonic flows using two-dimensional and three-dimensional simulations, specifically employing large eddy simulations (LES) with finite rate chemistry (FRC). To facilitate these investigations, the LES and direct numerical simulations (DNS) code PsiPhi, initially developed by Prof. Dr.-Ing. Andreas Kempf for simulating turbulent flames at low Mach numbers, was extended for compressible flows. The necessary modifications encompassed implementing an operator splitting approach to decouple temporal changes due to transport and reactive source terms, introducing a new density-based kernel for a single Runge-Kutta step, employing various approximate Riemann solvers based on the advection upstream splitting method (AUSM) to calculate convective fluxes, utilizing different high-order interpolation formulas, extending diffusive fluxes by incorporating the friction term for conserved energy, and employing characteristic boundary conditions with non-reflective properties. Additionally, a prototype for finite rate chemistry, originally developed by Fabian Proch, was expanded for simulating compressible flow. Further enhancements involved improving efficiency by implementing implicit and semi-implicit ordinary differential equation (ODE) solvers to handle the chemical source term, and incorporating subgrid models using a probability density function (PDF) model for temperature and a dynamic flame thickening (DTF) approach.

In the first study, a highly resolved three-dimensional LES on 2.2 billion cells was employed to investigate an experiment conducted by Meyer and Oppenheim [317] involving a stoichiometric hydrogen-oxygen mixture in a small rectangular shock tube. The remote ignition observed in the experiment was successfully replicated. The ignition delay time closely matched the experimental evidence, although there remains a significant uncertainty in the low-temperature range due to the kinetics model utilized. For analysis, numerous Lagrangian particles were randomly introduced into the domain at the beginning of the simulation. These particles were then integrated over time using the local flow velocity, while recording the experienced thermochemical state. Post-processing involved extracting the particles that were in close proximity to the ignition kernel at the time of ignition. Notably, these particles displayed a considerably higher temperature than those localized near the originally anticipated ignition location close to the end wall. To explain the observed higher temperature, a detailed analysis was conducted on the velocity field induced by reflected shock bifurcation. The analysis revealed that the bifurcation structure causes a displacement effect on the core flow, resulting in a Laval nozzle-like effect that accelerates the core flow significantly. This acceleration occurs first in a convergent section and subsequently in a divergent section, leading to the formation of a second normal shock with additional entropy production and correspondingly higher temperature. This premature ignition phenomenon has important implications as shock bifurcation affects real mixtures more frequently than mixtures diluted with argon. Failure to detect remote ignition can result in erroneous measurement of the ignition delay time, leading to inaccuracies in future kinetic models.

In the first study, the inlet boundary was assumed to have constant state variables. However, this assumption is highly simplifying and can deviate significantly from the actual values. The review criticized this assumption accordingly. Thus, the second study addressed this criticism by employing an inlet boundary condition that incorporates the development of a laminar boundary layer and its transition to a turbulent boundary layer. Outside the boundary layer, the state variables change according to Mirels' small perturbation theory [160]. To validate the approach, two-dimensional simulations and experiments conducted in Duisburg and Texas were compared, specifically examining pressure and temperature at the shock tube end wall for pure argon as well as mixtures of argon, carbon monoxide, and hydrogen. The experiments measured pressure end wall evolutions that follow a curve with an initial decline, followed by a monotonic pressure rise at low initial pressures. This differs from the commonly accepted assumption of a monotonic and linear pressure increase. The simulations demonstrated that this pressure curve can be attributed to an extended boundary layer transition. To match the experimental pressure and temperature histories, accurate estimation of the turbulent Reynolds transition number and boundary layer transition duration is crucial. The approach was further tested in the same study for shock tube experiments with hydrogen/oxygen mixtures diluted with argon [318], comparing cases with different Mach numbers of the incident shock. At high Mach numbers, ignition occurs directly at the shock tube end wall. As the Mach numbers decrease, the ignition delay time increases, and higher temperatures induced by the boundary layer far from the shock tube end lead to premature ignition upstream. While the ignition delay time differs from that in the experiments, the phenomenon of remote ignition was successfully reproduced. These results demonstrate that the proposed approach can effectively simulate shock tube experiments and represents a significant improvement over traditionally used Dirichlet boundary conditions.

The third study focused on the propagation of detonation waves in hydrogen/oxygen mixtures with and without ozone doping. Due to the demanding requirement of resolving the detonation structure on the numerical grid, two-dimensional simulations were employed, which correspond most closely to propagation in infinitely wide channels. Surprisingly, the agreement in detonation cell size between the simulations and experiments conducted in tubes was remarkably good. Additionally, the simulation successfully reproduced the effect of ozone, which leads to a decrease in cell size when added to the hydrogen-oxygen mixture in small amounts. The high temporal resolution data obtained from the simulation was employed to test a previously postulated hypothesis of cell size stabilization [319], which was confirmed. The hypothesis suggests that a small amount of fuel results in a weak detonation kernel with a relatively low propagation velocity of the overdriven shock wave front. This enhances the decoupling of the shock wave front and reaction zone, leading to a larger amount of fuel in the subsequent detonation kernel. The study also examined two different channel heights and the influence of viscous terms. Significantly, the inclusion of viscous fluxes, especially for the small channel height, revealed a notable velocity deficit. The formation of the boundary layer was identified as the dominant factor contributing to this observation. In contrast, the impact on the detonation cell structure was minimal.

The fourth study addressed the disparity in detonation dynamics and structure between three-dimensional and two-dimensional simulations. Due to the high computational cost, the majority of detonation simulations are still performed in 2D, which motivated this study. Three dimensional LES simulations were conducted for two distinct geometries: a square cross-section and a circular cross-section, both considering the hydrogen-oxygen mixture with ozone doping. To study the detonation front in terms of structure and dynamics, 3D fields with high temporal resolution were required, resulting in significant memory requirements. Consequently, new output routines were designed to reduce memory usage. The axial position of each point on the front was determined, and this information was sent to corresponding communicator root ranks, which collectively wrote 2D fields consisting of the x-coordinate, pressure, and temperature related to the wave front, significantly reducing memory requirements. This information enabled the reconstruction of soot foils along arbitrary surfaces. Furthermore, new message passing interface (MPI) communicators were created to facilitate writing reduced 3D fields, such as those from one-eighth of the domain. The results demonstrated highly organized detonation structures for the square cross-section, with transverse shock waves traveling parallel to the walls. In contrast, a chaotic and complex structure was observed for the circular cross-section. Therefore, the geometry of the confinement significantly influences the detonation structure. Moreover, 3D detonations exhibit different types of detonation kernels. In 2D simulations, detonation kernels form when two triple points collide. In 3D simulations, triple points exist along curves, and the collision of two curves leads to the formation of line kernels. Additionally, there are multi kernels where more than two blast waves intersect, resulting in more extreme conditions. The maximum pressures of detonation kernels in 2D lie between those encountered in line kernels and multi kernels in 3D, leading to a wider distribution of kernel states in 3D. Notably, the extracted cell sizes from the data were similar for both 2D and 3D simulations.

9.2 Outlook

The studies conducted in this thesis have successfully introduced a workflow for shock tube simulations. Several simulations have reproduced pressure evolutions at the shock-tube end wall and the occurrence of unwanted remote ignitions triggered by shock bifurcation or boundary layer-induced axial temperature distribution. The importance of accurately treating the inlet boundary, in addition to employing efficient and accurate solution algorithms, has been demonstrated.

One drawback of the current workflow is the requirement of a precursor simulation, which must have the same dimensions in the vertical and lateral directions as the main simulation. In this precursor simulation, the initial Riemann problem is calculated, and the incident shock wave can evolve naturally. At the end of the precursor simulation, the solution around the incident shock is stored and can be utilized in the main simulation to initialize the incident shock wave near the inlet. In contrast, if the incident shock is instead approximated by jump conditions, significant perturbations will arise, eventually interacting with the reflected shock. The workflow can be greatly simplified by fully modeling the fields behind the incident shock. In this case, the simulation starts precisely at the moment before the incident shock reaches the end wall. The boundary layer and core flow can be approximated using the same models employed at the inlet boundary, while artificial turbulence must be introduced using the turbulence generator within the turbulent part of the boundary layer. This would involve estimating the Reynolds stress tensor and an average representative length scale using numerical or experimental data for compressible boundary layers.

Another important aspect is the development of low-order models. For the sake of efficiency and convenience, the boundary layer modeling and calculation of non-uniformities have been performed within PsiPhi at the beginning of the simulation so far. However, in order to distribute the models, the Python programming language is much better suited. Hence, porting these models into Python code is desirable. In the long term, pressure predictions should be used as a boundary condition in 0D reactor simulations to predict phenomena such as remote ignition efficiently. Currently, the models can only predict pressure, temperature, and axial velocity behind the incident shock. However, for their application as a boundary condition in reactors, the approach would need to be extended to account for the evolution behind the reflected shock. The work of Rudinger [320] can be employed to describe the variation of variables behind the reflected shock.

Another workflow has been established to simulate the propagation of detonation waves. In this case, a relative coordinate system is used, which moves at the speed of the detonation wave. Consequently, Dirichlet boundary conditions are applied at the inlet, with the axial velocity component equaling the detonation wave speed, while a non-reflecting boundary condition is used at the outlet, where the flow might still be subsonic. This approach offers the advantage of computing only the detonation wave front and the key region behind it, enabling the use of a finer grid resolution. Since the detonation velocity can only be estimated a priori (due to the presence of boundary layer losses), the inflow velocity may need to be adjusted to ensure that the detonation wave is stationary on average. An improvement would be achieved by automating the determination of the detonation wave velocity and implementing a correction mechanism. Additionally, while the current research has focused on mixtures with an ordered cell structure, other fuels, like methane, exhibit a more chaotic and complex cell structure. The proposed cell stabilization mechanism should be investigated for such mixtures as well.

In simulations of detonation waves, a conventional flame front does not exist. As a result, dynamic flame thickening methods cannot be employed for subgrid closure. Instead, assumed PDF methods, such as the tophat PDF for temperature, are more suitable and have already been utilized. In the context of Reynolds-averaged Navier-Stokes (RANS), a multivariate beta PDF for mass fractions has been employed Gerlinger [70]. However, before applying these methods in large eddy simulations (LES), their suitability needs to be verified through a posteriori analyses.

Furthermore, efficiency improvements are always desired to enable larger or more complex simulations. The implementation of CVODE has already yielded efficiency gains over explicit methods with sub-stepping for integrating the chemical source term. Semi-implicit methods with error control and adaptive step size offer the potential for additional performance improvements. Consequently, a prototype for a proprietary ODE solver suite in PsiPhi has been implemented, which currently includes the implicit Euler method, explicit Runge-Kutta methods with error control and step-size adjustment, and the classical Rosenbrock integration method. The interfaces are standardized and can also be used for integrating other stiff terms. The Jacobian matrix required for implicit and semi-implicit methods is estimated using finite differences, but alternatives for a more efficient approximation of the Jacobian matrix have been employed [92]).

Hybrid convective methods could further improve the simulation quality. Riemann solvers are known for their stability but also high numerical dissipation, which impacts the generation and decay of turbulence. Conversely, purely central differencing schemes exhibit low numerical dissipation at the expense of stability. In density-based solvers, artificial dissipation approaches must be employed along with central schemes to eliminate high-frequency components. To address this, central differencing schemes of higher order and suitable filters [100, 101] have already been implemented in PsiPhi. Alternatively, matrix artificial dissipation methods can be employed [102]. A promising approach could involve primarily applying central differencing schemes and artificial dissipation, except in a few cells near discontinuities where approximate Riemann solvers are used. For this purpose, sensors already exist that reliably detect compression shocks [321].

Appendix A
Additional publications

A.1 Impact of shock-tube facility-dependent effects on incident- and reflected-shock conditions over a wide range of pressures and Mach numbers

Authors: D. Nativel, S. P. Cooper, J. T. Lipkowicz, M. Fikri, E. L. Petersen, C. Schulz
This paper was previously published in 'Combustion and Flame, 217, D. Nativel, S. P. Cooper, J. T. Lipkowicz, M. Fikri, E. L. Petersen and C. Schulz, Impact of shock-tube facility-dependent effects on incident- and reflected-shock conditions over a wide range of pressures and Mach numbers, 200-211, Copyright ©Elsevier (2020)' [322] and the abstract is reprinted with permission from Elsevier. The author J. T. Lipkowicz contributed by corrections, discussions, proof reading, and by providing a numerical tool that predicts boundary layer growth rates of both laminar and turbulent boundary layers.

Abstract

In real shock tubes, deviations from the ideal gas-dynamic behavior can affect experiments and complicate data analysis and interpretation. These non-ideal effects depend on the shock-tube geometry and therefore, results (e.g., ignition delay times) may vary between different experimental facilities. To clarify the influence of geometry and operating procedures, these effects were investigated in four geometrically different shock tubes located in two laboratories, Texas A&M University and the University of Duisburg-Essen. Incident shock-wave attenuation and pressure rise (dp*/dt) were measured behind reflected shock waves over a 2.1–4.1 Mach number and a 0.1–3.0 MPa post-reflected-shock pressure range. A strong influence of the Mach number on dp*/dt was observed for all facilities and conditions, whereas only a slight influence was found for shock-wave attenuation. Both dp*/dt and attenuation were higher by about a factor of two for the shock tubes with approximately half the inner diameter (8.0 vs. 16.2 cm). These findings are analyzed through correlations with initial pressure, inner diameter, Mach number, and specific heat ratio. The implication of non-ideal effects on experiments with reactive mixtures and related combustion experiments is discussed. Extreme conditions of dp*/dt were derived from the correlations and used to understand the effects of an equivalent dT*/dt on simulated ignition delay times of two reactive systems (CH4/air and C7H16/air). It was found that smaller shock-tube diameters with respectively larger dp*/dt show shorter ignition delay times (especially at temperatures below 1000 K for the C7H16/air case). Therefore, the geometry constraints must be considered in simulations through dp*/dt inputs in the chemical kinetics simulation for the extreme cases to account for non-ideal effects.

A.2 Geometric modeling and analysis of detonation cellular stability

Authors: J. Crane, X. Shi, J. T. Lipkowicz, A. M. Kempf, H. Wang
This paper was previously published in 'Proceedings of the Combustion Institute, 38(3), J. Crane, X. Shi, J. T. Lipkowicz, A. M. Kempf and H. Wang, Geometric modeling and analysis of detonation cellular stability, 3585-3593, Copyright ©Elsevier (2021)' [241] and the abstract is reprinted with permission from Elsevier. The author J. T. Lipkowicz contributed by providing data from 2D numerical simulations of detonation propagation that helped in the model development. The author J. T. Lipkowicz also contributed by corrections, discussions and proof reading.

Abstract

A geometric model with a low computational complexity capable of simulating detonation behavior in physical systems is proposed. In support of the geometric model development, a series of cylindrical 1D simulations with a variable size initiation kernel are performed in hydrogen-oxygen mixtures. From these 1D simulations a detonation cell stabilization mechanism is identified. The stabilization mechanism is predicated on the size of the gap between the pressure and temperature fronts at the point where the average pressure front velocity along one cell length is equal to the CJ velocity. This gap, in a multidimensional detonation, is the ignition kernel of a subsequent blast, and dictates the formation of the subsequent cell. Serial analysis of blasts in this context leads to a unique stable blast kernel size for any mixture, which, within the uncertainty of the initial kernel state, can predict the experimental cell length for mixtures considered in this study. Using a tabulation of the 1D simulations as an input, a formulation and sample results of the geometric model are shown. The geometric model can reproduce both qualitative and quantitative features of experimental detonation cellular structure.

A.3 An experimental/numerical investigation of non-reacting turbulent flow in a piloted premixed Bunsen burner

Authors: J. Pareja, J. T. Lipkowicz, E. Inanc, C. D. Carter, A. M. Kempf, I. Boxx
This paper was previously published in 'Experiments in Fluids, 63, J. Pareja, J. T. Lipkowicz, E. Inanc, C. D. Carter, A. M. Kempf and I. Boxx, An experimental/numerical investigation of non-reacting turbulent flow in a piloted premixed Bunsen burner, Copyright ©Springer (2022)' [323] and the abstract is reprinted with permission from Springer. The author J. T. Lipkowicz contributed by code development, running all non-reactive simulations and by post-processing tasks for statistics. The author J. T. Lipkowicz also contributed by corrections, discussions and proof reading.

Abstract

In this paper, an experimental study of the non-reacting turbulent flow field characteristics of a piloted premixed Bunsen burner designed for operational at elevated pressure conditions is presented. The generated turbulent flow fields were experimentally investigated at atmospheric and elevated pressure by means of high-speed particle image velocimetry (PIV). The in-nozzle flow through the burner was computed using large-eddy simulation (LES), and the turbulent flow field predicted at the burner exit was compared against the experimental results. The findings show that the burner yields a reasonably homogeneous, nearly isotropic turbulence at the nozzle exit with highly reproducible boundary conditions that can be well predicted by numerical simulations. Similar levels of turbulence intensities and turbulent length scales were obtained at varied pressures and bulk velocities with turbulent Reynolds numbers up to 5300. This work demonstrates the burner's potential for the study of premixed flames subject to intermediate and extreme turbulence at the elevated pressure conditions found in gas turbine combustors.

A.4 Numerical Analysis of a Turbulent Pulverized Coal Flame Using a Flamelet/Progress Variable Approach and Modeling Experimental Artifacts

Authors: D. Meller, J. T. Lipkowicz, M. Rieth, O. Stein, A. Kronenburg, C. Hasse, A. M. Kempf
This paper was previously published in 'Energy Fuels, 35(9), D. Meller, J. T. Lipkowicz, M. Rieth, O. Stein, A. Kronenburg, C. Hasse and A. M. Kempf, Numerical Analysis of a Turbulent Pulverized Coal Flame Using a Flamelet/Progress Variable Approach and Modeling Experimental Artifacts, 7133-7143, Copyright ©ACS Publications (2021)' [324] and the abstract is reprinted with permission from ACS Publications. The author J. T. Lipkowicz contributed by support in the code development, by corrections, discussions and proof reading.

Abstract

A coaxial burner with a hydrogen-supported pulverized coal flame, operated by the Central Research Institute of Electric Power Industry (CRIEPI, Japan), is investigated numerically. The flame is modeled using massively parallel large eddy simulation (LES). A flamelet/progress variable (FPV) approach is used for modeling the complex multiphase flow of the laboratory coal flame. A four-dimensional tabulation method based on non-premixed flamelets is introduced, which uses two mixture fractions for the hydrogen pilot and coal volatiles, respectively, as well as the absolute enthalpy and the reaction progress to parametrize the thermochemical space. Simulations are compared to the experiments in terms of the temperature, gas-phase velocities (with and without consideration of buoyancy), and gas compositions along the centerline and in the radial direction at different heights. The effect of the suction probe on the scalar field measurements is tested by simulating this probing, observing relative changes up to 50% in various quantities and locations. By consideration of these probe effects, the agreement between the experiment and simulation can be improved significantly; at the same time, the simulation also provides the unperturbed scalar fields, without probing effects. The new flamelet model gives a robust and cost-effective prediction of the investigated laboratory flame, provided that the probing effects are considered.

A.5 A conservative Eulerian-Lagrangian decomposition principle for the solution of multi-scale flow problems at high Schmidt or Prandtl numbers

Authors: M. Leer, M. W. A. Pettit, J. T. Lipkowicz, P. Domingo, L. Vervisch, A. M. Kempf
This paper was previously published in 'Journal of Computational Physics, 464, M. Leer, M. W. A. Pettit, J. T. Lipkowicz, P. Domingo, L. Vervisch and A. M. Kempf, A conservative Eulerian-Lagrangian decomposition principle for the solution of multi-scale flow problems at high Schmidt or Prandtl numbers, Copyright ©Elsevier (2022)' [325] and the abstract is reprinted with permission from Elsevier. The author J. T. Lipkowicz contributed by support in the code development, by corrections, discussions and proof reading.

Abstract

The simulation of turbulent flow that involves scalar transport at high Schmidt or Prandtl numbers is a major challenge. Enhanced Schmidt and Prandtl numbers demand an excessive increase in numerical resolution. Otherwise, the accuracy of transport would suffer substantially through unresolved information and numerical diffusion. With the aim of providing an efficient alternative for such applications, this paper presents a simulation method that is based on a novel Eulerian-Lagrangian decomposition principle (ELD) of the transported quantity. Low-pass filtering of the initial scalar quantity field separates it into a smooth low-frequency component and a fine-structured high-frequency component. The low-frequency component is represented and transported according to the Eulerian description by applying the Finite Volume Method (FVM) with a numerical resolution according to the Kolmogorov scale. The high-frequency component is translated into the Lagrangian description by the formation of particles, which are transported in parallel. By exchanging information between the two components, a re-initialisation mechanism ensures that the frequency-based decomposition is maintained throughout the simulation. Such ELD approach combines the efficiency of the FVM with the numerical stability of Lagrangian particles. As a result of the frequency-separation, the latter are by principle limited to zones of small scales and thus effectively complement the FVM. Furthermore, the particle information allows details of the scalar quantity field to be reconstructed that extend into the sub-grid level. By using a mixing layer setup, the proposed method is tested for a range of Schmidt numbers, and the numerical costs are considered and discussed.

A.6 Detailed simulations of the DLR auto-igniting pulsed jet experiment

Authors: E. Inanc, J. T. Lipkowicz, A. M. Kempf

This paper was previously published in ‘Fuel, 284, E. Inanc, J. T. Lipkowicz and A. M. Kempf, Detailed simulations of the DLR auto-igniting pulsed jet experiment, Copyright ©Elsevier (2022)’ [326] and the abstract is reprinted with permission from Elsevier. The author J. T. Lipkowicz contributed by support in the code development, by corrections, discussions and proof reading.

Abstract

Numerical simulations of an auto-igniting pulsed jet in a vitiated co-flow experiment by DLR (German Aerospace Center) are conducted by highly-resolved large-eddy simulations using direct chemistry with an augmented reduced mechanism. The experiments consist of two operation modes: continuous injection used for code-verification and pulsed injection utilized for fundamental investigation of auto-ignition dynamics. Initially, reference one-dimensional self-igniting counter-flow flames are investigated. Then, a grid convergence study has been performed. It is shown that even a coarser grid would be sufficient to describe the ignition chemistry since the ignition kernel appears at low velocities and fuel-lean conditions in zones of low scalar dissipation rates. For the statistically steady jet, numerical predictions are in a very good agreement with the experiments, giving confidence in the applied models. For the pulsed jet, all of the predicted ignition delay times and locations are in the range of the experimental observations. Time-resolved statistics reveal that thermochemical properties of the gas in a pulsed jet achieve states that are impossible to reproduce in laminar conditions. For further analysis, hydroxyl and formaldehyde are chosen as a marker for the established flame and for the ignition, respectively. In laminar conditions, these two species are perfectly correlated. However, the unsteady dynamics of the pulsed jet invalidates the correlation between the minor species chemistry prior to ignition. This yields the discrepancy in the auto-ignition delay time and the location of the ignition kernel between different pulses, as the thermochemical state needed for the ignition occurs in a random manner.

Bibliography

[1] C. Hirsch. *Numerical computation of internal and external flows: The fundamentals of computational fluid dynamics*. Elsevier, 2007.

[2] J.I. Steinfeld. Atmospheric chemistry and physics: from air pollution to climate change. *Environment: Science and Policy for Sustainable Development*, 40(7):26–26, 1998.

[3] V. Masson-Delmotte, H. O. Pörtner P. Zhai, D. Roberts, P.R. Shukla J. Skea, A. Pirani, W. Moufouma-Okia, C. Péan, R. Pidcock, S. Connors, J. B. R. Matthews, Y. Chen, X.Zhou, M. I. Gomis, E. Lonnoy, T. Maycock, M. Tignor, and T. Waterfield. An ipcc special report on the impactsof global warming of 1.5°c above pre-industrial levels and related global greenhouse gas emissionpathways, in the context of strengthening the global response to the threat of climate change, sustainabledevelopment, and efforts to eradicate poverty. In *Global warming of 1.5°C*. Intergovernmental Panel on Climate Change, 2018.

[4] G. P. Smith, D. M. Golden, M. Frenklach, N. W. Moriarty, B. Eiteneer, M. Goldenberg, C. T. Bowman, R. K. Hanson, S. Song, W. C. Gardiner, V. V. Lissianski, and Z. Qin. Gri-mech 3.0, 2023. URL `http://www.me.berkeley.edu/gri_mech/`.

[5] M. Chaos and F.L. Dryer. Chemical-kinetic modeling of ignition delay: Considerations in interpreting shock tube data. *Int. J. Chem. Kinet.*, 42(3):143–150, 2010. doi: 10.1002/kin.20471. URL `https://doi.org/10.1002%2Fkin.20471`.

[6] J. T. Lipkowicz, I. Wlokas, and A. M. Kempf. Analysis of mild ignition in a shock tube using a highly resolved 3d-les and high-order shock-capturing schemes. *Shock Waves*, 29(4):511–521, 2019.

[7] J. T. Lipkowicz, D. Nativel, S. Cooper, I. Wlokas, M. Fikri, E. Petersen, C. Schulz, and A. M. Kempf. Numerical investigation of remote ignition in shock tubes. *Flow Turbul. Combust.*, 106: 471–498, 2021.

[8] J. Crane, J. T. Lipkowicz, X. Shi, I. Wlokas, A. M. Kempf, and H. Wang. Three-dimensional detonation structure and its response to confinement. *Proc. Combust. Inst.*, 2022.

[9] T. J. Poinsot and D. Veynante. *Theoretical and numerical combustion*. RT Edwards, Inc., 2005.

[10] K.K. Kuo. *Principles of Combustion*. John Wiley & Sons, 2005.

[11] R. J. Kee, M. E. Coltrin, and P. Glarborg. *Chemically reacting flow: theory and practice*. John Wiley & Sons, 2005.

[12] D.G. Goodwin, R.L. Speth, H.K. Moffat, and B.W. Weber. Cantera: An object-oriented software toolkit for chemical kinetics, thermodynamics, and transport processes. `https://www.cantera.org`, 2018. Version 2.4.0.

[13] R.J. Kee, F.M. Rupley, E. Meeks, and J.A. Miller. Chemkin-iii: A fortran chemical kinetics package for the analysis of gas-phase chemical and plasma kinetics. Technical report, Sandia National Labs., Livermore, CA (United States), 1996.

[14] F.A. Lindemann. Discussion on “the radiation theory of chemical action”. *Trans. Faraday Soc.*, 1922.

[15] R.G. Gilbert, K. Luther, and J. Troe. Theory of thermal unimolecular reactions in the fall-off range. ii. weak collision rate constants. *Berichte der Bunsengesellschaft für physikalische Chemie*, 87(2): 169–177, 1983.

[16] P.H. Stewart, C.W. Larson, and D.M. Golden. Pressure and temperature dependence of reactions proceeding via a bound complex. 2. application to 2ch3→ c2h5+ h. *Combust. Flame*, 75(1):25–31, 1989.

[17] C.L.M.H. Navier. Mémoire sur les lois du mouvement des fluides. *Mémoires de l'Académie Royale des Sciences de l'Institut de France*, 6(1823):389–440, 1823.

[18] G.G. Stokes. On the theories of the internal friction of fluids in motion, and of the equilibrium and motion of elastic solids. *Trans. Cambridge Philos. Soc.*, 8, 1880.

[19] R.B. Bird, W.E. Stewart, and E.N. Lightfoot. *Transport phenomena*, volume 1. John Wiley & Sons, 2006.

[20] C. R. Wilke. A viscosity equation for gas mixtures. *J. Chem. Phys.*, 18(4):517–519, 1950.

[21] W. Sutherland. The viscosity of gases and molecular force. *Lond. Edinb. Dubl. Phil. Mag.*, 36 (223):507–531, 1893.

[22] S. Mathur, P.K. Tondon, and S.C. Saxena. Thermal conductivity of binary, ternary and quaternary mixtures of rare gases. *Mol. Phys.*, 12(6):569–579, 1967.

[23] K.K. Kuo and R. Acharya. *Applications of turbulent and multiphase combustion*. John Wiley & Sons, 2012.

[24] R. Friedman. Kinetics of the combustion wave. *J. Am. Rocket Soc.*, 23(6):349–354, 1953.

[25] S. Browne, J. Ziegler, and J.E. Shepherd. Numerical solution methods for shock and detonation jump conditions. *GALCIT report FM2006*, 6:90, 2008.

[26] F.A. Williams. *Combustion Theory*. CRC Press, 2018.

[27] W.H. Press, S.A. Teukolsky, W.T. Vetterling, and B.P. Flannery. *Numerical recipes 3rd edition: The art of scientific computing*. Cambridge University Press, 2007.

[28] D.L. Chapman. Vi. on the rate of explosion in gases. *The London, Edinburgh, and Dublin Philosophical Magazine and Journal of Science*, 47(284):90–104, 1899.

[29] W. Fickett and W.C. Davis. Detonation university of california press. *Berkeley, CA*, 17, 1979.

[30] N. Peters. *Turbulent Combustion*. Cambridge Monographs on Mechanics. Cambridge University Press, 2000. doi: 10.1017/CBO9780511612701.

[31] S.B. Pope. *Turbulent Flows*. Cambridge University Press, 2000. doi: 10.1017/CBO9780511840531.

[32] O. Reynolds. On the dynamical theory of incompressible viscous fluids and the determination of the criterion. *Philos. Trans. R. Soc. London, Ser. A*, 4(186):123–164, 1895.

[33] L.F. Richardson. *Weather prediction by numerical process*. Cambridge University Press, 2007.

[34] H. Tennekes and J.L. Lumley. *A first course in turbulence*. MIT press, 2018.

[35] G.I. Taylor. The transport of vorticity and heat through fluids in turbulent motion. *Proc. R. Soc. London, Ser. A*, 135(828):685–702, 1932.

[36] A.N. Kolmogorov. The local structure of turbulence in incompressible viscous fluid for very large reynolds numbers. *P Roy. Soc. A-Math. Phy.*, 434(1890):9–13, 1991.

[37] M. Rieth, F. Proch, M. Rabaçal, B.M. Franchetti, F. Cavallo Marincola, and A.M. Kempf. Flamelet les of a semi-industrial pulverized coal furnace. *Combust. Flame*, 173:39–56, 2016. ISSN 0010-2180. doi: https://doi.org/10.1016/j.combustflame.2016.07.013. URL `https://www.sciencedirect.com/science/article/pii/S0010218016301730`.

[38] T. Nguyen, P. Janas, T. Lucchini, G. D'Errico, S. Kaiser, and A.M. Kempf. Les of flow processes in an si engine using two approaches: Openfoam and psiphi. Technical report, SAE, 2014.

[39] P. Gruhlke, C. Beck, B. Janus, and A.M. Kempf. Les analysis of co emissions from a high pressure siemens gas turbine prototype combustor at part load. *Energies*, 13(21):5751, 2020.

[40] A. Favre. Turbulence: Space-time statistical properties and behavior in supersonic flows. *Phys. Fluids*, 26(10):2851–2863, 1983.

[41] A. Leonard. Energy cascade in large-eddy simulations of turbulent fluid flows. In *Advances in geophysics*, volume 18, pages 237–248. Elsevier, 1975.

[42] P. Sagaut. *Large eddy simulation for incompressible flows: an introduction*. Springer Science & Business Media, 2006.

[43] T. Dubois, J.A. Domaradzki, and A. Honein. The subgrid-scale estimation model applied to large eddy simulations of compressible turbulence. *Phys. Fluids*, 14(5):1781–1801, 2002.

[44] U. Piomelli. Large-eddy simulation: achievements and challenges. *Prog. Aerosp. Sci.*, 35(4):335–362, 1999.

[45] B. Kosović, D.I. Pullin, and R. Samtaney. Subgrid-scale modeling for large-eddy simulations of compressible turbulence. *Phys. Fluids*, 14(4):1511–1522, 2002.

[46] S. Ragab, S.-C. Sheen, and M. Sreedhar. An investigation of finite-difference methods for large-eddy simulation of a mixing layer. In *30th Aerospace Sciences Meeting and Exhibit*, page 554, 1992.

[47] B. Vreman, B. Geurts, and H. Kuerten. A priori tests of large eddy simulation of the compressible plane mixing layer. *J. Eng. Math.*, 29(4):299–327, 1995.

[48] B. Vreman. *Direct and large-eddy simulation of the compressible turbulent mixing layer*. Universiteit Twente, 1995.

[49] M.P. Martín, U. Piomelli, and G.V. Candler. Subgrid-scale models for compressible large-eddy simulations. *Theor. Comput. Fluid Dyn.*, 13(5):361–376, 2000.

[50] A. Yoshizawa. Statistical theory for compressible turbulent shear flows, with the application to subgrid modeling. *Phys. Fluids*, 29(7):2152–2164, 1986.

[51] C.G. Speziale G. Charles, G. Erlebacher, T.A. Zang, and M.Y. Hussaini. The subgrid-scale modeling of compressible turbulence. *Phys. Fluids*, 31(4):940–942, 1988.

[52] G. Erlebacher, M.Y. Hussaini, C.G. Speziale, and T.A. Zang. Toward the large-eddy simulation of compressible turbulent flows. *J. Fluid Mech.*, 238:155–185, 1992.

[53] D. Knight, G. Zhou, N. Okong'o, and V. Shukla. Compressible large eddy simulation using unstructured grids. In *AIAA*, page 535, 1998.

[54] J. Smagorinsky. General circulation experiments with the primitive equations: I. the basic experiment. *Mon. Weather Rev.*, 91(3):99–164, 1963.

[55] F. Nicoud, H.B. Toda, O. Cabrit, S. Bose, and J. Lee. Using singular values to build a subgrid-scale model for large eddy simulations. *Phys. Fluids*, 23(8):085106, 2011.

[56] F. Nicoud and F. Ducros. Subgrid-scale stress modelling based on the square of the velocity gradient tensor. *Flow, turbulence and Combustion*, 62(3):183–200, 1999.

[57] A.W. Vreman. An eddy-viscosity subgrid-scale model for turbulent shear flow: Algebraic theory and applications. *Phys. Fluids*, 16(10):3670–3681, 2004.

[58] M. Rieth, F. Proch, O.T. Stein, M.W.A. Pettit, and A.M. Kempf. Comparison of the sigma and smagorinsky les models for grid generated turbulence and a channel flow. *Comput. Fluids*, 99: 172–181, 2014.

[59] M. Germano, U. Piomelli, P. Moin, and W.H. Cabot. A dynamic subgrid-scale eddy viscosity model. *Phys. Fluids A-Fluid*, 3(7):1760–1765, 1991.

[60] P. Moin, K. Squires, W. Cabot, and S. Lee. A dynamic subgrid-scale model for compressible turbulence and scalar transport. *Phys. Fluids A-Fluid Dynamics*, 3(11):2746–2757, 1991.

[61] E.T. Spyropoulos and G.A. Blaisdell. Evaluation of the dynamic model for simulations of compressible decaying isotropic turbulence. *AIAA*, 34(5):990–998, 1996.

[62] D.K. Lilly. A proposed modification of the germano subgrid-scale closure method. *Phys. Fluids A*, 4(3):633–635, 1992.

[63] R. Stoll and F. Porté-Agel. Dynamic subgrid-scale models for momentum and scalar fluxes in large-eddy simulations of neutrally stratified atmospheric boundary layers over heterogeneous terrain. *Water Resour. Res.*, 42(1), 2006.

[64] C. Fureby. Comparison of flamelet and finite rate chemistry les for premixed turbulent combustion. In *AIAA*, page 1413, 2007.

[65] C. Duwig, K.-J. Nogenmyr, C.-K. Chan, and M.J. Dunn. Large eddy simulations of a piloted lean premix jet flame using finite-rate chemistry. *Combust. Theor. Model.*, 15(4):537–568, 2011.

[66] P. Givi. Model-free simulations of turbulent reactive flows. *Prog. Energy Combust. Sci.*, 15(1): 1–107, 1989.

[67] S.B. Pope. Computations of turbulent combustion: progress and challenges. In *Symp. (Int.) Combust.*, volume 23, pages 591–612. Elsevier, 1991.

[68] S.B. Pope. A monte carlo method for the pdf equations of turbulent reactive flow. *Combust. Sci. Technol.*, 1981.

[69] L. Valino. A field monte carlo formulation for calculating the probability density function of a single scalar in a turbulent flow. *Flow Turbul. Combust.*, 60(2):157–172, 1998.

[70] P. Gerlinger. Investigation of an assumed pdf approach for finite-rate chemistry. *Combust. Sci. Technol.*, 175(5):841–872, 2003.

[71] S.S. Girimaji. Assumed β-pdf model for turbulent mixing: Validation and extension to multiple scalar mixing. *Combust. Sci. Technol.*, 78(4-6):177–196, 1991.

[72] H. Wang, N. Qin, M. Sun, H. Wu, and Z. Wang. A hybrid les (large eddy simulation)/assumed sub-grid pdf (probability density function) model for supersonic turbulent combustion. *Sci. China Technol. Sci.*, 54(10):2694–2707, 2011.

[73] R.A. Baurle, G.A. Alexopoulos, and H.A. Hassan. Assumed joint probability density function approach for supersonic turbulent combustion. *J. Propul. Power*, 10(4):473–484, 1994.

[74] A.W. Cook and J.J. Riley. A subgrid model for equilibrium chemistry in turbulent flows. *Phys. Fluids*, 6(8):2868–2870, 1994.

[75] N. Branley and W.P. Jones. Large eddy simulation of a turbulent non-premixed flame. *Combust. Flame*, 127(1-2):1914–1934, 2001.

[76] J. Floyd, A.M. Kempf, A. Kronenburg, and R.H. Ram. A simple model for the filtered density function for passive scalar combustion les. *Combust. Theor. Model.*, 13(4):559–588, 2009.

[77] T.D. Butler and P.J. O'Rourke. A numerical method for two dimensional unsteady reacting flows. In *Symposium (international) on combustion*, volume 16, pages 1503–1515. Elsevier, 1977.

[78] H.G. Weller, G. Tabor, A.D. Gosman, and C. Fureby. Application of a flame-wrinkling les combustion model to a turbulent mixing layer. In *Symp. (Int.) Combust.*, volume 27, pages 899–907. Elsevier, 1998.

[79] C. Fureby. A fractal flame-wrinkling large eddy simulation model for premixed turbulent combustion. *Proc. Combust. Inst.*, 30(1):593–601, 2005.

[80] O. Colin, F. Ducros, D. Veynante, and T. Poinsot. A thickened flame model for large eddy simulations of turbulent premixed combustion. *Phys. Fluids*, 12(7):1843–1863, 2000.

[81] F. Charlette, C. Meneveau, and D. Veynante. A power-law flame wrinkling model for les of premixed turbulent combustion part i: non-dynamic formulation and initial tests. *Combust. Flame*, 131(1-2):159–180, 2002.

[82] E.R. Hawkes, O. Chatakonda, H. Kolla, A.R. Kerstein, and J.H. Chen. A petascale direct numerical simulation study of the modelling of flame wrinkling for large-eddy simulations in intense turbulence. *Combust. Flame*, 159(8):2690–2703, 2012.

[83] N. Chakraborty and S. Cant. Unsteady effects of strain rate and curvature on turbulent premixed flames in an inflow–outflow configuration. *Combust. Flame*, 137(1-2):129–147, 2004.

[84] G. Wang, M. Boileau, and D. Veynante. Implementation of a dynamic thickened flame model for large eddy simulations of turbulent premixed combustion. *Combust. Flame*, 158(11):2199–2213, 2011.

[85] F. Charlette, C. Meneveau, and D. Veynante. A power-law flame wrinkling model for les of premixed turbulent combustion part ii: dynamic formulation. *Combust. Flame*, 131(1-2):181–197, 2002.

[86] L. Durand and W. Polifke. Implementation of the thickened flame model for large eddy simulation of turbulent premixed combustion in a commercial solver. In *Turbo Expo: Power for Land, Sea, and Air*, volume 47918, pages 869–878, 2007.

[87] J.-P. Legier, T. Poinsot, and D. Veynante. Dynamically thickened flame les model for premixed and non-premixed turbulent combustion. In *Proceedings of the Summer Program 2000*, volume 12, pages 157–168. Citeseer, 2000.

[88] J.H. Ferziger, Milovan M. Perić, and R.L. Street. *Computational methods for fluid dynamics*, volume 3. Springer, 2002.

[89] R. Courant, K. Friedrichs, and H. Lewy. Über die partiellen differenzengleichungen der mathematischen physik. *Mathematische Annalen*, 100(1):32–74, 1928.

[90] E. Anderson, Z. Bai, C. Bischof, L.S. Blackford, J. Demmel, J. Dongarra, J. Du Croz, A. Greenbaum, S. Hammarling, and A. McKenney. *LAPACK users' guide*. SIAM, 1999.

[91] G. Strang. On the construction and comparison of difference schemes. *SIAM J. Numer. Anal.*, 5(3): 506–517, sep 1968. doi: 10.1137/0705041. URL `https://doi.org/10.1137%2F0705041`.

[92] H. Wu, P.C. Ma, and M. Ihme. Efficient time stepping for reactive turbulent simulations with stiff chemistry. In *2018 AIAA Aerospace Sciences Meeting*. American Institute of Aeronautics and Astronautics, jan 2018. doi: 10.2514/6.2018-1672. URL `https://doi.org/10.2514%2F6.2018-1672`.

[93] D.J. Gardner, D.R. Reynolds, C.S. Woodward, and C.J. Balos. Enabling new flexibility in the SUNDIALS suite of nonlinear and differential/algebraic equation solvers. *ACM Transactions on Mathematical Software (TOMS)*, 2022. doi: 10.1145/3539801.

[94] A.C. Hindmarsh, P.N. Brown, K.E. Grant, S.L. Lee, R. Serban, D.E. Shumaker, and C.S. Woodward. SUNDIALS: Suite of nonlinear and differential/algebraic equation solvers. *ACM Trans. Math. Software*, 31(3):363–396, 2005. doi: 10.1145/1089014.1089020.

[95] C.W. Gear. The automatic integration of ordinary differential equations. *Communications of the ACM*, 14(3):176–179, mar 1971. doi: 10.1145/362566.362571. URL `https://doi.org/10.1145%2F362566.362571`.

[96] L. Liang, C. Jung, S.-C. Kong, and R.D. Reitz. Development of a semi-implicit solver for detailed chemistry in i.c. engine simulations. In *ASME 2005 Internal Combustion Engine Division Spring Technical Conference*. ASMEDC, jan 2005. doi: 10.1115/ices2005-1005. URL `https://doi.org/10.1115%2Fices2005-1005`.

[97] V.R. Katta and W.M. Roquemore. Calculation of multidimensional flames using large chemical kinetics. *AIAA Journal*, 46(7):1640–1650, jul 2008. doi: 10.2514/1.33131. URL `https://doi.org/10.2514%2F1.33131`.

[98] S. Yang, V. Yang, W. Sun, S. Nagaraja, W. Sun, Y.J., and X. Gou. Parallel on-the-fly adaptive kinetics for non-equilibrium plasma discharges of c2h4/o2/ar mixture. In *54th AIAA Aerospace Sciences Meeting*. American Institute of Aeronautics and Astronautics, jan 2016. doi: 10.2514/6.2016-0195. URL `https://doi.org/10.2514%2F6.2016-0195`.

[99] O. Forster. *Analysis 3: Maß-und Integrationstheorie, Integralsätze im IRn und Anwendungen*, volume 3. Springer-Verlag, 2012.

[100] C.A. Kennedy. *Comparison of several numerical methods for simulation of compressible shear layers*, volume 3484. NASA, Langley Research Center, 1997.

[101] J. Ray, C.A. Kennedy, S. Lefantzi, and H.N. Najm. Using high-order methods on adaptively refined block-structured meshes: derivatives, interpolations, and filters. *SIAM Journal on Scientific Computing*, 29(1):139–181, 2007.

[102] E. Turkel and V.N. Vatsa. Effect of artificial viscosity on three-dimensional flow solutions. *AIAA journal*, 32(1):39–45, 1994.

[103] P. Gerlinger, J. Algermissen, and D. Brüggemann. Matrix dissipation for central difference schemes with combustion. *AIAA journal*, 33(10):1865–1870, 1995.

[104] A. Harten. High resolution schemes for hyperbolic conservation laws. *J. Comput. Phys.*, 135(2): 260–278, 1997.

[105] P.K. Sweby. High resolution schemes using flux limiters for hyperbolic conservation laws. *SIAM journal on numerical analysis*, 21(5):995–1011, 1984.

[106] P.L. Roe. Characteristic-based schemes for the euler equations. *Annual review of fluid mechanics*, 18(1):337–365, 1986.

[107] B. Van Leer. Towards the ultimate conservative difference scheme. *J. Comput. Phys.*, 135(2): 229–248, 1997.

[108] G. Zhou. *Numerical simulations of physical discontinuities in single and multi-fluid flows for arbitrary Mach numbers*. Chalmers University of Technology, 1995.

[109] A.M. Kempf. *Large-eddy simulation of non-premixed turbulent flames*. PhD Thesis. TU Darmstadt, 2004.

[110] F. Proch. *Highly-resolved numerical simulation of turbulent premixed and stratified combustion under adiabatic and non-adiabatic conditions with tabulated chemistry*. PhD thesis, University of Duisburg-Essen, Mar 2017. URL `https://duepublico2.uni-due.de/receive/duepublico_mods_00043491`.

[111] W.K. Anderson, J.L. Thomas, and B. Van Leer. Comparison of finite volume flux vector splittings for the euler equations. *AIAA journal*, 24(9):1453–1460, 1986.

[112] B. Van Leer. Towards the ultimate conservative difference scheme. ii. monotonicity and conservation combined in a second-order scheme. *J. Comput. Phys.*, 14(4):361–370, 1974.

[113] B. Van Leer. Towards the ultimate conservative difference scheme i. the quest of monotonicity. In *Proceedings of the Third International Conference on Numerical Methods in Fluid Mechanics*, pages 163–168. Springer, 1973.

[114] S.K. Godunov. A difference scheme for numerical solution of discontinuous solution of hydrodynamic equations. *Math. Sbornik*, 47:271–306, 1959.

[115] N.P Waterson and H. Deconinck. Design principles for bounded higher-order convection schemes–a unified approach. *J. Comput. Phys.*, 224(1):182–207, 2007.

[116] P.L. Roe. Finite-volume methods for the compressible navier-stokes equations. *Numerical methods in laminar and turbulent flow*, 1987.

[117] G. Billet and O. Louedin. Adaptive limiters for improving the accuracy of the muscl approach for unsteady flows. *Journal of Computational Physics*, 170(1):161–183, 2001.

[118] X.-D. Liu, S. Osher, and T. Chan. Weighted essentially non-oscillatory schemes. *J. Comput. Phys.*, 115(1):200–212, 1994.

[119] A. Harten and S. Osher. Uniformly high order accurate essentially non-oscillatory schemes, i. In *Upwind and High-Resolution Schemes*, pages 187–217. Springer, 1997.

[120] A. Harten, B. Engquist, S. Osher, and S.R. Chakravarthy. Uniformly high order accurate essentially non-oscillatory schemes, iii. In *Upwind and high-resolution schemes*, pages 218–290. Springer, 1987.

[121] G.-S. Jiang and C.-W. Shu. Efficient implementation of weighted eno schemes. *Journal of computational physics*, 126(1):202–228, 1996.

[122] A. Suresh and H.T. Huynh. Accurate monotonicity-preserving schemes with runge–kutta time stepping. *J. Comput. Phys.*, 136(1):83–99, 1997.

[123] P. Colella and P.R. Woodward. The piecewise parabolic method (ppm) for gas-dynamical simulations. *J. Comput. Phys.*, 54(1):174–201, 1984.

[124] H.T. Huynh. Accurate monotone cubic interpolation. *SIAM Journal on Numerical Analysis*, 30(1): 57–100, 1993.

[125] R. Courant, E. Isaacson, and M. Rees. On the solution of nonlinear hyperbolic differential equations by finite differences. *Commun. Pure Appl. Math.*, 5(3):243–255, aug 1952. doi: 10.1002/cpa.3160050303. URL `https://doi.org/10.1002%2Fcpa.3160050303`.

[126] P.L. Roe. A survey of upwind differencing techniques. In *11th International Conference on Numerical Methods in Fluid Dynamics*, pages 69–78. Springer Berlin Heidelberg, 1989. doi: 10.1007/3-540-51048-6_6. URL `https://doi.org/10.1007%2F3-540-51048-6_6`.

[127] S. Osher. Numerical solution of singular perturbation problems and hyperbolic systems of conservation laws. In *Analytical and Numerical Approaches to Asymptotic Problems in Analysis, Proceedings ofthe Conference on Analytical and Numerical Approachesto Asymptotic Problems*, pages 179–204. Elsevier, 1981. doi: 10.1016/s0304-0208(08)71109-5. URL `https://doi.org/10.1016%2Fs0304-0208%2808%2971109-5`.

[128] P.L. Roe. Approximate riemann solvers, parameter vectors, and difference schemes. *Journal of Computational Physics*, 135(2):250–258, aug 1997. doi: 10.1006/jcph.1997.5705. URL `https://doi.org/10.1006%2Fjcph.1997.5705`.

[129] J.L. Steger and R.F. Warming. Flux vector splitting of the inviscid gasdynamic equations with application to finite-difference methods. *Journal of Computational Physics*, 40(2):263–293, apr 1981. doi: 10.1016/0021-9991(81)90210-2. URL `https://doi.org/10.1016%2F0021-9991%2881%2990210-2`.

[130] B. van Leer. Flux-vector splitting for the euler equation. In *Upwind and High-Resolution Schemes*, pages 80–89. Springer Berlin Heidelberg, 1997. doi: 10.1007/978-3-642-60543-7_5. URL `https://doi.org/10.1007%2F978-3-642-60543-7_5`.

[131] M.-S. Liou and C.J. Steffen. A new flux splitting scheme. *Journal of Computational Physics*, 107 (1):23–39, jul 1993. doi: 10.1006/jcph.1993.1122. URL `https://doi.org/10.1006%2Fjcph.1993.1122`.

[132] M. S. Liou. On a new class of flux splittings. In *Thirteenth International Conference on Numerical Methods in Fluid Dynamics*, pages 115–119. Springer Berlin Heidelberg, 1993. doi: 10.1007/3-540-56394-6_199. URL `https://doi.org/10.1007%2F3-540-56394-6_199`.

[133] J.J. Quirk. A contribution to the great riemann solver debate. In *Upwind and High-Resolution Schemes*, pages 550–569. Springer Berlin Heidelberg, 1997. doi: 10.1007/978-3-642-60543-7_22. URL `https://doi.org/10.1007%2F978-3-642-60543-7_22`.

[134] M.-S. Liou. A sequel to AUSM: AUSM+. *Journal of Computational Physics*, 129(2):364–382, dec 1996. doi: 10.1006/jcph.1996.0256. URL `https://doi.org/10.1006%2Fjcph.1996.0256`.

[135] E. Garnier, M. Mossi, P. Sagaut, P. Comte, and M. Deville. On the use of shock-capturing schemes for large-eddy simulation. *J. Comput. Phys.*, 153(2):273–311, 1999.

[136] M.-S. Liou. A sequel to ausm, part ii: Ausm+-up for all speeds. *J. Comput. Phys.*, 214(1):137–170, 2006.

[137] E. Shima and K. Kitamura. Parameter-free simple low-dissipation ausm-family scheme for all speeds. *AIAA J.*, 49(8):1693–1709, 2011.

[138] K. Kitamura and E. Shima. Towards shock-stable and accurate hypersonic heating computations: A new pressure flux for ausm-family schemes. *J. Comput. Phys.*, 245:62–83, 2013.

[139] K. Kitamura and A. Hashimoto. Reduced dissipation ausm-family fluxes: Hr-slau2 and hr-ausm+-up for high resolution unsteady flow simulations. *Comput. Fluids*, 126:41–57, 2016.

[140] A.L. Scandaliato and M.-S. Liou. Ausm-based high-order solution for euler equations. *Commun. Comput. Phys.*, 12(4):1096–1120, 2012.

[141] E.F. Toro. *Riemann solvers and numerical methods for fluid dynamics: a practical introduction*. Springer Science & Business Media, 2013.

[142] C.W. Shu, T.A. Zang, G. Erlebacher, D. Whitaker, and S. Osher. High-order eno schemes applied to two-and three-dimensional compressible flow. *Applied Numerical Mathematics*, 9(1):45–71, 1992.

[143] G. A. Gerolymos, D. Sénéchal, and I. Vallet. Very-high-order weno schemes. *J. Comput. Phys.*, 228(23):8481–8524, 2009.

[144] B. Thornber, A. Mosedale, D. Drikakis, D. Youngs, and R.Jr. Williams. An improved reconstruction method for compressible flows with low mach number features. *J. Comput. Phys.*, 227(10):4873–4894, 2008.

[145] T. J. Poinsot and S.K. Lele. Boundary conditions for direct simulations of compressible viscous flows. *J. Comput. Phys.*, 101(1):104–129, 1992.

[146] J. Oliger and A. Sundström. Theoretical and practical aspects of some initial boundary value problems in fluid dynamics. *SIAM J. Appl. Math.*, 35(3):419–446, 1978.

[147] O. Dutt. Stable boundary conditions and difference schemes for navier–stokes equations. *SIAM J. Numer. Anal.*, 25(2):245–267, 1988.

[148] K.W. Thompson. Time dependent boundary conditions for hyperbolic systems. *J. Comput. Phys.*, 68(1):1–24, 1987.

[149] L. Selle, F. Nicoud, and T. Poinsot. Actual impedance of nonreflecting boundary conditions: Implications for computation of resonators. *AIAA Journal*, 42(5):958–964, 2004.

[150] H. Mark. The interaction of a reflected shock wave with the boundary layer in a shock tube. Technical report, NACA, 1958.

[151] I.I. Glass, W. Martin, and G.N. Patterson. A theoretical and experimental study of shock-tube flows. *Journal of the Aeronautical Sciences*, 22(2):73–100, 1955.

[152] F.R. Ruckdeschel. *Basic Scientific Subroutines, Volume II.* ERIC, 1981.

[153] R. Courant and K.O. Friedrichs. *Supersonic flow and shock waves*, volume 21. Springer Science & Business Media, 1999.

[154] R.A. Hartunian, A.L. Russo, and P.V. Marrone. Boundary-layer transition and heat transfer in shock tubes. *J. Aerosp. Sci.*, 27(8):587–594, 1960. doi: 10.2514/8.8656. URL `https://doi.org/10.2514/8.8656`.

[155] H. Mirels. Laminar boundary layer behind shock advancing into stationary fluid. Technical report, NACA, Technical Note 3401, 1955.

[156] H. Mirels. Boundary layer behind shock or thin expansion wave moving into stationary fluid. Technical report, NACA, Technical Note 3712, 1956.

[157] H. Schlichting and K. Gersten. *Grundzüge der Grenzschicht-Theorie*. Springer, 2006.

[158] E.L. Petersen and R.K. Hanson. Improved turbulent boundary-layer model for shock tubes. *AIAA Journal*, 41(7):1314–1322, 2003.

[159] D.B. Spalding and C.W. Chi. The drag of a compressible turbulent boundary layer on a smooth flat plate with and without heat transfer. *Journal of Fluid Mechanics*, 18(1):117–143, 1964.

[160] H. Mirels and W.H. Braun. Nonuniformities in shock-tube flow due to unsteady-boundary-layer action. *NACA*, 1957.

[161] H. Mirels. *Attenuation in a shock tube due to unsteady-boundary-layer action*. United States, 1957.

[162] M. Klein, A. Sadiki, and J. Janicka. A digital filter based generation of inflow data for spatially developing direct numerical or large eddy simulations. *J. Comput. Phys.*, 186(2):652–665, 2003.

[163] A.M. Kempf, M. Klein, and J. Janicka. Efficient generation of initial-and inflow-conditions for transient turbulent flows in arbitrary geometries. *Flow, Turbulence and Combustion*, 74(1):67–84, 2005.

[164] D.R. White. Influence of diaphragm opening time on shock-tube flows. *J. Fluid Mech.*, 4(06):585, 1958. doi: 10.1017/s0022112058000677. URL `https://doi.org/10.1017%2Fs0022112058000677`.

[165] E. L. Petersen and R. K. Hanson. Nonideal effects behind reflected shock waves in a high-pressure shock tube. *Shock Waves*, 10(6):405–420, 2001. doi: 10.1007/pl00004051. URL `https://doi.org/10.1007%2Fpl00004051`.

[166] Meyer J.W. and Oppenheim A.K. On the shock-induced ignition of explosive gases. *Proc. Combust. Inst.*, 13(1):1153–1164, 01 1971. doi: 10.1016/s0082-0784(71)80112-1. URL `https://doi.org/10.1016%2Fs0082-0784%2871%2980112-1`.

[167] R. Blumenthal, K. Fieweger, K. H. Komp, and G. Adomeit. Gas dynamic features of self ignition of non diluted fuel/air mixtures at high pressure. *Combust. Sci. Technol.*, 123(1-6):1–30, 01 1997. doi: 10.1080/00102209708935637. URL `https://doi.org/10.1080%2F00102209708935637`.

[168] H. Mark. *The interaction of a reflected shock wave with the boundary layer in a shock tube*. NACA, 1958.

[169] Roger A. Strehlow and Arthur Cohen. Limitations of the reflected shock technique for studying fast chemical reactions and its application to the observation of relaxation in nitrogen and oxygen. *J. Chem. Phys.*, 30(1):257–265, 1959. doi: 10.1063/1.1729883. URL `https://doi.org/10.1063%2F1.1729883`.

[170] L. Davies. Influence of reflected shock and boundary-layer interaction on shock-tube flows. *Phys. Fluids*, 12(5):I–37, 1969. doi: 10.1063/1.1692625. URL `https://doi.org/10.1063%2F1.1692625`.

[171] V.V. Voevodsky and R.I. Soloukhin. On the mechanism and explosion limits of hydrogen-oxygen chain self-ignition in shock waves. *Proc. Combust. Inst.*, 10(1):279–283, 1965. doi: 10.1016/s0082-0784(65)80173-4. URL `https://doi.org/10.1016%2Fs0082-0784%2865%2980173-4`.

[172] D. J. Berets, E. F. Greene, and G. B. Kistiakowsky. Gaseous detonations. i. stationary waves in hydrogen—oxygen mixtures1. *J. Am. Chem. Soc.*, 72(3):1080–1086, 1950. doi: 10.1021/ja01159a008.

[173] J.A. Fay. Some experiments on the initiation of detonation in 2h2-o2 mixtures by uniform shock waves. *Proc. Combust. Inst.*, 4(1):501–507, 1953. doi: 10.1016/s0082-0784(53)80071-8. URL `https://doi.org/10.1016%2Fs0082-0784%2853%2980071-8`.

[174] M. Steinberg and W.E. Kaskan. The ignition of combustible mixtures by shock waves. *Proc. Combust. Inst.*, 5(1):664–672, 1955. doi: 10.1016/s0082-0784(55)80092-6. URL `https://doi.org/10.1016%2Fs0082-0784%2855%2980092-6`.

[175] E.S. Oran, T.R. Young, J.P. Boris, and A. Cohen. Weak and strong ignition. i. numerical simulations of shock tube experiments. *Combust. Flame*, 48:135–148, 1982. doi: 10.1016/0010-2180(82)90123-7. URL `https://doi.org/10.1016%2F0010-2180%2882%2990123-7`.

[176] E.S. Oran and V.N. Gamezo. Origins of the deflagration-to-detonation transition in gas-phase combustion. *Combust. Flame*, 148(1-2):4–47, 2007. doi: 10.1016/j.combustflame.2006.07.010. URL `https://doi.org/10.1016%2Fj.combustflame.2006.07.010`.

[177] M. Ihme, Y. Sun, and R. Deiterding. Detailed simulations of shock-bifurcation and ignition of an argon-diluted hydrogen/oxygen mixture in a shock tube. In *51st AIAA Aerospace Sciences Meeting including the New Horizons Forum and Aerospace Exposition*, page 538, 2013.

[178] K. P. Grogan and M. Ihme. Weak and strong ignition of hydrogen/oxygen mixtures in shock-tube systems. *Proc. Combust. Inst.*, 35(2):2181–2189, 2015. doi: 10.1016/j.proci.2014.07.074. URL `https://doi.org/10.1016%2Fj.proci.2014.07.074`.

[179] A. Khokhlov, J. Austin, and A. Knisely. *Development of Hot Spots and Ignition Behind Reflected Shocks in 2H2 + O2*. Proc. 25th Int. Colloq. Dynamics of Explosions and Reactive Systems. ICDERS, Leeds, UK, 2015.

[180] E. Dziemińska and A. Koichi Hayashi. Auto-ignition and DDT driven by shock wave – boundary layer interaction in oxyhydrogen mixture. *Int. J. Hydrogen Energy*, 38(10):4185–4193, 04 2013. doi: 10.1016/j.ijhydene.2013.01.111. URL `https://doi.org/10.1016%2Fj.ijhydene.2013.01.111`.

[181] F. Proch and A.M. Kempf. Numerical analysis of the cambridge stratified flame series using artificial thickened flame LES with tabulated premixed flame chemistry. *Combust. Flame*, 161(10):2627–2646, 2014. doi: 10.1016/j.combustflame.2014.04.010. URL `https://doi.org/10.1016%2Fj.combustflame.2014.04.010`.

[182] A. Rittler, L. Deng, I. Wlokas, and A.M. Kempf. Large eddy simulations of nanoparticle synthesis from flame spray pyrolysis. *Proc. Combust. Inst.*, 36(1):1077–1087, 2017. doi: 10.1016/j.proci.2016.08.005. URL `https://doi.org/10.1016%2Fj.proci.2016.08.005`.

[183] M. Rieth, F. Proch, M. Rabaçal, B.M. Franchetti, F. Cavallo Marincola, and A.M. Kempf. Flamelet LES of a semi-industrial pulverized coal furnace. *Combust. Flame*, 173:39–56, 2016. doi: 10.1016/j.combustflame.2016.07.013. URL `https://doi.org/10.1016%2Fj.combustflame.2016.07.013`.

[184] T. Nguyen and A. M. Kempf. Investigation of numerical effects on the flow and combustion in LES of ICE. *Oil Gas Sci. Technol.*, 72(4):25, 07 2017. doi: 10.2516/ogst/2017023. URL `https://doi.org/10.2516%2Fogst%2F2017023`.

[185] T. J. Poinsot and D. Veynante. *Theoretical and Numerical Combustion*. Aquaprint, Bordeaux, France, 3rd edition, 2012.

[186] J. H. Williamson. Low-storage runge-kutta schemes. *J. Comput. Phys.*, 35(1):48–56, 1980. doi: 10.1016/0021-9991(80)90033-9. URL `https://doi.org/10.1016%2F0021-9991%2880%2990033-9`.

[187] Goodwin D.G. Cantera. http://code.google.com/p/cantera, 2009.

[188] R. B. Bird, W. E. Stewart, E. N. Lightfoot, and D. B. Spalding. Transport phenomena. *J. Appl. Mech.*, 28(2):317, 1961. doi: 10.1115/1.3641697. URL `https://doi.org/10.1115%2F1.3641697`.

[189] N. Peters and J. Warnatz. *Numerical Methods in Laminar Flame Propagation*. Vieweg+Teubner Verlag, 1982. doi: 10.1007/978-3-663-14006-1. URL `https://doi.org/10.1007%2F978-3-663-14006-1`.

[190] R. J. Kee, M. E. Coltrin, and P. Glarborg. *Chemically Reacting Flow*. John Wiley & Sons, Inc., 2003. doi: 10.1002/0471461296. URL `https://doi.org/10.1002%2F0471461296`.

[191] S.D. Cohen, A.C. Hindmarsh, and P.F. Dubois. CVODE, a stiff/nonstiff ODE solver in C. *Comput. Phys.*, 10(2):138, 1996. doi: 10.1063/1.4822377. URL `https://doi.org/10.1063%2F1.4822377`.

[192] M. Ó Conaire, H. J. Curran, J. M. Simmie, W. J. Pitz, and C. K. Westbrook. A comprehensive modeling study of hydrogen oxidation. *Int. J. Chem. Kinet.*, 36(11):603–622, 2004. doi: 10.1002/kin.20036. URL `https://doi.org/10.1002%2Fkin.20036`.

[193] L. Wang and N. Peters. The length-scale distribution function of the distance between extremal points in passive scalar turbulence. *J. Fluid Mech.*, 554(-1):457, 2006. doi: 10.1017/s0022112006009128. URL `https://doi.org/10.1017%2Fs0022112006009128`.

[194] Y. S. Weber, E. S. Oran, J. P. Boris, and J. D. Anderson. The numerical simulation of shock bifurcation near the end wall of a shock tube. *Phys. Fluids*, 7(10):2475–2488, 1995. doi: 10.1063/1.868691. URL `https://doi.org/10.1063%2F1.868691`.

[195] K. Matsuo, S. Kawagoe, and K. Kage. The interaction of a reflected shock wave with the boundary layer in a shock tube. *Bulletin of JSME*, 17(110):1039–1046, 1974. doi: 10.1299/jsme1958.17.1039. URL `https://doi.org/10.1299%2Fjsme1958.17.1039`.

[196] M. Lamnaouer, A. Kassab, E. Divo, N. Polley, R. Garza-Urquiza, and E. Petersen. A conjugate axisymmetric model of a high-pressure shock-tube facility. *Int. J. Numer. Methods Heat Fluid Flow*, 24(4):873–890, 2014. doi: 10.1108/hff-02-2013-0070. URL `https://doi.org/10.1108%2Fhff-02-2013-0070`.

[197] R. K. Hanson, G. A. Pang, S. Chakraborty, W. Ren, S. Wang, and D. F. Davidson. Constrained reaction volume approach for studying chemical kinetics behind reflected shock waves. *Combust. Flame*, 160(9):1550–1558, 09 2013. doi: 10.1016/j.combustflame.2013.03.026. URL `https://doi.org/10.1016%2Fj.combustflame.2013.03.026`.

[198] K. Fieweger, R. Blumenthal, and G. Adomeit. Self-ignition of s.i. engine model fuels: A shock tube investigation at high pressure. *Combust. Flame*, 109(4):599–619, 06 1997. doi: 10.1016/s0010-2180(97)00049-7. URL `https://doi.org/10.1016%2Fs0010-2180%2897%2900049-7`.

[199] Alfred Gordon Gaydon and Ian Roy Hurle. *The shock tube in high-temperature chemical physics*. Chapman and Hall, 1963.

[200] KA Bhaskaran and P Roth. The shock tube as wave reactor for kinetic studies and material systems. *Prog. Energy Combust. Sci.*, 28(2):151–192, 2002.

[201] Harold Mirels and JF Mullen. Small perturbation theory for shock-tube attenuation and nonuniformity. *Phys. Fluids*, 7(8):1208–1218, 1964.

[202] H. Mirels and W.H. Braun. Nonuniformities in shock-tube flow due to unsteady-boundary-layer action. *NACA*, 1957.

[203] H. Mirels. *Attenuation in a shock tube due to unsteady-boundary-layer action*. United States, 1957.

[204] G. Rudinger. Effect of boundary-layer growth in a shock tube on shock reflection from a closed end. *Phys. Fluids*, 4(12):1463–1473, 1961.

[205] H Mirels. Flow nonuniformity in shock tubes operating at maximum test times. *Phys. Fluids*, 9 (10):1907–1912, 1966.

[206] DF Davidson and RK Hanson. Interpreting shock tube ignition data. *Int. J. Chem. Kinet.*, 36(9): 510–523, 2004.

[207] E. Inanc and A. M. Kempf. Numerical study of a pulsed auto-igniting jet flame with detailed tabulated chemistry. *Fuel*, 252:408–416, 2019.

[208] L. Cifuentes, A. M. Kempf, and C. Dopazo. Local entrainment velocity in a premixed turbulent annular jet flame. *Proc. Combust. Inst.*, 37(2):2493–2501, 2019.

[209] M. Rieth, F. Proch, O.T. Stein, M.W.A. Pettit, and A.M. Kempf. Comparison of the sigma and smagorinsky les models for grid generated turbulence and a channel flow. *Computers & Fluids*, 99: 172 – 181, 2014. ISSN 0045-7930. doi: https://doi.org/10.1016/j.compfluid.2014.04.018. URL `http://www.sciencedirect.com/science/article/pii/S004579301400156X`.

[210] K. Kitamura and A. Hashimoto. Reduced dissipation AUSM-family fluxes: HR-SLAU2 and HR-AUSM + -up for high resolution unsteady flow simulations. *Comput. Fluids*, 126:41–57, 2016. doi: 10.1016/j.compfluid.2015.11.014. URL `https://doi.org/10.1016%2Fj.compfluid.2015.11.014`.

[211] A. Suresh and H.T. Huynh. Accurate monotonicity-preserving schemes with Runge–Kutta time stepping. *J. Comput. Phys.*, 136(1):83–99, 1997. doi: 10.1006/jcph.1997.5745. URL `https://doi.org/10.1006%2Fjcph.1997.5745`.

[212] Angelo L Scandaliato and Meng-Sing Liou. Ausm-based high-order solution for euler equations. *Communications in Computational Physics*, 12(4):1096–1120, 2012.

[213] Guoyan Zhao, Mingbo Sun, Antonio Memmolo, and Sergio Pirozzoli. A general framework for the evaluation of shock-capturing schemes. *J. Comput. Phys.*, 376:924–936, 2019.

[214] Sergio Pirozzoli. On the spectral properties of shock-capturing schemes. *J. Comput. Phys.*, 219(2): 489–497, 2006.

[215] Johan Larsson. Effect of shock-capturing errors on turbulence statistics. *AIAA*, 48(7):1554–1557, 2010.

[216] James J Quirk. A contribution to the great riemann solver debate. In *Upwind and High-Resolution Schemes*, pages 550–569. Springer, 1997.

[217] Randall J LeVeque. Nonlinear conservation laws and finite volume methods. In *Computational methods for astrophysical fluid flow*, pages 1–159. Springer, 1998.

[218] A. Harten, B. Engquist, S. Osher, and S. R. Chakravarthy. Uniformly high order accurate essentially non-oscillatory schemes, III. *J. Comput. Phys.*, 71(2):231–303, 1987. ISSN 0021-9991. doi: https://doi.org/10.1016/0021-9991(87)90031-3. URL `http://www.sciencedirect.com/science/article/pii/0021999187900313`.

[219] Ben Thornber, Dimitris Drikakis, Robin JR Williams, and David Youngs. On entropy generation and dissipation of kinetic energy in high-resolution shock-capturing schemes. *J. Comput. Phys.*, 227(10):4853–4872, 2008.

[220] B. Thornber, A. Mosedale, D. Drikakis, D. Youngs, and R.J.R. Williams. An improved reconstruction method for compressible flows with low mach number features. *J. Comput. Phys.*, 227 (10):4873 – 4894, 2008. ISSN 0021-9991. doi: https://doi.org/10.1016/j.jcp.2008.01.036. URL `http://www.sciencedirect.com/science/article/pii/S0021999108000429`.

[221] C. R. Wilke. A viscosity equation for gas mixtures. *J. Chem. Phys.*, 18(4):517–519, 1950. doi: 10.1063/1.1747673. URL `https://doi.org/10.1063%2F1.1747673`.

[222] GP Smith, Y Tao, and H Wang. Foundational fuel chemistry model version 1.0 (FFCM-1), http://nanoenergy.stanford.edu/ffcm1, 2016.

[223] M. Oconaire, H.J. Curran, J.M. Simmie, W.J. Pitz, and C.K. Westbrook. A comprehensive modeling study of hydrogen oxidation. *Int. J. Chem. Kinet.*, 36(11):603–622, 2004. doi: 10.1002/kin.20036. URL `https://doi.org/10.1002%2Fkin.20036`.

[224] Gary A Sod. A survey of several finite difference methods for systems of nonlinear hyperbolic conservation laws. *J. Comput. Phys.*, 27(1):1–31, 1978.

[225] Chi-Wang Shu and Stanley Osher. Efficient implementation of essentially non-oscillatory shock-capturing schemes. *J. Comput. Physics*, 77(2):439–471, 1988.

[226] Yu. N. Denisov and Ya. K. Troshin. On the mechanism of detonative combustion. In *Symp. (Int.) Combust.*, volume 8, pages 600–610, 1961.

[227] J. H. S. Lee. *The detonation phenomenon*. Cambridge University Press, 2008.

[228] F. A. Bykovskii, S. A. Zhdan, and E. F. Vedernikov. Continuous spin detonations. *J. Propul. Power*, 22(6):1204–1216, 2006.

[229] H. D. Ng and J. H. S. Lee. Comments on explosion problems for hydrogen safety. *Journal of Loss Prevention in the Process Industries*, 21(2):136–146, 2008.

[230] J. Yanez, M. Kuznetsov, and A. Souto-Iglesias. An analysis of the hydrogen explosion in the fukushima-daiichi accident. *Int. J. Hydrogen Energy*, 40(25):8261–8280, 2015.

[231] M. Fischer. Safety aspects of hydrogen combustion in hydrogen energy systems. *Int. J. Hydrogen Energy*, 11(9):593–601, 1986.

[232] J. E. Shepherd. Detonation in gases. *Proc. Combust. Inst.*, 32(1):83–98, 2009.

[233] K. I. Shchelkin and Ya. K. Troshin. Non-stationary phenomena in the gaseous detonation front. *Combust. Flame*, 7:143–151, 1963.

[234] M. I. Radulescu, A. Papi, J. J. Quirk, P. Mach, and B. M. Maxwell. The origin of shock bifurcations in cellular detonations. In *22nd International Colloquium on the Dynamics of Explosions and Reactive Systems*, Minsk, Belarus, 2009.

[235] F. Pintgen, C. A. Eckett, J. M. Austin, and J. E. Shepherd. Direct observations of reaction zone structure in propagating detonations. *Combust. Flame*, 133(3):211–229, 2003.

[236] C. K. Westbrook and P. A. Urtiew. Chemical kinetic prediction of critical parameters in gaseous detonations. *Symp. (Int.) Combust.*, 19(1):615–623, 1982.

[237] C. M. Guirao, R. Knystautas, J. H. Lee, W. Benedick, and M. Berman. Hydrogen-air detonations. Technical Report No. SAND–82-1494C, Sandia National Laboratories, 1982.

[238] J. E. Shepherd. Chemical kinetics of hydroge-air-dilunet detonations. *Progress in Astronautics and Aeronautics*, 106:263–293, 1986.

[239] A. I. Gavrikov, A. A. Efimenko, and S. B. Dorofeev. A model for detonation cell size prediction from chemical kinetics. *Combust. Flame*, 120(1-2):19–33, 2000.

[240] H. D. Ng. *The effect of chemical reaction kinetics on the structure of gaseous detonations*. PhD thesis, McGill University, 2005.

[241] J. Crane, X. Shi, A. V. Singh, Y. Tao, and H. Wang. Isolating the effect of induction length on detonation structure: Hydrogen–oxygen detonation promoted by ozone. *Combust. Flame*, 200: 44–52, 2019. ISSN 0010-2180. doi: https://doi.org/10.1016/j.combustflame.2018.11.008. URL `http://www.sciencedirect.com/science/article/pii/S0010218018304838`.

[242] Matei I Radulescu. A detonation paradox: Why inviscid detonation simulations predict the incorrect trend for the role of instability in gaseous cellular detonations? *Combustion and Flame*, 195:151–162, 2018.

[243] P. Mach and M. I. Radulescu. Mach reflection bifurcations as a mechanism of cell multiplication in gaseous detonations. *Proc. Combust. Inst.*, 33(2):2279–2285, 2011.

[244] A. Sow, S.-M. Lau-Chapdelaine, and M. I. Radulescu. The effect of the polytropic index γ on the structure of gaseous detonations. *Proc. Combust. Inst.*, 38(3):3633–3640, 2021.

[245] M. Short and G. J. Sharpe. Pulsating instability of detonations with a two-step chain-branching reaction model: theory and numerics. *Combust. Theor. Model.*, 7(2):401, 2003.

[246] H. D. Ng, M. I. Radulescu, A. J. Higgins, N. Nikiforakis, and J. H. S. Lee. Numerical investigation of the instability for one-dimensional chapman–jouguet detonations with chain-branching kinetics. *Combust. Theor. Model.*, 9(3):385–401, 2005.

[247] P. A. Meagher, X. Shi, J. P. Santos, N. K. Muraleedharan, J. Crane, A. Y. Poludnenko, H. Wang, and X. Zhao. Isolating gasdynamic and chemical effects on the detonation cellular structure: a combined experimental and computational study. *Proc. Combust. Inst.*, 39:in press, 2022.

[248] J. Crane, X. Shi, J. T. Lipkowicz, A. M. Kempf, and H. Wang. Geometric modeling and analysis of detonation cellular stability. *Proc. Combust. Inst.*, 38:3585, 2021.

[249] B. Taylor, D. Kessler, V. Gamezo, and E. S. Oran. The influence of chemical kinetics on the structure of hydrogen-air detonations. In *50th AIAA Aerospace Sciences Meeting including the New Horizons Forum and Aerospace Exposition*, pages 1–14, 2012.

[250] B. D. Taylor, D. A. Kessler, V. N. Gamezo, and E. S. Oran. Numerical simulations of hydrogen detonations with detailed chemical kinetics. *Proc. Combust. Inst.*, 34(2):2009–2016, 2013.

[251] G. J. Sharpe and J. J. Quirk. Nonlinear cellular dynamics of the idealized detonation model: Regular cells. *Combust. Theor. Model.*, 12(1):1–21, 2008.

[252] V. N. Gamezo, D. Desbordes, and E. S. Oran. Formation and evolution of two-dimensional cellular detonations. *Combust. Flame*, 116(1-2):154–165, 1999.

[253] J. Y. Choi, F. H. Ma, and V. Yang. Some numerical issues on simulation of detonation cell structures. *Combust. Explos. Shock Waves*, 44(5):560–578, 2008.

[254] S. Gallier, F. Le Palud, F. Pintgen, R. Mével, and J. E. Shepherd. Detonation wave diffraction in h2–o2–ar mixtures. *Proc. Combust. Inst.*, 36(2):2781–2789, 2017.

[255] K. Mazaheri, Y. Mahmoudi, and M. I. Radulescu. Diffusion and hydrodynamic instabilities in gaseous detonations. *Combust. Flame*, 159(6):2138–2154, 2012.

[256] Y. Mahmoudi, N. Karimi, R. Deiterding, and S. Emami. Hydrodynamic instabilities in gaseous detonations: comparison of euler, navier–stokes, and large-eddy simulation. *J. Propul. Power*, 30 (2):384–396, 2014.

[257] B. McN. Maxwell, R. R. Bhattacharjee, S. S. M. Lau-Chapdelaine, S. A. E. G. Falle, G. J. Sharpe, and M. I. Radulescu. Influence of turbulent fluctuations on detonation propagation. *J. Fluid Mech.*, 818:646–696, 2017. doi: 10.1017/jfm.2017.145.

[258] X. Cai, R. Deiterding, J. Liang, M. Sun, and Y. Mahmoudi. Diffusion and mixing effects in hot jet initiation and propagation of hydrogen detonations. *J. Fluid Mech.*, 836:324–351, 2018.

[259] Y. Tao, G. P. Smith, and H. Wang. Critical kinetic uncertainties in modeling hydrogen/carbon monoxide, methane, methanol, formaldehyde, and ethylene combustion. *Combust. Flame*, 195: 18–29, 2018.

[260] H. Zhao, X. Yang, and Y. Ju. Kinetic studies of ozone assisted low temperature oxidation of dimethyl ether in a flow reactor using molecular-beam mass spectrometry. *Combust. Flame*, 173: 187–194, 2016. ISSN 0010-2180. doi: https://doi.org/10.1016/j.combustflame.2016.08.008. URL `http://www.sciencedirect.com/science/article/pii/S001021801630219X`.

[261] S. Browne, J. Ziegler, and J. E. Shepherd. Numerical solution methods for shock and detonation jump conditions. *GALCIT Report FM2006*, 6:90, 2008.

[262] D. H. Rudy and J. C. Strikwerda. A nonreflecting outflow boundary condition for subsonic navier-stokes calculations. *J. Comput. Phys.*, 36(1):55–70, 1980.

[263] J. Koch, M. Kurosaka, C. Knowlen, and J. N. Kutz. Mode-locked rotating detonation waves: Experiments and a model equation. *Phys. Rev. E*, 101(1):013106, 2020.

[264] X. Shi, P. A. Meagher, J. Crane, S. S. Dammati, X. Zhao, A. Y. Poludnenko, and H. Wang. On cellular multiplicity of detonations in confined channels. In *28th International Colloquium on the Dynamics of Explosions and Reactive Systems*, Naples, Italy, 2022.

[265] X. Shi, J. Crane, and H. Wang. Detonation and its limit in small tubes with ozone sensitization. *Proc. Combust. Inst.*, 38(3):3547–3554, 2021.

[266] A. Camargo, H. D. Ng, J. Chao, and J. H. S. Lee. Propagation of near-limit gaseous detonations in small diameter tubes. *Shock Waves*, 20(6):499–508, 2010.

[267] M. Dormal, J.-C. Libouton, and P. J. Van Tiggelen. Evolution of induction time in detonation cell. In A.K. Oppenheim, editor, *Gasdynamics of Explosions and Reactive Systems*, pages 875–884. Pergamon, 1980. ISBN 978-0-08-025442-5. doi: https://doi.org/10.1016/B978-0-08-025442-5.50053-6. URL `https://www.sciencedirect.com/science/article/pii/B9780080254425500536`.

[268] Q. Xiao, A. Sow, B. M. Maxwell, and M. I. Radulescu. Effect of boundary layer losses on 2d detonation cellular structures. *Proc. Combust. Inst.*, 38(3):3641–3649, 2021.

[269] A. Higgins. Steady one-dimensional detonations. In *Shock Waves Science and Technology Library, Vol. 6: Detonation Dynamics*, pages 33–105. Springer, 2011.

[270] M. Pandolfi and R. Marsilio. Frozen and equilibrium speeds of sound in non-equilibrium flows. In *Advances in Kinetic Theory and Continuum Mechanics: Proceedings of a Symposium Held in Honor of Professor Henri Cabannes at the University Pierre et Marie Curie, Paris, France, on 6 July 1990*, pages 185–194. Springer, 1991.

[271] A. R. Kasimov and D. S. Stewart. On the dynamics of self-sustained one-dimensional detonations: A numerical study in the shock-attached frame. *Phys. Fluids*, 16(10):3566–3578, 2004.

[272] H. Mirels. Boundary layer behind shock or thin expansion wave moving into stationary fluid. Discussion paper, NACA, 1956.

[273] R. A. Hartunian, A. L. Russo, and P. V. Marrone. Boundary-layer transition and heat transfer in shock tubes. *J. Aerosp. Sci.*, 27(8):587–594, 1960.

[274] V. Monnier, V. Rodriguez, P. Vidal, and R. Zitoun. An analysis of three-dimensional patterns of experimental detonation cells. *Combust. Flame*, 245:112310, 2022.

[275] J. Floyd, A. M. Kempf, A. Kronenburg, and R. H. Ram. A simple model for the filtered density function for passive scalar combustion les. *Combust. Theor. Model.*, 13(4):559–588, 2009. doi: 10.1080/13647830802632200. URL `https://doi.org/10.1080/13647830802632200`.

[276] A. A. Konnov. Yet another kinetic mechanism for hydrogen combustion. *Combust. Flame*, 203: 14–22, 2019.

[277] M. P. Burke, M. Chaos, Y. Ju, F. L. Dryer, and S. J. Klippenstein. Comprehensive H_2/O_2 kinetic model for high-pressure combustion. *Int. J. Chem. Kinet.*, 44(7):444–474, 2012.

[278] Mechanical and University of California at San Diego Aerospace Engineering (Combustion Research). Chemical-kinetic mechanisms for combustion applications, http://combustion.ucsd.edu, 2016.

[279] H. Wang and D. A. Sheen. Combustion kinetic model uncertainty quantification, propagation and minimization. *Prog. Energy Combust. Sci.*, 47:1–31, 2015.

[280] J. Crane, J. T. Lipkowicz, X. Shi, I. Wlokas, A. M. Kempf, and H. Wang. Three-dimensional detonation structure and its response to confinement. *Proc. Combust. Inst.*, 39(3):2915–2923, 2023.

[281] W. Fickett and W. C. Davis. *Detonation: theory and experiment*. Courier Corporation, 2000.

[282] J. H. S. Lee. Dynamic parameters of gaseous detonations. *Annu. Rev. Fluid Mech.*, 16(1):311–336, 1984.

[283] M. Kuznetsov, G. Ciccarelli, S. Dorofeev, V. Alekseev, Y. Yankin, and T. H. Kim. DDT in methane-air mixtures. *Shock Waves*, 12(3):215–220, 2002.

[284] M. Kuznetsov, V. Alekseev, I. Matsukov, and S. J. S. W. Dorofeev. DDT in a smooth tube filled with a hydrogen–oxygen mixture. *Shock Waves*, 14(3):205–215, 2005.

[285] R. Knystautas, J. H. S. Lee, and C. M. Guirao. The critical tube diameter for detonation failure in hydrocarbon-air mixtures. *Combust. Flame*, 48:63–83, 1982.

[286] M. I. Radulescu and J. H. S. Lee. The failure mechanism of gaseous detonations: experiments in porous wall tubes. *Combust. Flame*, 131(1-2):29–46, 2002.

[287] X. Shi, J. Crane, and H. Wang. Detonation and its limit in small tubes with ozone sensitization. *Proc. Combust. Inst.*, 38(3):3547–3554, 2021.

[288] F. Haloua, M. Brouillette, V. Lienhart, and G. Dupré. Characteristics of unstable detonations near extinction limits. *Combust. Flame*, 122(4):422–438, 2000.

[289] S. B. Murray and J. H. S. Lee. On the transformation of planar detonation to cylindrical detonation. *Combust. Flame*, 52:269–289, 1983.

[290] B. A. Rankin, M. L. Fotia, A. G. Naples, C. A. Stevens, J. L. Hoke, T. A. Kaemming, S. W. Theuerkauf, and F. R. Schauer. Overview of performance, application, and analysis of rotating detonation engine technologies. *J. Propul. Power*, 33(1):131–143, 2017.

[291] D. A. Kessler, V. N. Gamezo, and E. S. Oran. Simulations of flame acceleration and deflagration-to-detonation transitions in methane–air systems. *Combust. Flame*, 157(11):2063–2077, 2010.

[292] R. Takai, K. Yoneda, and T. Hikita. Study of detonation wave structure. In *Symp. (Int.) Combust.*, volume 15, pages 69–78. Elsevier, 1975.

[293] D. N. Williams, L. Bauwens, and E. S. Oran. Detailed structure and propagation of three-dimensional detonations. In *Symp. (Int.) Combust.*, volume 26, pages 2991–2998. Elsevier, 1996.

[294] M. Hanana, M. H. Lefebvre, and P. J. Van Tiggelen. On rectangular and diagonal three-dimensional structures of detonation waves. *Gaseous and heterogeneous detonations: science to applications*, pages 121–130, 1999.

[295] N. Tsuboi, S. Katoh, and A. K. Hayashi. Three-dimensional numerical simulation for hydrogen/air detonation: Rectangular and diagonal structures. *Proc. Combust. Inst.*, 29(2):2783–2788, 2002.

[296] K. Eto, N. Tsuboi, and A. K. Hayashi. Numerical study on three-dimensional CJ detonation waves: detailed propagating mechanism and existence of OH radical. *Proc. Combust. Inst.*, 30(2):1907–1913, 2005.

[297] K. Eto, N. Tsuboi, and K. Hayashi. Three-dimensional cj detonation in rectangular tube. In *42nd AIAA Aerospace Sciences Meeting and Exhibit*, page 311, 2004.

[298] V. Deledicque and M. V. Papalexandris. Computational study of three-dimensional gaseous detonation structures. *Combust. Flame*, 144(4):821–837, 2006.

[299] Cheng C. Wang, C.-W. Shu, W. Han, and J. Ning. High resolution WENO simulation of 3D detonation waves. *Combust. Flame*, 160(2):447–462, 2013.

[300] C. Wang, X. Dong, and C.-W. Shu. Parallel adaptive mesh refinement method based on WENO finite difference scheme for the simulation of multi-dimensional detonation. *J. Comput. Phys.*, 298: 161–175, 2015.

[301] X. Cai, J. Liang, R. Deiterding, Y. Che, and Z. Lin. Adaptive mesh refinement based simulations of three-dimensional detonation combustion in supersonic combustible mixtures with a detailed reaction model. *Int. J. Hydrogen Energy*, 41(4):3222–3239, 2016.

[302] N. Tsuboi, K. Eto, and A. K. Hayashi. Detailed structure of spinning detonation in a circular tube. *Combust. Flame*, 149(1-2):144–161, 2007.

[303] N. Tsuboi, Y. Daimon, and A. L. Hayashi. Three-dimensional numerical simulation of detonations in coaxial tubes. *Shock Waves*, 18(5):379, 2008.

[304] D.-R. Cho, S.-H. Won, J.-R. Shin, and J.-Y. Choi. Numerical study of three-dimensional detonation wave dynamics in a circular tube. *Proc. Combust. Inst.*, 34(2):1929–1937, 2013.

[305] W. Chen, J. Liang, X. Cai, and Y. Mahmoudi. Three-dimensional simulations of detonation propagation in circular tubes: Effects of jet initiation and wall reflection. *Physics of Fluids*, 32(4):046104, 2020.

[306] R. A. Strehlow, R. Liaugminas, R. H. Watson, and J. R. Eyman. Transverse wave structure in detonations. In *Symp. (Int.) Combust.*, volume 11, pages 683–692. Elsevier, 1967.

[307] A. A. Vasiliev and Y. Nikolaev. Closed theoretical model of a detonation cell. In *Gasdynamics of Explosions and Reactive Systems*, pages 983–996. Elsevier, 1980.

[308] J. Crane, X. Shi, J. T. Lipkowicz, A. M. Kempf, and H. Wang. Geometric modeling and analysis of detonation cellular stability. *Proc. Combust. Inst.*, 38(3):3585–3593, 2021.

[309] S. Taileb, J. Melguizo-Gavilanes, and A. Chinnayya. The influence of the equation of state on the cellular structure of gaseous detonations. *Phys. Fluids*, 33(3):036105, 2021.

[310] Z. Weng and R. Mével. Real gas effect on steady planar detonation and uncertainty quantification. *Combust. Flame*, 245:112318, 2022.

[311] B. D. Taylor, D. A. Kessler, and E. S. Oran. Estimates of vibrational nonequilibrium time scales in hydrogen-air detonation waves. In *24th International Colloquium on the Dynamics of Explosive and Reactive Systems, Taipei, Taiwan, July*, volume 23, page 44, 2013.

[312] L. Shi, H. Shen, P. Zhang, D. Zhang, and C. Wen. Assessment of vibrational non-equilibrium effect on detonation cell size. *Combust. Sci. Technol.*, 189(5):841–853, 2017.

[313] J. Braun, J. Sousa, and G. Paniagua. Numerical assessment of the convective heat transfer in rotating detonation combustors using a reduced-order model. *Applied Sciences*, 8(6):893, 2018.

[314] F. K. Lu and E. M. Braun. Rotating detonation wave propulsion: experimental challenges, modeling, and engine concepts. *J. Propul. Power*, 30(5):1125–1142, 2014.

[315] J. Crane, X. Shi, A. V. Singh, Y. Tao, and H. Wang. Isolating the effect of induction length on detonation structure: Hydrogen–oxygen detonation promoted by ozone. *Combust. Flame*, 200: 44–52, 2019.

[316] V. P. Korobeinikov. *Problems of point blast theory*. Springer Science & Business Media, 1991.

[317] J.W. Meyer and A.K. Oppenheim. On the shock-induced ignition of explosive gases. In *Symp. (Int.) Combust.*, volume 13, pages 1153–1164. Elsevier, 1971.

[318] R.K. Hanson, G.A. Pang, S. Chakraborty, W. Ren, S. Wang, and D.F. Davidson. Constrained reaction volume approach for studying chemical kinetics behind reflected shock waves. *Combust. Flame*, 160(9):1550–1558, 2013.

[319] J. Crane, X. Shi, J.T. Lipkowicz, A.M. Kempf, and H. Wang. Geometric modeling and analysis of detonation cellular stability. *Proc. Combust. Inst.*, 38(3):3585–3593, 2021.

[320] G. Rudinger. Effect of boundary-layer growth in a shock tube on shock reflection from a closed end. *Phys. Fluids*, 4(12):1463–1473, 1961.

[321] M. Carlsson, L. Davidson, S.-H. Peng, and S. Arvidson. Investigation of low-dissipation low-dispersion schemes for incompressible and compressible flows in scale-resolving simulations. *Comput. Fluidsuids*, 251:105741, 2023.

[322] D. Nativel, S. P. Cooper, J. T. Lipkowicz, M. Fikri, E. L. Petersen, and C. Schulz. Impact of shock-tube facility-dependent effects on incident-and reflected-shock conditions over a wide range of pressures and mach numbers. *Combusti. Flame*, 217:200–211, 2020.

[323] J. Pareja, J. T. Lipkowicz, E. Inanc, C. D. Carter, A. M. Kempf, and I. Boxx. An experimental/numerical investigation of non-reacting turbulent flow in a piloted premixed bunsen burner. *Exp. Fluids*, 63(1):33, 2022.

[324] D. Meller, J. T. Lipkowicz, M. Rieth, O. T. Stein, A. Kronenburg, C. Hasse, and A. M. Kempf. Numerical analysis of a turbulent pulverized coal flame using a flamelet/progress variable approach and modeling experimental artifacts. *Energy & Fuels*, 35(9):7133–7143, 2021.

[325] M. Leer, M. W. A. Pettit, J. T. Lipkowicz, P. Domingo, L. Vervisch, and A. M. Kempf. A conservative eulerian-lagrangian decomposition principle for the solution of multi-scale flow problems at high schmidt or prandtl numbers. *J. Comput. Phys.*, 464:111216, 2022.

[326] E. Inanc, J. T. Lipkowicz, and A. M. Kempf. Detailed simulations of the dlr auto-igniting pulsed jet experiment. *Fuel*, 284:118947, 2021.

DOI: 10.17185/duepublico/82246
URN: urn:nbn:de:hbz:465-20240809-133916-0